The integration of bulk PZT transducers in a microfabricated cuff implant for Vagus Nerve ultrasound neuromodulation

Simulation, design and fabrication

EEMCS - Microelectronics - Bioelectronics
Niels van Damme

Delft University of Technology

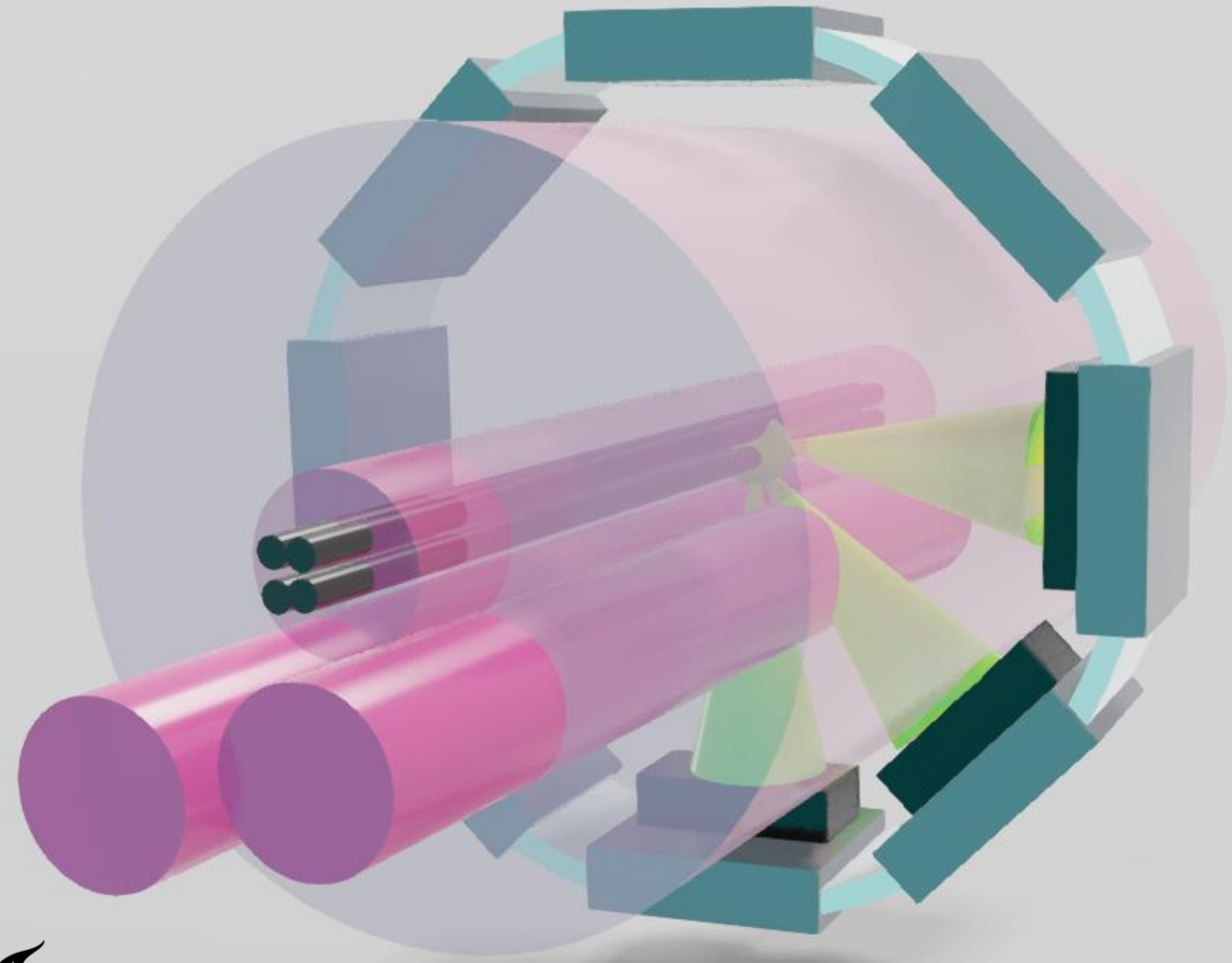

TU Delft Fraunhofer

The integration of bulk PZT transducers in a microfabricated cuff implant for Vagus Nerve ultrasound neuromodulation

Simulation, design and fabrication

by

Niels van Damme

to obtain the degree of Master of Science
at the Delft University of Technology,
to be defended publicly on Monday September 25, 2023 at 10:30 AM.

Student number: 4928237

Project duration: September 5, 2022 – September 25, 2023

Thesis committee:

Dr. T. Costa,	TU Delft, supervisor
Dr. V. Giagka,	TU Delft & Fraunhofer IZM, supervisor
Dr. M. Mastrangeli,	ECTM
MSc. G. Wardhana,	TU Delft Bioelectronics
MSc. A. Velea,	Fraunhofer IZM Bioelectronics

This thesis is confidential and cannot be made public until September 30, 2025.

Cover: The cuff implant concept, drawn in Vectary
Style: TU Delft Report Style, with modifications by Niels van Damme

An electronic version of this thesis is available at `http://repository.tudelft.nl/`.

TU Delft Fraunhofer IZM

Preface

This thesis project has been done in collaboration with and under the supervision of the Bioelectronics research group at Delft University of Technology. For the microfabrication, the Else Kooi Lab at the EEMCS faculty has been used. The topic of this thesis work is the integration of bulk Lead Zirconate Titanate (PZT) ultrasound transducers in a microfabricated cuff implant for Vagus Nerve acoustic stimulation. Topics like ultrasound neuromodulation and microfabrication are involved. As this project required both knowledge about ultrasound and implants, it has been done in a shared collaboration with the research group of Dr. Tiago Costa which has expertise in ultrasound, and with the research group of Dr. Vasiliki Giagka which has expertise in implants.

In this thesis, you will find simulation results, designs for a cuff implant, the wafer-level microfabrication process and the ultrasonic characterization of fabricated cuff implants. The project demonstrates a wafer-level microfabrication process to fabricate an island-bridge, 2 mm in diameter curved cuff implant for Vagus Nerve stimulation. Moreover, the prototypes are being tested with an ultrasound setup, thus demonstrating the integration of piezoelectric ultrasound transducers in a cuff-shaped substrate. The curvature of the cuff-substrate leads to the constructive interference of ultrasound waves from multiple ultrasound transducers.

First of all, I would like to thank Dr. Tiago Costa and Dr. Vasiliki Giagka for their time, support and help. In all the meetings they gave great feedback and assisted me during the time of this thesis project. Besides them, I would like to express my thankfulness to the members of both research groups. Thank you, Gandhika Wardhana for being my daily supervisor. You assisted me with practical things in the cleanroom and were always available to answer questions or help solve problems. Thank you, Andrada Velea for your support and critical reflections on the process and my work. With your useful feedback, you helped to improve the thesis work.

Moreover, I would like to express my appreciation to Gonzalo León González, Hidde Woerdman and Eduardo Puchol for the good collaboration. Besides, I would like to thank the Else Kooi Lab staff, especially Hande Aydogmus, for their support, giving me the necessary training and tools to do the wafer-level microfabrication process.

My gratitude is large to my parents and family who guided me through, showed their interest and supported me, even if I had less time for them during this busy period. After all, I would like to express my gratitude to God who helped me in my work and gave me the capabilities to complete this thesis work. *Soli Deo Gloria*

Niels van Damme
Heinkenszand, September 2023

Abstract

In the emerging research field of bioelectronic medicine, it has been indicated that neuromodulation of the Vagus Nerve (VN) has the potential to treat various conditions such as epilepsy, depression, and autoimmune diseases. In order to reduce side effects, as well as to increase the effectiveness of the delivered therapy, sub-fascicle stimulation specificity is required. In the electrical domain, increasing spatial selectivity can only be achieved using invasive and potentially damaging approaches like compressive forces or nerve penetration. To avoid these invasive methods, while obtaining a high spatial selectivity, a 2 mm diameter extraneural cuff-shaped proof-of-concept design with integrated Lead Zirconate Titanate (PZT) based ultrasound (US) transducers is proposed in this paper. For the development of the proposed concept, wafer-level microfabrication techniques are employed. Moreover, acoustic measurements are performed on the device, in order to characterize the ultrasonic beam profiles of the integrated PZT-based US transducers. A focal spot size of 200 μm by 200 μm is measured for the proposed cuff. Moreover, the curvature of the device leads to constructive interference of the US waves originating from multiple PZT-based US transducers, which in turn leads to an increase of 45% in focal pressure compared to the focal pressure of a single PZT-based US transducer. Integrating PZT-based US transducers in an extraneural cuff-shaped design has the potential to achieve high-precision US neuromodulation of the Vagus Nerve without requiring intraneural implantation.

Contents

List of Figures

List of Tables

1

Introduction

The medical field has been developing at a high pace. The number of new medical methods for healing or suppressing diseases has risen very fast. Next to biological, medical, and biochemical research, technology is taking an ever greater place in medicine. Devices for monitoring, sensing, and adjusting biological parameters have existed for several decades. However, technology is currently shifting to the treatment of diseases. Especially the electronic field is being involved in therapeutics more and more. Innovative techniques are being developed for electronic drug delivery [1], specialistic surgery [2], and organ research [3].

Within the bioelectronics field, research on implants and electroceuticals in bioelectronic medicine is advancing. Electronic devices are being developed to modulate and measure the electrical signals of the body. In this thesis, the focus will be on ultrasound neuromodulation devices. The application of ultrasound technologies in the medical field has been extended from diagnostic imaging to therapeutic neuromodulation [4]–[6]. Among several stimulation targets, Vagus Nerve Stimulation (VNS) using focused ultrasound has been explored in recent years [7]–[10].

The Vagus Nerve (VN) is a cranial nerve, part of the parasympathetic nervous system, consisting of afferent and efferent neurons [11]–[14]. The VN fascicles comprise of different nerve fibers, classified, according to Erlanger Gasser as type A, B, and C, each having their own functions, sizes (ranging from $<$0.5 μm up to 10 μm), and conduction velocities (ranging from 0.5 to 120 m/s) [12], [14].

The VN is involved in the autonomic, cardiovascular, respiratory, gastrointestinal, immune, and endocrine systems [12]. Research shows that stimulation is useful in the therapy of epilepsy, depression, and several chronic diseases like Alzheimer's disease, anxiety, congestive heart failure, pain, tinnitus, and inflammatory diseases [11], [12], [15]–[19]. Targeted stimulation on the sub-fascicle level is needed since unintended stimulation of other fascicles can lead to severe side effects [15], [20].
The spatial resolution of electrical stimulation by means of electrodes is limited extraneurally and can only be increased using invasive and potentially damaging approaches like compressive forces or nerve penetration. Ultrasound (US) neuromodulation is an emerging technique that uses focused ultrasound waves to modulate neuronal activity with high-spatial resolution [7]–[9], [21]–[23]. The waves can propagate through tissue up to several centimeters, depending on the tissue and transducer parameters [4], [6], [24]. This allows for a minimally invasive and yet precise (a focal spot as small as 110 μm by 570 μm) manner to neuromodulate neural tissue [10], [25]. Integrating piezoelectric ultrasound transducers in an extraneural cuff-shaped design has the potential to achieve high-precision ultrasound neuromodulation of the VN without requiring intraneural implantation.

This thesis is about the integration of Lead Zirconate Titanate (PZT) piezoelectric transducers in a wafer-level microfabricated cuff implant form factor for Vagus Nerve Stimulation (VNS). In Chapter 2 the core of the thesis project is summarized in a paper. Each summarized topic in the paper is extended in the subsequent chapters. Chapter 3 gives the context of the main research themes and provides relevant background information on topics like the VN, neuromodulation, ultrasound stimula-

tion, ultrasound transducers and wafer-level microfabrication. In Chapter 4 the finite element methods (FEM) simulations can be found. These simulations are done to set requirements for the design of the cuff implant. The design of the cuff implant is described in Chapter 5 explaining the requirements and calculations. The wafer-level microfabrication process flow can be found in Chapter 6. This chapter describes all the process steps that have been taken to obtain a working cuff implant with integrated bulk PZT transducers. Chapter 7 gives an overview of the measurement setup and the results obtained. Afterwards, the results are discussed and compared. This thesis is summarised with Chapter 8 in which recommendations are given and with Chapter 9 for the future work. The thesis concludes with Chapter 10.

2

A high-frequency flexible ultrasonic cuff implant for high-precision Vagus Nerve ultrasound neuromodulation

A High-Frequency Flexible Ultrasonic Cuff Implant for High-Precision Vagus Nerve Ultrasound Neuromodulation

Cornelis van Damme, Gandhika Kumara Wardhana, Andrada Iulia Velea, Vasiliki Giagka*, *Senior Member, IEEE* and Tiago Costa*, *Member, IEEE*
*These authors contributed equally

***Abstract*— In the emerging research field of bioelectronic medicine, it has been indicated that neuromodulation of the Vagus Nerve (VN) has the potential to treat various conditions such as epilepsy, depression, and autoimmune diseases. In order to reduce side effects, as well as to increase the effectiveness of the delivered therapy, sub-fascicle stimulation specificity is required. In the electrical domain, increasing spatial selectivity can only be achieved using invasive and potentially damaging approaches like compressive forces or nerve penetration. To avoid these invasive methods, while obtaining a high spatial selectivity, a 2 mm diameter extraneural cuff-shaped proof-of-concept design with integrated Lead Zirconate Titanate (PZT) based ultrasound (US) transducers is proposed in this paper. For the development of the proposed concept, wafer-level microfabrication techniques are employed. Moreover, acoustic measurements are performed on the device, in order to characterize the ultrasonic beam profiles of the integrated PZT-based US transducers. A focal spot size of 200 μm by 200 μm is measured for the proposed cuff. Moreover, the curvature of the device leads to constructive interference of the US waves originating from multiple PZT-based US transducers, which in turn leads to an increase of 45% in focal pressure compared to the focal pressure of a single PZT-based US transducer. Integrating PZT-based US transducers in an extraneural cuff-shaped design has the potential to achieve high-precision US neuromodulation of the Vagus Nerve without requiring intraneural implantation.**

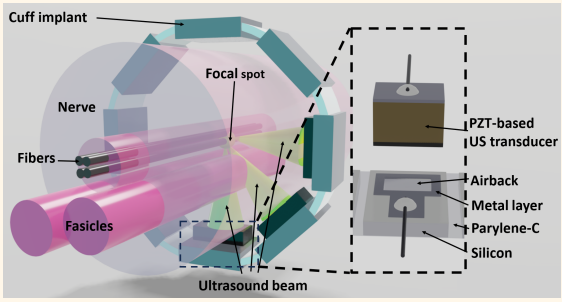

***Index Terms*— cuff implant, flex-to-rigid, microfabrication, piezoelectric ultrasound transducers, PZT integration, ultrasound neuromodulation, Vagus Nerve**

I. Introduction

The application of ultrasound (US) technologies in the medical field has been extended from diagnostic imaging to therapeutic neuromodulation [1]–[3]. Among several stimulation targets, Vagus Nerve Stimulation (VNS) by means of focused US has been explored in recent years [4]–[7]. The Vagus Nerve (VN) is a cranial nerve, part of the parasympathetic nervous system, consisting of afferent and efferent neurons [8]–[11]. The VN nerve fascicles comprise of different nerve fibers, classified, according to Erlanger Gasser as type A, B, and C, each having their own functions, sizes (ranging from <0.5 μm up to 10 μm), and conduction velocities (ranging from 0.5 to 120 m/s) [8], [9]. The VN is involved in the autonomic, cardiovascular, respiratory, gastrointestinal, immune, and endocrine systems [8]. Research shows that stimulation is useful in the therapy of epilepsy, depression, and several chronic diseases like Alzheimer's disease, anxiety, congestive heart failure, pain, tinnitus, and inflammatory diseases [8], [11]–[16]. Targeted stimulation on the sub-fascicle level is needed since unintended stimulation of other fascicles can lead to severe side effects [16], [17].

Conventionally, electricity is used to interact with the peripheral nervous system [18]. Transcutaneous VNS (tVNS) is mentioned as a non-invasive method [16], [19]–[23]. Although studies show that activation is elicited, the envisioned sub-fascicle stimulation resolution is not met [24]. Improved resolution can be achieved with implantable devices having embedded electrodes. A promising type of electrode for stimulation is the cuff electrode [25]–[29]. To reach the sub-

Submitted 25th September 2023. This work was supported in part by the ECSEL Joint Undertaking project Moore4Medical, grant number H2020-ECSEL-2019IA-876190.

C. van Damme, G. K. Wardhana, A. I. Velea, V. Giagka and T. Costa are with the Department of Microelectronics, Delft University of Technology, Delft, The Netherlands (e-mail: v.giagka@tudelft.nl; t.m.l.dacosta@tudelft.nl).

A. I. Velea and V. Giagka, are also with the Department of System Integration and Interconnection Technologies, Fraunhofer IZM, Berlin, Germany

Highlights

- **Integration of PZT transducers in a wafer-level microfabricated cuff-implant for Vagus Nerve stimulation.**
- **The wafer-level microfabricated cuff-implant can be bent having a diameter of 2 mm and shows in the bent configuration constructive interference at the focal spot.**
- **A highly specific, high-frequency extraneural ultrasonic neuromodulation cuff-implant that gives the opportunity to stimulate the Vagus Nerve on sub-fascicle level.**

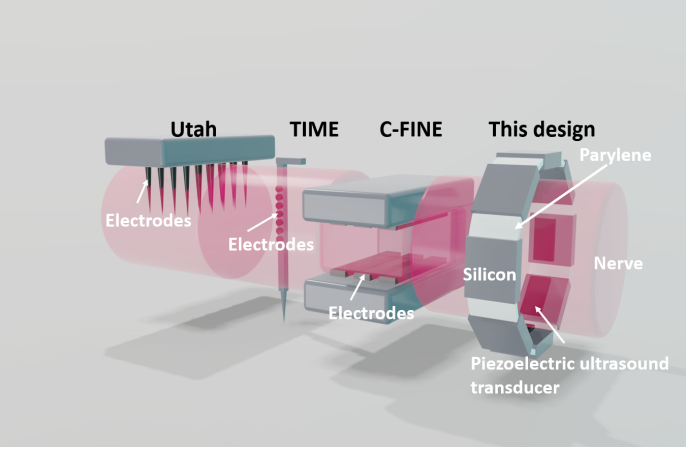

Fig. 1. A comparison of the Utah, TIME, and C-FINE electrodes with the current design.

fascicle resolution with electrodes, techniques like composite flat interface nerve electrodes (C-FINE) [30], slowly penetrating inter-fascicular nerve electrodes (SPINE) [31] and intra-fascicular techniques like longitudinal intra-fascicular electrode (LIFE) [25] and transverse intra-fascicular multichannel electrode (TIME) [25] and microelectrode arrays (MEAs), for example, the Utah array [32], are being developed [33]. The disadvantages of the aforementioned techniques are the needed compressive force and high invasiveness which increase the risk of damage to the nerve during implantation (Fig. 1). Therefore, this makes these techniques unsuitable for chronic applications.

Instead of using electrodes, integrating Lead Zirconate Titanate (PZT) based US transducers in a cuff implant form factor would enable the possibility of delivering US neuromodulation, extraneurally, yet with a high spatial resolution (Fig. 1). It has been previously demonstrated that a focal spot of 110 μm by 570 μm can be achieved when capacitive micromachined ultrasound transducers (cMUTs) are placed under the nerve and are geometrically curved at radii matching that of the VN [7]. Based on the well-described physical phenomena of US, it has been shown that US can be beamsteered [34], [35] and can propagate through tissue for several centimeters without causing damage and side effects [2], [3], [36], [37]. Despite the biological mechanisms of US neuromodulation not yet being perfectly understood, it is likely that different combinations of partially overlapping mechanisms occur in the cell membrane depending on the US pulse regime [2]–[4], [38]–[41]. Several studies show that focused US can elicit a physiological response in nerves [4]–[6], [28], [41]–[44].

US waves are generated by either bulk piezoelectric transducers, or by flexural mode transducers, such as cMUTs and piezoelectric micromachined ultrasound transducers (pMUTs) [34], [45]–[48]. For bulk mode PZT-based US transducers, which are characterized by a high transmit electroacoustic sensitivity (S_{tx}) and a high-quality factor [34], PZT ceramics are commonly used due to their superior piezoelectric constants [49]. These are important characteristics for US neuromodulation as they lead to higher and more stable pressure amplitudes per driving voltage [34], [45], [46]. pMUT and cMUT devices have a lower S_{tx} and lower quality factor, and hence are more suitable for high-quality imaging and sensing applications where bandwidth is important [34], [49]. The pressure output of an integrated cMUT-array in a cuff implant form factor using 60 V_{pp} for excitation with beamsteering has been measured to generate 1.7 MPa at most (S_{tx} = 28.3 kPa/V) [35]. Another planar design with a 2D PZT-array with 5 V_{pp} generated up to 0.1 MPa (S_{tx} = 20 kPa/V) [34]. As the output pressure correlates with the driving voltage [50] and the focusing of the beam, the S_{tx} is a good parameter for comparison.

Currently, there is no consensus on the amount of intensity or pressure needed for neuromodulation of peripheral nerves. However, research suggests that peripheral nerves require higher pressures than e.g. brain tissue for neuromodulation and that pressures in the range of 3 MPa are sufficient [4]. To date, a method to integrate bulk PZT-based US transducers in a flexible cuff compatible with VNS was not yet demonstrated [24].

In this paper, a form factor compatible with the VN with integrated PZT-based US transducers is proposed. We investigate whether this design can reach high acoustic pressures with low peak-to-peak driving voltages and still maintain high spatial resolution. The organization of the paper is as follows: in section II the design choices and the necessary COMSOL Multiphysics [51] simulations are elaborated upon. Section III describes the design and elaborates on the wafer-level microfabrication process flow and the assembly of the PZT-based cuff prototypes (section III-A). In section IV the device is characterized and the acoustic measurements are described. The results are discussed in section V, whereas section VI gives an overview of the future work. Section VII draws the conclusions.

II. Simulations

The concept, shown in Fig. 1, is a cuff-shaped, airbacked, island-bridge structure with three 8.4 MHz PZT-based US transducers. In Table I the main design parameters are given. The inner diameter of the cuff is 2 mm, as the VN has a

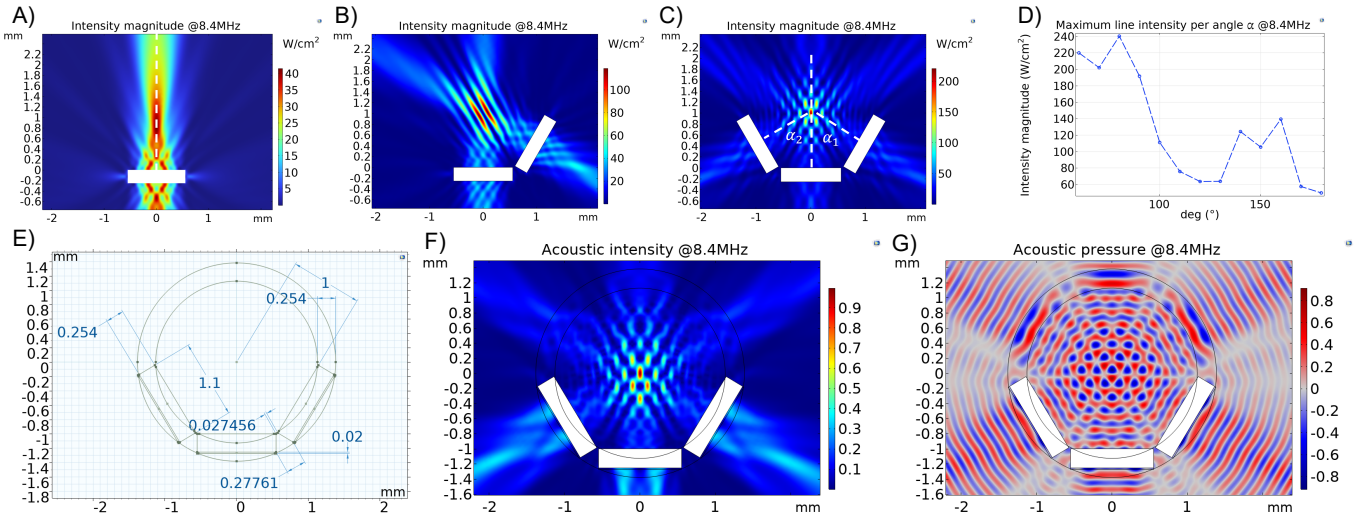

Fig. 2. Simulation results A), B), and C) show the focal spot size and acoustic intensity for one, two, and three non-airbacked PZT-based US transducers in a curved configuration. D) shows the relation between the angle between three non-airbacked PZT-based US transducers and the maximum acoustic intensity magnitude. E) shows the dimensions for the simulated cuff design, whereas F) and G) show the non-airbacked acoustic magnitude and pressure profiles respectively.

diameter of about 2-4 mm [7]. The aperture of the PZT relates to the focal length and driving frequency according to [52]:

$$N = \frac{f_p L^2}{4v} \tag{1}$$

where N is the focal length [m], L the aperture [m], f_p the driving frequency [Hz] and v the speed of sound in the medium [m/s]. The focal length of each PZT-based US transducer has been designed to be around 1 mm, such that the focal point of all PZT-based US transducers comprising the cuff is in the center of the design, as well as, of the nerve. As the cuff form factor is defined with a radius of 1 mm, the aperture of single PZTs can also not be larger than the chord of 12.5 % of the circumference otherwise it will limit the circular shape.

Frequencies for neuromodulation in pre-clinical or clinical research can scale from sub-MHz (transcranial US neuromodulation) to a few MHz (VNS). Increasing the frequency leads to a tradeoff between spatial resolution and absorption, hence the frequency should be carefully set. The driving frequency is inversely proportional to the aperture (1), the focal spot size (2) and (3), and the thickness (4) of the PZT [45], [52]. The equations for the full width at half bandwidth *FHWM* [34], the depth of field *DOF* [34], and thickness of the PZT at resonance (t_{PZT}) [49] are given in (2), (3), and (4) respectively.

$$FWHM \propto \frac{\lambda Z_m}{L} \tag{2}$$

where λ is the wavelength of the US waves [m], Z_m is the focal depth [m] and L the aperture [m].

$$DOF \propto \frac{\lambda Z_m^2}{L^2} \tag{3}$$

$$t_{PZT} = \frac{\lambda}{2} \tag{4}$$

In this study, it has been assumed that the acoustic wave is propagating in a homogeneous medium and that there is no gap between the implant and the nerve. Therefore, attenuation caused by the tissue can be neglected. The PZT thickness, defining the resonance frequency, can constrain the curvature of the design as the top of the PZTs could touch each other for large PZT thicknesses. As the thickness of the PZTs is in the range of the silicon thickness (around 300 μm), it does not constrain the design. Moreover, the frequency determines the aperture, whereas the aperture has a tradeoff between the focal length and the maximum size for curvature. Therefore, the frequency should be set to be as high as possible to have a high spatial resolution, yet with the PZT-based US transducer size fitting the design dimensions. Therefore, a frequency of 8.4 MHz has been set. Moreover, other research shows that similar driving frequencies (9.56 and 8.4 MHz) provide resolution in the μm-range [34], [52].

TABLE I
DESIGN PARAMETERS

Parameters	Numbers
Frequency $[MHz]$	8.4
Diameter $[mm]$	2
# of PZT-based US transducers	3
PZT thickness $[\mu m]$	254
PZT aperture $[\mu m]$	1100
PZT length $[\mu m]$	450
Focal length $[mm]$	1
Active area $[mm^2]$	1.18

A. Methods

To define the effect of the number of non-airbacked PZT-based US transducers, the impact of an airbacking layer, and to verify the design, COMSOL Multiphysics simulations have been performed. The 2D finite element method simulations

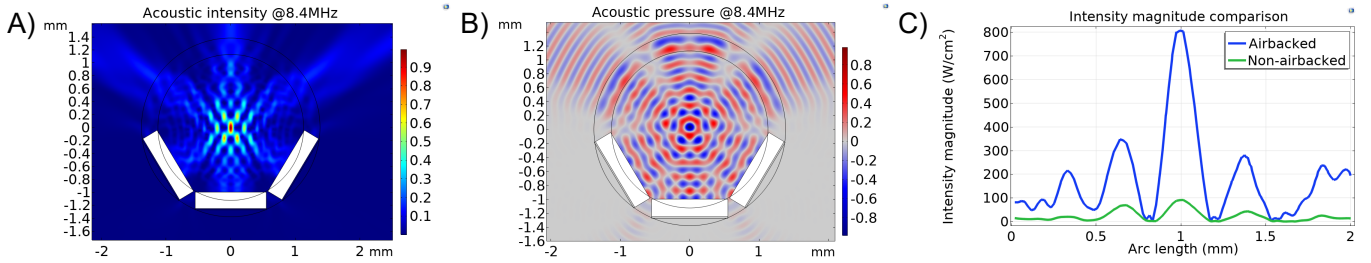

Fig. 3. Simulation results for an airbacked design. In A) and B) the acoustic intensity magnitude profile and acoustic pressure profile of the 8.4 MHz, three PZT-based US transducers, airbacked cuff design is shown. C) shows the comparison between the acoustic magnitude of the airbacked and non-airbacked device.

have been done in the frequency domain, using the pressure acoustics, solid mechanics, and electrostatics COMSOL models. A free triangular mesh with a maximum element size of $v/f_p/8$ has been used. Water medium has been used as a replacement for nerve tissue since the acoustic properties are similar [45]. The boundary of the water medium is set to be perfectly matched to avoid reflections at the edges. In addition, PZT-5H has been used as a piezoelectric material for the PZT-based US transducers and a driving voltage of 10 V_{pp} has been defined, being the maximum output voltage of the function generator used during measurements. To ensure the focal point is in the center of the device, the distance between the surface of a PZT-based US transducer and the center has been set to 1 mm.

The first simulation has been done to investigate the effect of the number of non-airbacked PZT-based US transducers on the pressure profile and pressure levels. The number of PZT-based US transducers has been swept from an individual PZT-based US transducer to three PZT-based US transducers. The next simulation is a rotational sweep of the angles α_1, α_2 which are the angles between one of the side PZT-based US transducers and the bottom-middle PZT-based US transducer (Fig. 2C). These angles are equal for the left and right side ($\alpha_1 = \alpha_2$) and are being swept from 50° to 180°.

A disadvantage of bulk PZT-based US transducers is the large acoustic mismatch with tissue (34 MRayl for PZT material and 1.5 MRayl for tissue) resulting in reflections of the incident power, reducing the transmitted power according to (5) [45].

$$T = 1 + R = 1 + \frac{Z_2 - Z_1}{Z_2 + Z_1} \tag{5}$$

where T is the amplitude transmission coefficient and R the amplitude transmission coefficient. Z_1 and Z_2 are the acoustic impedances of the materials in medium 1 and 2 respectively.

An acoustic matching layer at the top and a backing layer at the bottom of the PZT-based US transducer can be implemented to increase the transmission efficiency [34]. For a backing material airbacking shows good properties and can be implemented in a wafer-level microfabrication process flow [53]. Therefore, the third simulation is the implementation of an airbacking layer below the PZT-based US transducer. This has been modeled as a rectangle below the PZT-based US transducer filled with air as the material. After sweeping the depth from 10 μm to 100 μm the pressure magnitude reached the maximum and saturated around 20 μm. Therefore a height of 20 μm has been taken for the airbacking layer.

After, a full design with three PZT-based US transducers and a polymer ring of parylene-C was simulated to verify the focal spot and the design dimensions. The cuff implant form factor has been modeled as a perfect circle. The first simulations have been performed with non-airbacked devices, filling the 20 μm thick rectangles with silicon as material. The final simulations include the airbacked PZT-based US transducer. The simulation dimensions are shown in Fig. 2E.

B. Results

From simulations, it was found that the increase of the number of non-airbacked PZT-based US transducers increases the acoustic intensity magnitude in case they are placed in a curved configuration. According to the simulations, the focal pressure is 40 W/cm^2 for one PZT-based US transducer and increases to 120 W/cm^2 for two PZT-based US transducers and to 210 W/cm^2 for three PZT-based US transducers (Fig. 2A, Fig. 2B, and Fig. 2C) respectively. The increase of the acoustic intensity becomes less significant the more PZT-based US transducers are added. Moreover, with more PZT-based US transducers the focal spot size decreases and destructive interference patterns appear.

The result of a sweep of three PZT-based US transducers is shown in Fig. 2D. It can be observed that for smaller angles between the PZT-based US transducers, a higher acoustic intensity magnitude exists in this form factor. The intensity for an angle of 180°, so the PZT-based US transducers oppose each other, is reduced to 75% of the maximum acoustic intensity magnitude. Although opposite PZT-based US transducers might be beneficial in different designs and in cases of beamsteering, in this design, it has been concluded based on this simulation that opposing PZT-based US transducers should be avoided. This limits the placement of PZT-based US transducers to only 40% of the cuff circumference.

Moreover, the number of PZT-based US transducers is determined by the aperture of the PZTs and the inter-PZT distance. The aperture of the PZTs is set by the aforementioned driving frequency. The inter-PZT distance between the PZT-based US transducers when curved, is optimized to be a multiple of $\lambda_{water}/2$ for minimizing the side lobes while having the smallest distance (Fig. 2D). For a driving frequency of 8.4 MHz, three PZT-based US transducers do fit in the 2 mm cuff design (Fig. 2E).

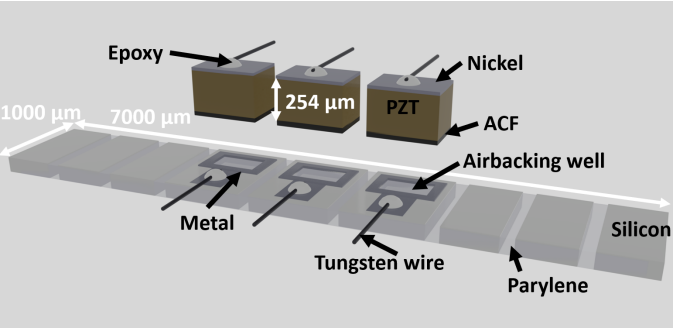

Fig. 4. Planar design of the proposed cuff implant.

The cuff implant design has first been simulated without airbacking of which the acoustic magnitude and pressure profiles can be found in Fig. 2F and 2G respectively. The acoustic waves are emitted from both the front- and back-side of the PZT-based US transducer. The simulation results for a complete airbacked cuff implant design can be found in Fig. 3A and Fig. 3B. In these figures, it is shown that the acoustic waves are emitted to the front side due to the airbacking. The acoustic intensity magnitude is increased by 8 times compared to the non-airbacked acoustic magnitude (Fig. 3C) at the focal spot (distance of 1 mm). Therefore, based on this simulation result, a 20 μm-deep airbacking well has been embedded in the design below the PZT-based US transducer to increase the acoustic intensity. Note that in COMSOL the intensity is a vector whereas the pressure is a scalar, resulting in different profiles. It can be observed that the focal spot for the acoustic intensity in the airbacked and non-airbacked design have a size of 80 μm by 170 μm and it is located in the center of the cuff shape. An extension of the finite element modelling can be found in Chapter 4.

III. Design

The development of the proposed cuff is based on wafer-level microfabrication processes [34], [54]–[56]. The flexibility of the final device is provided by the island-bridge approach where silicon islands are etched and interconnected with each other via a parylene-C layer. As silicon is used as a substrate, airbacking wells can be embedded [53]. The metal rings around the 20 μm-deep airbacking wells provide the electrical connection to the PZT-based US transducers (Fig. 4). The contact pads (500 μm by 500 μm) are directly connected to the metal rings with 500 μm-width traces.

The single planar device is 7 mm by 1 mm (Fig. 4). According to simulations in section II the resonance frequency and thus the driving frequency of the airbacked cuff concept is 8.4 MHz resulting in a PZT thickness of around 254 μm. Taking the design constraints into account, only three PZT-based US transducers can be placed (Fig. 4). The sizes of the PZT-based US transducers can be found in table I. The design is explained in more detail in Chapter 5.

A. Wafer-level microfabrication

The processing steps for the proposed wafer-level microfabrication process can be found in Fig. 5. A 300 μm-thick double-sided polished 100 mm diameter p-type silicon wafer has been used as a starting material (Fig. 5A). On top of the wafer 1 μm of Plasma-Enhanced Chemical Vapor Deposition (PECVD) oxide is deposited at 400°C for insulation and as a landing layer for deep reactive ion etching (DRIE) required later in the process, on the backside of the wafer. On top of this layer, a metal interconnect layer of 1 μm-thick AlSi (99%/1%) is sputtered at 50°C (Fig. 5B). AlSi (99%/1%) has been used as the material due to its high conductivity, low cost, and availability. This metal layer is patterned using a 2.1 μm-thick positive photoresist (SPR3012, Shipley) as a soft mask and is etched using HBr/Cl_2-based dry etching processes (Fig. 5C).

To remove the AlSi residues at the backside of the wafer and to open the SiO_2 layer for the airback wells, a combination of a wet and dry etching process has been used (Fig. 5D). A 4.0 μm-thick positive photoresist (SPR3027, Shipley) has been used as soft mask. The wet etching part consists of a 1-minute dip in a BHF (1:7) solution, whereas the dry etching process consists of a 2-minute dry etch (C_2F_6/CHF_3) in the plasma etcher (Triode 384T, Drytek). Next, a 4 μm-thick PECVD SiO_2 layer at 400° is deposited at the backside as a hard mask (Fig. 5E).

The 20 μm deep airback wells are etched in the silicon layer (Fig. 5F) using a DRIE process (Rapier Omega i2L DRIE etcher, SPTS). It uses the Bosch process to create high aspect-ratio trenches in the silicon substrate. As a masking layer, 4.0 μm-thick positive photoresist (SPR3027, Shipley) has been used. After, the PECVD oxide layer at the backside is opened using a fully dry etch step (Fig. 5G). For this etch step a 3.1 μm-thick positive photoresist (SPR3012, Shipley) as soft mask has been used. Afterward, the bulk silicon of the wafer is etched till the SiO_2 layer at the top side using DRIE (Fig. 5H). This creates a 1 μm-thick SiO_2 membrane in between rigid, silicon islands. This SiO_2 membrane serves as support during the parylene-C coating later on in the process.

Next, the wafer is diced in a 2-phase dicing process (Fig. 5I) using the dicer (DAD3221, Disco). In the first phase, the wafer is attached with the top side to a UV-sensitive dicing foil and the wafer is diced into several larger pieces of around 3 mm^2 by 3 mm^2. After releasing, each piece is individually diced into separate devices. For this phase, the acetone-sensitive dicing foil is used, since the devices can be self-released from the foil using acetone, thus preserving the thin SiO_2 membrane. To maintain the thin SiO_2 membrane during dicing, the dicing speed is set to 1 mm/s and a thin silicon edge (10μm) is preserved, which does not interfere during the bending process (Fig. 6B).

Commercial PZT-5H 8 MHz sheets from piezo.com are used for the PZT-based US transducers. For conduction purposes, a 30 μm-thick anisotropic conductive film (ACF, ARclad 9032-70) is attached to one side of the PZT-5H sheet before dicing. The other side of the PZT has a 0.1 μm sputtered nickel layer (Fig. 4). The PZT-sheet with ACF is diced into the sizes presented in Table I. With the pick-and-place tool (Accelonix, T-300 bonder), the PZTs are placed on the metal contact rings at the silicon substrate (Fig. 5J). Despite the beamsplitter being used for alignment, some spatial variation exists, which results

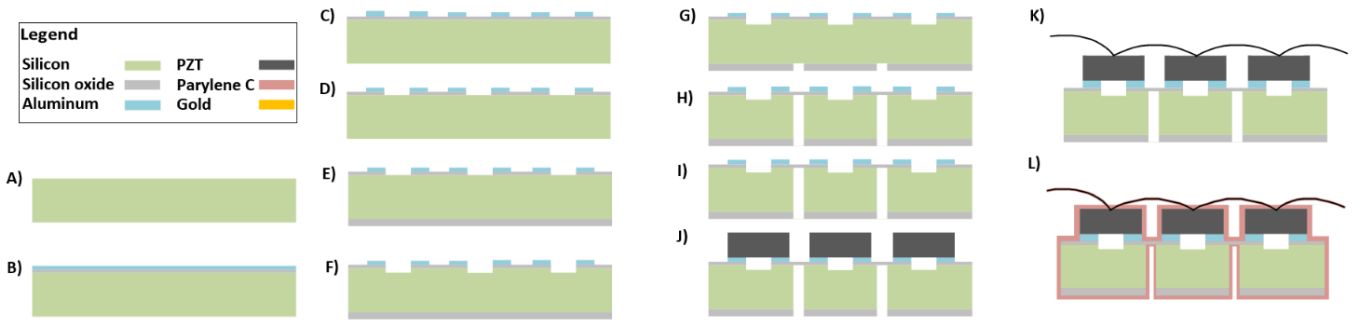

Fig. 5. The wafer-level microfabrication process steps A) the process starts with a wafer on which alignment markers are etched B) a layer of SiO_2 and on top a layer of $AlSi$ is deposited C) the $AlSi$ layer is patterned D) the SiO_2 is etched E) a SiO_2 layer is deposited at the backside F) the airbacking wells are etched in the silicon on the top side G) the SiO_2 at the backside is patterned H) the silicon substrate is etched from the backside I) the wafer is diced J) PZTs are placed on top K) tungsten wire is attached on top of the PZTs L) the device is encapsulated with parylene-C.

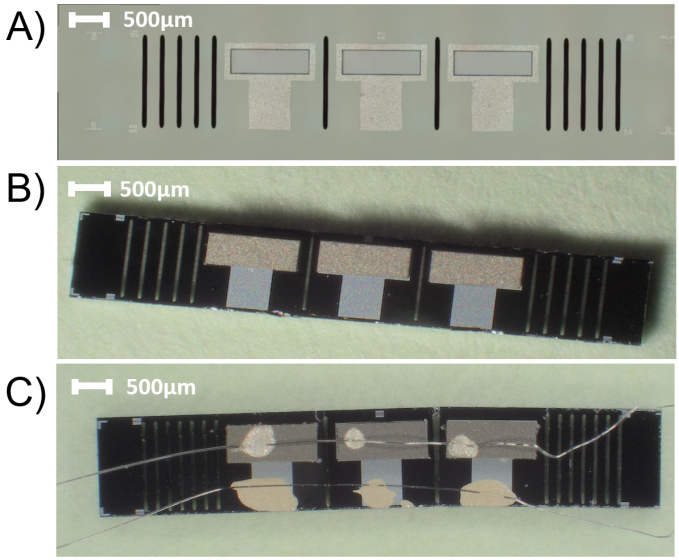

Fig. 6. The design and fabricated device. A) is a micrograph of the microfabricated device without PZT-based US transducer. B) is a microscopic topview of a single, microfabricated device after step H, whereas C) is a micrograph of the fabricated device after the attachment of tungsten wire.

in microcavities between the ACF and the metal contact rings.

The top connection between the PZT-based US transducers is made with 50 μm-thick tungsten wire which is connected using a layer of silver conductive paste (42469, Thermofischer). After curing, a layer of conductive epoxy (Epoxy technology, EPOTEK-H20E) is applied. This gives a mechanically robust and electrically conductive connection. To avoid, mechanical interference of the wires during the curvature of the device, each PZT and contact pad is individually connected with a tungsten wire (Fig. 5K). Afterwards, the wires of the three contact pads are bundled, likewise the wires of the three PZT-based US transducers. In this way, two connections, one for the ground and one for the signal, are available during the measurements. After the attachment of the tungsten wire, the device is encapsulated (Fig. 5L) using a 5 μm-thick parylene-C coating (PDS 2010, Specialty coating systems). Parylene-C is known due to its conformal coating properties and high chemical inertness [57]. In addition, it is mechanically flexible and therefore used as the flexible interconnect between the silicon islands in the island-bridge design (Fig. 4). A micrograph of a single device after step H (Fig. 5H) is shown in Fig. 6A. Fig. 6C shows a micrograph of a device with attached wires. Additional background information regarding wafer-level microfabrication can be found in Chapter 6.

IV. Characterization

The characterization has been done to show the impact of curvature on the focal spot. For the measurements, a non-airbacked device has been measured in a planar and curved configuration. The measurements are done in a watertank in which the device is fixed in a 3D-printed holder. The measurement setup is shown in Fig. 7. A function generator (DG4202, RIGOL) drives the device, generating a 10 V_{pp}, 30 pulses, 8.3 MHz, 1 ms period burst. The US pressure is measured using a fibre-optic hydrophone (FSV2-5580-10, Precision Acoustics) which is put into position with a 3D-axis motorized stage (SFS630, GAMPT soundfield scanning drive). The fibre-optic hydrophone is connected to the fibre-optic hydrophone system (FOHSv2, Precision Acoustics) and the signal is read out with an oscilloscope (DSO-X 3032A, Agilent Technologies). The oscilloscope, function generator and 3D-axis motorized stage can be controlled using a Matlab-GUI on a computer. The hydrophone has a sensitivity of 268 mV/MPa at a frequency of 8 MHz. Linear interpolation gives a sensitivity of 281 mV/MPa for 8.4 MHz. The 3D-printed holder for the measurements in the planar configuration can be seen in Fig. 9A. A small custom-made PCB board is attached to connect the device to the oscilloscope connectors.

Before the acoustic measurements, a frequency sweep (from 1 to 16 MHz) was applied to the PZT-based US transducers to obtain the resonance frequency of the device (Fig. 9D). For this measurement, a resonance frequency of 8.3 MHz was obtained which is used as the driving frequency for the function generator. The acoustic profiles are measured in a zy-plane parallel to the front of the device for different distances in the x-direction. The data is post-processed using a cubic interpolation method with 100 in between points at both axes. The scans for the 0.3 mm (near-field) and 1 mm (focal spot)

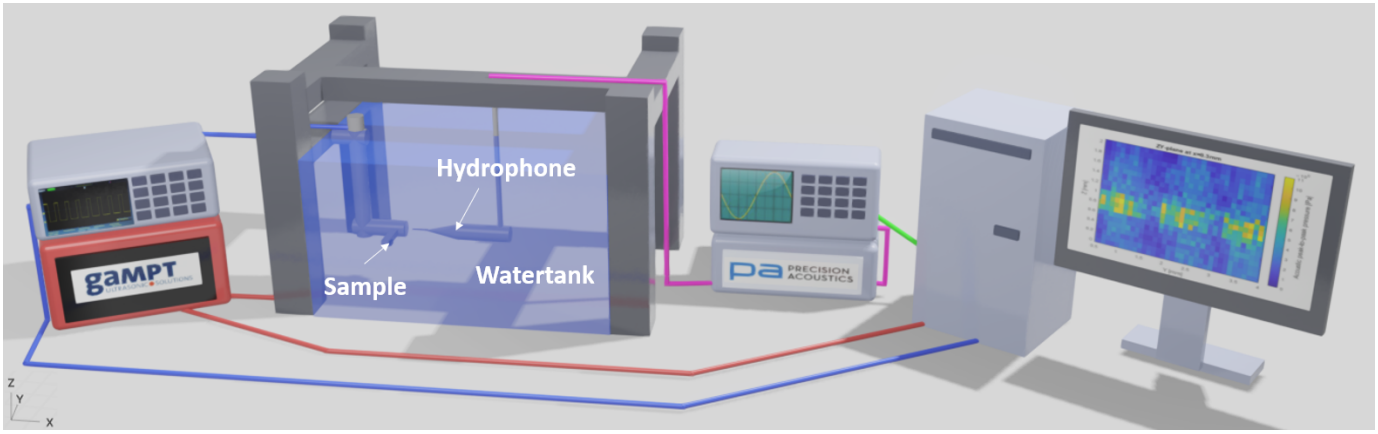

Fig. 7. The measurement setup from left to right: the function generator, the 3D-axis motorized stage, the watertank with a hydrophone, the oscilloscope, the hydrophone amplifier, the computer with software.

Fig. 8. The curvature of the island-bridge structure.

distance can be found in Fig. 9B and Fig. 9C respectively. Each PZT-based US transducer has its own acoustic profile and some profile distortion is visible. The acoustic peak pressure varies among the PZT-based US transducers from 1.1 MPa to 700 kPa (Fig. 9C) gaining 900 kPa on average. The focal spot of a single PZT-based US transducer has a size of around 100 μm by 200 μm. The S_{tx} reaches 110 kPa/V.

A fully curved device can be observed in Fig. 8 with an inner radius of 0.95 mm. A topview of the setup of the curved sample in the watertank is given in Fig. 9E. The 3D-printed holder contains a half-circle which, together with the device, has an inner diameter of 2 mm. The device is pushed inside the half-circle into a thin layer of glue pad that holds the device in a half-curved position. The acoustic profiles are scanned in the same way as for the planar configuration. The scans for 0.3 mm and 1 mm in the x-direction are shown in Fig. 9F and Fig. 9G respectively. The focal spot size is 200 μm by 200 μm and is slightly larger than the simulations (Fig. 9G).

The focal pressure magnitude in the curved configuration is increased by 0.7 MPa compared to the average focal pressure magnitude of the single PZT-based US transducer in the planar configuration (Fig. 9I and Fig. 9J). Having a peak focal pressure of 1.6 MPa results in a S_{tx} of 160 kPa/V. The pressure profiles of Fig. 9I and Fig. 9J are obtained from the cross sections of Figures 9B and 9C at Z=0.9 mm, from Figure 9F at Z=0.7 mm, and from Figure 9G at Z=1 mm. For the planar pressure profile lines the location of the PZT-based US transducers in the graph is indicated with the numbers 1,2,3. In Figure 9H, the maximum focal pressures for each measurement in the curved and planar configuration are combined in a distance plot. The crosses indicate the maximum values, whereas the dashed line is an interpolation. Additional information regarding characterization and measurements can be found in Chapter 7.

V. Discussion

Comparing the results with the simulations, it can be observed that the resonance frequency is well preserved after the fabrication of the device. The simulated resonance frequency is 8.4 MHz whereas the measured resonance frequency is 8.3 MHz. The distortion and harmonics at lower frequencies could be explained by the loading of the PZT-based US transducers due to the attachment of the tungsten wire changing the frequency behavior. Another reason might be the partial detachment of the PZT from the substrate as research shows that that can induce harmonics [58]. The detachment of the PZT from the substrate might be a consequence of poor adhesion to the ACF, placement variations of the PZTs, mechanical vibrations during operation or corrosion of the metal tracks due to water inlet via microcracks in the parylene-C encapsulation. To reduce the variations and distortions, some assembly steps could be fine-tuned. The process parameters of the pick-and-place of the PZTs can be refined and it can be automated, as this is a standard packaging step. This will result in more precise PZT placement. Moreover, it could be transformed into a top and backside dicing approach in which the dicing determines the alignment of the PZTs [34]. The manual attachment of the tungsten wire could be replaced by adding an evaporated or sputtered top metal plane on top of the PZT-based US transducers which will hypothetically reduce the distortion in the US profile.

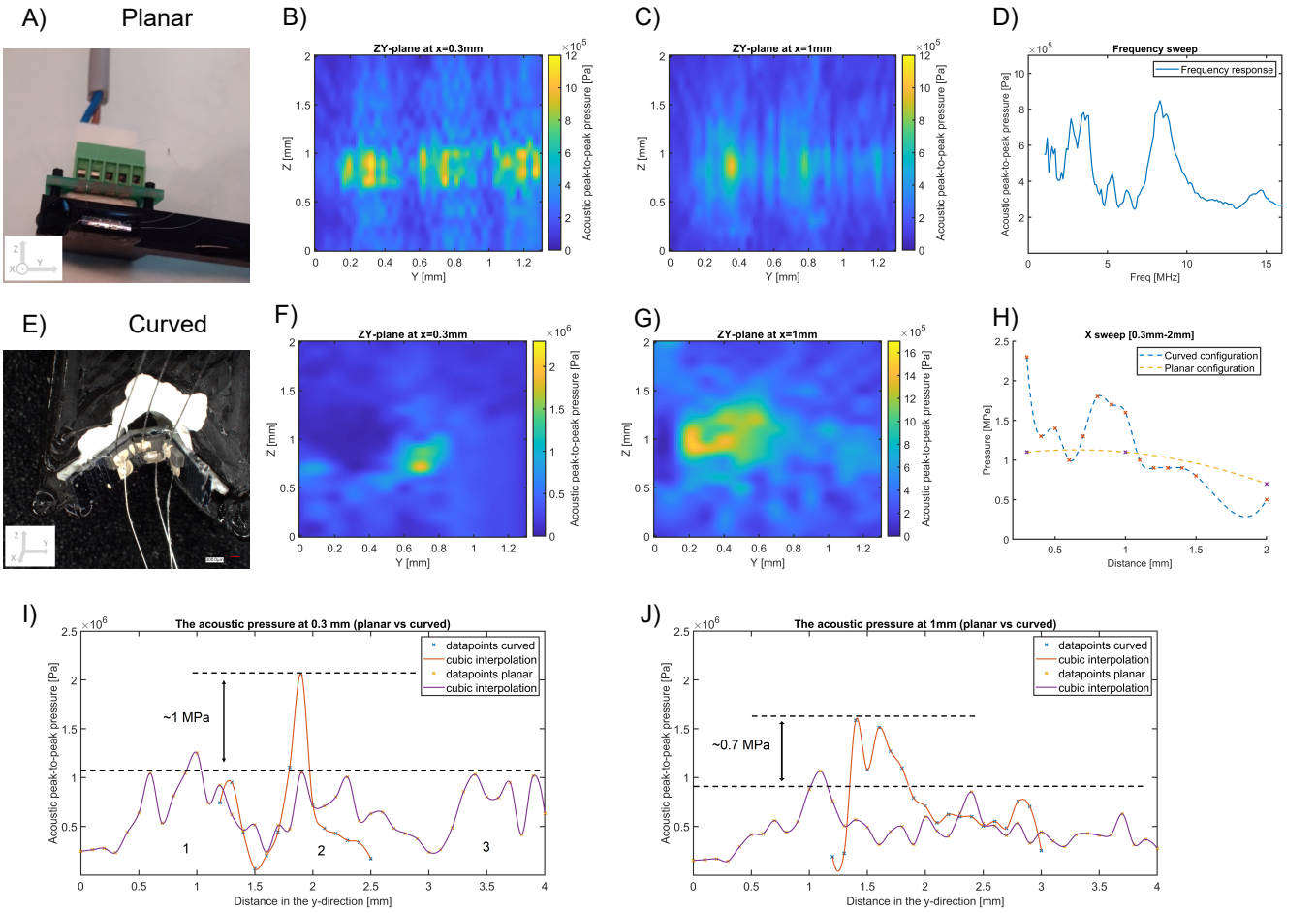

Fig. 9. The measurements A) shows a photograph of the 3D-printed holder with the device in a planar configuration B) and C) show the acoustic profile for an x-distance parallel to the surface of the PZT-based US transducers of 0.3 and 1 mm respectively D) shows the frequency response of one of the PZT-based US transducers from the planar configuration E) shows a micrograph of the design being curved in the 3D-printed holder F) and G) show the acoustic profile for an x-distance parallel to the surface of the middle PZT-based US transducer of 0.3 and 1 mm respectively H) shows the pressure profiles of both the planar and curved configuration I) shows the pressure profiles along the white dashed lines in the acoustic profile of the curved and planar configuration at and x-distance of 0.3 mm J) shows the pressure profiles along the white dashed lines in the acoustic profile of the curved and planar configuration at and x-distance of 1 mm.

Another reason for the difference between the pressure profile in the simulations and the measured profile is the simplifications and idealities in the simulation model. In the simulation, only the PZT, an airbacking well, and a perfectly cylindrical parylene-C ring are taken into account. In reality, fabrication non-idealities, island-bridge instead of pure parylene-C, manual variations during PZT placement, and the attachment of the tungsten wire degrade the PZT-based US transducer's performance leading to a different pressure profile. Moreover, the distortion of the focal spot might result from the non-perfect curvature and PZT placement variations. Due to small misalignments and tilting of the sample in the watertank during measurements in the planar configuration, there is a difference between the measured acoustic pressures among the PZT-based US transducers.

The island-bridge structure with silicon islands and parylene-C interconnects gives flexibility and the ability of the device to have a curvature of 2 mm in diameter (Fig. 8). However, as parylene-C is brittle by nature, it is still a vulnerability and the device should be handled with care. The robustness could be improved by increasing the layer thickness or creating a multilayer on top which protects the underlying parylene-C layer. However, this might affect the acoustic performance as the attenuation could increase, depending on the layer thickness, material properties, and the driving frequency. A biocompatible, transparent and cuff-implant-suitable alternative is Polydimethylsiloxane (PDMS) [59]. Research shows that this material can be used in combination with parylene-C as an encapsulation layer [60], [61].

For the metal layer, AlSi (99%/1%) is used. However, during measurements, device failure occurs. This is likely due to the non-optimized adhesion between the parylene-C and the metal tracks and the high water vapor transmission rate (WVTR) of parylene-C [62]. In that case, a multilayer encapsulation might increase the robustness [63]. A multilayer encapsulation could be used for acoustic matching as well (section VI). Post-treatment of the metal layer could improve the robustness as well [64].

VI. Future work

The design can be extended to increase the acoustic output pressure and improve the acoustic profile. The PZT-5H piezoelectric material could be replaced by the PMN-PT piezoelectric material as it has better electromechanical properties [65].

Beam steering could be implemented by dicing each individual PZT-based US transducer into a 2D-phased array [34]. This opens the potential to target the VN at various locations within the radius of the cuff implant. Another benefit of beamsteering is the ability to compensate for mechanical deformation.

Besides a backing layer, a matching layer could be included in the wafer-level microfabrication process as well [45]. The multi-layer polymer-metal structure for acoustic matching might be promising as parylene-C can still be used as an encapsulation layer [66]–[68]. A matching layer will increase the acoustic power transfer between two non-matching media (PZT and water) and will increase the acoustic output pressure. More about the future work can be found in Chapter 9.

VII. Conclusion

In this paper, a 1 mm by 7 mm wafer-level microfabricated, island-bridge cuff implant with an inner diameter of 2 mm has been proposed. COMSOL Multiphysics simulations have been performed to investigate the effect of the number of PZT-based US transducers, simulate the impact of airbacking, and verify the design. The wafer-level microfabrication and assembly consist of standardized and scalable process steps.

The device is being driven at 8.3 MHz and has a focal length of 1 mm. Three commercial PZT-5H US transducers are integrated generating 0.9 MPa on average at the focal spot of each individual PZT-based US transducer in a planar configuration (S_{tx} = 110 kPa/V) whereas, 1.6 MPa is generated at the focal spot in curved configuration (S_{tx} = 160 kPa/V). The focal spot of the curved cuff implant is 200 μm by 200 μm which is slightly larger than in the simulations.

The measurements show the potential of a cuff-shape design with a PZT-based US transducer array as the output focal pressure is increased by at least 45% (taking the peak pressures at the focal spot for both the planar (1.1 MPa) and curved (1.6 MPa) configuration) compared to the measured focal pressures of the single PZT-based US transducers in the planar configuration. Moreover, comparing this focal pressure of the curved configuration with research regarding the integration of cMUT technology into a cuff-implant or other PZT-based designs, this device can generate more output pressure. In conclusion, the integration of PZT-based US transducers in a cuff-shaped design opens a new path towards a technique for high-precision VNS.

Acknowledgment

The authors highly appreciated the support of the staff of the Else Kooi Lab at Delft University of Technology.

References

[1] Oluigbo, C. & Rezai, A. Addressing Neurological Disorders With Neuromodulation. *IEEE Transactions On Biomedical Engineering*. **58**, 1907-1917 (2011)

[2] Blackmore, J., Shrivastava, S., Sallet, J., Butler, C. & Cleveland, R. Ultrasound Neuromodulation: A Review of Results, Mechanisms and Safety. *Ultrasound In Medicine & Biology*. **45**, 1509-1536 (2019)

[3] Kamimura, H., Conti, A., Toschi, N. & Konofagou, E. Ultrasound neuromodulation: mechanisms and the potential of multimodal stimulation for neuronal function assessment. *Front Phys*. **8** (2020), 2296-424x Kamimura, Hermes A S Conti, Allegra Toschi, Nicola Konofagou, Elisa E. Journal Article 2020/06/09 Front Phys. 2020 May;8:150. doi: 10.3389/fphy.2020.00150. Epub 2020 May 26.

[4] Downs, M., Lee, S., Yang, G., Kim, S., Wang, Q. & Konofagou, E. Non-invasive peripheral nerve stimulation via focused ultrasound less or greater in vivo less or greater. *Physics In Medicine And Biology*. **63**, 035011 (2018,1), doi:10.1088/1361-6560/aa9fc2

[5] Kim, M., Kamimura, H., Lee, S., Aurup, C., Kwon, N. & Konofagou, E. Image-guided focused ultrasound modulates electrically evoked motor neuronal activity in the mouse peripheral nervous system in vivo. *Journal Of Neural Engineering*. **17**, 026026 (2020)

[6] Cotero, V., Miwa, H., Graf, J., Ashe, J., Loghin, E., Di Carlo, D. & Puleo, C. Peripheral Focused Ultrasound Neuromodulation (pFUS). *Journal Of Neuroscience Methods*. **341** pp. 108721 (2020)

[7] Kawasaki, S., Giagka, V., De Haas, M., Louwerse, M., Henneken, V., Van Heesch, C. & Dekker, R. Pressure measurement of geometrically curved ultrasound transducer array for spatially specific stimulation of the vagus nerve. *2019 9th International IEEE EMBS Conference On Neural Engineering (NER)*, 2019, doi: 10.1109/NER.2019.8717064

[8] Yuan, H. & Silberstein, S. Vagus Nerve and Vagus Nerve Stimulation, a Comprehensive Review: Part I. *Headache: The Journal Of Head And Face Pain*. **56**, 71-78 (2016)

[9] Settell, M., Knudsen, B., Dingle, A., McConico, A., Nicolai, E., Trevathan, J., Ross, E., Pelot, N., Grill, W., Gustafson, K., Shoffstall, A., Williams, J., Zeng, W., Poore, S., Populin, L., Suminski, A. & Ludwig, K. Functional Vagotopy in the Cervical Vagus Nerve of the Domestic Pig: Implications for the Study of Vagus Nerve Stimulation. (Cold Spring Harbor Laboratory,2019)

[10] Jayaprakash, N., Song, W., Toth, V., Vardhan, A., Levy, T., Tomaio, J., Qanud, K., Mughrabi, I., Chang, Y., Rob, M., Daytz, A., Abbas, A., Nassrallah, Z., Volpe, B., Tracey, K., Al-Abed, Y., Datta-Chaudhuri, T., Miller, L., Barbe, M., Lee, S., Zanos, T. & Zanos, S. Organ- and function-specific anatomical organization of vagal fibers supports fascicular vagus nerve stimulation. *Brain Stimulation*. **16**, 484-506 (2023)

[11] Groves, D. & Brown, V. Vagal nerve stimulation: a review of its applications and potential mechanisms that mediate its clinical effects. *Neuroscience & Biobehavioral Reviews*. **29**, 493-500 (2005)

[12] Johnson, R. & Wilson, C. A review of vagus nerve stimulation as a therapeutic intervention. *Journal Of Inflammation Research*. **Volume 11** pp. 203-213 (2018)

[13] Panebianco & Marson, A. Vagus nerve stimulation for focal seizures. *Cochrane Database Of Systematic Reviews*. (2022), doi:10.1002/14651858.CD002896

[14] Howland, R. Vagus Nerve Stimulation. *Current Behavioral Neuroscience Reports*. **1**, 64-73 (2014)

[15] Lee, S., Peh, W., Thakor, N., Yen, S. & Lee, C. Vagus nerve stimulation (VNS) for heart rate control using novel neural interfaces. (2017)

[16] Yuan, H. & Silberstein, S. Vagus Nerve and Vagus Nerve Stimulation, a Comprehensive Review: Part II. *Headache: The Journal Of Head And Face Pain*. **56**, 259-266 (2016)

[17] Dirr, E., Patel, Y., Lester, L., Delgado, F. & Otto, K. Targeted Vagus Nerve Stimulation does not Disrupt Cardiac Function in the Diabetic Rat. (2019)

[18] Giagka, V. & Serdijn, W. Realizing flexible bioelectronic medicines for accessing the peripheral nerves – technology considerations. *Bioelectronic Medicine*. **4** (2018), doi: 10.1186/s42234-018-0010-y

[19] Yap, J., Keatch, C., Lambert, E., Woods, W., Stoddart, P. & Kameneva, T. Critical Review of Transcutaneous Vagus Nerve Stimulation: Challenges for Translation to Clinical Practice. *Frontiers In Neuroscience*. **14** (2020)

[20] De Smet, S., Baeken, C., Seminck, N., Tilleman, J., Carrette, E., Vonck, K. & Vanderhasselt, M. Non-invasive vagal nerve stimulation enhances cognitive emotion regulation. *Behaviour Research And Therapy*. **145** pp. 103933 (2021)

[21] Shin, K., Bae, Y., Park, H., Kang, D. & Kang, M. The Effect of Electrode Distance on the Voltage Distribution during Non-invasive Vagus Nerve Stimulation – a Preliminary Study. (2023)

[22] Levitsky, A., Klein, J., Artemiadis, P. & Buneo, C. Effects of Transcutaneous Electric Nerve Stimulation on Upper Extremity Proprioceptive Function. (2020)

[23] Gurel, N., Shandhi, M., Bremner, J., Vaccarino, V., Ladd, S., Shallenberger, L., Shah, A. & Inan, O. Toward closed-loop transcutaneous vagus nerve stimulation using peripheral cardiovascular physiological biomarkers: A proof-of-concept study. (2018)

[24] Pashaei, V., Dehghanzadeh, P., Enwia, G., Bayat, M., Majerus, S. & Mandal, S. Flexible Body-Conformal Ultrasound Patches for Image-Guided Neuromodulation. *IEEE Transactions On Biomedical Circuits And Systems*. **14**, 305-318 (2020)

[25] Rijnbeek, E., Eleveld, N. & Olthuis, W. Update on Peripheral Nerve Electrodes for Closed-Loop Neuroprosthetics. *Frontiers In Neuroscience*. **12** (2018)

[26] Rodriguez, F., Ceballos, D., Schuttler, M., Valero, A., Valderrama, E., Stieglitz, T. & Navarro, X. Polyimide cuff electrodes for peripheral nerve stimulation. *Journal Of Neuroscience Methods*. **98**, 105-118 (2000)

[27] Stieglitz, T., Beutel, H., Schuettler, M. & Meyer, J. Micromachined, Polyimide-Based Devices for Flexible Neural Interfaces. *Biomedical Microdevices*. **2**, 283-294 (2000)

[28] Forssell, M., Fedder, G., Sciullo, M., Mou, C., Sun, F., Simpson, T., Xiao, G., Fisher, L., Bettinger, C. & Horn, C. Compliant adhesive cuff electrode for selective stimulation in rat vagus nerve. (2019)

[29] Haugland, M. A flexible method for fabrication of nerve cuff electrodes. *18th Annual International Conference Of IEEE Engineering-in-Medicine-amd-Biology-Society*. **18** pp. 359-360 (1997)

[30] Freeberg, M., Stone, M., Triolo, R. & Tyler, D. The design of and chronic tissue response to a composite nerve electrode with patterned stiffness. *Journal Of Neural Engineering*. **14**, 036022 (2017), doi:10.1088/1741-2552/aa6632

[31] Tyler, D. & Durand, D. A slowly penetrating interfascicular nerve electrode for selective activation of peripheral nerves. *IEEE Transactions On Rehabilitation Engineering*. **5**, 51-61 (1997)

[32] Kim, G., Kim, K., Lee, E., An, T., Choi, W., Lim, G. & Shin, J. Recent Progress on Microelectrodes in Neural Interfaces. *Materials*. **11**, 1995 (2018), doi:10.3390/ma11101995

[33] Yildiz, K., Shin, A. & Kaufman, K. Interfaces with the peripheral nervous system for the control of a neuroprosthetic limb: a review. *Journal Of NeuroEngineering And Rehabilitation*. **17** (2020)

[34] Costa, T., Shi, C., Tien, K., Elloian, J., Cardoso, F. & Shepard, K. An Integrated 2D Ultrasound Phased Array Transmitter in CMOS With Pixel Pitch-Matched Beamforming. *IEEE Transactions On Biomedical Circuits And Systems*. **15**, 731-742 (2021)

[35] Kawasaki, S., Dijkema, E., Saccher, M., Giagka, V., Schleipen, J. & Dekker, R. Schlieren visualization of focused ultrasound beam steering for spatially specific stimulation of the vagus nerve. *2021 10th International IEEE EMBS Conference On Neural Engineering (NER)*, 2021, doi: 10.1109/NER49283.2021.9441225 (2021)

[36] O'Brien, W. Ultrasound–biophysics mechanisms. *Progress In Biophysics And Molecular Biology*. **93**, 212-255 (2007), Effects of ultrasound and infrasound relevant to human health

[37] Kele, H. Ultrasonography of the peripheral nervous system. *Perspectives In Medicine*. **1** pp. 417-421 (2012,9)

[38] Plaksin, M., Shoham, S. & Kimmel, E. Intramembrane Cavitation as a Predictive Bio-Piezoelectric Mechanism for Ultrasonic Brain Stimulation. *Physical Review X*. **4** (2014)

[39] Heimburg, T. & Jackson, A. On soliton propagation in biomembranes and nerves. *Proceedings Of The National Academy Of Sciences*. **102**, 9790-9795 (2005), doi:10.1073/pnas.0503823102

[40] Oh, S., Lee, J., Kim, H., Lee, J., Han, S., Bae, J., Hong, G., Koh, W., Kwon, J., Hwang, E. & Al. Ultrasonic Neuromodulation via Astrocytic TRPA1. *Current Biology*. **29**, 3386-3401.e8 (2019)

[41] Colucci, V., Strichartz, G., Jolesz, F., Vykhodtseva, N. & Hynynen, K. Focused ultrasound effects on nerve action potential in vitro. *Ultrasound In Medicine & Biology*. **35**, 1737-47 (2009)

[42] Lee, S., Jung, J., Chae, Y., Kang, J. & Ieee Fabrication and Characteristics of the Implantable and Flexible Nerve Cuff Electrode for Neural Interfaces. *4th International IEEE/EMBS Conference On Neural Engineering*. pp. 80-+ (2009)

[43] Juan, E., González, R., Albors, G., Ward, M. & Irazoqui, P. Vagus nerve modulation using focused pulsed ultrasound: Potential applications and preliminary observations in a rat. *International Journal Of Imaging Systems And Technology*. **24**, 67-71 (2014), doi:10.1002/ima.22080

[44] Foley, J., Little, J. & Vaezy, S. Effects of high-intensity focused ultrasound on nerve conduction. *Muscle & Nerve*. **37**, 241-50 (2008), Foley JL Little JW Vaezy S

[45] Rathod, V. A Review of Acoustic Impedance Matching Techniques for Piezoelectric Sensors and Transducers. *Sensors*. **20**, 4051 (2020)

[46] Shen, K. & Maharbiz, M. Design of Ceramic Packages for Ultrasonically Coupled Implantable Medical Devices. *IEEE Transactions On Biomedical Engineering*. **67**, 2230-2240 (2020)

[47] Wang, Z., Xue, Q., Chen, Y., Shu, Y., Tian, H., Yang, Y., Xie, D., Luo, J. & Ren, T. A Flexible Ultrasound Transducer Array with Micro-Machined Bulk PZT. *Sensors*. **15**, 2538-2547 (2015)

[48] Yang, Y., Tian, H., Yan, B., Sun, H., Wu, C., Shu, Y., Wang, L. & Ren, T. A flexible piezoelectric micromachined ultrasound transducer. *RSC Advances*. **3**, 24900 (2013)

[49] Akasheh, F., Myers, T., Fraser, J., Bose, S. & Bandyopadhyay, A. Development of piezoelectric micromachined ultrasonic transducers. *Sensors And Actuators A: Physical*. **111** pp. 275-287 (2004,3)

[50] Rivandi, H. & Costa, T. A 2D Ultrasound Phased-Array Transmitter ASIC for High-Frequency Ultrasound Stimulation and Powering. *IEEE Transactions On Biomedical Circuits And Systems*. pp. 1-12 (2023)

[51] Comsol Acoustics Module User's Guide. (https://doc.comsol.com/5.4/doc/com.comsol.help.aco/AcousticsModuleUsersGuide.pdf)

[52] Gougheri, H., Dangi, A., Kothapalli, S. & Kiani, M. A Comprehensive Study of Ultrasound Transducer Characteristics in Microscopic Ultrasound Neuromodulation. *IEEE Transactions On Biomedical Circuits And Systems*. **13**, 835-847 (2019)

[53] Wardhana, G., Mastrangeli, M. & Costa, T. Maximization of Transmitted Acoustic Intensity from Silicon Integrated Piezoelectric Ultrasound Transducers. *2022 IEEE International Ultrasonics Symposium (IUS)*. pp. 1-4 (2022)

[54] Shi, C., Costa, T., Elloian, J. & Shepard, K. Monolithic Integration of Micron-scale Piezoelectric Materials with CMOS for Biomedical Applications. *2018 IEEE International Electron Devices Meeting (IEDM)*. pp. 4.5.1-4.5.4 (2018)

[55] Shi, C., Andino-Pavlovsky, V., Lee, S., Costa, T., Elloian, J., Konofagou, E. & Kenneth L. Shepard Application of a sub–0.1-mm¡sup¿3¡/sup¿ implantable mote for in vivo real-time wireless temperature sensing. *Science Advances*. **7**, eabf6312 (2021), doi:10.1126/sciadv.abf6312

[56] Shi, C., Costa, T., Elloian, J., Zhang, Y. & Shepard, K. A 0.065-mm3 Monolithically-Integrated Ultrasonic Wireless Sensing Mote for Real-Time Physiological Temperature Monitoring. *IEEE Transactions On Biomedical Circuits And Systems*. **14**, 412-424 (2020)

[57] Ortigoza-Diaz, J., Scholten, K., Larson, C., Cobo, A., Hudson, T., Yoo, J., Baldwin, A., Weltman Hirschberg, A. & Meng, E. Techniques and Considerations in the Microfabrication of Parylene C Microelectromechanical Systems. *Micromachines*. **9**, 422 (2018), doi:10.3390/mi9090422

[58] Yelve, N., Mitra, M. & Mujumdar, P. Higher harmonics induced in lamb wave due to partial debonding of piezoelectric wafer transducers. *NDT & E International*. **63** pp. 21-27 (2014)

[59] Miranda, I., Souza, A., Sousa, P., Ribeiro, J., Castanheira, E., Lima, R. & Minas, G. Properties and Applications of PDMS for Biomedical Engineering: A Review. *Journal Of Functional Biomaterials*. **13** pp. 2 (2021,12)

[60] Babaroud, N., Dekker, R., Serdijn, W. & Giagka, V. PDMS-Parylene Adhesion Improvement via Ceramic Interlayers to Strengthen the Encapsulation of Active Neural Implants. *2020 42nd Annual International Conference Of The IEEE Engineering In Medicine & Biology Society (EMBC)*. pp. 3399-3402 (2020), doi: 10.1109/EMBC44109.2020.9175646

[61] Bakhshaee, N., Dekker, R., Hölck, O., Tiringer, U., Taheri, P., Horváth, D., Nánási, T., Ulbert, I., Serdijn, W. & Giagka, V. Investigation of the long-term adhesion and barrier properties of a PDMS-Parylene stack with PECVD ceramic interlayers for the conformal encapsulation of neural implants. 2021 23rd IEEE European Microelectronics and Packaging Conference (EMPC), 2021, doi: 10.23919/EMPC53418.2021.9584961.

[62] Nanbakhsh, K., Kluba, M., Pahl, B., Bourgeois, F., Dekker, R., Serdijn, W. & Giagka, V. Effect of Signals on the Encapsulation Performance of Parylene Coated Platinum Tracks for Active Medical Implants. *2019 41st Annual International Conference Of The IEEE Engineering In Medicine And Biology Society (EMBC)*. pp. 3840-3844 (2019), doi: 10.1109/EMBC.2019.8857702

[63] Pak, A., Nanbakhsh, K., Hölck, O., Ritasalo, R., Sousa, M., van Gompel, M., Pahl, B., Wilson, J., Kallmayer, C., & Giagka, V. Thin Film Encapsulation for LCP-Based Flexible Bioelectronic Implants:

Comparison of Different Coating Materials Using Test Methodologies for Life-Time Estimation. *Micromachines*. vol. 13, no. 4, pp. 544 (2022). doi: 10.3390/mi13040544.

[64] Mahmood, M., Chioibasu, D., Ur Rehman, A., Mihai, S. & Popescu, A. Post-Processing Techniques to Enhance the Quality of Metallic Parts Produced by Additive Manufacturing. *Metals*. **12**, 77 (2022)

[65] Kim, K., Hsu, D., Ahn, B., Kim, Y. & Barnard, D. Fabrication and comparison of PMN-PT single crystal, PZT and PZT-based 1-3 composite ultrasonic transducers for NDE applications. *Ultrasonics*. **50**, 790-797 (2010)

[66] Fei, C., Ma, J., Chiu, C., Williams, J., Fong, W., Chen, Z., Zhu, B., Xiong, R., Shi, J., Hsiai, T. & Al. Design of matching layers for high-frequency ultrasonic transducers. *Applied Physics Letters*. **107**, 123505 (2015), doi:10.1063/1.4931703

[67] Toda, M. & Thompson, M. Detailed investigations of polymer/metal multilayer matching layer and backing absorber structures for wide-band ultrasonic transducers. *IEEE Transactions On Ultrasonics, Ferroelectrics, And Frequency Control*. **59**, 231-242 (2012)

[68] Yang, X., Fei, C., Xinhaosun, Hou, S. & Chen, J. Multi-layer polymer-metal structures for acoustic impedance matching in high-frequency broadband ultrasonic transducer design. (2019)

3

Context and background of neuromodulation, wafer-level microfabrication and ultrasound

In this chapter, the general background for this thesis will be given. Topics like the general biology of the nerve, neuromodulation, the physics of ultrasound, piezoelectricity and material properties are included.

3.1. The nerve

Living tissue consists of cells. Cells have a cell membrane consisting of phospholipid molecules, cholesterol, proteins and carbohydrates [26]. Due to the distribution of ions at the outer and inner sides of the membrane, every cell exhibits a potential across its membrane: the resting potential (-70 mV to -90 mV). In the resting state, the membrane is slightly permeable to Na^+ and highly permeable to K^+ and Cl^-. Since there is a higher concentration of ions inside the cell than outside there is a diffusion gradient outwards. However, the electric field over the membrane is pointing inward. This results in an equilibrium at the resting potential. This equilibrium transmembrane resting potential can be described by the Goldman-Hodgkin-Katz equation [27]:

$$\phi = \frac{RT}{F} ln(\frac{P_K[K]_o + P_{Na}[Na]_o + P_{Cl}[Cl]_i}{P_K[K]_i + P_{Na}[Na]_i + P_{Cl}[Cl]_o} \tag{3.1}$$

R is the gas constant ($8.314\, JK^{-1}mol^{-1}$), T the temperature $[K]$, F the Faraday constant ($96.485\, Cmol^{-1}$), $[M]$ the ion concentration of a specific ion and P_M the permeability coefficient of the membrane for a specific ion. The subscript denotes whether the flow goes in (i) or out (o) of the cell.

Nerve and muscle cells are excitable, which means that they can excite impulses over their membrane that propagate along the membrane of neighboring cells. This excitation can occur in response to electrical, chemical, mechanical or thermal stimuli [4]. These excitable cells in the nerves are neurons. A neuron consists of dendrites, the Soma, and the axon (Figure 3.1a). The dendrites receive impulses while the axon transmits impulses to another axon. The axon can be myelinated or unmyelinated. The myelinated axon has a higher propagation speed of the impulses since the impulses propagate between the Nodes of Ranvier [27]. The impulse transfer along the neuron occurs via electrical conduction.

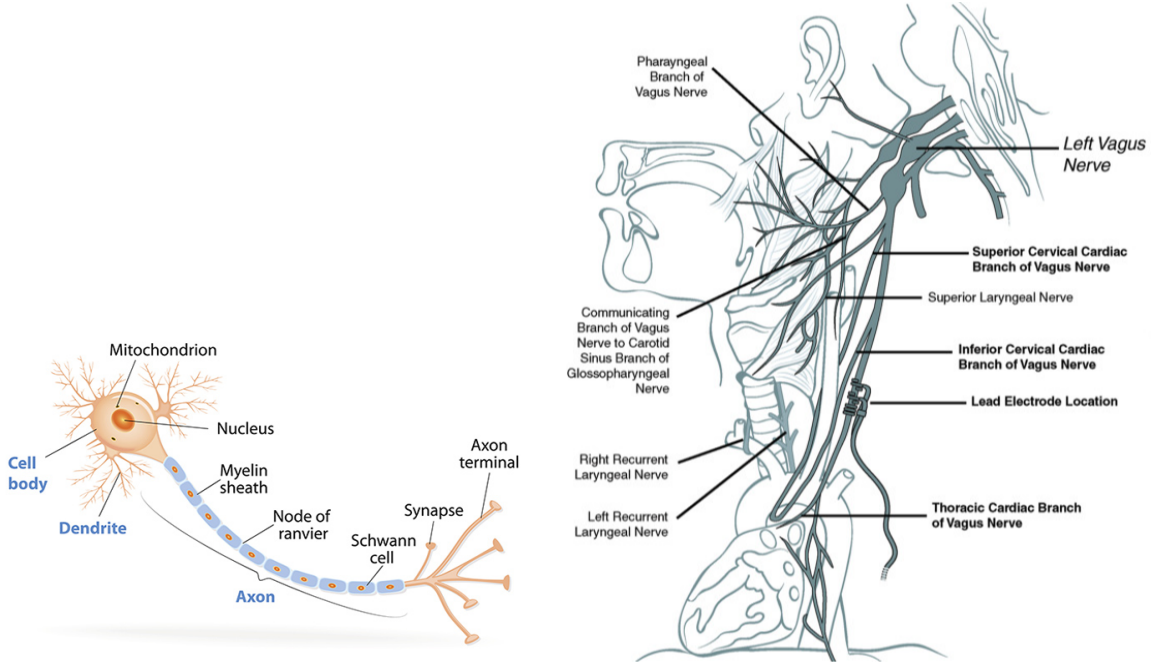

(a) A schematic overview of a neuron [28].

(b) The anatomy of the VN [15].

Figure 3.1: The anatomy of a neuron and the VN.

In the process of electrical stimulation, ion channels play an important role. Ion channels are proteins in the cell membrane that are selective to the type of ion(s) it allows to pass [26]. Different kinds of channels do exist. First, there are leakage or non-gated channels. These channels are always open. Second, gated channels exist. These gated channels are proteins that change shape in correspondence to specific signals. There are chemically gated channels, voltage-gated channels and mechanically gated channels [26]. The voltage-gated ion channels of potassium ($K+$) and sodium ($Na+$) are key players in the propagation of action potentials. In case the depolarisation of the membrane due to a stimulus reaches the threshold of -60 mV, an action potential is excited which propagates down the axon. The size and shape of this pulse are independent of stimulus intensity or duration (all-or-none property). After the action potential, the nerve is non-excitable for up to 2 ms (refractory period).

The axon can be modeled using an axon cable model [27] [29] (Figure 3.2). From this model, the general cable equation can be obtained:

$$\frac{\partial^2 V'}{\partial x^2} = (r_i + r_o) i_m \tag{3.2}$$

From Equation 3.2 the length constant and the time constant can be obtained for a specific stimulation step current. The length constant is the measure of distance from the site of stimulation over which a significant response is obtained. This is a characteristic of the axon. The time constant is a measure of time for the signal in the neuron to reach the maximum amplitude after depolarisation. Larger time constants mean more time needed to depolarise after stimulation.

In this thesis, the focus will be on the VN, since the cuff to be designed will be used for VNS. The VN is one of the cranial nerves and part of the peripheral nervous system (PNS) which are the nerves outside the brain and the spinal cord [26]. The VN is the only cranial nerve that extends beyond the head and neck to the thorax and the abdomen [26] (Figure 3.1b). It contains both sensory (afferent) and motor (efferent) neurons and it is involved in both the somatic and autonomic systems even as the sympathetic and the parasympathetic division. Cardiovascular, respiratory, gastrointestinal, immune and endocrine systems are influenced by the VN [12]. The VN consists of A-, B- and C-fibers, classified, according to Erlanger Gasser [12]. The A-fibers are subdivided into α, β and δ. The functions and the anatomy of each type are shown in Table 3.1. The VN nerve fascicles comprise of different nerve fibers, each having their own functions, sizes (ranging from $<$0.5 μm up to 10 μm), and conduction

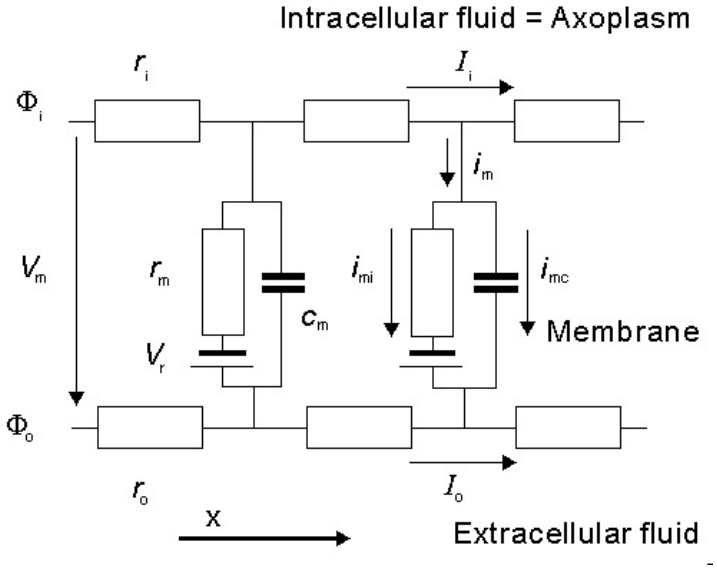

Figure 3.2: The general axon cable model [27].

Table 3.1: The anatomy of VN fibers and their functions [12].

Fiber Type	Fiber Size (μm)	Conduction velocity (m/s)	Main function	
			Afferent	**Efferent**
Aα	13-20	8-120	Somatic; Touch; Pain; Temperature	Muscle
Aβ	6-12	35-75	Somatic; Touch	Muscle; Preganglionic
Aδ	1-5	3-30	Visceral; Pain; Stretch; Chemical; Temperature	Preganglionic
B	1-5	3-15	Visceral	Preganglionic
C	0.4-2	0.5-2	Visceral; Pain; Stretch; Chemical; Temperature	Preganglionic

velocities (ranging from 0.5 to 120 m/s) [12], [14]. The typical dimensions of the VN at the site of stimulation are about 2 mm [10]. To avoid mechanical trauma like nerve swelling and blood flow occlusion, the Association for the Advancement of Medical Instrumentation (AAMI) recommends having the cuff implant 50% wider in diameter than the external diameter of the target nerve [30] [31].

Normally, the first trails are done with animals. In animals the VN is small and the effect of stimulation is hard to measure. Therefore, in animal testing the sciatic nerve (SN) is often used [32] [7] [33]. This large nerve in the lower limb has larger fascicules compared to the VN. Therefore, this nerve is easier to stimulate since the stimulation specificity can be lower. In addition, stimulation can be visually validated since the muscle will contract resulting in a movement of the leg.

VNS has been used to show the role of the VN in regulating the neuro-endocrine-immune axis, mood, pain and memory. Currently, VNS is being used for investigating its potential in headache, arthritis, asthma, pain, fibromyalgia, bipolar disorder, epilepsy, depression and dementia [12] [10]. It is important to stimulate the correct fiber without stimulating neighboring fibers to reduce side effects like neck pain, coughing, voice alteration and dyspnea of the treatment [10]. In current stimulation, the B- and C-fibers are mainly targeted [15]. Examples are the left cervical VNS which received US Food and Drug Administration (FDA) approval in 2013. Although right cervical VNS is difficult to perform without side effects, devices are still being made to make this possible.

3.2. Neuromodulation

Three major neuromodulation techniques do exist. Optogenetics, electrical stimulation and US neuromodulation. The main disadvantage of optogenetics is the need for genetic modification of neurons to make them sensitive to light. Since this will not be possible in the case of VNS in humans, only

electrical and US stimulation techniques are explored in this section.

3.2.1. Electrical stimulation

Electrical stimulation is based on injecting currents or potentials to activate neurons. For stimulating electrodes the current flows are in the range of milli-amperes. The relation between the stimulus current and the pulse duration or pulse width for activation of a neuron can be shown in a strength-duration plot [27]. Electrodes for stimulations can be used in multiple configurations. The monopolar configuration is used for current injection through the working electrode and a second large neutral electrode is placed far away as the zero potential node. In the bipolar configuration, the working and return electrodes are equal and close to each other. For the multipolar configuration, the current injected and returned goes through more than one pair of electrodes.

To increase the stimulation specificity and efficiency, new stimulation techniques are used. An example is the current focusing and steering technique used in cochlear implants [34]. The technique of current steering gives also promising results in a VNS trail [35]. Another example is electrical stimulation by means of temporal interference [36].

To understand how a nerve is electrically stimulated it is necessary to understand the electrode-tissue interface. The electrode-tissue interface can be modeled with a small electrical circuit (Figure 3.3).

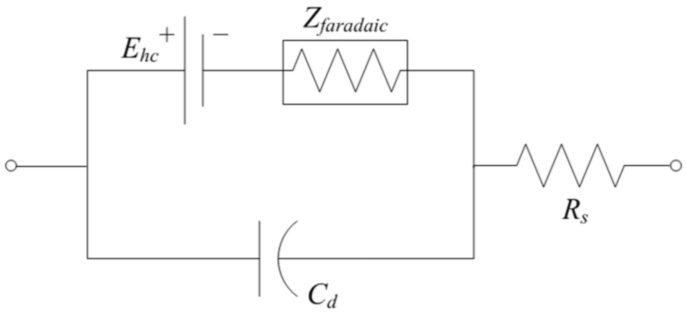

Figure 3.3: The modeled electrode tissue interface [27].

E_{hc} is the half-cell potential. $Z_{faradaic}$ is representing the Faradaic current flow which is the transfer of electrons through oxidation or reduction. This is a non-reversible process. R_s represents the effect of electrolyte. C_d is representing the non-Faradaic currents which are the redistribution of chemical species. This is a reversible process. To avoid Faradaic currents the potential should be within the water window. Triggering action potentials can be done both cathodic and anodic. In case prolonged stimuli below the excitation threshold exist, the threshold value increases (accommodation). Stimulation can be voltage-controlled, current-controlled and charge-controlled. For each technique, waveforms like monophasic, biphasic and charge-balanced can be implemented.

Electrically interfacing with peripheral nerves can be done with myoelectric systems and nerve electrodes [37]. Since myoelectric systems fundamentally rely on muscle electrodes, this way of interfacing is unsuitable for VNS. Therefore, nerve electrodes are used. Nerve electrodes are classified as extraneural (Table 3.3) or intraneural (Table 3.4) [37]. The legend for these tables can be found in Table 3.2. This division is based on the location of the implant with respect to the epineurium. Intraneural electrodes can be subdivided based on their penetration depth. Inter-fascicular electrodes penetrate the epineurium but not the fascicles while intra-fascicular electrodes penetrate both (Table 3.4) [37], [38].

Extraneural electrodes are the least invasive nerve electrodes and come in four major types: the epineural electrode, the helical electrode, the book electrode [39] and the cuff electrode [37] (Figure 3.4). Cuff electrodes are the most widely researched and are mainly used for peripheral nerve stimulation. They have robust structures and good adhesion to the nerve with self-closing options. Moreover, in some designs, suturing is not needed which makes implantation easier. Intraneural electrodes are mainly

Table 3.2: Legend for Table 3.3 and Table 3.4.

Visual	Meaning
bold	Main category
italic	Sub category
•	Main item
○	Sub item
⋆	Subsub item

Table 3.3: The different extraneural nerve electrodes with their advantages and disadvantages.

Electrodes	Advantages	Disadvantages	Notes
Extraneural electrodes	Least invasive	Low selectivity	-
• Epineural electrodes	High longevity (18 years), accurate and reproducible nerve signals	Electrode failure due to wire breakage	Muscle stimulation
○ Flexible epineural strip electrode (FLESE)	Flexible structure, lower failure rate	-	-
⋆ Concentric bipolar electrode	-	-	-
⋆ Hook electrode	Good adhesion, no suturing needed	-	-
• Helical electrodes	-	Surgical complications	VNS
• Book electrodes	-	Severe surgical complications	Sacral anterior root stimulation
• Cuff electrodes	Broadly researched, robust structures, high longevity (11 years)	Several failure modes	-
○ Split cylinder cuff electrodes	High longevity, easy-to-use for laparoscopic placement	-	Pelvic nerves stimulation
○ Spiral cuff electrode	Self-sizing, stable and selective stimulation, no serious adverse body-reactions	-	-
○ Flat interface nerve electrode (FINE)	Stable and selective stimulation	-	-
⋆ Composite flat interface nerve electrode (C-FINE)	Minimal bulk and stiffness	-	-
○ Flexible neural clip	Easy-to-use during implantation	-	VN, pelvic and SN stimulation
○ Flexible split ring electrode	Easy-to-use during implantation	-	SN stimulation
○ Self-locking parylene-C cuff electrode	No suturing needed	-	SN stimulation
⋆ Lyse-and-attract cuff electrode (LACE)	Microfluidics included	-	-
○ Neural ribbon electrode	Self-sizing	-	-
○ Nano-clip	-	-	Tracheal syringeal nerve

used for muscle signal recording and muscle stimulation. Applications are restoring touch sensation, controlling a prosthetic hand or restoring tactile sensations [37]. However, due to the invasiveness and the high risk of nerve trauma these types of implants are not suited for VNS. The different nerve electrode implants are listed in Table 3.3 and Table 3.4. The most important advantages and disadvantages are shown together with the implantation side.

Table 3.4: The different intraneural nerve electrodes with their advantages and disadvantages.

Electrodes	**Advantages**	**Disadvantages**	**Notes**
Intraneural electrodes	High selectivity	Invasive	**-**
Inter fascicular electrodes	No fascicle penetration, high selectivity	Epineural penetration, stability and reliability undetermined	-
• Slowly penetrating interfascicular nerve electrode (SPINE)	Selective axonal recruitment	-	SN stimulation
• Multi-groove electrode	Selective fascicle stimulation, minimizing muscle fatigue	-	-
• Nylon tube electrode	Interfacing with subpopulations of nerve fibers	-	-
Intra-fascicular electrodes	High selectivity, highest spatial resolution	Fascicle penetration, nerve trauma	-
• Longitudinal intra-fascicular electrode (LIFE)	Activate separate axonal subsets within a fascicle, graded responses	Electrode breakage leading to device failure	-
○ Thin-film LIFE (tf-LIFE)	Multiple contacts, enables transverse implantation	-	-
○ Distributed intra-fascicular multielectrode (DIME)	Access multiple fascicles within a nerve, robustness, more selectivity, facilitate implantation	-	-
• Transverse intra-fascicular multichannel electrode (TIME)	Higher selectivity than LIFE	-	Median and ulnar nerves
○ Self-opening intra-fascicular neural interface (SELINE)	Higher stability	-	-
• Penetrating microelectrode arrays (MEAs)	-	Electrode breakage	-
○ Utah Slanted Electrode Array (USEA)	High selectivity	-	Muscle stimulation

Currently, examples of cuff implants for VNS in the neck do exist [10]. In 1997, the US FDA approved an implanted left cervical VNS device for treatment-refractory epilepsy [15]. There are also trials for right cervical VNS treating heart failure. Implantation can be done in several ways. The implant can be wrapped around (e.g. the helical electrode or the spiral cuff implant), for which shape memory alloys can be used [41]. Moreover, wires can be attached to the implant to help the surgeon stretch the flexible cuff implant in order to wrap it around the nerve [42]. Some implants have a small split at one side (split cylinder cuff electrodes) at which the implant can be opened to be put around the nerve [43]. If the adhesion is not good enough implants are often fixated with sutures [41] [37].

The best type of extraneural electrodes for VNS is a variant of the cuff implant, since it is the most robust shaped implant and can be designed to be easy to use during surgery. The cuff implant is directly attached to the exterior of the nerve. This means that the distance between the nerve and the cuff is minimal without penetrating the nerve and increasing the risk of nerve trauma, leading to a good power transfer [30]. Although intraneural electrodes show higher selectivity, cuff implants can reach high selectivity compared to other extraneural electrodes. Cuff implants are classified according to their morphological properties. Important types are mentioned in Table 3.3. The split cylinder, spiral cuff and

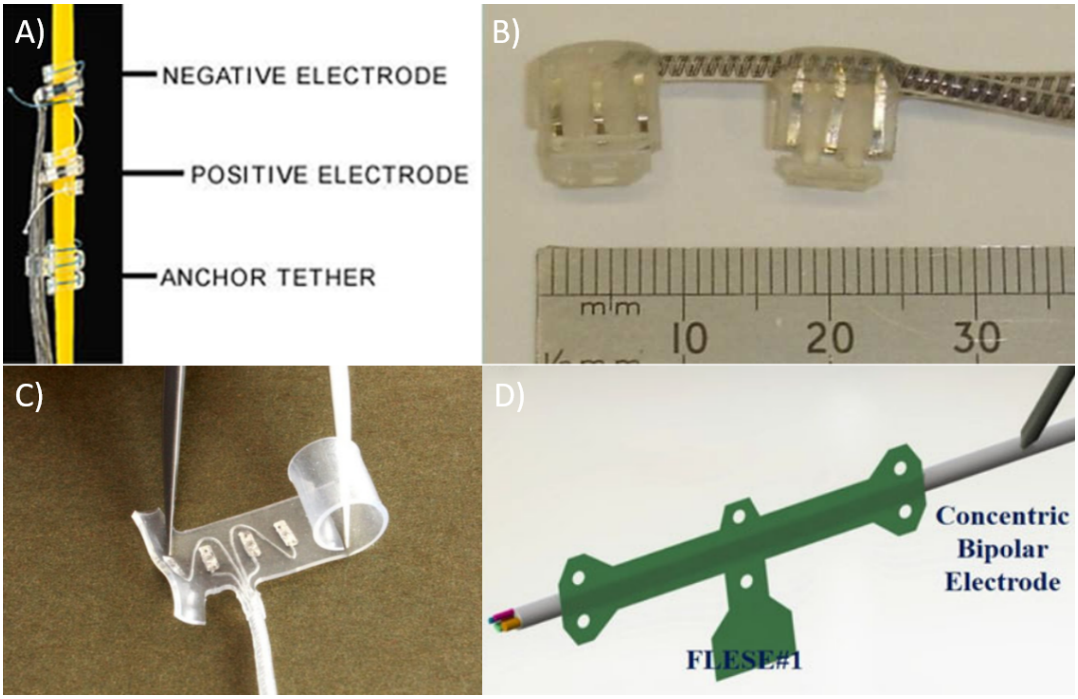

Figure 3.4: Four main types of extraneural electrodes: A) Helical electrode [37] B) Book electrode [37] C) Spiral cuff electrode [37] D) Flexible Epineural strip electrode (FLESE) [40].

neural ribbon electrodes are the most well-known and can be fabricated in multiple ways. From using a mandrel with platinum foil electrodes in 1996 [44] to shape-memory alloys (SMP) nowadays [41]. A more refined spiral cuff electrode is the 3D twinning electrode with self-climbing properties [41]. To lock the cuff implants, smart designs exist of which an example is the self-locking parylene-C cuff electrode [45]. Another type of cuff implant is the flat interface nerve electrode (FINE) and the improved composite flat interface nerve electrode (C-FINE) [37], [46]–[48]. However, with this design nerve trauma is a serious risk, since some force is needed to flatten the nerve. As a final category, some easy-to-use designs during implantation are the clip designs like the nano-clip and the neural clip [37].

3.2.2. US stimulation

Sound is the rapid motion of molecules when they transfer energy via molecular vibrations from the source to the receiver [24]. This movement is referred to as a wave. Sound waves come in two categories: longitudinal waves and shear waves (Figure 3.5). For longitudinal waves, the ultrasonic energy travels in the direction of the movement of the particles (black dots). For shear waves, the ultrasonic energy is traveling in a perpendicular direction with respect to the movement of the particles. Shear waves only exist in solid materials, while longitudinal waves also exist in gases and liquids.

US propagation in the tissue occurs via longitudinal waves and can be described in two phases: the compressional and the rarefaction phase [6] [24]. Besides longitudinal waves, both shear and thermal waves might be induced at the boundaries with other surfaces [49]. The compressional phase displaces tissue particles and fluid molecules, generating an elastic restoring force. When the tissue and fluids return to their normal positions, the rarefaction phase occurs. The propagating wave through tissue causes an acoustic radiation force (ARF) of which part of the energy is stored in the form of elastic deformation and part is dissipated as heat due to viscous frictional forces [6]. This heat dissipation depends on the frequency of the wave. The energy deposition in the tissue occurs through absorption.

Another phenomenon that can occur in the rarefaction phase is cavitation [6]. The probability of occurrence increases for stimulations at higher pressures and lower frequencies. Cavitation is the generation of voids or bubbles within the tissue [4]. These cavities oscillate in response to the acoustic wave, resulting in acoustic emissions, jetting and streaming, which can induce bioeffects [4].

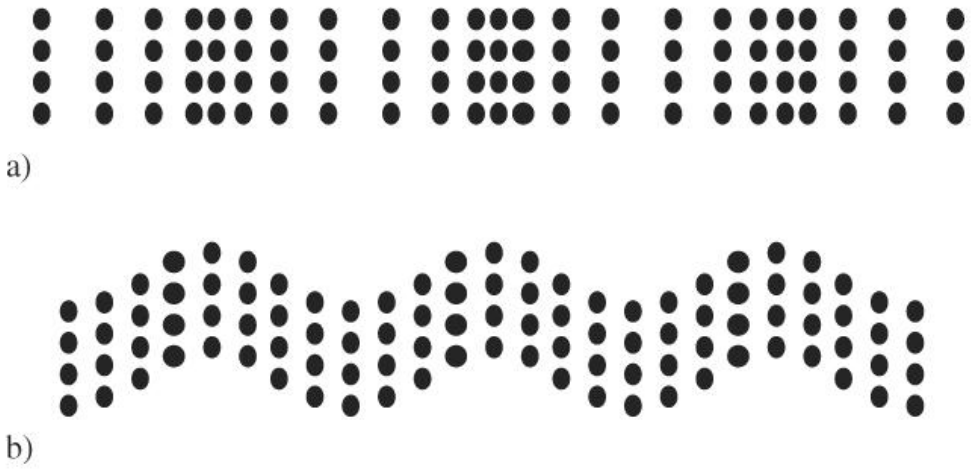

Figure 3.5: Sound waves: a) longitudinal waves b) shear wave [24].

Although tissue consists of all different kinds of materials with their own physical properties, the main component is water. Therefore, water is often used as a test medium in experiments. This is a valid replacement of tissue since the acoustic properties appear to be similar. The typical wave speed for medical applications is therefore assumed to be constant at 1540 m/s [24] (compared to 1575 m/s for nerve tissue and 1590 m/s for muscle tissue [50]). The relation between the speed, wavelength and frequency of a wave is shown in the following equation:

$$c = \lambda f \tag{3.3}$$

The higher the stimulation frequency the higher the resolution which can be achieved with stimulating or imaging. However, the penetration depth decreases for higher frequencies. In addition, a higher frequency often requires a larger threshold intensity to stimulate neural tissue [51]. Typically therapeutic applications operate around 1 MHz. Diagnostic applications operate between 2.5 and 7.5 MHz. For superficial body parts, even higher frequencies are used like 7.5-15 MHz.

For unguided waves, three particular geometries can be defined [52]. These geometries are defined by the shape of the locus of all the medium particles that are in phase. Spherical waves have phasefronts with concentric spheres. Cylindrical waves exhibit concentric cylinders. Plane waves have phasefronts which are planar. When observed over a small region all waves can be modeled as plane waves. This is called locally planar [52].

Since tissue can be modeled with water, the waves in the body are assumed to be planar longitudinal waves. It is assumed that the liquid is in equilibrium and that it has a density ρ_m [kg/m^3], a static pressure P [Pa] and a temperature T [$^\circ C$] [49]. These parameters can be related to each other by means of the isothermal compressibility β^p and the thermal expansion coefficient β. Since water has good thermal conductivity (0.53 $Wm^{-1}K^{-1}$ at 37 $^\circ C$) temperature variations in the liquid due to the waves are rapidly smoothed out. Therefore, only considering the isothermal compressibility is valid. The variation of the pressure in the case of a plane sound wave is then expressed in the following wave equation [49]:

$$\frac{\partial^2 P}{\partial x^2} = \frac{1}{c_m^2}\frac{\partial^2 P}{\partial t^2} \tag{3.4}$$

where c_m is the sound speed [m/s]. Equation 3.4 is only valid for uniform, homogeneous liquids with negligible attenuation due to viscous and thermal effects. Moreover, the acoustic pressure should be small compared to the equilibrium pressure [49]. Although it is a simplified equation, it turns out to be adequate in practice. The solution of Equation 3.4 is a pressure wave traveling in the positive x-direction and can be written as [49]:

$$P(x,t) = P_0 e^{-\alpha_m x} e^{j(\omega t - \phi)} \tag{3.5}$$

where α_m is the attenuation of the medium, ω is the frequency of US and P_0 is the initial amplitude of the pressure. The attenuation coefficient α_m is related to frequency and distance. For soft tissue, the frequency relation is 0.7 $dB/cm\ MHz$ [24]. For the distance relation, it holds that the further the wave travels from the source the more it attenuates.

In fluids, the acoustic pressure and the wave velocity in the fluid are related via the acoustic impedance Z (with units [kg/m^2s] or [Rayl]). The acoustic impedance is defined as [49]:

$$Z = \frac{P}{v} \tag{3.6}$$

where P is the pressure and v the velocity of the particles.
This can be rewritten as the acoustic impedance of a material [49]:

$$Z_m = \rho_m c_m (1 - j\frac{\alpha_m \lambda}{2\pi}) \tag{3.7}$$

To simplify the acoustic impedance, in many cases α_m can be set to zero [24]. Then [53]:

$$Z_m = \rho_m c_m \tag{3.8}$$

The specific acoustic impedance (intensive property of a medium) also includes the area [53]:

$$Z_{ms} = Z_m A = A\rho_m c_m \tag{3.9}$$

Due to acoustic impedance discontinuities, the acoustic wave flow can encounter opposition. This causes transmission, reflection and refraction of the wave [6]. The result is low sensitivity, narrow bandwidth, longer US pulses and longer transducer ring-down time [53]. Snell's law for light waves also applies to acoustic waves [49]. In case of normal incidence ($\theta_i = \theta_t = 0$) and aiming for the best continuity of the pressure wave the following relations hold [49] [53]:

$$\frac{P_r}{P_i} = \frac{Z_2 - Z_1}{Z_2 + Z_1} \tag{3.10}$$

and

$$\frac{P_t}{P_i} = \frac{2Z_2}{Z_2 + Z_1} \tag{3.11}$$

where P_r is the reflected pressure, P_t the transmitted pressure, P_i the incident pressure, Z_1 the acoustic impedance of the first material and Z_2 the acoustic impedance of the second material. To avoid destructive interference, $Z_2 > Z_1$, since in that case the reflected pressure wave is in phase with the incident wave.

Due to the interference of the incident wave with the reflected wave, standing waves are buildup. In the case of a non-perfect reflection multilayer design, standing waves can superimpose with the traveling waves. This can be derived analytically for a three-layer design in the case of normal incidence [49]. From this derivation, there are two cases when the second layer becomes acoustically transparent. First, when the thickness of the second layer is much less than the wavelength ($l_2 << l_2/4$). Second, when the thickness of the second layer fulfills $l_2 = n\lambda/2$.

In case of acoustic impedance mismatch between layers, matching layers can be used to minimize reflections. Using the traditional quarter wavelength matching method [53], the optimal acoustic impedance of the matching layer (Z_2) is then [32]:

$$Z_2 = \sqrt{Z_1 * Z_3} \tag{3.12}$$

where Z_1 is the acoustic impedance of the first material and Z_3 is the acoustic impedance of the load material. In the case of water, materials having a similar acoustic impedance as water and having a thickness of a quarter wavelength increase the acoustic power transfer [54]. To fulfill Equation 3.12 the sound speed in the matching layer should be higher than that in the medium [51]. More about matching layers can be found in section 3.3.3.

As seen before, the distance from the source determines the attenuation of the wave. In the case of layers, this translates to the thickness of the layer. Therefore, the thinner the matching layer the smaller the attenuation and thus the better. However, these matching layers are not readily available and are primarily custom-made. In addition, these layers become too thin in the case of high-frequency neuromodulation (>100 MHz).

There are two different generation modes for ultrasound. A continuous mode (CW ultrasound) and a pulsed mode (PW ultrasound) [24]. In continuous mode, the ultrasonic transducer is driven by an electrical sine wave at a constant amplitude which gives continuous excitation. In pulsed mode, the ultrasonic transducer is electrically excited for a short period of time which results in pulsed excitation. PW US is used for imaging, while stimulation sequences consist of CW US [25]. CW US has the advantage of allowing higher available power and thus meets the pulse duration (PD) required for neuromodulation [25].

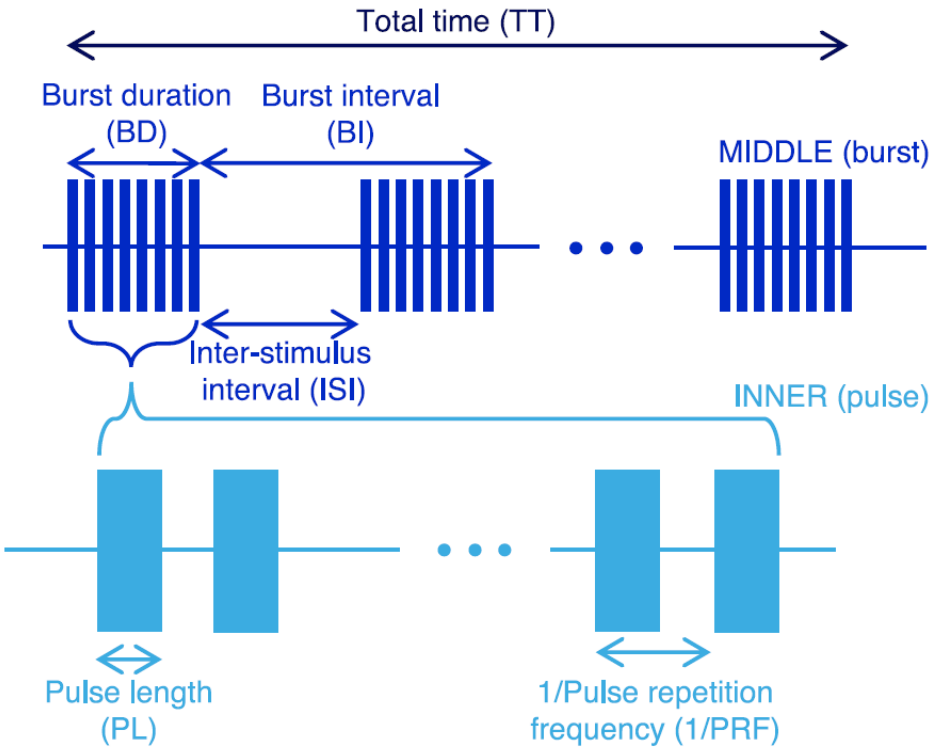

Figure 3.6: Overview of US sequences and associated parameters [4].

The US sequence can be represented in a sonication profile. An overview of US sequences and associated parameters can be seen in Figure 3.6. In the case of PW ultrasound, the pulses have a pulse repetition frequency (PRF) and are repeated at this frequency for a length of time defined by the burst duration (BD) [4]. The burst duty cycle (BDC) is the pulse length (PL) or pulse duration (PD) multiplied by the PRF. One distinct trail is a burst which can be delivered at a burst repetition frequency (BRF). The time in between these bursts is the inter-stimulus interval (ISI). The total time (TT) is the total time of the experiment with its related total duty cycle (TDC). In the case of CW ultrasound, the BD and the burst interval are irrelevant. To define the fractional amount of time that the pulse is activated the duty factor (DF) can be used. Is expressed as:

$$DF = \frac{PL}{(\frac{1}{PRF})} \tag{3.13}$$

The pressure of the wave determines the intensity of US [49]. To stimulate peripheral nerves, pressures above 3 MPa should be generated [4], [7]. In addition, a break period of 20-30 seconds improves the

success rate of subsequent stimulation to 92% [7]. The instantaneous intensity is defined as [55]:

$$I_{inst} = Pc_m \tag{3.14}$$

Using the acoustic impedance relations of Equation 3.6 and 3.8 and rewriting Equation 3.14 gives:

$$I_{RMS} = \frac{P^2}{\rho_m c_m} \tag{3.15}$$

Assuming a sinusoidal oscillation the average intensity is expressed as [49] [10] [56]:

$$I_{RMS} = \frac{P^2}{2\rho_m c_m} \tag{3.16}$$

Based on the parameters used from the sonication profile, different intensity metrics are used throughout literature [4]:

- I_{SPPA} (spatial-peak, pulse-averaged intensity) the average intensity of an individual pulse
- I_{SPBA} (spatial-peak, burst-averaged intensity) the intensity averaged over one BD
- I_{SPTA} (spatial-peak, temporal-averaged intensity) the intensity averaged over the total experimental time (including the ISI)

The sound pressure levels can be obtained from the hydrophone output. The sensitivity converts the output voltage into an acoustic pressure. These hydrophone-specific sensitivity values are given in the datasheet of the hydrophone.

From the intensity, the force per unit area can be obtained. The force per unit volume of tissue for a time-harmonic, progressive, plane wave is given by [4]:

$$F_{ARF} = \frac{2\alpha I}{c_0} \approx \frac{\alpha_0}{\rho_0 c_0^2} f p^2 \tag{3.17}$$

where α is the attenuation, I the local intensity of the acoustic field, c_0 is the speed of sound and ρ_0 is the density.

Although the impact of US propagation can be described, the underlying mechanisms behind neuromodulation are not well understood. There are hypotheses that US does interfere with mechanosensitive ion channels [4]. Ion channels being mechanosensitive are TREK-1, TREK-2, TRAAK, voltage-gated Na+ and Ca+, Piezo1 and Piezo2 [6]. There is also a hypothesis that not mechanical effects, but thermal effects drive neuromodulation. Until now, thermal effects are associated with the inactivation of nerves [22] while mechanical effects are connected to the activation of nerves [7].

Other hypotheses assume that membrane deformation causes capacitance changes eliciting an action potential [4]. Capacitance could be changed by membrane volume changes or can be associated with the flexoelectric effect (a spontaneous electric polarization of the membrane when subject to mechanical strain gradients) [6]. The idea of capacitance changes is the idea behind the intramembrane cavitation model. In that model, intramembrane cavitation within the bilayer membrane induces a current through capacitance changes [57]. Another hypothesis model is the so-called soliton model [58]. In this model, it is proposed that a mechanical pulse propagates in phase with an electrical pulse along the axon. There is coupling into membrane waves along the axon [4]. In addition to nerves, also astrocytes may be involved. There is a hypothesis that US opens TPRA1 channels in astrocytes. This induces glutamate-releasing Best1 as a mediator of glianeuronal interaction [59].

In the end, it is likely that different combinations of partially overlapping mechanisms would occur in the cell membrane depending on the US pulse regime [6] [4]. Although the mechanisms are not well-defined yet, it has been demonstrated that focused ultrasound stimulation (FUS) can elicit a physiological response in peripheral nerves [7] [32] [21].

Although US stimulation is less invasive compared to nerve electrodes, the risk of tissue damage still

exists. This mainly happens due to the sonication profile when using excessive durations (>100 ms) or pressures (>5.7 MPa). As the excitation is not being improved, high pressures and excessive durations are not necessary and should be avoided [7].
Examples of damage are red blood cell extravasation, abnormal cell morphology, inflammation and destruction of cellular membranes [7]. In some situations, temporal or permanent damage is preferred. High-intensity focused ultrasound (HIFU) has been used to decrease or block nerve conduction in order to treat severe spasticity and certain types of chronic pain [23] [22]. In these systems, the intensities are greater than 1000 W/cm^2, but the energy can be focused on a small region ($\approx$0.5 x 5 mm ellipsoid) [23]. Applying these intensities leads to immediate damage like myelin disruption and axon swelling.

Thermal heating of tissue is another consideration to take into account. This could be measured using thermocouples embedded in the tissue. However, in case normal stimulation parameters are used no significant thermal effects occur [7] [21].

3.2.3. Conclusion

In Section 3.2.1 and 3.2.2 electrode and US stimulation have been described. Achieving high specificity with electrode stimulation is still a challenge. Intraneural electrodes and transverse intra-fascicular multichannel electrodes (TIME) [38] can obtain high sensitivities, but the invasiveness of these electrodes is a risk for fragile nerves. Therefore, these techniques cannot be used for VNS. In addition, the placement of the electrodes during implantation influences the location of the stimulation spot. Therefore, the electrode stimulation spot is vulnerable to implantation misalignments reducing the accuracy.

US stimulation is a relatively new technique. The benefit of US is the possibility to penetrate through tissue. This means that less invasive implants are needed to target the right tissue. In addition, US can obtain higher specificity than electrical stimulation [10]. With the technique of FUS it can be focused on small spots without affecting neighboring areas.

Due to the advantages of US over electrical stimulation, this technique will be used in this thesis. As the VN is a delicate nerve, the least invasive technique with the highest specificity is crucial. As the cuff implants give the best specificity, the US technique will be integrated into a cuff-shaped implant.

3.3. The piezoelectric transducer

To generate ultrasound, transducers are needed. A transducer converts a type of energy into another energy type. In the case of a piezoelectric transducer based on the inverse piezoelectric effect, electrical energy is converted into mechanical energy. A piezoelectric transducer can consist of a piezoelectric element, electrical connections, a backing layer, a matching layer and an acoustic lens [60] [61]. Two connections on the top and bottom of the piezoelectric element are attached for driving the element. By generating a regime of electrical pulses, the crystal is excited.

Two main types of transducers exist, bulk mode and flexural mode. In bulk mode, the inverse piezoelectric effect of lead zirconate titanate (PZT, $Pb(Zr_xTi_{1-x})O_3$) ceramics is used to generate acoustic waves. PZT ceramics are popular due to their superior dielectric and piezoelectric constants and thermal stability [54]. In flexural mode, a piezoelectric flexural membrane generates acoustic waves. There are typically two types of flexural mode transducers: piezoelectric micro-fabricated US transducer (pMUT) and capacitive micro-fabricated US transducer (cMUT). PZT bulk mode transducers will be used in this project since they are characterized by a high transmit electroacoustic sensitivity (S_{tx} $[V/Pa]$) and a high quality factor (Q), which is important for stimulation [25] [62] [53]. However, the acoustic mismatch of the transducer with tissue is large. This means that an acoustic matching layer is necessary to increase transmission efficiency [25]. It is recommended to use a backing layer to increase bandwidth. pMUT and cMUT devices are suitable for imaging or sensor applications [54]. The cMUT devices have higher bandwidth and sensitivity, but lower acoustic power compared to pMUT devices [63]. In general, they have lower S_{tx}. The acoustic matching with soft tissue is higher which means that matching layers are not required [25]. In addition, their high bias voltages limit their applications in vivo [64]. Moreover, the movement of the flexible membrane is limited, as the membrane should not stick to either wall.

3.3.1. Piezoelectricity

PZT bulk mode transducers are related to piezoelectricity. Piezoelectricity is a property of certain dielectric materials to generate an electric charge when the material is physically deformed. PZT bulk mode transducers use the reverse piezoelectric effect [65]. In that case, the material physically deforms in the presence of an electric field. Piezoelectricity occurs in the case of spontaneous polarization which is caused by the displacement of electron clouds relative to their individual atomic centers. This produces an electric dipole. Some materials can be made piezoelectric by poling (ferroelectric materials). This means that the randomly oriented polar domains inside the material will be aligned with a strong electric field outside. Once poled, the material exhibits macroscopic polarization. The material can be depolarized by a large opposite electric field (maximal $600\ V/mm$ @$60Hz$) or by excessive heat. The maximum depoling field is the coercive field (E_c [V/m]) and the maximum temperature is the Curie temperature (T_c [$^\circ C$]). For the operating temperature, it is recommended to use a maximum of half the Curie temperature [62]. This reduces depoling, the aging process, electrical and mechanical losses and assures the maximum safe stress level.

If a voltage is applied to create an electric field in the same direction as the poling of the piezo material, the material will elongate along that axis and contract in the transverse direction (Figure 3.7). In case stress is applied to the piezo material an electric field arises in the material [65]. Compressive stress generates an electric field in the same direction as the poling field. Tensile stress on the other hand generates an electric field opposite to the original poling field.

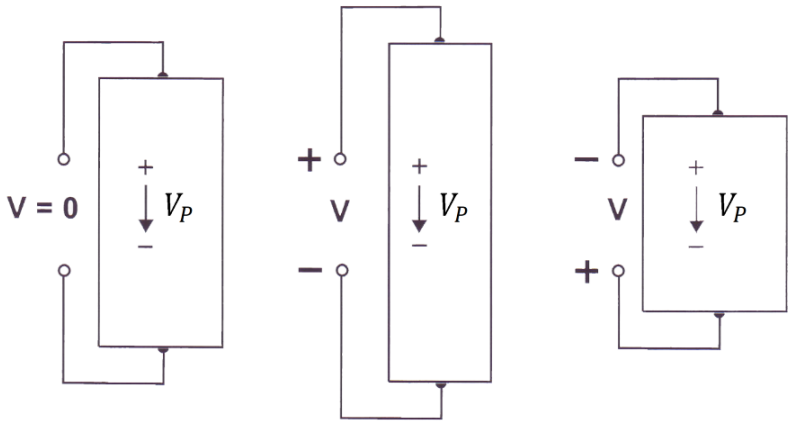

Figure 3.7: An overview of a piezoelement with internal poling voltage (V_P) and different externally applied voltages (V) [66].

In a piezoelectric material, the elastic and electrical properties are coupled. In a linear regime, this can be represented by the constitutive relations consisting of the sensing 3.18 and actuation law 3.19 [53].

$$D_m = d_{mkl}\sigma_k l + \epsilon_{mn}E_n \tag{3.18}$$

$$\epsilon_{ij} = S_{ijkl}\sigma_{kl} + d_{nij}E_n \tag{3.19}$$

in which D is the dielectric displacement, σ the stress, ϵ the strain and E the electric field. S_{ijkl} represents the short-circuit mechanical compliances of the medium while d_{mkl} is a tensor of the piezoelectric material [53].

A piezoelement has two strongly exciting vibration modes, the thickness extensional (TE) mode and the planar expander (PE) mode. In the case of a disc-shaped transducer for which the aspect ratio (D_0/t) is large, the TE mode is dominant. D_0 is the outer diameter while t is the thickness of the transducer [51]. This large aspect ratio is an important geometrical design consideration [32].

Piezoelectric material can be characterized by multiple parameters and subsequent notations. These parameters and the notation are listed in Appendix B. The two most important material parameters are the piezoelectric charge coefficient d and the piezoelectric voltage coefficient g.

The charge coefficient describes the electric polarization generated in a certain direction with respect to the direction of the applied stress [53]. The three common coupling factors are d_{33} (longitudinal coefficient), d_{31} (transverse coefficient) and d_{15} (shear coefficient). In the case of a thickness or out-of-plane vibration the piezoelectric material with the largest d_{33} is selected, ignoring the other two coefficients. The voltage coefficient g is an indication of the sensitivity of the piezoelectric material in a direction with respect to the direction the stress is applied. The same subscripts as for the charge coefficient can be used for the voltage coefficient. d and g are related as follows:

$$g = \frac{d}{\epsilon_r \epsilon_0} \tag{3.20}$$

where ϵ_r is the relative permittivity of the piezoelectric element and ϵ_0 is the permittivity of free space [53].

As a figure of merit (FOM) the relation $d_h g_h$ can be used. Here $d_h = d_{33} + 2d_{31}$ and $g_h = g_{33} + 2g_{31}$. The charge coefficient d is related to transmission capability while the voltage coefficient g is closely related to the reception capability [53].

To maximize efficiency the losses should be minimized. Dielectric losses are related to the dielectric loss factor $tan\delta$:

$$\frac{d_h g_h}{tan\delta} \tag{3.21}$$

Minimizing the dielectric loss factor is essential for low dielectric losses [53].

Moreover, the mechanical quality factor Q_m is related to losses. It indicates the amount of mechanical loss due to internal friction or acoustic viscosity.

$$Q = \frac{\pi}{ln(\eta)} \tag{3.22}$$

where η is the damping coefficient defined as the ratio between the amplitudes of the first and second cycles of oscillation. The quality factor should be as low as possible, but since it is related to bandwidth (Equation 3.23) a trade-off exists.

$$BW_{-3dB} = \frac{f_R}{Q} \tag{3.23}$$

where f_R is the resonance frequency. The bandwidth can be increased by using a matched backing material. However, this increases the damping and thus the energy loss. There is a trade-off between transducer efficiency and bandwidth. In the case of a small damping factor η, the resonance frequency can be assumed to be the same as the characteristic frequency of the transducer f_0 defined as [53] [63]:

$$f_0 = \frac{v}{2d} \tag{3.24}$$

where d is the thickness of the transducer.

To indicate the effectiveness of the conversion of electrical energy to mechanical energy the electromechanical coupling factor k is used. For thickness mode transducers k_{33} should be high while k_{31} should be low. k_{33} and k_{31} are defined as:

$$k_{33} = \frac{d_{33}}{\sqrt{S_{33}\epsilon_{33}}} \tag{3.25}$$

$$k_{31} = \frac{d_{31}}{\sqrt{S_{11}\epsilon_{33}}} \tag{3.26}$$

The electromechanical coupling factor can be brought in relation to the resonance frequency (f_r) and the anti-resonance frequency (f_a) [54] [61] [53] [64] [63].

$$k_{eff} = \sqrt{\frac{f_a^2 - f_r^2}{f_a^2}} \tag{3.27}$$

For the thickness mode configuration, the electromechanical coupling coefficient (k_t) can be expressed as:

$$k_t = k_{eff} = \sqrt{\frac{\pi f_r}{2 f_a} tan(\frac{\pi}{2} \frac{f_a - f_r}{f_a})} \tag{3.28}$$

In this thesis, the focus will be on piezoelectric motors, since stimulation is the purpose. In Appendix A an overview of the trade-offs for commonly considered piezoelectric motor transducers is shown. In addition, the formulas for displacement, force and resonant frequency are depicted.

For specifying the specific movement and the specific force of a piezo motor a force versus deflection line can be used. On the y-axis, the free deflection and on the x-axis the blocked force is depicted. The larger these values the more voltage should be applied. A 45° line shows the operating points to produce maximum work.

The speed or expressed response time of the piezo motor depends on the resonant frequency. It can work up to its resonant frequency, but in general, it is preferred to limit this to 3/4*f_{res}. In a bipolar operation, the response time is 1/4 cycle.

To achieve large deflections at low voltages (so high efficiency) operating at resonance is useful. At resonance frequencies, the stored energy becomes large compared to the excitation energy. The thickness of the PZT layer does determine the frequency. For resonance, the thickness of the layer should be equal to half the wavelength at the speed of sound in PZT [54]:

$$t_{PZT} = \frac{\lambda}{2} \tag{3.29}$$

where t_{PZT} is the PZT thickness. However, it should be taken into account to avoid overstraining or cracking of the piezo motor. The maximum tensile stress should be in the range of $20 - 35 * 10^6$ N/m^2, the compressive stress should be smaller than $-50 * 10^6\ N/m^2$ and the maximum strain should be lower than $500 * 10^6$. Working at resonance also reduces the bandwidth since the resonant peak is small in general.

Another effect that is exhibited by piezo materials is the pyroelectric effect. This means that an electric field is induced on the electrodes when a thermal change occurs. This can be described by:

$$E = \frac{\alpha(\Delta T)}{\epsilon_0 K_3} \tag{3.30}$$

Where α [C/m^2] is the pyroelectric coefficient.

A depoling voltage can be built up in case the temperature drops. This should be considered in the case of processing and testing. In normal use, this will not be an issue since the piezoelements will be used in an implant in the body at which the temperature deviations are small. To avoid poling voltages larger than the coercive field the electrodes should be shorted during cool-down procedures.

Other effects to take into account are the thermal expansion coefficient ($4\ \mu m/m°C$ for PZT-5A) and the vacuum operation. In low-pressure ranges, arcing and outgassing might occur depending on the construction materials. This is important to consider while processing. In the end, aging plays a role, but this depends on the ceramic material, the manufacturing processes, and the ambient conditions like temperature, vibration and shock [65].

3.3.2. Piezoelectric materials

There are multiple types of piezoelectric materials in use. They can be classified as natural materials and synthetic materials [53]. Examples of natural materials are quartz, berlinite and sucrose. Synthetic materials can be subdivided into synthetic crystals, ceramics, polymers and composites. Examples of crystals are orthophosphate and langasite. Some ceramics are barium titanate and lead zirconate titanate (PZT). The most widely used polymer is polyvinylidene fluoride (PVDF). Composite materials are developed to satisfy certain requirements. For example, to overcome the brittleness of ceramics,

the low sensitivity of polymers or the acoustic mismatch between the piezo material and the media. For neuromodulation high pressures are necessary, therefore good piezoelectric properties are important. As piezoceramic materials excel with strong and stable piezoelectric characteristics, these materials will be investigated more.

PZT is most often used in applications as piezoceramic material. It has high strength, a high Curie point and it is relatively easy to fabricate [53]. However, the big disadvantage of PZT material is the embedded lead. During the processing stages, lead oxide vaporizes in the environment which is toxic. Therefore, lead-free materials exist as alternatives. Examples are barium titanate and lithium niobate [53]. The piezoelectric properties of the lead-free alternatives are slightly lower compared to PZT. Moreover, these materials are more expensive. Therefore, in this research PZT material will be used. Since the embedded lead can be potentially toxic, the encapsulation of the materials, when used as an implant is crucial.

There are different PZT ceramics available on the market. Each of them has its own parameters. Different PZT ceramics with their parameters obtained from literature and Piezo.com are shown in Appendix C.

An effective method to improve the electromechanical properties of PZT is texture engineering. This method introduces directionally oriented template seed crystals into the ceramics [61]. These seed crystals guide the grain growth to produce oriented grains in the ceramic. Although research results about these textured PZT ceramics are promising and could replace the expensive single crystals, the method cannot be performed in the Else Kooi Lab (EKL) and is therefore outside the scope of this thesis work.

Another option could be PNN-PZT ceramics. These ceramics have the advantage of a simple sintering process and high reproducibility [61]. For the texturing, calcined powders with small particle sizes are needed. To texture PNN-PZT ceramics, the calcination temperature is lowered, making the use of these powders easier. Therefore, textured PNN-PZT ceramics is a promising ceramic.

Based on these parameters the PMN-PT single-crystal piezoelectric material has the best performance. Another promising single-crystal piezoelectric material is the PZN-PT [63]. However, the disadvantages are the high cost [32] and the difficulty in machining [53]. In addition, they have low phase-transition temperatures ($T_{RT} = 124\ ^{\circ}C$ for PZN-PT and $T_{RT} = 90\ ^{\circ}C$ for PMN-PT [63]). If the working temperature is above the T_{RT}, the piezoelectric properties are significantly reduced. Therefore, the working temperatures should be controlled to maintain a high coupling and to achieve high piezoelectric constants [63]. In case the temperature is exceeded during fabrication, the properties can be regained by means of poling [63]. For this process, high electric fields are needed (2 kV/mm [63] or 0.35 kV/mm [67]).

Second-generation piezoelectric single crystals exist. These materials have a higher T_{RT} and the growing process is adapted so the production costs are reduced [63]. One of them is PMN-PZT (Appendix C). However, the T_{RT} is not improved (85 °C).

The thickness of the PZT can be controlled using a so-called thinning process [18] or by means of lapping [63] [68] [18].

3.3.3. Matching layer

The acoustic impedance of PZT material (34 MRayl) has a large mismatch with the acoustic impedance of tissue (and in experiments with water (1.5M Rayl)). As explained in section 3.2.2 an acoustic mismatch causes reflections of the incident power, reducing the transmitted power. Reflections therefore often occur due to layer junctions. An example is the junction between polyimide and polydimethylsiloxane (PDMS) in the case of [64]. These reflections can be minimized by using the concept of matching. In the traditional quarter wavelength matching method the acoustic impedance of the matching material should be the acoustic impedance of material one times the acoustic impedance of material two and

taking the square root of that number. Using multiple matching layers (n) the formula becomes:

$$Z_M^{(j)} = \sqrt[n+1]{Z_A^{(n-j+1)} Z_B^{(j)}} \tag{3.31}$$

For higher frequencies the layer thicknesses needed for traditional quarter wavelength matching are technically challenging to fabricate. Instead of using the traditional quarter wavelength matching method, the matching layer properties can be obtained using the Krimholtz, Leedom and Matthaei (KLM) transmission line model [53] [51]. With this technique, the number of matching layers and their respective acoustic impedances can be obtained while maximizing bandwidth and efficiency. The model is shown in Figure 3.8.

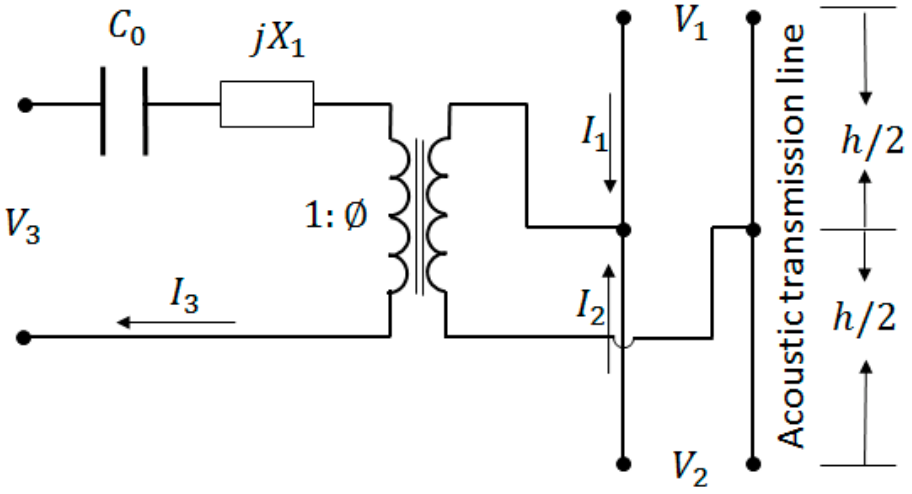

Figure 3.8: The KML model of a piezoelectric transducer [53].

An input electrical port drives the transducer, which consists of two acoustic ports (front and back). The equivalent electrical model is based on Masons model which considers the electric effects due to insertion loss, acoustic load and backing impedances on the acoustic port [53]. By means of the material characteristics, the different lumped elements can be calculated. Based on the equivalent model the optimal number of matching layers and their acoustic impedances can be obtained by maximizing efficiency and bandwidth. A more elaborate explanation of KLM modeling and formulas can be found in Appendix D.

To simplify the calculations of the lumped elements the mass-spring approach has been developed [53]. In that approach, high impedance materials are considered masses while low impedances are considered as springs. However, the accuracy depends on the estimated equivalent masses and there should be a significant impedance difference between the masses and the springs.

As a matching layer, several materials have been used in previous research. [61] used E-51 epoxy resin mixed with 100 nm alumina at a mass ratio of 1:1. [51] used EPOTEK-301 [1] as a focusing lens, encapsulation layer and matching layer. Moreover, EPOTEK-301 with Al_2O_3 was used as a matching layer. Adding alumina increases the acoustic impedance, leading to a lower R_0 (Appendix D for equation D.5) and lower Q-factor [51]. Adding a focusing lens in the matching layer does lead to increased power efficiencies and higher resolutions [51]. However, it is challenging to implement this technique on small-scale transducers.

3.3.4. Backing layer

The backing layer impacts the generated acoustic intensity and affects the transducer electrical impedance [51]. The KLM model can also be used for obtaining the parameters of the backing layer in a transducer. The transducer impedance at resonance (Appendix D for equation D.5) is inversely proportional

[1] https://www.epotek.com/product/301/

to Z_B. A small Z_B causes reflection of the waves at the back, generating higher acoustic pressure in the medium leading to a higher Q-factor [51]. In imaging, the backing material has high Z_B and large damping to increase bandwidth (low Q) by reducing the reflections of waves to the backside of the transducer [25]. In US stimulation materials with low Z_B are preferred since this results in higher signal amplitude while the resolution increases [32]. A suitable backing layer with a low Z_B is air ($403\ Rayl$).

Other materials used as a backing layer are E-51 epoxy resin mixed with $5\ \mu m$ tungsten powder at a mass ratio of 1:8.5 [61]. [32] uses epoxy resin mixed with $25\ \mu m$ tungsten powder. Mixing epoxy with metal gives the opportunity to tune the acoustic impedance for optimal matching. However, mixing two materials and obtaining a uniform mixture is difficult in practice. Especially for high-frequency transducers for which the layers need to be thin.

3.3.5. Beam profile

An unfocused transducer has a natural focus. The acoustic beam profile consists of a near-field zone, the Fresnel zone, and a far-field zone, the Fraunhofer zone [51] (Figure 3.9).

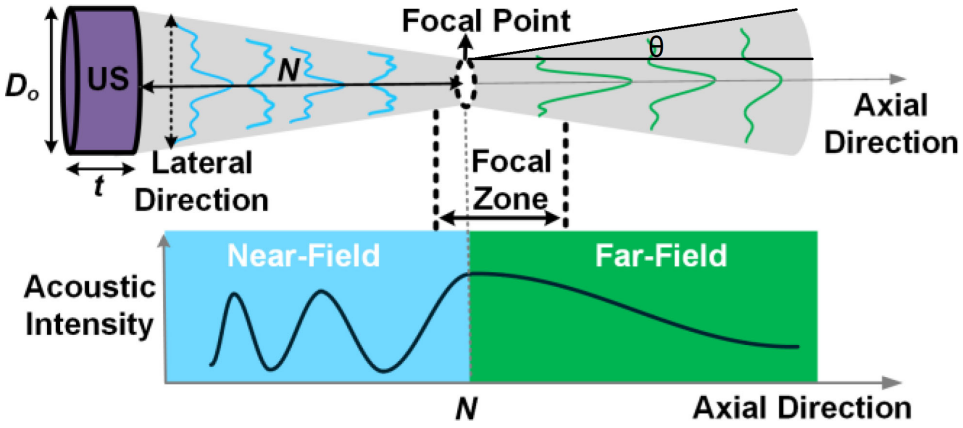

Figure 3.9: The acoustic beam profile of an unfocused transducer [51].

In the region between these fields, a natural focal zone exists with a small beam width and a high acoustic intensity. The length of the near-field is called the focal length (N) and can be calculated [51] using:

$$N = \frac{f_p L^2}{4v} \tag{3.32}$$

where v is the sound velocity in the medium and L [m] the aperture. In the near-field, local maxima and minima exist, but these depend on the medium and are difficult to model. The far-field beam profile can be predicted with higher accuracy. The far field is a diverging acoustic beam of which the angle is defined as:

$$sin(\theta) = \frac{1.2\lambda}{L} \tag{3.33}$$

where θ [°] is the angle.

The beam profile is sensitive to the driving frequency. It is important to sweep this frequency around the resonance frequency to find the optimal driving frequency and maximize I^2PR. According to [51], the optimal driving frequency for I^2PR is close to the parallel resonance frequency. This frequency might be different from the center frequency of the transducer for which the pulse-echo frequency spectrum is maximum.

An array of multiple unfocused transducers can be used for beamforming when the signals become phased [69]. These phased arrays can be passive or active. An example of a passive phased array is the design in [70]. They use a metascreen with Helmholtz resonators to phase the acoustic signals of a single acoustic source. These structures are difficult to miniaturize and can steer the signal in only one direction the screen is designed for. Therefore, active phased arrays are more common on a

small-scale level. In active phased arrays each piezoelement is driven individually. To these individual signals, phase delays are added. These delays are used to steer the US beam to the wanted spot. The transducers closer to the target will transmit their signal later than the transducers further away, this results in a beam focused on a particular spot (Figure 3.10).

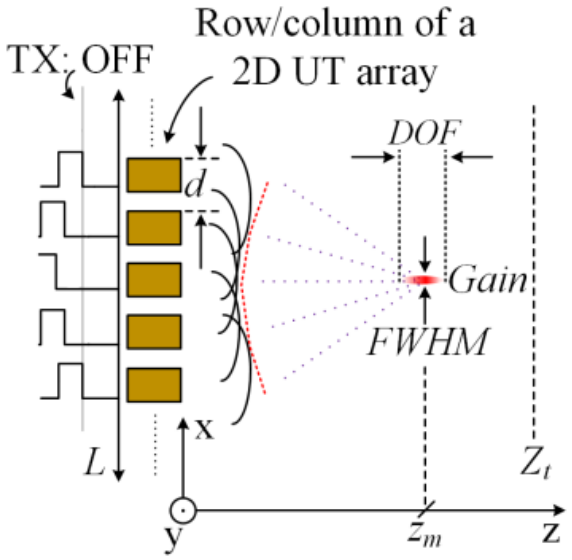

Figure 3.10: A phased array [25].

The piezoelements are organized in a 2D array. Each piezoelectric transducer has an aperture L and an inter-element pitch d. These are related as[25]:

$$L = d(\sqrt{N} - 1) \tag{3.34}$$

where N is the number of transducers of a squared 2D phased array [25]. In addition, d must respect equation 3.35 to avoid grating lobes in the field of view of the transducer array [25].

$$d = \frac{\lambda}{1 + sin(\theta_{max})} \tag{3.35}$$

The focused US beam can be described by the depth (Z_m up to a maximum Z_t (Equation 3.36)) and steering angle (θ_{XZ} for the XZ-plane and θ_{YZ} for the YZ-plane) [25].

$$Z_t \approx \frac{L^2}{\pi\lambda} \tag{3.36}$$

The focal spot properties are the full width at half maximum (FHWM, see Equation 3.37), the depth of field (DOF, see Equation 3.38) and the focusing gain (Gain, see Equation 3.39) [25].

$$FWHM \propto \frac{\lambda Z_m}{L} \tag{3.37}$$

$$DOF \propto \frac{\lambda Z_m^2}{L^2} \tag{3.38}$$

$$Gain \propto \frac{L}{\lambda Z_m} \tag{3.39}$$

Decreasing λ and increasing L leads to a lower FHWM and DOF and larger Z_t and Gain. However, decreasing λ results in a smaller d, leading to a smaller area for each transmitting circuit channel. In

addition, the attenuation of the acoustic pressure increases linearly with distance and exponentially with frequency. Increasing L leads to a larger number of N reducing the power per channel.

From equation D.3 and 3.32 the dependence of the beam profile and the transducer performance on the dimensions of the transducer are clearly visible [51]. In general, smaller D_0 improves the lateral resolution at shorter N. The energy efficiency improves for relatively large D_0/t ratios.

Having an array of transducers of which the kerfs are filled with flexible materials can cause crosstalk. [71] simulate the crosstalk using three transducers with a pitch of 4.5 mm filled with silicone elastomer. The middle one is stimulated while the other two are measured. This results in a crosstalk value of -97 dB (5 V stimulation over 0.07 mV measured).

3.3.6. Packaging

Packaging is really important for implantable devices since mechanical damage to leads and connectors, corrosion and electrical shorts due to moisture penetration are primary causes of device failure [62]. Problems with traditional polymeric encapsulations are the vulnerability to water vapor transmission, delamination and degradation. It has been shown that a 100 nm thick ceramic (thermally grown SiO_2) has a superior moisture barrier compared to microns-thick polymers like polyimide, SU-8, PDMS and parylene-C [72]. That is the reason why [62] proposes a package consisting of an alumina housing with a thin titanium lid for US coupling. In case the thickness of the lid becomes small relative to the interrogation wavelength, the lid becomes acoustically transparent at ultrasonic frequencies since [62]:

$$\frac{2\pi d}{\lambda_0} \tag{3.40}$$

In the case of [62], a thickness of 10 μm for titanium is transparent to 90% of the transmitted pressure. The transmission coefficient is a function of the thickness-to-wavelength ratio. For the interconnects gold has been used, so in case of moisture, no spontaneous galvanic corrosion will occur. This ensures the biocompatibility of this design. By means of microwelding a seal was made. A gold ring was used as filler material. Since this process only applies local heat, it avoids the depoling of the PZT. The package was calculated to have a lifetime of 158 days [62]. However, also in this package microcracks existed, reducing the lifetime.

The lifetime of a package can be calculated using a reactive accelerated aging test [62]. From this, the mean time to failure (MTTF) can be calculated from an Arrhenius model [62]:

$$MTTF(T) = R_0 e^{(\frac{E_a}{k_B T})} \tag{3.41}$$

where R_0 is the gas constant, E_a is the activation energy for the reaction, k_B is the Boltzmann constant and T the temperature.

Packages have also an impact on US transmission. As said before, they can block part of the transmitted power. However, they can also affect the resonant frequency and the vibration displacement. Small PDMS thicknesses have been proven not to impact these parameters [64]. However, the damping of a package on the PZT vibrations cannot be ignored [64].

The interconnect should also be considered when designing a flexible transducer array. One of the options is using a serpentine-like structure [56]. This is developed for an island-bridge layout [71]. Each PZT transducer can be driven independently using a matrix activation scheme (inspired by the active matrix and the top-crossover-to-bottom structure).

3.3.7. Safety metrics

For US techniques, there are no general safety measures regarding stimulation parameters. However, for US imaging, there are typically three metrics to ensure safety. Although this thesis deals with stimulation and not with imaging, these metrics give some insides into the effects that might be harmful. These metrics are the intensity, the thermal index (TI) and the mechanical index (MI) [4]. For the intensity, multiple values are used due to different time scales. The TI is a measure of heating within

the tissue and is defined as the ratio of the acoustic power (W_p) to the power required to raise the tissue by 1 $^\circ C$ (W_{deg}).

$$TI = \frac{W_p}{W_{deg}} \tag{3.42}$$

Using an approximation to the Pennes bioheat transfer equation, the estimated temperature rise comes as follows [4]:

$$\frac{dT}{dt} = \frac{2\alpha I}{\rho_0 c_p} \approx \frac{\alpha_0}{\rho_0^2 c_0 c_p} f p^2 \tag{3.43}$$

The MI is a measure of cavitation and is thus related to the probability of mechanical damage occurring within the tissue.

$$MI = \frac{PNP}{\sqrt{f}} \tag{3.44}$$

where PNP [MPa] is the peak negative pressure and f [MHz] is the frequency. The US FDA guidelines for diagnostic US imaging are that the I_{SPTA} must not exceed 720 mW/cm^2, the I_{SPPA} must not exceed 190 W/cm^2, the TI must not exceed 6 and the MI must not exceed 1.9 [4]. From the British Medical US Society other regulations exist. The TI must not exceed 0.7 for unlimited time and should be less than 3 if the duration is less than 1 minute. Moreover, the MI should be less than 0.7 [4].

3.4. Materials

Selecting the proper materials for the cuff implant is crucial. Since the cuff implant will be implanted, the materials used should be biocompatible. This means that the material is not toxic within the body [73]. Since the cuff implant does contain electronics, shortening of interconnects or discharge of capacitors to the tissue should be avoided. Selecting proper encapsulation materials with a high water penetration barrier is essential. A relatively new group of materials are metamaterials. These are artificial materials and exhibit unprecedented physical properties [74]. Since the fabrication is still under research and fabrication cannot be performed within the range of this thesis project, these materials will not be used. However, for future use, these metamaterials could be interesting.

3.4.1. Flexible polymers

Since the implant will be cuff-shaped and the processing can only be done on a planar surface, the implant itself should be flexible in the end. This can be achieved by using a flexible material as a substrate or connecting rigid silicon parts with a flexible material (island-bridge structure). Polymers are often used in biomedical applications as certain types are biocompatible and they have good mechanical properties. Moroever, they have good acoustic properties and can therefore be used as matching layers.

Parylene is a good electrical insulator and is often used as an encapsulation. In some cases, parylene is used as a matching layer as well, [68]. Like other polymer films, it has a high optical transmittance and excellent mechanical properties. Parylene comes in different types. The most popular type is parylene-C. In addition to other polymer films, this type has a better water vapor barrier, high heat resistance (melting point of 290 $^\circ$C [75]), easy molding and can be deposited using chemical vapor deposition resulting in thin and conformal layers [76] [77]. For performing chemical vapor deposition in EKL in Delft 5 grams dimer is needed for a ±2.5 μm parylene-C layer. Compared to other polymers parylene-C has an excellent ionic barrier. A layer thickness of 25 μm withstood 0.9% saline solution for 30 days, while thin layers (<10 μm) can withstood for shorter timer periods [75].

The disadvantage of parylene-C as encapsulation is its vulnerability to cracking [76] and delamination over time [78]. This drastically reduces the vapor barrier and mechanical properties.

To enhance these properties a polyurethane acrylate coating can be used [76]. This reduces the water vapor transmittance rate to 0.5636 $g * (m^{-2} * day^{-1}$ and the elongation at break and the impact energy are increased to 48.36% and 41.67% respectively [76]. Another technique is thermal annealing. It shows property improvement, but whether this step can be performed depends on the thermal budget of materials that are on the wafer [75].

Although parylene-C is an inert polymer it can be etched in several ways: dry etching, wet etching and laser ablation. The most basic dry etching procedure is using oxygen plasma. The etch rates do depend on the pressure, gas flow and the etch power [79] [75]. Oxidation occurs at temperatures higher than 100 °C [75]. For etching both a spin-coated photoresist (AZ9260) mask or a hard mask (titanium) can be used [80]. As the photoresist is etched as well, it should be thicker than the etch depth. This limitation requires a metal hard mask in deep etch processes. Using only oxygen as an etchant, nanoforest structures can appear on the etched surface of parylene. To improve the etching SF_6 can be added [80]. In that case, higher aspect ratios are obtained.
Wet etching of parylene-C is difficult but there is a chemical solvent that provides reliable parylene-C removal from structures: tetrahydrofuran (THF) [81].
Finally, laser ablation is also an option for opening parylene-C layers. In these cases, a pulsed laser is used. The wavelength, the number of pulses and the environment (vacuum, oxygen, nitrogen) determine the final removed spot of parylene-C [82].

Another aspect to take into account is the adhesion between parylene-C and metals [83]. As adhesion between parylene-C and metals is typically a combination of hydrogen bonding and Van der Waals forces, the adhesion is not strong [75]. Both thermal annealing and plasma-enhanced parylene-C are methods to improve the adhesion between parylene-C and metals.

PDMS is a widely-used and inexpensive polymer [84]. The $-Si-O-Si-$ bonding and the $-CH_3$ group lead to thermal stability, elasticity and hydrophobicity [85] [77]. In addition, PDMS is physiologically inactive, very low in toxicity and therefore does not present health hazards [85]. Besides being biocompatible, this material presents only mild foreign body reactions [86] [84].

PDMS can be spincoated, with layer thicknesses of a micron up to several microns. Moreover, it can be molded [43], although it maintains a rough surface. The thermal expansion coefficient is different compared to metals [64]. This can result in crushed PDMS while sputtering gold at a high temperature for example. Sputtering of metals at room temperature can be a solution for the difference in thermal expansion.

Since PDMS has a similar acoustic impedance as tissue, this material is often used as a matching material. Depending on the thickness, using PDMS as the encapsulation of a PZT does decrease the transmit power [62]. PDMS has a high transmission coefficient compared to other polymers. Panskus et. al. ”publication in preparation” did some simulations and the results are shown in Figure 3.11a and 3.11b. It can be seen that the thickness and the frequency do matter, but that PDMS has the best transmission coefficients compared to other materials.

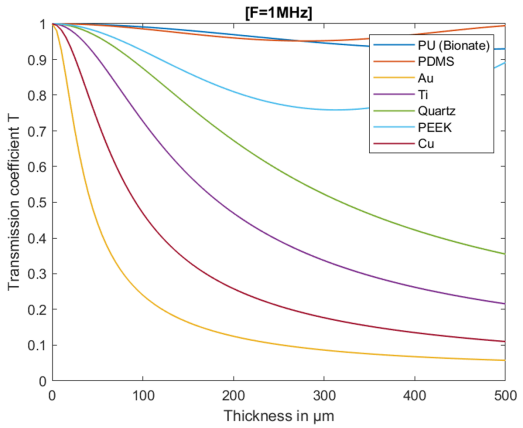

(a) The transmission coefficients for different materials for a range of thicknesses and a frequency of 1 MHz (Panskus et. al. ”publication in preparation”).

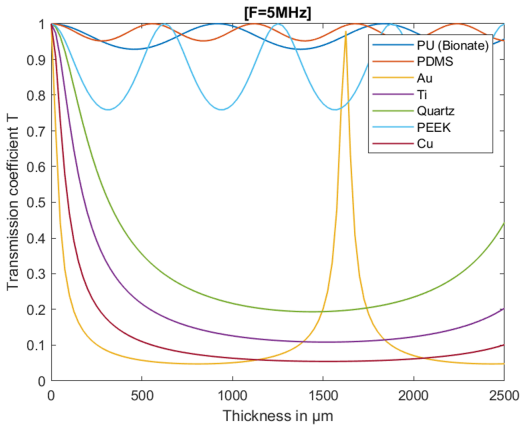

(b) The transmission coefficients for different materials for a range of thicknesses and a frequency of 5 MHz (Panskus et. al. ”publication in preparation”).

Figure 3.11: Simulations of Panskus et. al. ”publication in preparation” of the transmission coefficients of different materials

A well-known type of PDMS is Sylgard 184 [87] [85] [51] [43] [84]. This is a two-part chemical. Part A is the silicone base and part B is the curing agent. As seen from Figure 3.12 the ratio A:B does not influence the transmission coefficient much. The biggest impact will be on the mechanical properties.

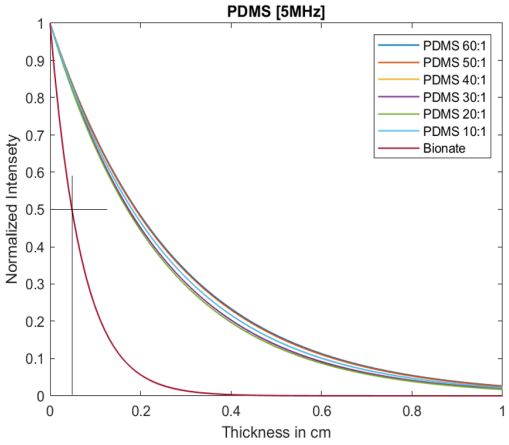

Figure 3.12: The transmission coefficients for different ratios of part A and B of PDMS related to a polyurethane variant (Bionate) (Panskus et. al. "publciation in preparation").

PDMS is hydrophobic, but this hydrophobicity can be increased by soft lithography. Fabricating micro- or nanostructures on a PDMS surface increases the water contact angle above 150° [85]. However, the water barrier of the bonding between PDMS is not large. Trapped air pockets attract water, which leads to the penetration of water droplets in the PDMS bonding.

Enhancing the layer properties can be done by blending. Moreover, bonding additional layers on top can help as well. PDMS strongly bonds to glass, other PDMS and Polyurethane [87]. For these bindings, a corona or air plasma surface treatment does increase the bond strength even more [87].

Polyimide has a different Young modulus than the body, but it has good biocompatibility and flexibility [64]. In addition, it is suited as a substrate since it has a smooth surface. Polyimide can be spincoated as a conformal layer. The optimal layer thickness for flexibility is between 10 and 15 μm [86]. However, the curing temperatures are high (200-400 °C) [42]. Types of polyimide found in the literature are VTEC PI-1388 [42], PI2611 (DuPont) [33] and Pyralin PI 2611 (HD Microsystems) [86]. Polyimide can be thermally cured to maintain a certain shape.[42] uses a thermal curing step at 230 °C and [33] uses a temperature of 350 °C for creating a cylindrical shape for their cuff implant [33] [42].

Polyurethane is a thermoplastic with good mechanical and biocompatible characteristics. Polyurethane can be ordered from different manufacturers. Some often mentioned types of polyurethane in literature are GS PU elastomer from GS Polymers Inc. which has a 1552-2A and a 1552-2B component (1:1) [87] and ClearFlex PU elastomer from Smooth-On (American company) which contains part A and B (1:2) [87] [85]. Polyurethane can be spincoated using a liquid form (Bionate) or it can be laminated as a film (Platilon). As Polyurethane is a thermoplastic, two layers of polyurethane can be attached as one single layer without any edges or gaps.

PMMA is another polymer being used in designs. It is a rigid thermoplastic and exhibits low moisture absorbing capacity and good resistance to extreme temperature changes [77]. Moreover, it is biocompatible and has high chemical resistance. It can be processed using x-ray exposure, hot embossing, laser machining and injection molding [77]. However, this material has a high Young's modulus and is therefore not flexible.

Another flexible substrate is SU-8. This negative thick-film photoresist consists of EPON Resin SU-8 as the main component (Shell Chemicals) [77]. It is biocompatible, has good chemical compatibility and can be conformally coated.

To enhance material properties or combine material properties blending can be performed. It is an inexpensive technique for preparing products with unique properties [85]. Interesting blendings are the PDMS:PU blendings. PDMS:PU blends are interesting due to the combination of material characteristics of PU and PDMS. The hydrophobicity and the acoustic transparency of PDMS together with the thermoplastic and mechanical properties of PU. Using a ratio of 95:5 (PDMS:PU) does give high hydrophobicity (WCA > 100°), good mechanical properties and high acoustic transmittance [85].

3.4.2. Metals

Metals can be used as encapsulation [64] or as interconnect. However, using metals as encapsulation makes the fabrication process more difficult than using polymers. Moreover, sealing metal encapsulations requires special tools for microwelding, since other methods require high temperatures damaging the PZT transducers [64]. Moreover, metals can only be flexible if they are applied in a thin layer (atomic layer deposition for example), but then the sealing can crack easily, reducing the robustness of the encapsulation. Therefore, metals will only be used as interconnect in this thesis. Although moisture penetration should be avoided by encapsulation, every material has a penetration rate for moisture. The metals inside the implant should thus be stable in a wet environment. This means that no corrosion or other chemical reaction should occur. Biocompatible metals used in previous designs are titanium [62], gold [86], zirconium, platinum [86] [33] [42], iridium [33] [42], Nitinol and stainless steel [33].

Nitinol, an alloy of nickel and titanium, is a shape memory alloy meaning that it has the ability to recover its original shape [73]. The metal has two phases the martensite and the austenite phase [73]. Both with their start and finish temperatures. The transformation temperatures of Nitinol are below or close to the body temperature. The shape memory effect means that the alloy is deformed in the martensite phase. The alloy recovers its original shape when heated up to the austenite phase. Another effect that can occur is superelasticity. When the alloy is deformed in the austenite phase under a certain pressure, the alloy recovers its original shape immediately when the pressure is released [73].

As it is biocompatible, this material has many applications in the medical field [73]. Examples are stents [88], orthodontic archwire, guided wire and bone fixation [73]. The stent shapes are particularly interesting since they have the same shapes as cuff implants. Nitinol stents are fabricated from Nitinol tubes having diameters ranging from 1.5 to 10 mm [89]. These Nitinol tubes are laser cut to make a flexible braid or serpentine structure [90].

To avoid sharp edges or pollution of nickel, coatings are applied to Nitinol structures. Examples are polyurethane [88] or diamond-like carbon (DLC) [73]

Another way of providing electrical conduction is using conductive epoxies or conductive films. These conductive epoxies or films can be isotropic or anisotropic, which means that they are uniformly conducting in all directions or only in a specific direction respectively. The conductive epoxies need to be cured at specific temperatures to adhere to surfaces. Conductive films are conductive after pressure activation. Several conductive epoxies are Epo-Tek H20E-PFC, Polytec [33], E-solder 3022 (can also be used as a backing layer) [68], silver paste 5 μm ELCOAT [63] [64] or solder paste [56]. An example of an anisotropic conductive film is ACF (AC-7206U ACF) [25] [91].

As there are multiple options regarding materials, the possibilities within EKL have been researched. Based on regulations regarding processing and availability of materials, the most common materials have been selected to ease the fabrication process flow (Chapter 6).

4

Finite element modelling

In this chapter, the simulations done for the circular PZT-based US transducer array will be explained. For the simulations, COMSOL Multiphysics, a finite element method (FEM) simulator, has been used. Opposite to k-wave it can handle curved and circular arrays and the material selection can be simulated. The disadvantage is that COMSOL is more complex to use. First, the simulations are shown in which the impact of certain parameters is researched. The number of elements, the orientation and position of the PZT-based US transducers and the frequency. For these simulations, a frequency of 12.7 MHz has been chosen. Later on, during the design process (Chapter 5), the final frequencies for the different designs were determined and the simulations for the full design were performed using 8.4, 10.1, and 16.2 MHz.

For simulating a PZT-based US transducer, COMSOL has a special acoustic module. This module combines pressure acoustics with structural mechanics driven by electrical potentials. The Multiphysics coupling part, couples these different physical behaviors into one simulation. The simulation results can be evaluated using different outputs. During this thesis, the acoustic intensity (vector **I**, $[W/m^2]$) and the acoustic pressure (p, $[Pa]$) have been used for evaluation. Moreover, a free triangular mesh with a maximum element size of $v/f_p/8$ has been used. The boundary of the water medium is set to be perfectly matched to avoid reflections at the edges.

The VN to design for has a diameter of 2 mm. This means that the cuff implant should have an inner radius of 1 mm. As a starting point, the focal spot of the PZT-based US transducer is selected to be around 1 mm. To select the frequency there are multiple trade-offs to consider. The stimulation frequency determines the effectiveness of the stimulation of tissue, the aperture size and thickness of the PZT, the resolution of the focal spot and the penetration depth. According to the literature, stimulation frequencies range from 1 MHz to 15 MHz for stimulation. Since the cuff implant is directly attached to the nerve and the nerve diameter is only 2 mm, the penetration depth is not a show-stopper. The effectiveness of certain frequencies on nerve stimulation is still under debate. There are results showing that lower frequencies (around 1-5 MHz) are more effective in the realm of stimulation [51]. Due to this uncertainty, this trade-off is not considered crucial and does not determine the selected stimulation frequency.

The size of the focal spot is important since the nerve fibers are in the order of micrometers. Therefore, low frequencies around 1 MHz are not possible in this case since the focal spot is too large and the PZT-size does not fit into a 1 mm circular design. Other papers like [25], [10] and [91] use stimulation frequencies between the 8 and 15 MHz. Selecting a frequency in that range is sufficient as the focal spot size is small and the PZT fits inside a 1 mm circular cuff implant. Therefore an in-between frequency around 12 MHz was selected for the first part of the simulations. According to Equations 3.32 and 3.29 and some finetuning in COMSOL the best results were obtained for:

- PZT thickness of 167 μm
- PZT aperture of 730 μm

- Frequency of 12.7 MHz

As tissue can best be modeled with water, every simulation is done in a water medium. For all simulations, the driving voltage for the PZT-based US transducers is 10 V and the selected piezomaterial is PZT-5H. The results for a single PZT-based US transducer, with the specifications described above, are shown in Figure 4.1.

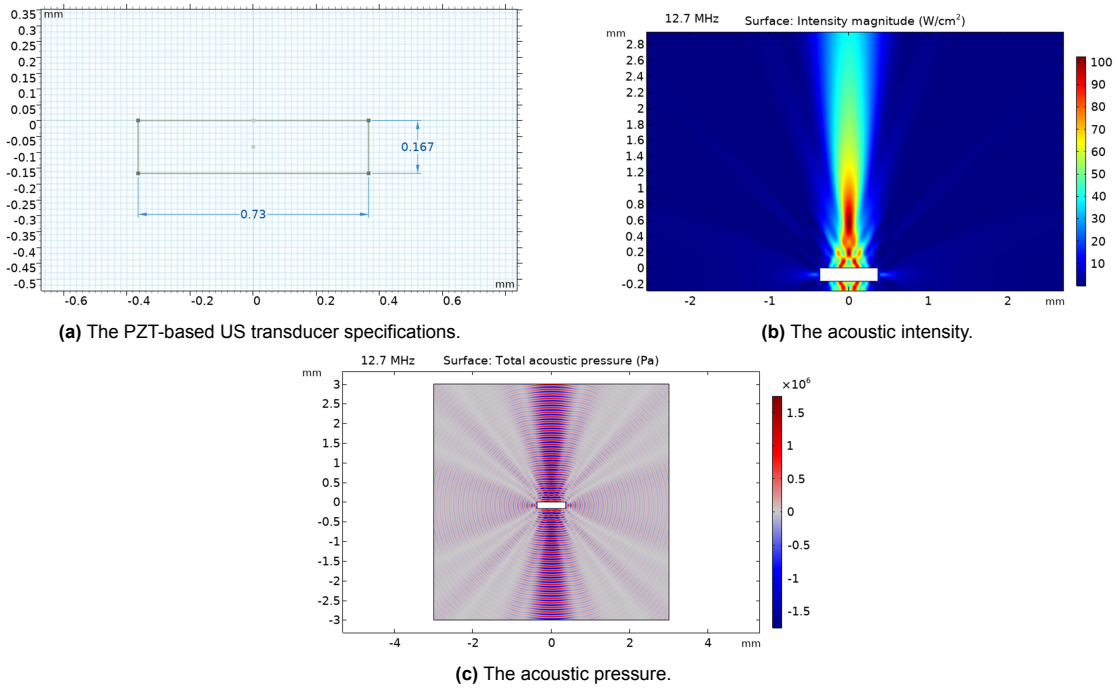

(a) The PZT-based US transducer specifications.

(b) The acoustic intensity.

(c) The acoustic pressure.

Figure 4.1: The characteristics of a PZT-based US transducer driven at 12.7 MHz.

4.1. Two transducer configuration

The second thing to research is the interaction of a PZT-based US transducer with another PZT-based US transducer. For this purpose, several simulations were run. As the PZT-based US transducer will interfere with each other under an angle, as it is a circular cuff, the coordinate frame of each PZT should be correctly set in COMSOL. The piezomaterial PZT-5H from the library is defined in a certain coordinate frame. It represents the crystal structure of the PZT and defines the directionality of for example the d_{33} direction. To generate acoustics in COMSOL a solid mechanics model should be added to the PZT. The coordinate frame of this solid mechanics model should match the coordinate frame of the PZT. In case this does not match, the acoustic response of the material is not perpendicular to the sides of the actual PZT and the beam profile is distorted.

In the 2D-plane of COMSOL, a PZT-based US transducer placed at the origin with the transmitting surface up should have the solid mechanics Material XY-plane system. This means that the crystal structure is oriented in the standard XYZ-system. However, if you rotate the PZTs in the 2D-plane, a rotated system should be created. The rotated system gives rotation with respect to the Material XY-plane system. Figure 4.2 shows at the left the Material XY-plane system. As the PZT is symmetric over the x-axis, the direction of the z-axis is not of importance. According to the definition of the rotated system in COMSOL, the z-axis is pointing inward opposite to the outward pointing z-axis in the Material XY-plane system. In the rotated frame, you define the angle α which is the anti-clockwise rotation with respect to the Material XY-plane system (see the right part of Figure 4.2).
In the case of these simulations it is not only the rotation of the PZT-based US transducer itself but also the rotation of the PZT-based US transducer over the circle of the cuff-implant (Figure 4.3). The front of the PZT-based US transducer should follow a circle with a radius of 1 mm. This means that the middle point of the PZT-based US transducer moves over a circle of radius 1 mm plus half the thickness of the PZT.

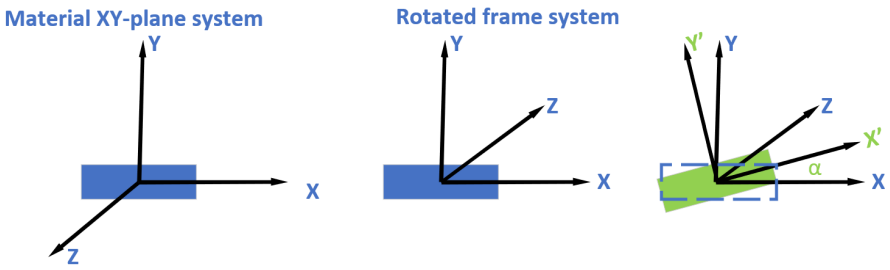

Figure 4.2: The Material XY-plane system and the rotated system.

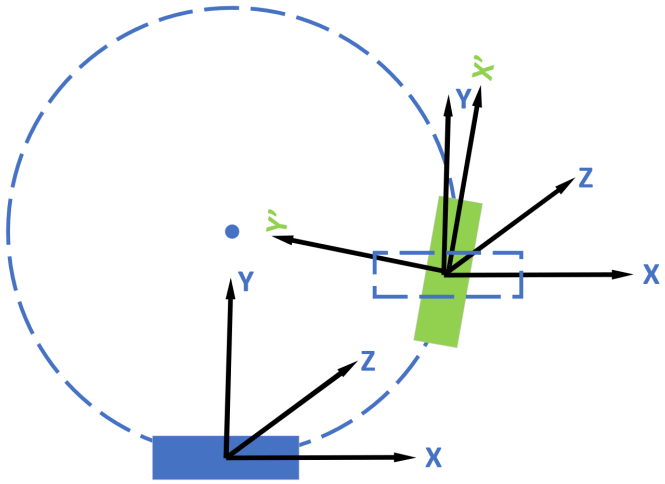

Figure 4.3: Movement of the PZT-based US transducer around a circle.

Building geometries in COMSOL can be facilitated by using parameters. The following parameters have been used in the simulations:

- *thick_PZT*, the thickness (or height) of the PZT
- *aperture*, the width of the PZT
- *freq*, the frequency for the simulation
- *deg*, the absolute angle of one of the PZTs at the right or left with respect to the middle PZT
- *airback*, the thickness of the airbacking layer
- *deg2*, the angle of the PZT itself
- *radius*, the radius of the cuff implant

The rotation of the PZT and the movement of the PZT over the circle can be coupled. In this part of the simulations, the first PZT-based US transducer is placed at an angle of 0 degrees and uses the Material XY-plane system. The second PZT-based US transducer is defined by *deg* and uses the rotated system. The rotated frame matches the rotation of the PZT itself. The position of the PZT at the right half of the circle (the green part in Figure 4.4) is defined as:

$$X_{direction} : radius * cos(deg) + cos(deg) * (\frac{thick\_PZT + airback}{2}) \tag{4.1}$$

$$Y_{direction} : radius * sin(deg) + sin(deg) * (\frac{thick\_PZT + airback}{2}) \tag{4.2}$$

In the case of the left half of the circle (the orange part in Figure 4.4), both parts of Equation 4.1 should be multiplied by a factor -1. The definitions of the parts in Equations 4.1 and 4.2 are shown in Figure 4.4.

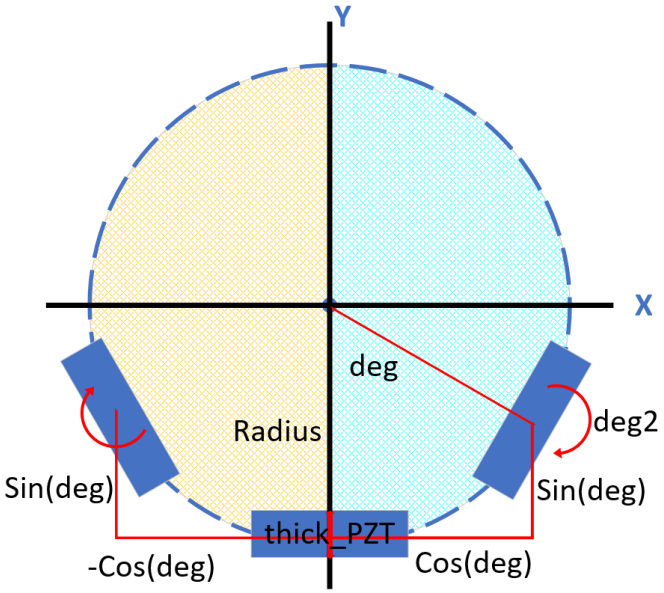

Figure 4.4: The definitions of the parts in Equations 4.1 and 4.2.

As the PZT-based US transducer generates the same acoustic profile at the top and bottom (if there is no backing layer) it is symmetric and can therefore be mirrored. This means that PZT-based US transducers that are placed at the same y-value and the same absolute x-value can be defined by the same parameter for the angle (*deg2*, see Figure 4.4).

The first simulation has been done to find a relation between the intensity or power and the relative angle between two PZT-based US transducers. The dimensions can be seen in Figure 4.5.

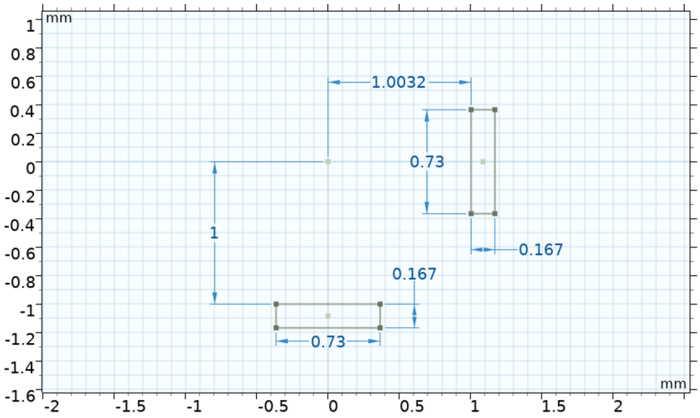

Figure 4.5: The dimensions of the two PZTs used in the two-PZT simulations.

The angle is defined as the anti-clockwise angle between the bottom PZT-based US transducer and the PZT-based US transducer which is swept anti-clockwise. In Figure 4.4 it is defined as deg. The PZT has been swept from $50°$ till $180°$ in steps of $10°$. The sweep starts at $50°$ to avoid weird behavior due to overlapping of the PZT-based US transducers for smaller angles. In reality, it would not be possible to have overlapping PZT-based US transducers and therefore, these data points have been regarded as invalid and are not taken into account in the sweep.

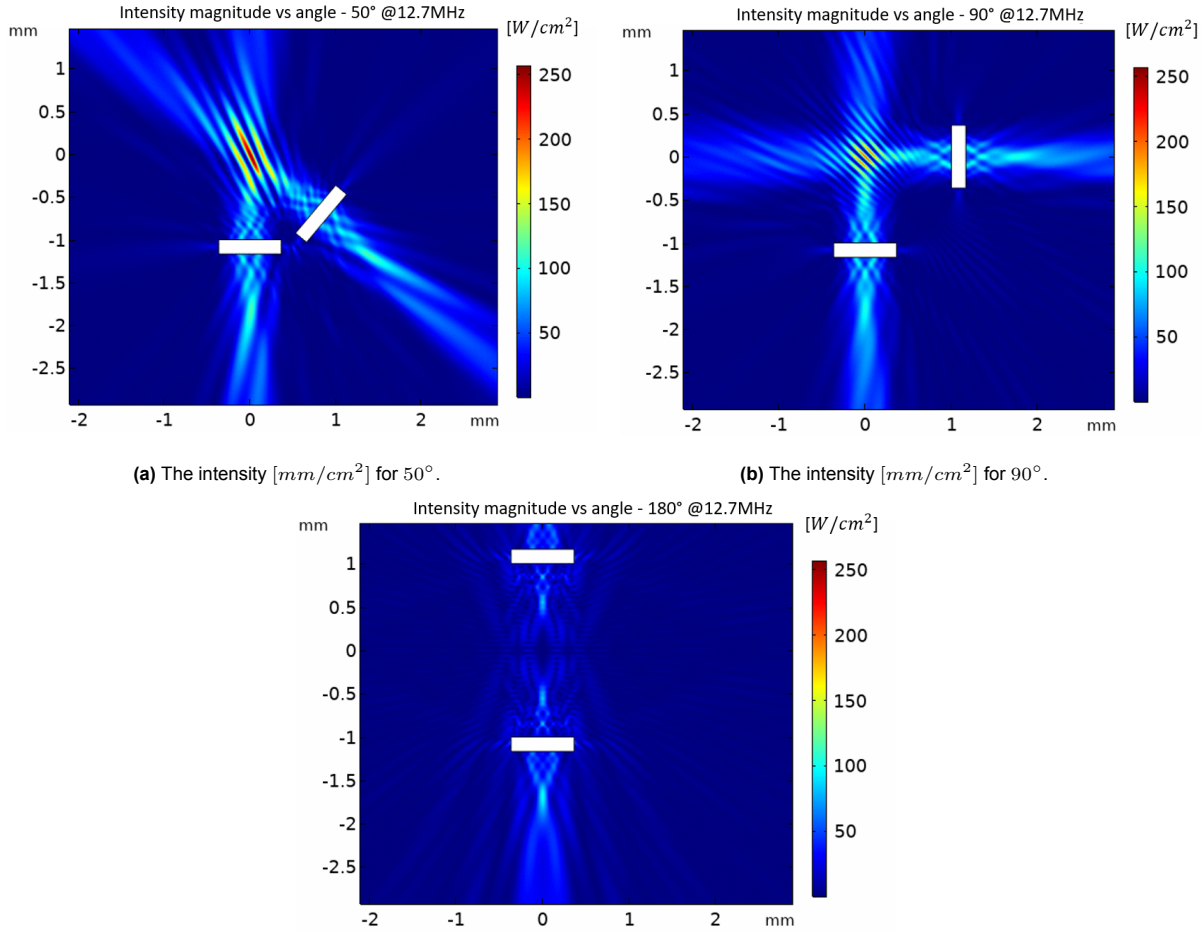

(a) The intensity $[mm/cm^2]$ for $50°$.

(b) The intensity $[mm/cm^2]$ for $90°$.

(c) The intensity $[mm/cm^2]$ for $180°$.

Figure 4.6: Certain intensity profiles at different angles between two PZTs.

From Figure 4.6 it can be observed that the highest intensity is achieved at smaller angles. At an angle of $180°$ the intensity is almost zero. Comparing this to the acoustic power in Figure 4.7 it can be seen that the profile is comparable for the $50°$ and $90°$ angles. However, there is a difference between the intensity and pressure profiles at the angle of $180°$. The acoustic intensity is almost zero between the PZT-based US transducers, while the acoustic pressure has similar magnitudes compared to the other angles. This behavior can be explained by the properties of the intensity and the pressure. As mentioned above, the intensity is a vector quantity and has a direction, while the pressure is a scalar. The acoustic intensity in COMSOL is defined as the time average of the instantaneous rate of energy transfer per unit area [92].

$$\mathbf{I} = \frac{1}{T}\int_0^T p\mathbf{u}\,dt \tag{4.3}$$

p is the pressure and **u** is the particle velocity. In the case of opposing PZT-based US transducers that are in phase, the particle velocity vector has opposing signs. This means that they cancel out and the acoustic intensity is almost zero. However, the acoustic pressure is still there. Therefore, the acoustic pressure adds up, since the quantity is a scalar. This explains the difference between acoustic intensity and acoustic power in COMSOL.

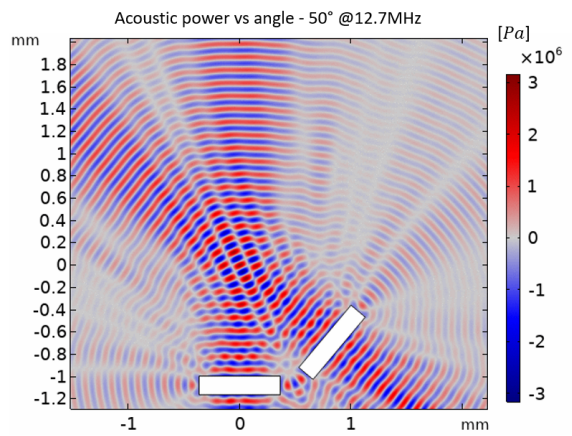

(a) The acoustic pressure $[Pa]$ for $50°$.

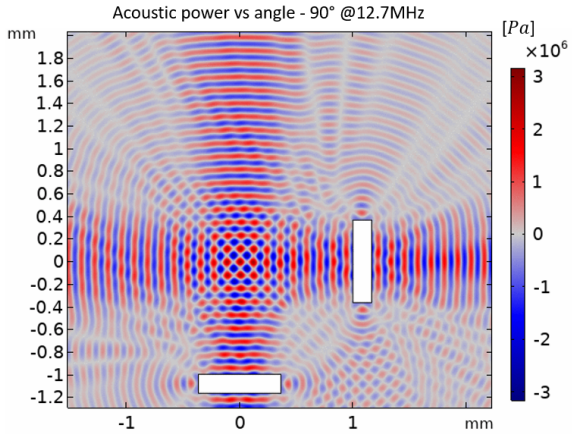

(b) The acoustic pressure $[Pa]$ for $90°$.

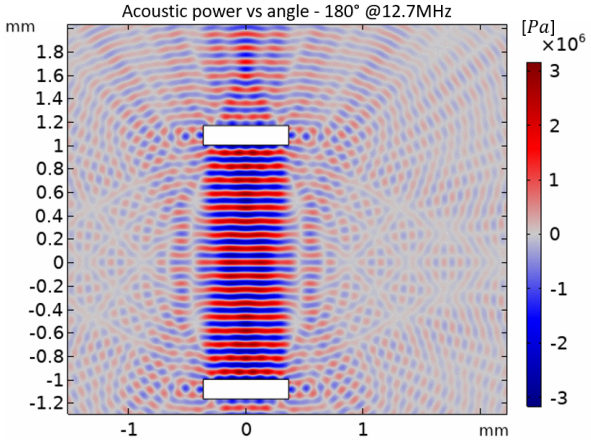

(c) The acoustic pressure $[Pa]$ for $180°$.

Figure 4.7: Certain acoustic pressure profiles at different angles between two PZTs.

To achieve the highest acoustic intensity, the angle between the PZT-based US transducers should be small (Figure 4.9). The values from Figure 4.9 are obtained by obtaining the maximal value of all the points on the red line in Figure 4.8a for each angle point in the sweep.

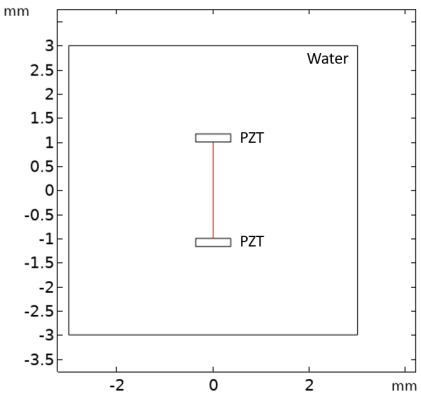

(a) The red line along the maximal acoustic intensity value has been obtained for each angle point.

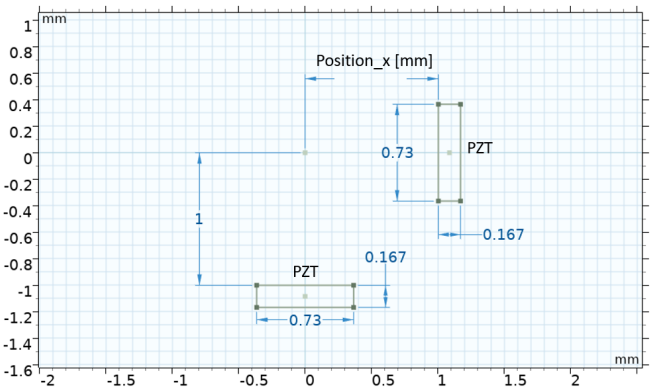

(b) The position parameter which has been swept.

Figure 4.8: Definitions for the measurements in COMSOL.

As it is not well understood whether high intensity or high power is preferred in US stimulation, it was

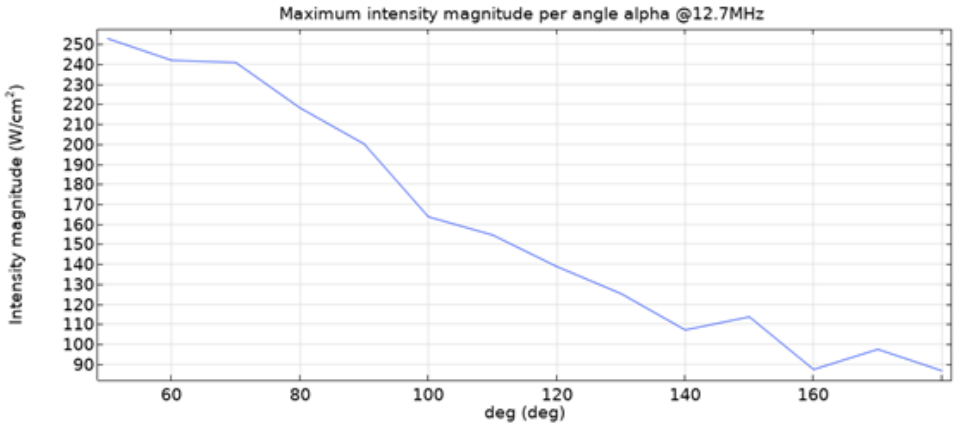

Figure 4.9: The maximal acoustic intensity of the points on the red line in 4.8a for each angle point for two PZTs.

chosen to select a design in which both can be guaranteed. This means that opposing PZT-based US transducers are avoided and the angle between the PZT-based US transducers is made small. Although opposite PZT-based US transducers might be beneficial in different designs and in cases of beamsteering, in this design, it has been concluded based on this simulation that opposing PZT-based US transducers should be avoided. This limits the placement of PZT-based US transducers to only 40% of the cuff circumference. Moreover, the phase of the US waves from each transducer is important as well. The phase of the waves on points in space is defined by the physical position of the PZT-based US transducers and the phases of the electric stimulation bursts for each PZT-based US transducer. It is assumed and therefore simulated that all the PZT-based US transducers have an in-phase electrical stimulation burst.

To get insights into how the physical position of the PZT-based US transducer is influencing the phase of waves and therefore has an effect on whether the waves have constructive or destructive interference on particular points in space, the position of one of the two PZT-based US transducers is swept. This is defined in Figure 4.8b as $position_x$. The PZT at the right, which is $90°$ turned, is moved in the x-direction by sweeping the parameter $position\_x$ around 1 mm from 0.9 mm to 1.1 mm. During this sweep the acoustic intensity magnitude has been measured at the intersection point of the x- and y-direction. The result is shown in Figure 4.10.

As expected, based on the physical placement of the PZT both constructive and destructive interference occur. This means that the physical placement between PZT-based US transducers has an influence. Moving the PZTs with respect to each other does change the focal spot. In this thesis, the exact place of the focal spot should be around the center of the cuff implant. This means that it should be around the 0,0 point in the simulations. As shown in Figure 4.10 the focal spot only moves in small amounts with respect to the center. In addition, compensating for physical deformation in the device itself is also not feasible. Therefore, it has been decided to keep a fixed distance between the PZT-based US transducers and simulate the design based on that distance. The distance between the front of the PZT-based US transducer and the center point 0,0 is 1 mm, such that the cuff implant has a 2 mm diameter.

4.2. Three transducer configuration

The next simulation step is to find the impact of adding an additional PZT-based US transducer. As stated above, the design will not have opposing PZT-based US transducers and the angle between the PZT-based US transducers will be kept small. In addition, the distance between the front of the PZT-based US transducer and the center is 1 mm. These restrictions result in the configuration shown in Figure 4.11. The configuration consists of a center PZT-based US transducer and two PZT-based US transducers at the left and right which have the same angle with respect to the center PZT-based US transducer. This means that the acoustic profiles are symmetric. Comparing the magnitudes of the acoustic intensity and acoustic pressure shows that adding a PZT-based US transducer increases the

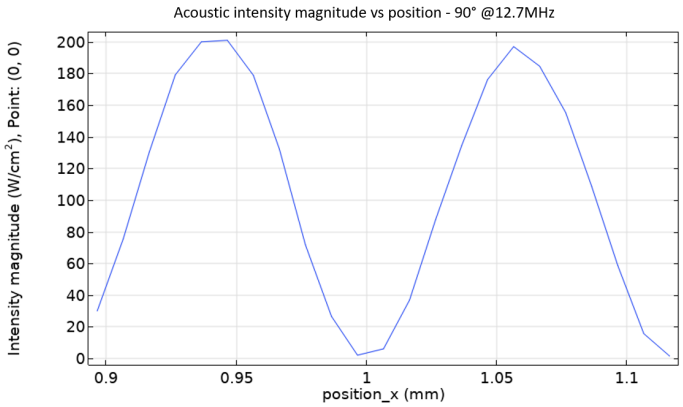

Figure 4.10: The acoustic intensity magnitude at the 0,0 point for the position sweep of the $90°$ turned PZT for a frequency of 12.7 MHz.

acoustic intensity by almost 80% and the acoustic pressure by almost 30%. In addition, the focal spot size is reduced, while the side lobes still appear.

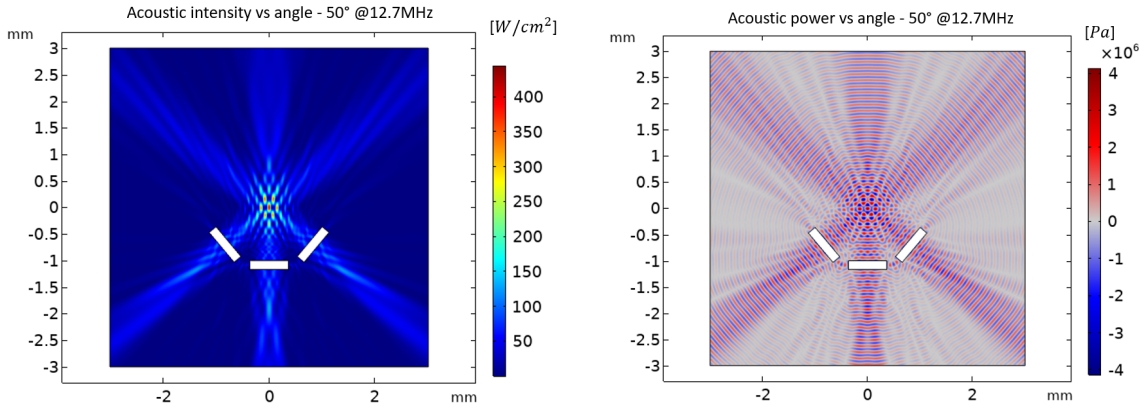

(a) The intensity $[mm/cm^2]$ for $50°$.

(b) The acoustic pressure $[Pa]$ for $50°$.

Figure 4.11: The acoustic intensity and pressure for three PZT-based US transducers at an angle of $50°$.

Sweeping both PZTs with a step of $10°$ from $50°$ to $180°$ at the same time and obtaining the maximum acoustic intensity along the red line as depicted in Figure 4.8a, results in Figure 4.12. Also in this case the highest acoustic intensity is obtained by the smallest angle between the left and right PZT and the center PZT.

4.3. Airbacking verification

In section 3.3.4 it is mentioned that adding a backing layer to the transducer can increase the acoustic intensity and pressure at the transmission side of the transducer. In this case, the acoustic intensity and acoustic pressure should be as high as possible in order to stimulate nerve tissue. Having a backing material with a large acoustic impedance mismatch compared to water increases the acoustic pressure at the transmission side of the transducer. Using air as backing material and including an air-cavity under the PZT increases the acoustic intensity [93]. To investigate the effect of airbacking on the devices being simulated above, new simulations with airbacking were performed. In Figure 4.13 two PZT-based US transducers are compared having the same dimensions and are being driven at 12.7 MHz. From the comparison, it can be concluded that the acoustic intensity is greatly improved (up to 3 times) by adding an air cavity of 20 μm under the PZT.

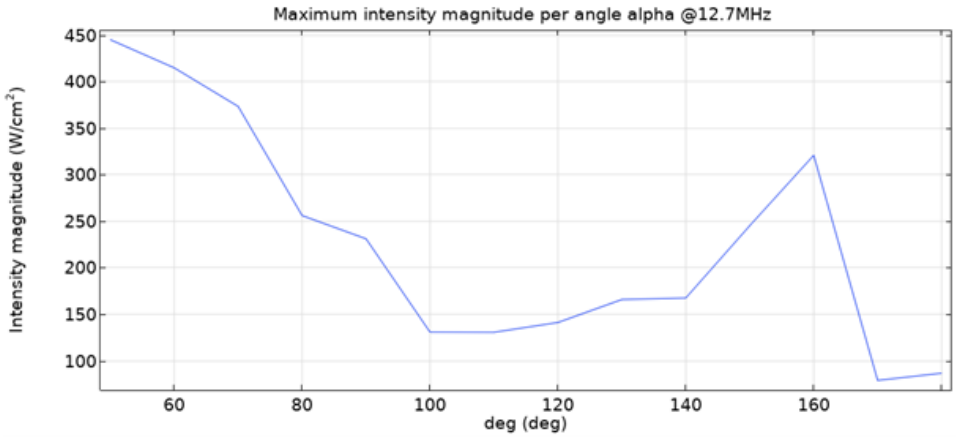

Figure 4.12: The maximal acoustic intensity of the points on the red line in 4.8a for each angle point for three PZTs.

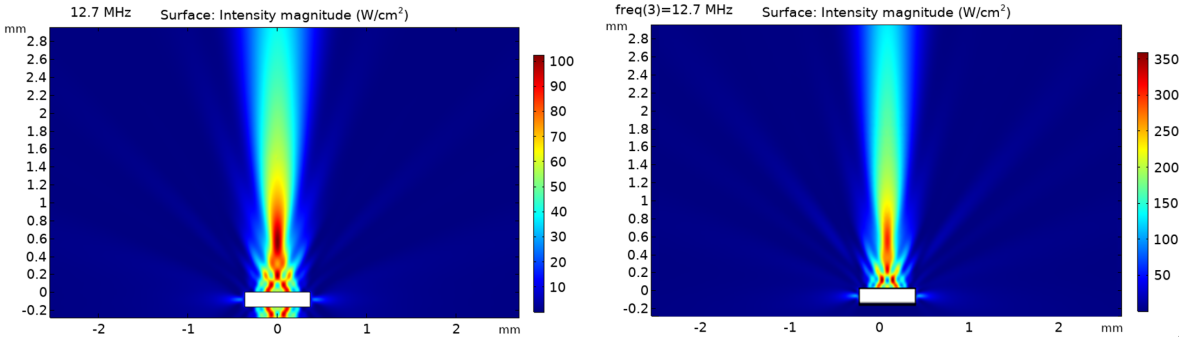

(a) The acoustic intensity of a PZT-based US transducer without airbacking.

(b) The acoustic intensity of a PZT-based US transducer with airbacking.

Figure 4.13: The acoustic intensities of a PZT-based US transducer with and without airbacking.

The airbacking layer has a thickness of 20 μm which is in correspondence with the thickness proposed in the paper of [93]. In addition, this thickness has been verified by simulations of which the result is depicted in Figure 4.14. The plot starts around 303 W/cm^2 which is a simulation artifact due to the thickness approaching zero. From a thickness of around 2.5 μm the intensity increases until it stabilizes around 20 μm. Increasing the depth after this point does not gain any increase in intensity.

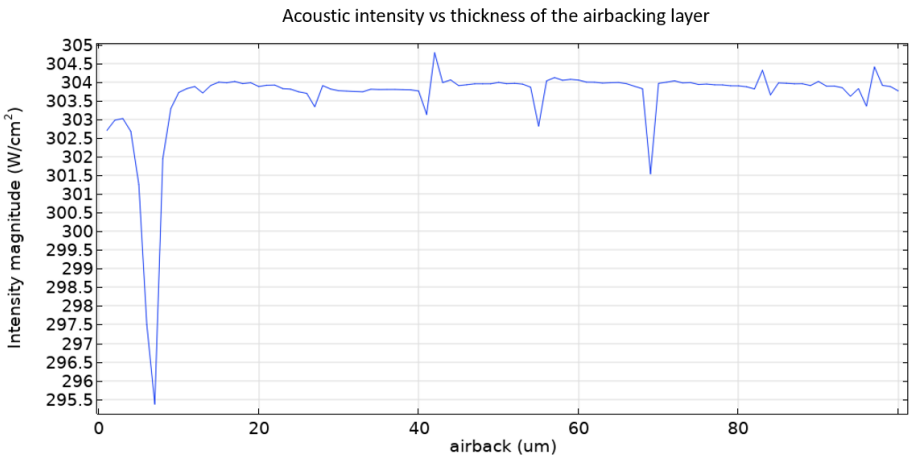

Figure 4.14: The acoustic intensity for different depths of the airbacking layer.

Adding the airbacking layer to all the PZT-based US transducers in the 3-PZT-based US transducer

configuration explained above gives the acoustic pressure and intensity plots as shown in Figure 4.15. The acoustic intensity is increased up to 2.5 times, while the pressure is increased up to 0.5 times compared to the non-airbacking configuration.

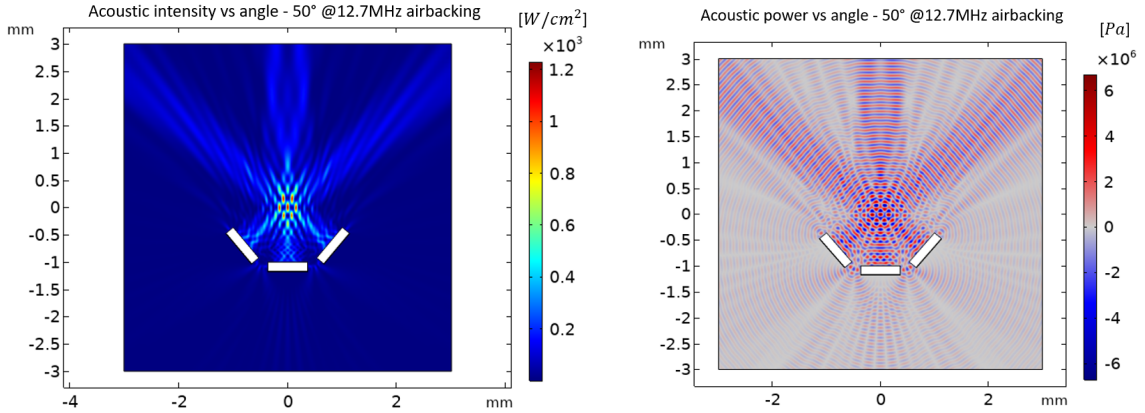

(a) The intensity $[mm/cm^2]$ for 50° with airbacking.

(b) The acoustic pressure $[Pa]$ for 50° with airbacking.

Figure 4.15: The acoustic intensity and pressure for three PZT-based US transducers at an angle of 50° with airbacking.

4.4. Ring material sweep

In the end, the PZT-based US transducers are embedded in a cuff-shaped design. As explained in the section 3.4, polymers are often used in biomedical applications as certain types are biocompatible and have good mechanical properties. To research the impact of different polymers as substrates for a cuff-shaped design on the US profile, a ring has been added in which the PZT-based US transducers together with the airbacking layer are embedded. It is a simplified model as in reality, it will never be a perfect ring and additional components will be embedded in the cuff implant, like silicon or metal traces. However, these simulations can show a relation between the acoustic transparency of the ring material and reflections and what the influence is on the acoustic profile inside the ring. Additionally, as PZTs mechanically vibrate, the substrate material does influence this mechanical movement and might impact the US profile inside the ring as well. The ring structure has been parameterized in COMSOL and is defined by two circles depending on the radius of the cuff design:

$$Ring_{inner} : radius + \frac{thick\_PZT}{2} \tag{4.4}$$

$$Ring_{outer} : radius + 1.5 * thick\_PZT \tag{4.5}$$

The ring thickness is therefore equal to the PZT thickness (167 μm).
For this simulation five different materials for the ring have been selected. Those are the most common, flexible polymers used within the biomedical field. The ones used are PDMS, polyimide, polyurethane, SU8 photoresist and parylene-C. Figure 4.16 shows the acoustic intensity over the y-axis from the top surface of the bottom PZT-based US transducer till a distance of 3 mm from that surface. With a material sweep the ring material is changed and for each material the acoustic intensity is plotted.
From figure 4.16 it can be observed that parylene-C as ring material gives the highest and most focused intensity in the middle of the ring, while polyimide has the lowest intensity at the middle of the ring. The acoustic pressure and intensity profiles for parylene-C as ring material are shown in Figure 4.17. It can be seen that the reflections of the US against the ring are small and that the focal spot is small and nicely centered. The acoustic pressure and intensity profiles of the other four materials can be found in Appendix E.

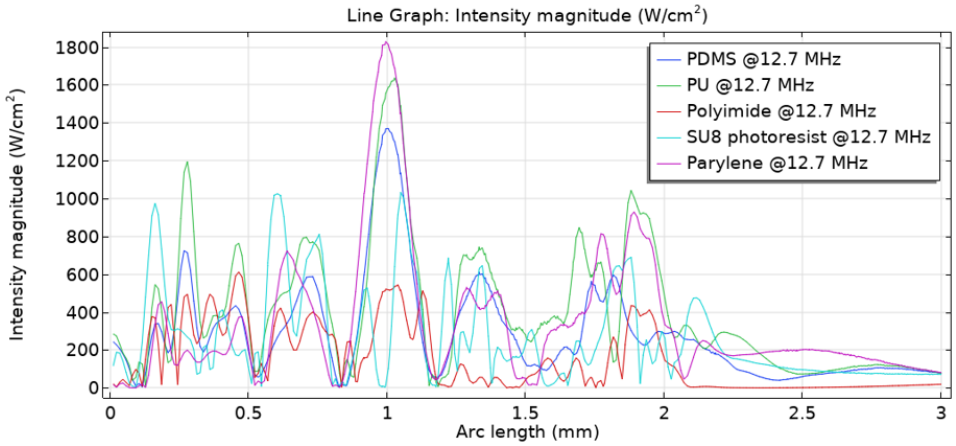

Figure 4.16: The acoustic intensity along the y-axis within the cuff-shaped design for different polymers.

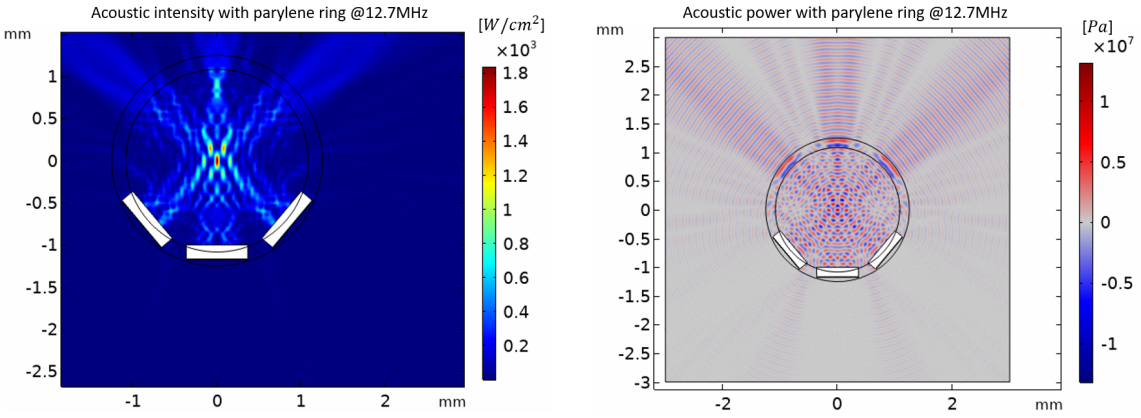

(a) The acoustic intensity $[mm/cm^2]$.

(b) The acoustic pressure $[Pa]$.

Figure 4.17: The acoustic intensity and pressure for a cuff-shaped design with parylene-C as ring material.

5

Design of a cuff implant

In this chapter, the design will be discussed. First, a concept analysis will be conducted including context analysis, benchmarking, and requirements. After, the design process will be discussed and design choices will be explained.

5.1. Context analysis

Neuromodulation as a therapeutic option is promising in addressing neurological disorders [5]. Neuromodulation involves implantable devices which can apply electrical, chemical, or biological agents to the nervous system to alter or adjust its function. Many neurological disorders can be therapeutically addressed like movement disorders, chronic pain, epilepsy, spasticity, urinary incontinence or psychiatric and neurobehavioral disorders [5].

As explained in Chapter 3, US is a promising technique for neuromodulation. With US high spatial resolution can be obtained without the need for intraneural implantation. This is especially an important characteristic in the case of VN stimulation, which is the topic of this thesis. As mentioned in Chapter 3, the VN is an important nerve in the neck that can be as small as 2 mm in diameter. As the VN is a cranial nerve, higher pressures are needed compared to for example brain tissue. Although the literature is not clear about an exact minimal pressure level, having pressures larger than 3 MPa shows stimulation of peripheral nerves [7]. Generating US in the most effective way means using PZT-based US transducer (Chapter 3). In addition, the most common and effective implantable devices for nerve stimulation are cuff implants (Chapter 3). This all together results in the following research question:

> **How can PZT-based US transducers be integrated with a cuff-shaped design for Vagus Nerve stimulation and what pressure profile and levels can be obtained with this configuration?**

For a better view of the context, four questions need to be answered regarding the design:

- **Who?** The device which will be designed is meant for research purposes only. No implantation in animals or humans is involved. This means that the end user is the student performing the measurements.
- **Where?** The device will be deployed at the technical university in Delft at the faculty of electronics, mathematics and computer science (EEMCS).
- **What?** The device is a PZT-based US transducer cuff-shaped implant having a minimum inner diameter of 2 mm.
- **Why?** This device is useful to investigate the possibility of integration of PZT-based US transducers in a cuff-shaped implant and to research the US pressure and profile.

5.2. Benchmarking

Comparing this design and research with the literature, criteria are set for benchmarking. The criteria used for this thesis are listed below:

- **Fabrication process:** the way the implant is fabricated and how PZT is integrated with this process flow. Microfabrication is needed to make a small form factor for implantation and the process should be scalable.

- **Performance:** the output pressures which can be obtained expressed in MPa. Moreover, the focal spot size is determined in μm and distortions of the acoustic pressure profile are assessed.

5.3. Requirements

In Table 5.1 the requirements are listed for this thesis project. They are prioritized based on the MoSCoW method [1]. Each requirement has its own ID which will be used throughout the subsequent chapters. Besides, each requirement has a justification in which the background of that requirement is explained.

[1] It is a prioritization method often used in engineering and management. It consists of the four categories: must have, should have, could have and won't have

Table 5.1: The requirements and justifications.

ID	Requirement	Justification
Must haves	This list contains aspects that must be implemented in the final product	
M-1	The implant must contain bulk PZT	Bulk PZT is the most promising material for generating high pressure US
M-2	The implant must have a cuff-shape	Effective implants for nerve stimulation often have a cuff-shape form factor
M-3	The implant must be fabricated with microfabrication techniques	Microfabrication is the most common and reliable process for small device (sub-mm structures). It is available at the Else Kooi Lab at the EWI faculty.
M-4	The implant must be able to operate in DI water	During testing DI water is used to mimic the tissue environment so the device will be hung in DI water
M-5	The implant must contain a focal spot in between the inner radius of the cuff-shape	A focal spot is needed to increase the spatial resolution which is important for small nerves like the VN
M-6	The implant must be driven at 10 Vpp	This is the maximal voltage of the function generator used during testing in the bionsoniclab
M-7	The implant must be connected to a multi-contact Staubli clip	The function generator has two multi-contact Staubli clips as output connectors
M-8	The implant must fit in a water tank (1 mx0.5 mx0.5 m)	This is the water tank being used to conduct measurements
M-9	The inner radius of the cuff implant should be 1 mm.	This is the smallest size of the C-fibers at the stimulation side [12] [10]
Should haves	This list contains aspects that should be integrated into the product to improve its functionality	
S-1	The PZT-based US transducer(s) should have airbacking	Airbacking improves the output pressure of PZT-based US transducers and is a perfect backing material for stimulation purposes
S-2	The materials of the implant interfacing with tissue should be biocompatible	Biocompatibility of the outer materials is mandatory for implants
S-3	The threshold intensity of the implant should be smaller than 190 W/cm^2	This is the threshold intensity for US imaging from the FDA
Could haves	This list contains aspects that could be implemented to make the product more advanced	
C-1	The PZT-based US transducer(s) could have (a) matching layer(s)	Matching layers improve the transfer of acoustic pressure from the transducer to the tissue
C-2	The cuff implant could have a shape memory alloy	Shape memory alloys can be used for generating and maintaining a cuff-shape
Won't haves	This list contains aspects which will not be implemented in the product during this thesis	
W-1	The implant will not contain driving circuitry	The implant will only contain transducers as the driving part is done by means of a function generator
W-2	The implant will not be fully compliant to the regulations for implants like FDA	The device will be fabricated for testing purposes and therefore it is not needed to be compliant to all the regulations for implants

5.4. Configuration optimization

In literature, no examples were found in which bulk PZT was used as a transducer in a cuff-shaped design. Therefore, simulations were needed to identify which configurations of PZT-based US transducers in a cuff shape are possible and most optimal. In Chapter 4 the simulations are discussed. The best results regarding pressure and intensity levels were obtained by placing PZT-based US transducers at one side of the circle with the smallest possible angle in between. Moreover, having parylene-C as encapsulation does generate the best focal spot in the middle of the cuff implant.

The simulations were performed at a frequency of 12.7 MHz. However, by adjusting the positions and dimensions of the PZTs, similar results could be obtained for different frequencies. The optimization of the configuration will be explained in the next section.

For a straight 1D array of PZTs, different parameters need to be tuned in order to focus in one spot without the interference of side lobes. For a curved 1D array it is not well-known which parameters to tune to generate a focal spot without the interference of side lobes. Therefore, some assumptions are made. In figure 5.1 a straight 1D array is shown, which will be curved around the center placed at the left of the image. Each element is treated as a single PZT-based US transducer and therefore, the aperture (L) is defined by each individual element instead of the total of all elements like in a normal linear 1D array. Therefore, the aperture (L) is equal to the element width (W). The inter-element pitch is the element width together with the kerf. Normally, in a linear 1D array the kerf is defined by the blade thickness of the dicing blade. As in the curved configuration, each element is individual the kerf can be chosen.

As the aperture is defined by the focal length, the PZT width can be calculated from the focal length. The inter-element pitch is important to avoid interference from side lobes and therefore distortion of the acoustic profile. Normally, the inter-element pitch is $\lambda_{water}/2$ or a multiple of this number. In a curved configuration this inter-element pitch changes. As it is unknown which distance in a curved configuration mimics the inter-element pitch of a linear 1D array, the chord length between the center of two PZTs has been chosen as the inter-element pitch. This chord length has been taken as a multiple of $\lambda_{water}/2$. Based on the FEM simulations for this particular design, the distance between the PZT-based US transducers should be small to gain the highest intensity and pressure. Therefore, the chord length should be the smallest possible multiple of $\lambda_{water}/2$.

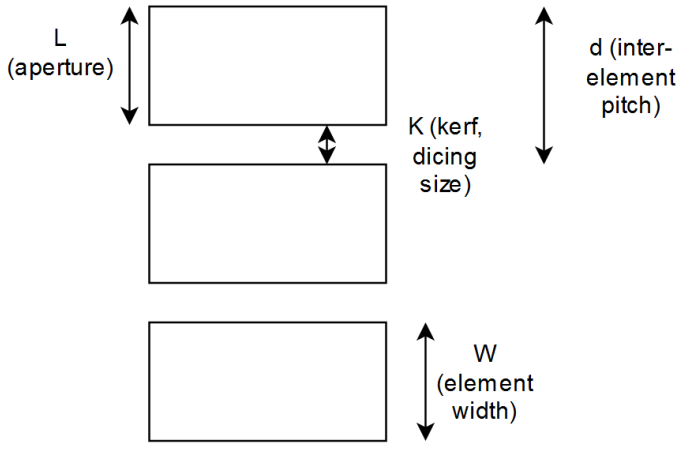

Figure 5.1: The definitions of parameters in a curved 1D array

The cuff shape is simulated as a circle with an inner and outer radius. In Figure 5.2 the radii are shown. In addition, after curvature, the distance between the top of two PZTs is smaller than the distance between the bottom of two PZTs. Therefore, two kerfs should be defined. The distance between the top of two PZTs is called the *kerf_inner*, whereas the distance between the bottom of two PZTs is called

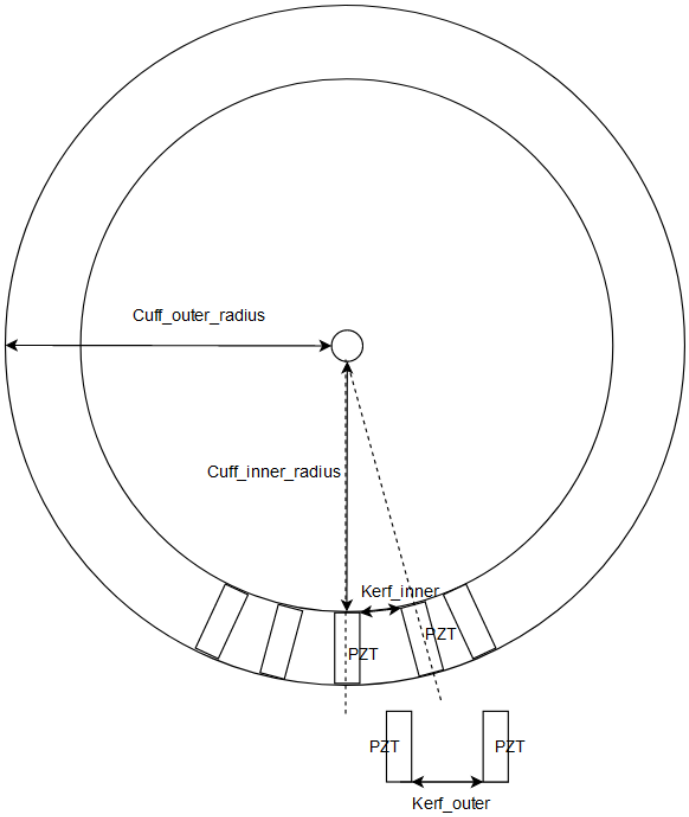

Figure 5.2: The radii and the kerfs of a curved PZT-based US transducer array

the *kerf_outer*. The *kerf_outer* determines the length of the design when processed straight.
Another constraint to take into account is the minimal distance between the top of the PZTs. They should not hit each other since that influences the US profile drastically. On the other hand, the chord length should be a multiple of $\lambda_{water}/2$. Moreover, each design needs to be verified by means of a COMSOL simulation. To ease these simulations it is best to parameterize. As the cuff shape is simulated as a circle, the best parameter to use is the angle. In Chapter 4 it has been explained that the position of the PZTs is based on the angle that is inputted by the user. It is therefore useful to generate the angle in between the PZTs based on the possible inner and outer kerfs.

Finally, from the simulations it appeared that opposing PZT-based US transducers are not efficient and do distort the acoustic profile. Avoiding opposing PZT-based US transducers in this particular design means that no more than 180° of the cuff shape should be covered by PZT-based US transducers. As the angle is determining the center of the element, even a smaller angle of the cuff shape should be covered. Therefore an angle of 160° for coverage was chosen to avoid opposing elements.

To take all these constraints into account and to ease the calculations a Matlab script was written. In the background of the Matlab script, some geometry is used, which needs to be explained to help understand the script itself. The geometry is shown in Figure 5.3. The hatched rectangles represent two PZTs.

The inner radius of the cuff shape design is defined as r and gives the distance between the top of the PZT to the center. This radius is equal to the smallest radius of the VN which is 1 mm. According to the literature it is advised to make the cuff diameter 50% larger to avoid tissue trauma [30] [31]. However, this design is not meant for stimulation in animals and humans. Besides, scaling it to a slightly larger size is relatively easy and therefore it is worth taking the smallest form factor into account while designing. If it can be fabricated in this small size, it can also be fabricated in a slightly larger form

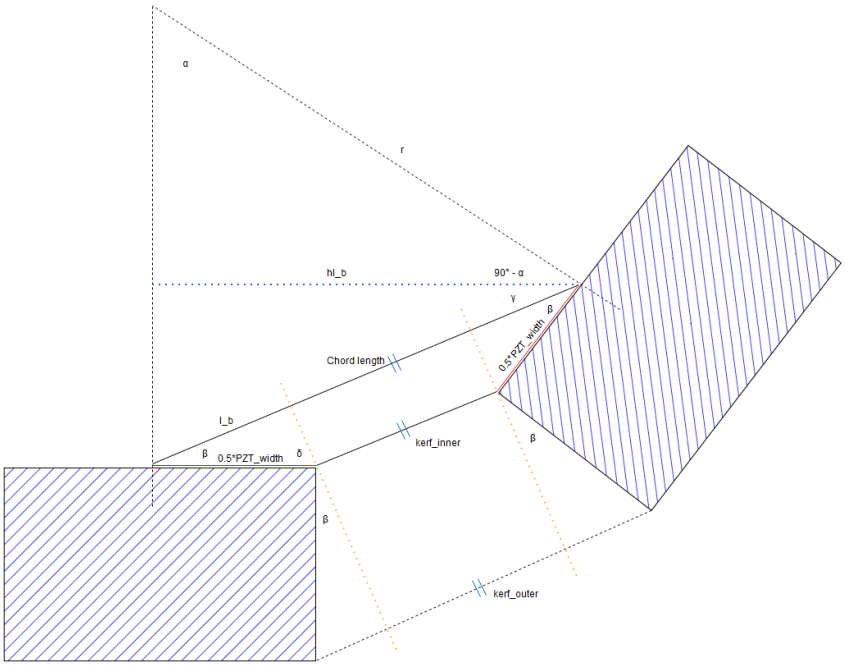

Figure 5.3: The geometry behind the configuration optimization Matlab script.

factor. Additionally, other research [10] used a radius of 1 mm and to compare this research with their work it should be the same radius. Therefore a radius of 1 mm is chosen and the *safety_factor* in the Matlab code is set at 1.

By drawing the blue helpline (Figure 5.3), a right-angled triangle appears with the angle α (in degrees). In that case, the length of the blue helpline can be calculated using:

$$hl_b = r * sin(\alpha) \tag{5.1}$$

A straight line between the two center points of the two PZTs is a chord. This chord length can be calculated:

$$chord\_length = 2 * r * sin(\alpha/2) \tag{5.2}$$

From the result above the angle γ can then be obtained:

$$\gamma = cos^{-1}(\frac{r * sin(\alpha)}{2 * r * sin(\alpha/2)}) = cos^{-1}(\frac{sin(\alpha)}{2 * sin(\alpha/2)}) \tag{5.3}$$

After, drawing the orange helplines, defining $\beta = \alpha - \gamma$ and calculating the side indicated by the black line (l_b) gives:

$$l_b = 0.5 * PZT_{width} * cos(\beta) \tag{5.4}$$

In that way, *kerf_inner* is defined as:

$$kerf_{inner} = 2 * r1 * sin(\alpha/2) - PZT_{width} * cos(\alpha - cos^{-1}(\frac{sin(\alpha)}{2 * sin(\alpha/2)})) \tag{5.5}$$

The outer kerf dimensions can be obtained by using the fact that the inner and outer kerf are parallel to each other. In addition, the angle between the orange helpline and the height side of the PZT has also an angle β. In that way, the outer kerf can simply be defined as:

$$kerf_{outer} = kerf_{inner} + 2 * element\_thickness * sin(\beta) \tag{5.6}$$

Rewriting this equation as a function of the angle α gives:

$$kerf_{outer} = kerf_{inner} + 2 * element\_thickness * sin(\alpha - cos^{-1}(\frac{sin(\alpha)}{2 * sin(\alpha/2)})) \tag{5.7}$$

The Matlab script consists of three parts. First, the constants and element characteristics are calculated based on the input values. Secondly, the angle for non-overlapping elements and having the chord length as a multiple (the boundary is set as +/- 0.15) of $\lambda_{water}/2$ is calculated in a for loop. Based on that angle the inner and outer kerf are calculated based on the geometry explained above. In the third part, it is calculated how many elements can be placed on 160° of the circle. This is done using the arc lengths. The most important values are outputted in the Matlab command window.

Four different designs are made. The design parameters are shown in Table 5.2. Initially, ideal frequency values of 8, 10 and 16 MHz were used. After fine-tuning the focal length and the maximum acoustic intensity in the simulations, frequencies of 8.4, 10.1 and 16.2 MHz were obtained. The dimensions of the PZTs are obtained from the aforementioned script. These dimensions have been changed afterward to reach a large active area fitting the design. The design for 16.2 MHz is made twice. Once with the most possible number of elements, the other time with only two elements mimicking the active area from the Kawasaki et al. research [10].

Table 5.2: The design parameters for the four different designs.

Frequency $[MHz]$	16.2	16.2	10.1	8.4
Diameter $[mm]$	2	2	2	2
# of PZTs	4	2	3	3
PZT thickness $[\mu m]$	127	127	203	254
PZT size $[\mu m]$	450x620	450x620	450x785	450x1100
Angle $[°]$	36.5	36.5	45	52
Inner kerf $[\mu m]$	37	37	40	27
Outer kerf $[\mu m]$	111	111	181	278
Focal length $[mm]$	1	1	1	1
Active area $[mm^2]$	1.12	0.558	1.06	1.51

There are multiple ways of obtaining a cuff-shaped implant (Req. M-2). As mentioned in Chapter 3 the two main methods are: using a flexible polymer as a substrate or using an island-bridge approach. As PZT-based US transducers are not flexible by nature, even though the substrate would be flexible, there will be not a perfect curvature. In addition, working with a polymer substrate gives limitations to the microfabrication process. There are strict rules regarding the handling of polymers in EKL which will reduce the design options (for example implementing airbacking) and it will make the fabrication process flow more complex. Therefore, the method of island-bridge has been chosen.

The four designs have been verified using COMSOL Multiphysics simulations. The peak pressure and the peak intensity for each simulated design are shown in Table 5.3. For the ring material, parylene-C has been chosen. From Table 5.3 it can be seen that the higher the frequency the higher the peak intensities. As the focal spot for higher frequencies is smaller (Table 5.3, where w is the width and l the length), the intensity which is calculated per unit area, is higher. Moreover, the active area is proportional to both the peak pressure and the peak intensity.

Due to the direct availability of 8 MHz and 16 MHz PZT-5H piezoelectric sheets, the designs of the 8.4 MHz and the 16.2 MHz have been used for further characterization after the wafer-level microfabrication. As the transducer size is larger for the 8.4 MHz, this device is more robust and can be handled more easily compared to the 16.2 MHz devices. This is beneficial during some steps of the wafer-level microfabrication process (Chapter 6). Therefore, the 8.4 MHz design has been fabricated and characterized first. Afterward, some tests have been done with the 16.2 MHz devices. Moreover, in this way, the impact of frequency can be nicely obtained.
In Figures 5.4 till 5.7 the simulated acoustic pressure and intensity profiles are shown. In addition, the sizes of the design for simulation are indicated. They correspond to the values that are shown in Table 5.2.

Table 5.3: The simulation values for the four different designs.

Frequency $[MHz]$	16.2	16.2	10.1	8.4
# of elements	4	2	3	3
Peak pressure $[MPa]$	15	6	8	6
Peak Intensity $[Watt/cm^2]$	8000	1600	1200	700
Focal spot size w**x**$l[\mu m]$	40x120 μm	40x600 μm	60x150 μm	80x170 μm

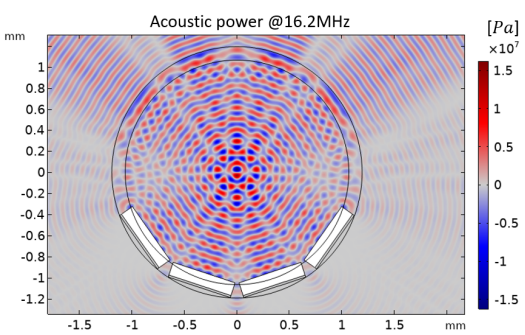

(a) The acoustic pressure $[Pa]$.

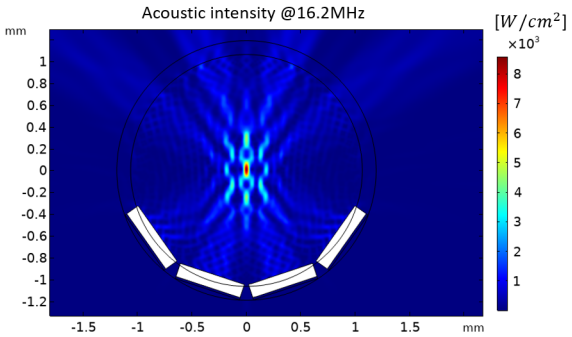

(b) The acoustic intensity $[W/cm^2]$.

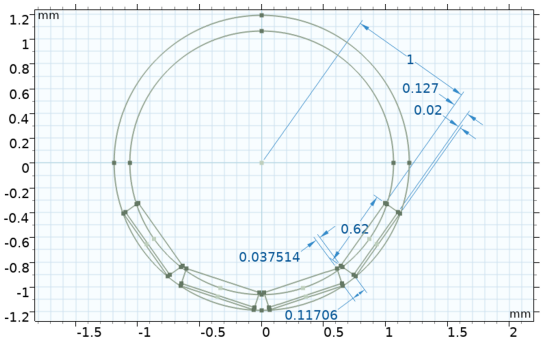

(c) The sizes [mm] of the design.

Figure 5.4: The 16.2 MHz design with 4 elements with sizes and the simulated acoustic pressure and intensity profiles.

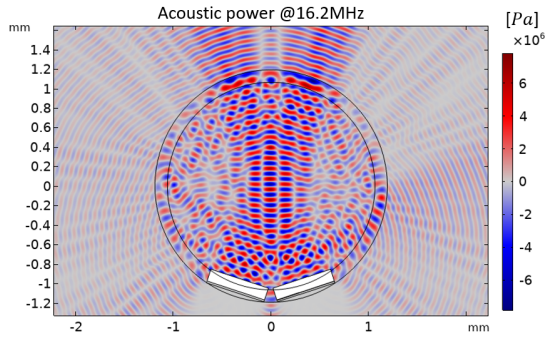

(a) The acoustic pressure $[Pa]$.

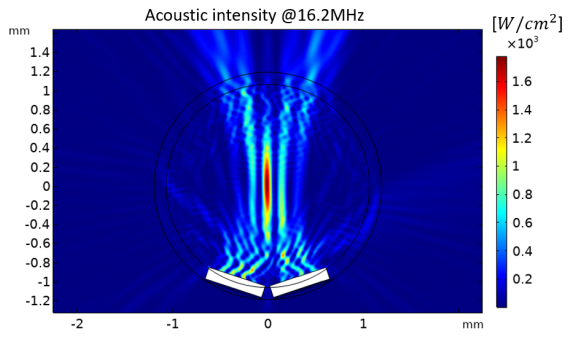

(b) The acoustic intensity $[W/cm^2]$.

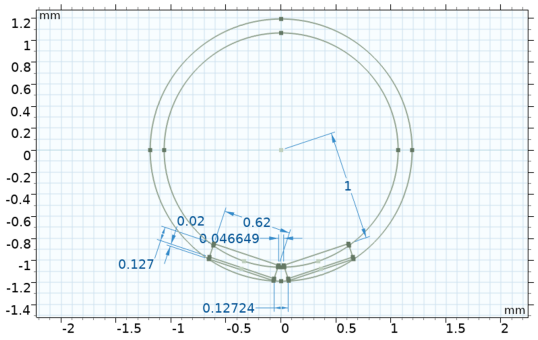

(c) The sizes [mm] of the design.

Figure 5.5: The 16 MHz design with 2 elements with sizes and the simulated acoustic pressure and intensity profiles.

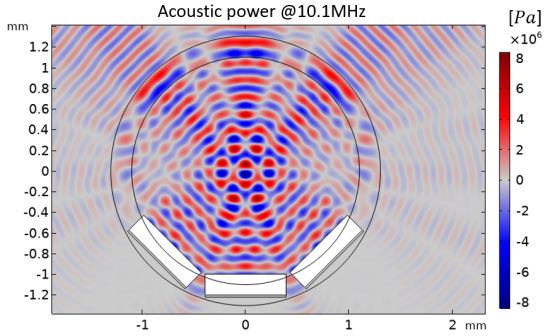

(a) The acoustic pressure $[Pa]$.

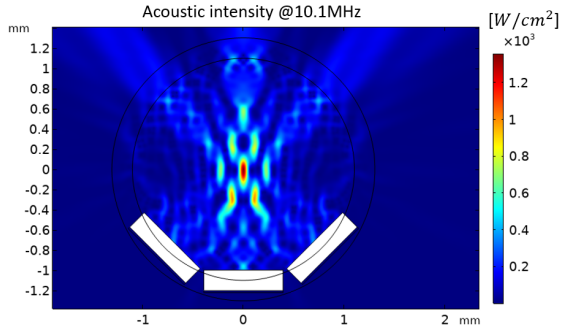

(b) The acoustic intensity $[W/cm^2]$.

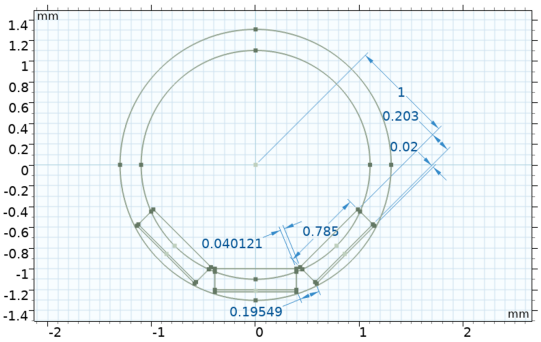

(c) The sizes [mm] of the design.

Figure 5.6: The 10 MHz design with sizes and the simulated acoustic pressure and intensity profiles.

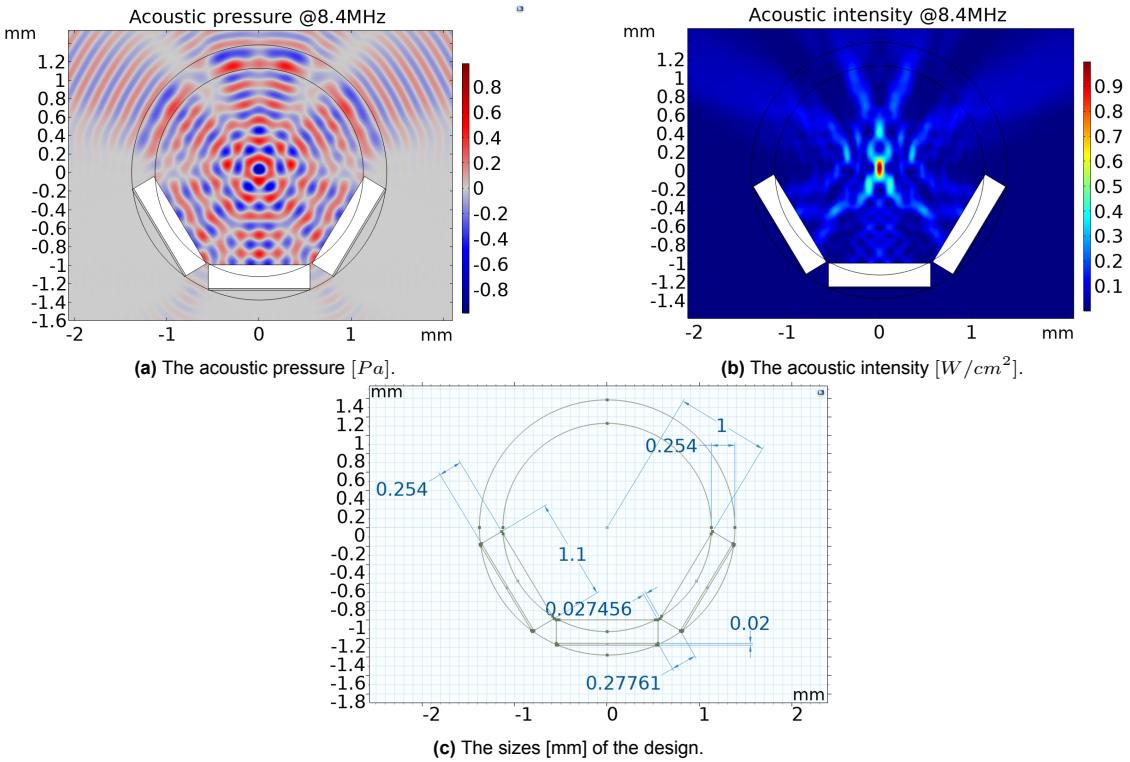

(a) The acoustic pressure $[Pa]$.

(b) The acoustic intensity $[W/cm^2]$.

(c) The sizes [mm] of the design.

Figure 5.7: The 8.4 MHz design with sizes and the simulated acoustic pressure and intensity profiles.

6

Wafer-level microfabrication process flow

In this chapter, the wafer-level microfabrication process flow will be discussed (Figure 6.1). As discussed before, it is an island-bridge design with airbacking implemented below the PZTs. Figure 6.2A shows the topview of a single device. The dark-green areas are the silicon substrate with a SiO_2 layer, whereas the light-green areas are the Deep Reactive Ion Etched (DRIE) wells in the silicon substrate. The black lines are the thin, DRIE SiO_2 membranes. The blue areas are the metal layer. Depending on the four designs (described in Chapter 5), each device has a different number of transducers. For the explanation of the wafer-level microfabrication flow, a design with three PZT-based US transducers has been chosen. The sideview of the design can be seen in Figure 6.2B. In this chapter, the mask design will be explained first and after, each wafer-level microfabrication step will be discussed. Decisions will be explained and alternatives are mentioned.

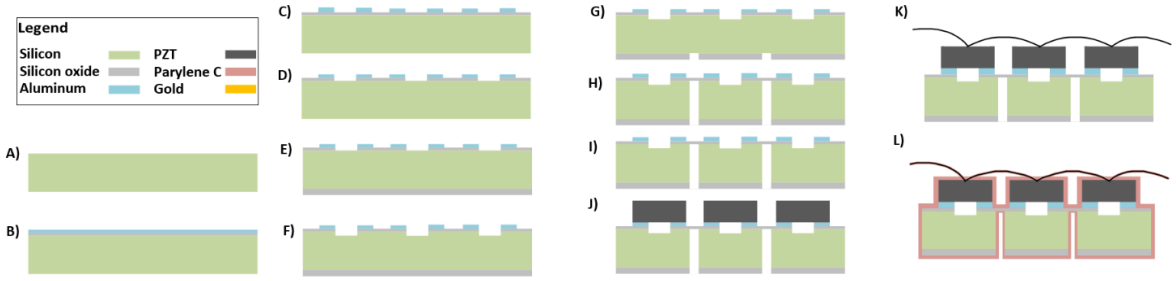

Figure 6.1: The wafer-level microfabrication process steps A) the process starts with a wafer on which alignment markers are etched B) a layer of SiO_2 and on top a layer of $AlSi$ is deposited C) the $AlSi$ layer is patterned D) the SiO_2 is etched E) a SiO_2 layer is deposited at the backside F) the airbacking wells are etched in the silicon on the top side G) the SiO_2 at the backside is patterned H) the silicon substrate is etched from the backside I) the wafer is diced J) PZTs are placed on top K) tungsten wire is attached on top of the PZTs L) the device is encapsulated with parylene-C.

6.1. Photolithography masks

The process flow requires three photomasks for photolithography (Figure 6.2C). The first mask, needed during step C, is a brightfield mask to pattern the metal layer. Therefore it is called the *Metal mask*. The second mask used during step D, is a darkfield mask to pattern the SiO_2 layer for the airbacking wells. It is called *Airback mask* The final mask, used during step G, is a darkfield backside mask for opening the SiO_2 layer at the backside. It is called *Backside mask*.

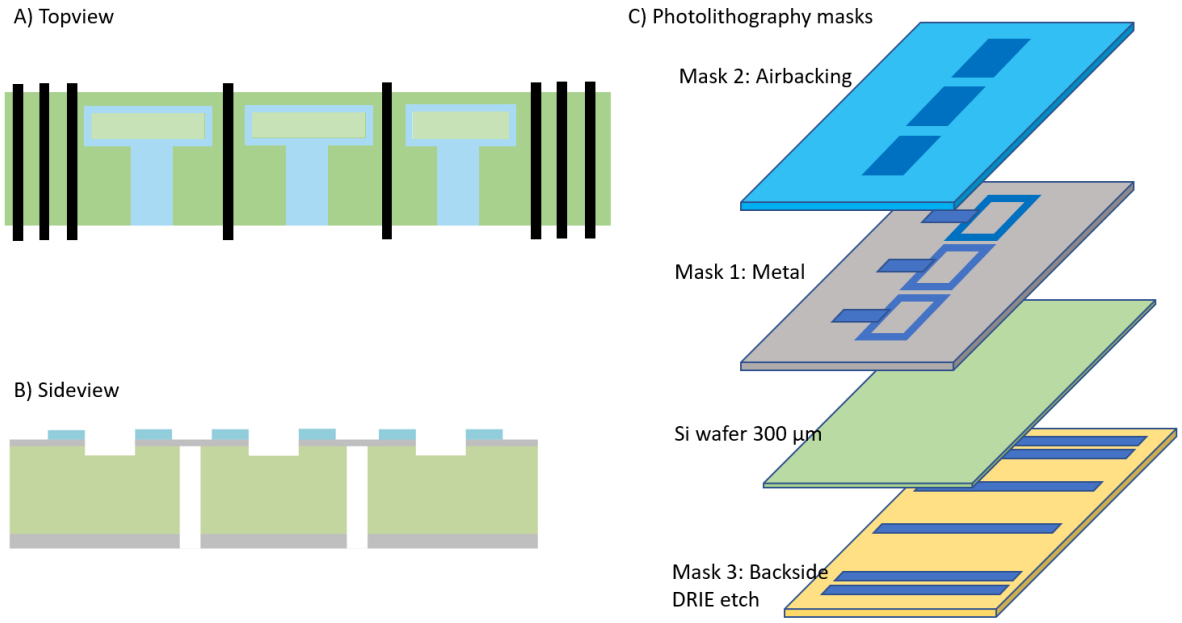

Figure 6.2: A) the topview and B) the sideview of the design. C) shows the three different photolithography masks.

The mask layout is divided into different regions (Figure 6.3a). The lower region has devices with small contact pads of 200 μm x 500 μm in case wire attachment is possible and to make the form factor as small as possible. The upper region has large contact pads of 500 μm x 500 μm so manual wire attachment is possible as well. The mask has 10 different rows with three rows of 16.2 MHz devices (both 4 and 2 transducer designs), four rows of 10.1 MHz devices and three rows of 8.4 MHz devices. For every frequency, there is one row with designs without airbacking. This is done to be able to research the impact of the airbacking well. The other rows have different metal edge widths around the airbacking well. The Anisotropic Conductive Film (ACF)[1], which has been used for PZT attachment, has a thickness of 25 μm. Therefore, the widths vary from 50 μm to 100 μm being such that there is a larger chance for good electrical conduction. In the top part, the distance between the DRIE lines (100 μm, 160 μm and 200 μm) has been varied. This is done, so the effect of this distance on the flexibility of the design can be researched. At both the top and bottom test structures are placed (Figure 6.3b) The test structures are meant for testing the conduction of the ACF, for testing the functioning of the airbacking wells beneath the PZT and for measuring the sheet resistance by means of the Van der Pauw structures.

[1] ARclad 9032-70 https://www.adhesivesresearch.com/wp-content/uploads/2021/03/ARclad%C2%AE-9032-70-Product-Information-Sheet.pdf

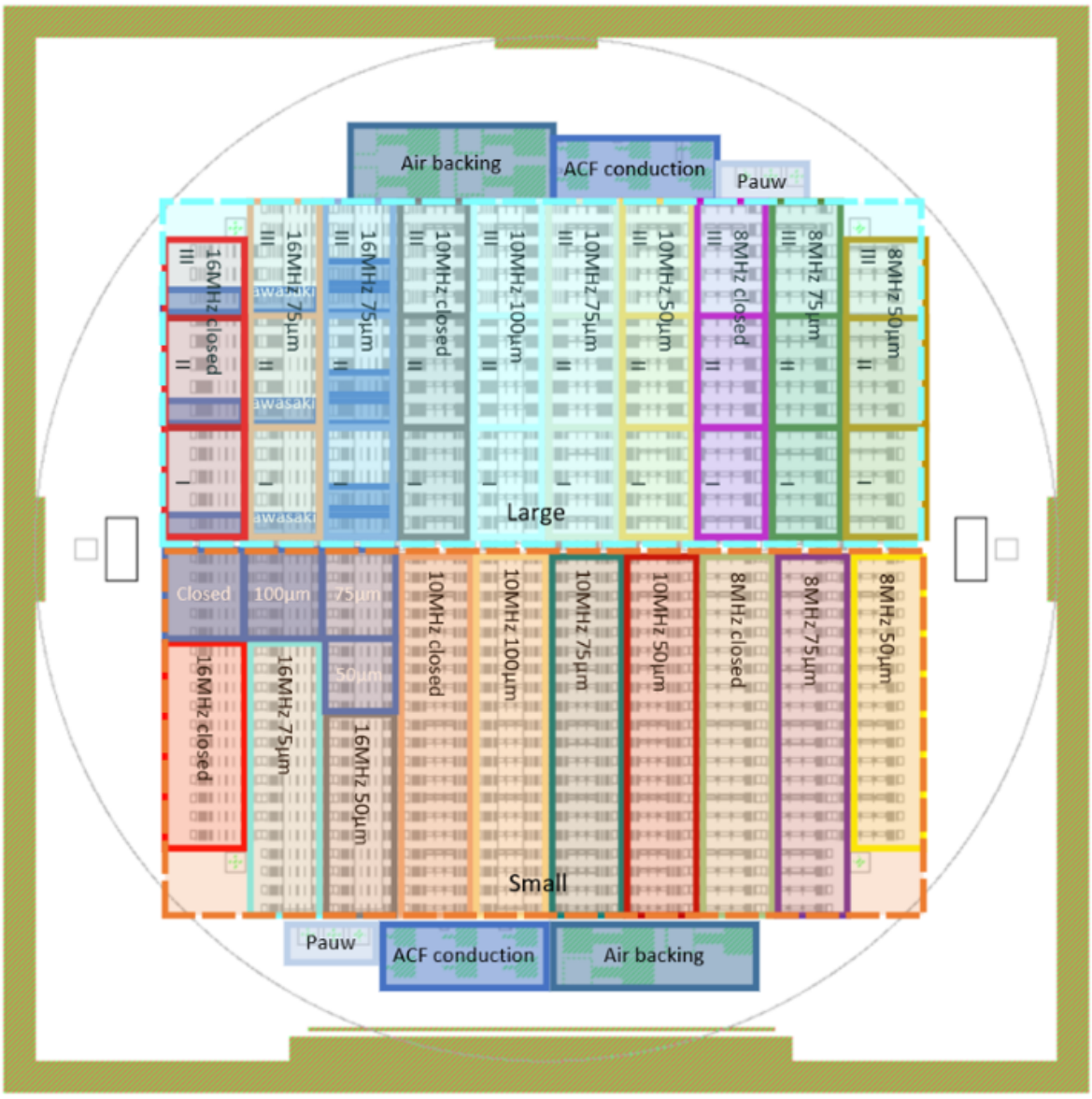

(a) The mask layout.

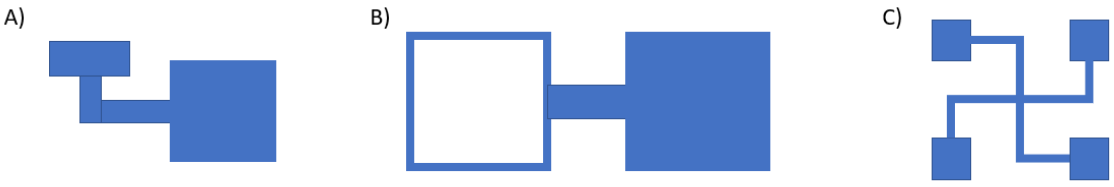

(b) The three test structures. A) shows the ACF test structure B) the airbacking test structure and C) the Van der Pauw test structure.

Figure 6.3: The mask layout and the test structures.

6.2. Processing steps

The processing has been done with a 300 μm-thick, double-sided polished, <100> oriented, P-type silicon wafer (Req. M-3). Double-sided polished is needed for both front and back processing. A thinner wafer was selected so the DRIE process at the end of the flow would take less time. The wafer diameter is 100 mm. All the following remarks regarding the process flow are specifically meant for the EKL environment.

Step A consists of adding alignment markers on top of the wafer. For the photolithography, an automatic wafer stepper (PAS5500/80, ASML) has been used. The dry etching takes place in an etcher (Omega 201 plasma etcher, Trikon). The alignment markers are etched 120 nm deep into the silicon.

Table 6.1: Process conditions for the *xxx_siostd* recipe.

Gasses & Flows	Pressure	HF power	LP power	Temperature	Etch time
$N_2/SiH_4/N_2O$ = 3150/205/6000sccm	2.2 Torr	1000 W	0 W	400°C	variable

After the alignment markers a SiO_2 deposition is needed. This can be done using thermal oxide growing in the furnace or deposition of Plasma-Enhanced Chemical Vapour Deposition (PECVD) oxide. Thermal oxide has a better quality compared to PECVD oxide, however, it can take several hours in the furnace to grow several hundreds of nanometers, while PECVD deposition takes several minutes for several micrometers. Moreover, the process of thermal oxide growth is limited to several hundreds of nanometers and that means that for a layer thickness of 1 μm the cycle should be repeated twice. Another difference is that thermal oxide has compressive stress, while PECVD oxide has tensile stress (Figure 6.4). In the end, a 1 μm PECVD oxide layer has been used, deposited by the Novellus PECVD reactor. This layer will serve as a membrane later on in the process. Initially, the layer thickness was set at 400 nm, but it appeared to be too fragile for a membrane and therefore the thickness was increased to 1 μm. The process conditions for this deposition are shown in Table 6.1. The quality and strength are good for fabrication and PECVD is faster and can be used more easily for thicker layers.

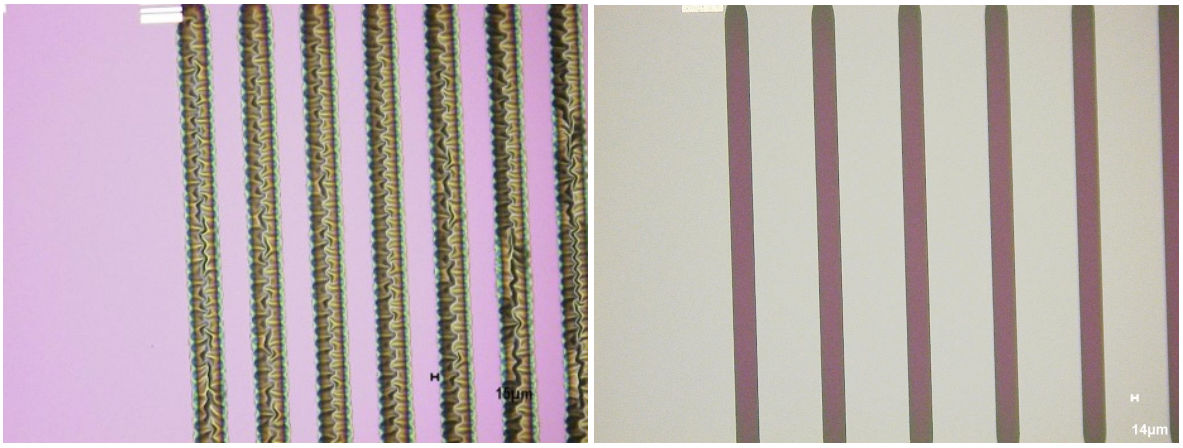

(a) The compressive stress in the thermal oxide layer. **(b)** The tensile stress in the PECVD oxide.

Figure 6.4: The stresses in the thermal oxide and PECVD oxide layers.

After the deposition of the SiO_2 layer a 1 μm thick AlSi (99%/1%) metal layer is sputtered on top (Sigma sputter coater, Trikon). This thickness is done on purpose so it will not break easily in case the PZTs are attached. In addition, the resistivity is low. The process conditions are shown in Table 6.2.
Aluminum is not resistant to corrosive degradation. This means that in case the encapsulation breaks, the aluminum decomposes and the device breaks. As this is a prototype and aluminum is a cheap, good-conducting metal, it was chosen during this wafer-level microfabrication process. The metal layer is sputtered around room temperature, so thermal stress is avoided.

Table 6.2: Process conditions for the *AlSi_1000nm_50* recipe.

Module recipe	Target	Electrode temp.	Gasses & flows	Target power
AlSi_1000nm_50	99% Al with 1% Si	350°C	Ar = 100 sccm	10 kW

After metal sputtering, the wafer is coated with a 2.1 μm thick positive photoresist (SPR3012, Shipley).

To guarantee good adhesion to the metal surface, before the coating, a treatment with hexamethyldisilazane (HDMS) vapor with nitrogen as a carrier gas is performed. The soft bake is done at 95°C for 90 seconds. For this coating the wafer track (EVG 120) is used.
After coating, the photoresist layer is exposed using the mask aligner (MA/BA8, SUSS MicroTec) together with the metal mask (1st brightfield mask). The alignment is manually done per wafer and the exposure time can be calculated based on the intensity of the exposure lamp which is written down in the logbook at the cleanroom.
After exposure, the wafertrack is used again for development. First, a post-exposure bake at 115°C for 90 seconds is performed. After the developer (MF322, Shipley) is used during the development. A double-pubble process is used (1-DEV-DP2), to avoid photoresist residues. The development step finishes with a hard bake of 100°C for 90 seconds.

Table 6.3: Process conditions for the *Al2mu_*50 recipe.

Step	Gasses & Flows	Pressure	Platen RF	ICP RF	Platen temp.	Etch time
1. breakthrough	HBr/Cl_2 = 40/30 sccm	5 mTorr	50 W	500 W	25°C	endpoint
2. bulk etch	HBr/Cl_2 = 40/30 sccm	5 mTorr	35 W	500 W	25°C	endpoint
3. Over-etch	HBr/Cl_2 = 30/15 sccm	5 mTorr	35 W	500 W	25°C	20% of bulk etch time

The aluminum can be etched after the coating, exposure and developing step with the dry etcher (Omega 201 plasma etcher, Trikon). Based on an end-point detection recipe (Table 6.3) the aluminum is removed from the silicon substrate except for the metal traces. Individual metal traces can be seen in Figure 6.5. The photoresist is removed by means of an oxygen plasma using the Tepla plasma stripper.

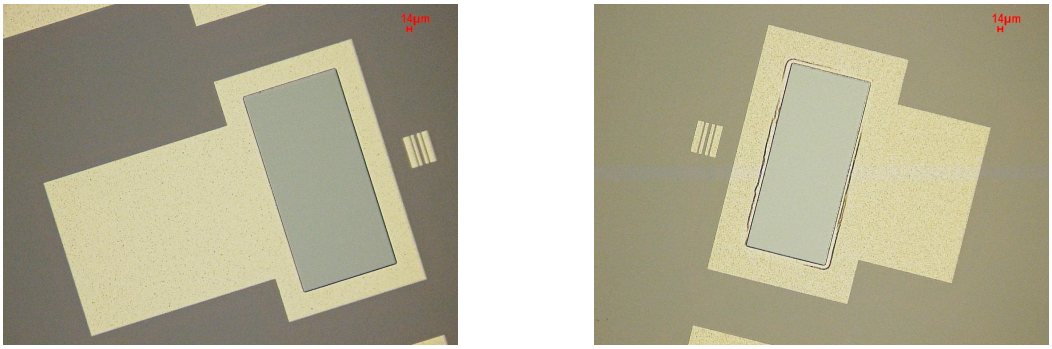

(a) Dry etching of SiO_2.

(b) Wet etching.

Figure 6.5: The different etching approaches for the SiO_2 layer.

The next phase consists of opening the SiO_2 layer for the airbacking wells. As a soft mask, a 4.0 μm thick positive photoresist (SPR3027, Shipley) is used. During the photolithography, the darkfield *Airback mask* is used. During the development step, a double-puddle recipe (1-DEV-DP3) is chosen with a longer development time than for the previous coating. The photoresist needs to be removed from small cavities and will leave residues if shorter development times are used. An additional step in this development process is the cross-link bake of the photoresist. This cross-link bake hardens the photoresist and makes it more resistant to the etching steps which will follow.

The etching of SiO_2 can be done wet or dry. A wet etching process consists of two steps. First, the wafer is rinsed in demi-water with Triton X-100 for 1 minute. Triton X-100 reduces the surface tension during etching and enhances the etching of fine features. After this rinse, the wafer is dipped in a BHF (1:7) solution and is left inside for the duration of the calculated time based on the etch rate and the depth of the features. The etch rate for SiO_2 is approximately 200-300 nm/min. For a 1 μm thick layer,

this means a dip of approximately 5 minutes as some over-etching time should be included. During wet etching, the metal surface becomes more rough as can be seen in Figure 6.5b.
Dry etching can be done in the plasma etcher (Triode 384T, Drytek). Dry etching is more selective and therefore more non-isotropic compared to wet etching. In addition, the metal surface is kept more smooth compared to wet etching (Figure 6.5a. The *STDOXIDE* recipe removes the SiO_2 layer with the process conditions listed in Table 6.4.

Table 6.4: Process conditions from the recipe *STDOXIDE*.

Step	Gasses & Flows	Pressure	RF power	He pressure	Etch time
1. bulk etch reactive ion etching (RIE)	C_2F_6/CHF_3 = 36/144 sccm	180 mTorr	300 W	12 Torr	2 minutes

In step B, during the sputtering of the metal layer some metal residue is left at the backside of the wafer (Figure 6.6). As the backside will be processed later on, this residue needs to be removed as it can negatively affect the coating of photoresist layers and the etching. The Aluminum residue is simultaneously etched during the wet etching of the SiO_2. Therefore, only dry etching for the SiO_2 is not sufficient. The disadvantage of only wet etching is its isotropic nature. Although the etching process is selective, some photoresist is consumed. As the photoresist is thinner at the sidewalls of the metal structure, compared to the thickness on top of the metal, after some time the photoresist is consumed and the metal structure is etched as well. This can be seen in Figure 6.5b.

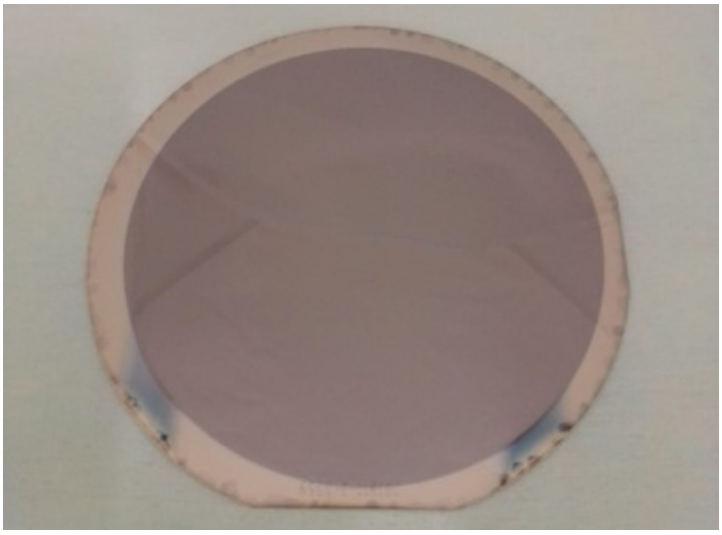

Figure 6.6: Aluminum residue at the backside of the wafer.

Therefore a combined etching process has been implemented. In which the wafer is first dipped for only 1 minute into the wet etching BHF batch and after is put in the Drytek for dry etching the leftover of the SiO_2 for 2 minutes. In this way the metal residue at the backside is removed, the metal structures on top are preserved and the SiO_2 is removed. In Figure 6.7a the result of this combined step is shown. After, the profilometer measurement was done on one of the cavities created after SiO_2 etching. The profile starts on the SiO_2 layer, moves over the Aluminum structure, measures inside the airback well where the SiO_2 is removed and goes over a metal structure and a dicing mark. It can be seen that the metal surface is rough and has sticking structures of 500 μm on top. During assembly, it appeared not to have any influence on the attachment of PZTs or the conductivity, so no additional measures are taken to remove it. After this process step, the photoresist is removed by means of the Tepla plasma stripper.

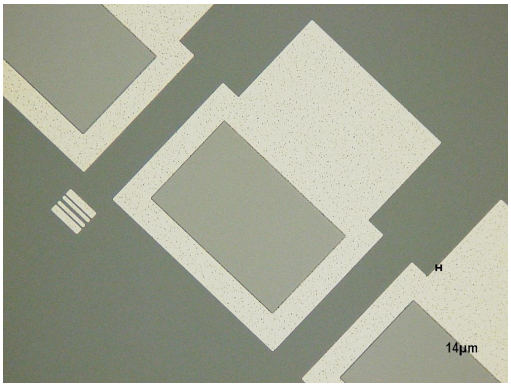

(a) Wet and dry etching.

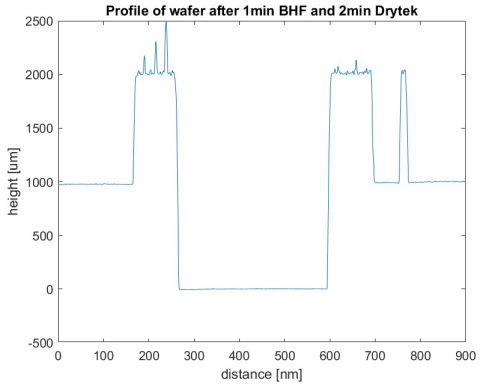

(b) The profilometer measurement for the surface of the structure.

Figure 6.7: The combined approach of wet etching and dry etching of the SiO_2 layer.

Since part of the process flow is performed at the backside of the wafer, it is important to take into account that cavities on the top of the wafer are not too large and too deep. Otherwise, issues might arise due to bad or no vacuum suction or the He-flow during electrostatic clamping is too large and processing is not possible. Therefore, a 4 μm thick SiO_2 layer has been deposited on the backside, before doing the etching of the Si airbacking wells. Tests show that vacuum or He-flow issues do not arise for 20 μm deep airbacking wells in the Drytek, EVG coater, SUSS Mask aligner and Rapier. As those are the only machines needed after the etching of silicon, it is made sure that the process flow will not stagnate due to clamping issues. The 4 μm thick SiO_2 layer at the backside will serve as a hard mask for the DRIE process at the backside. The process conditions are shown in Table 6.4.

Table 6.5: Process condition for the *EKL_smooth20xxx* recipe.

Depth	Module recipe	# of cycles
20 μm	EKL_smooth20xxx	25
300 μm	EKL_smooth20xxx	450

To protect the top structures during the DRIE process another coating, photolithography and development step is done. The same steps are taken as described in step D. Again the cross-link bake is meant for making the photoresist more rigid during the etching process.
For etching wells into silicon both a wet and a dry approach can be used. Wet etching is done with a 30% KOH solution at 85°C. As the wafer has an <100> orientation, KOH etching results in a well with angles of 54.7°. The dry etching process is a DRIE process, based on the Bosch process. It consists of a cycle in which first the sides are passivated and then the horizontal parts are opened and etched. This results in non-isotropic, high aspect-ratio etching.

For etching the airbacking wells, the dry etching approach in the Rapier DRIE has been used. Wet etching makes the process flow more complex since KOH etching is less selective regarding photoresist and therefore a thick photoresist layer or hard mask should be used. Including a hard mask in the process flow is difficult. The hard mask needs to be deposited, patterned and removed afterward. A thick photoresist (more than 4 μm) layer can only be coated manually. This makes the process flow more time-consuming. In addition, although a holder is available for protecting the backside of the wafer, during the KOH etching test, some leakage occurred during testing and the backside was etched. As backside processing is needed later on in the process flow, this chance of leakage is a risk. Moreover, in the case of the airbacking wells, no landing layer exists. In the case of KOH etching, the bottom surface is rough and not nicely etched.

The etch rate per cycle in the Rapier DRIE is approximately 0.9 μm/loop. However, it scales not linearly. Therefore, a test wafer has been used to find the correct number of cycles. The process conditions for the used recipe can be found in Table 6.5. The airbacking well is etched 20 μm deep. The result is shown in Figure 6.8.
In step G of the process flow, the backside of the wafer is coated with a 3.1 μm thick positive photoresist

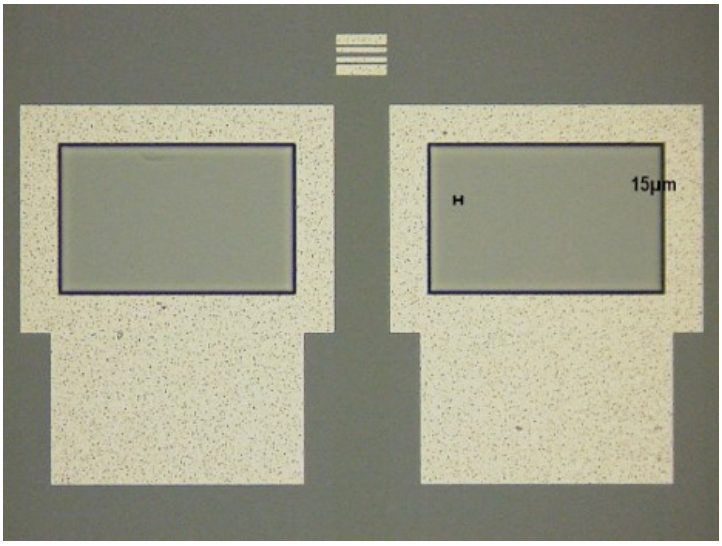

Figure 6.8: The metal and airbacking structure after the 20 μm deep DRIE etch.

(SPR3012, Shipley). During backside exposure, the brightfield backside mask (*backside mask*) is used. The development step consists of only a double-puddle step (1-DEV-DP2). As the aluminum residues are removed and dry etching gives the best surface smoothness and non-isotropic etching results, the plasma etcher (Triode 384T, Drytek) has been used. The process conditions for the recipe are shown in Table 6.1. However, the etching time, including some over-etching, is 11 minutes. The result is shown in Figure 6.9.

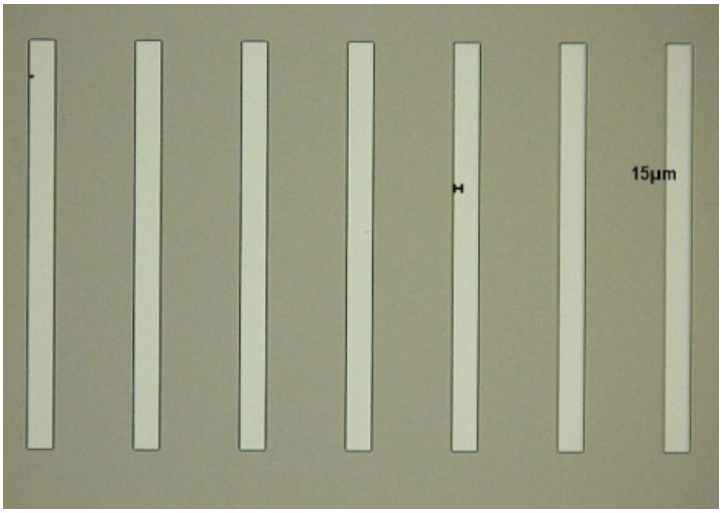

Figure 6.9: The SiO_2 removed areas at the backside of the wafer.

In step H, the bulk silicon is etched in the Rapier DRIE for 450 cycles. In that way, it lands on top of 1 μm thick SiO_2 layer and leaves a thin 1 μm thick SiO_2 membrane. This membrane is needed to cover the hinges in between the silicon islands and will serve as a support during the parylene-C coating. The membrane after the Rapier DRIE can be seen in Figure 6.4b. As it is fragile, care should be taken during the following process steps. After the etching, the photoresist is removed using the Tepla plasma stripper. To take care of the membrane, the wafer is put-in flat with the top facing the top of the chamber. In that way, the least amount of stress is put on the membrane during the stripping process. This photoresist stripping is the final step in the CR100 cleanroom. All the other processing steps are performed in biosoniclab or MEMS-lab. An overview of a microfabricated device till step H, is shown in Figure 6.10. The front and back of the wafer after completing step H of the process flow are shown in Figure 6.11a and Figure 6.11b respectively.

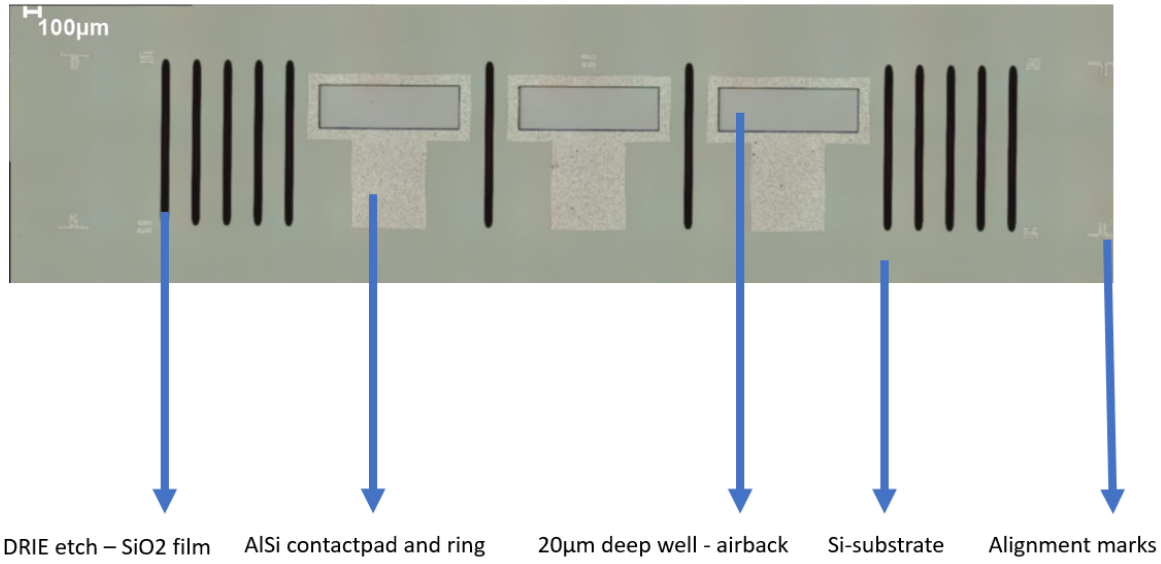

Figure 6.10: An overview of a microfabricated device.

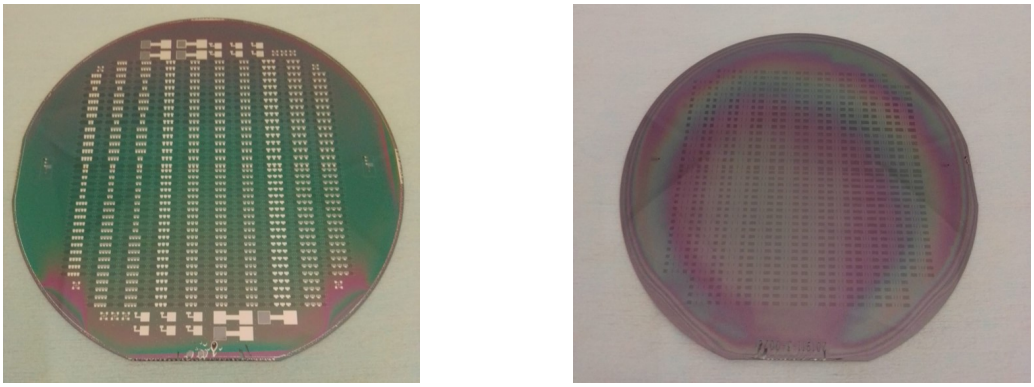

(a) The front side of the wafer.

(b) The back side of the wafer.

Figure 6.11: The front- and backside of the wafer after completing step H of the process flow.

Before continuing with the process flow, PZTs need to be diced using the dicer (DAD3221, Disco) in biosoniclab (Req. M-1). The PZT sheets that were available during the thesis project were the 8 MHz and 16 MHz sheets from Piezo.com. Although these sheets are defined as having these frequencies, the practical resonance frequency is determined by the fabrication and assembly processes and can fluctuate around these numbers. Therefore, experiments have been done with the 8.4 and 16.2 MHz designs. As explained in Chapter 3, PZT contains a small percentage of lead. As lead is toxic to humans, handling needs some precaution. Therefore, PZT was only handled with tweezers and exhaust was present during dicing. In addition, it is important to have a good encapsulation layer to make sure no lead can enter the body after implantation (Req. S-2). In the case of this design, this has been done by coating it entirely with a layer of parylene-C. To have a conductive connection between the PZT and the bottom metal pad, ACF has been used. This is applied to the PZT before dicing it in the dimensions mentioned in Chapter 5. In Figure 6.12 the diced elements of 8.4 and 16.2 MHz are shown. The black material is the ACF. On top of the 8.4 MHz PZTs a protective, transparent layer is still present. This caused a small deviation between the actual dimensions and the measured dimensions. After removing the protective, transparent layer, as done for the 16.2 MHz PZTs, the dimensions were as expected.

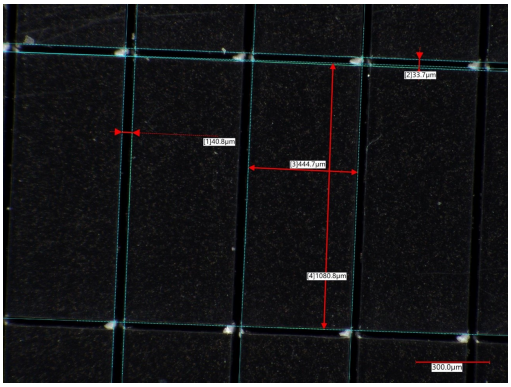

(a) The diced 8.4 MHz PZTs with ACF.

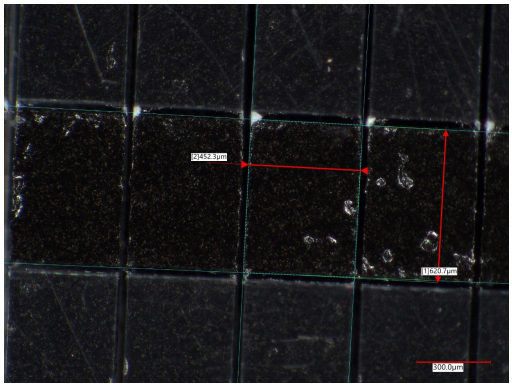

(b) The diced 16.2 MHz PZTs with ACF.

Figure 6.12: The diced PZTs with ACF.

The next step, step I, is dicing the wafer. This has been done with the dicer (DAD3221, Disco) in MEMS-lab as it has two varieties of dicingfoil. During testing it became clear that already placing the PZTs and dicing the wafer afterward, cause breakage of the wafer due to the vacuum suction during dicing (Figure 6.13a). In addition, applying a layer of parylene-C before dicing results in delamination of the parylene-C layer during cutting (Figure 6.13b). Therefore, parylene-C coating should be done after dicing.

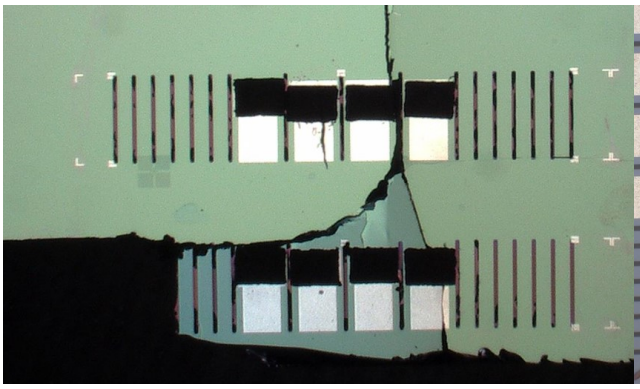

(a) The breakage of the wafer during dicing due to the attached PZTs.

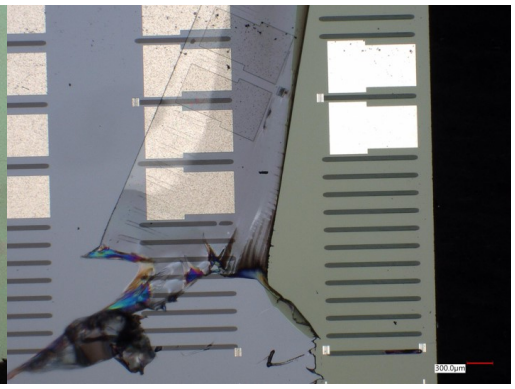

(b) Delamination of the parylene-C at the dicing side.

Figure 6.13: Issues occurred during dicing.

Another issue that appeared was the preservation of the SiO_2 membrane during dicing. The wafer needs to be sticked to dicingfoil. To avoid damage to the membrane due to the water jet of the dicing blade and to support the membrane during dicing, it is advised to attach the wafer with the membrane to the foil. After dicing the wafer can be released from the foil either by using UV-light or acetone liquid, depending on which dicing foil is used. However, as the dicing foil is also sticking to the membrane, removing the foil should be done with care. Otherwise, the membrane is damaged and part of it will be pulled off with the dicing foil. Figure 6.15 shows the damaged membrane at the left (Figure 6.14a) and parts of the membrane on the membrane at the right (Figure 6.14b).

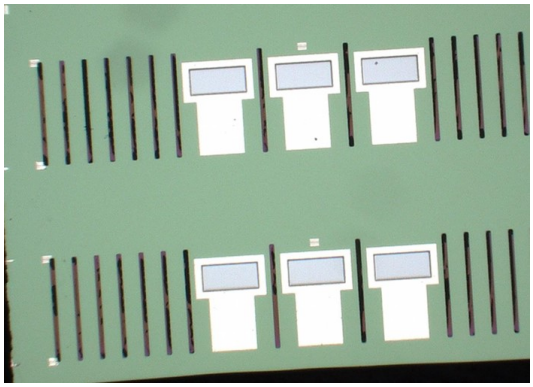

(a) Damage of the SiO_2 membrane.

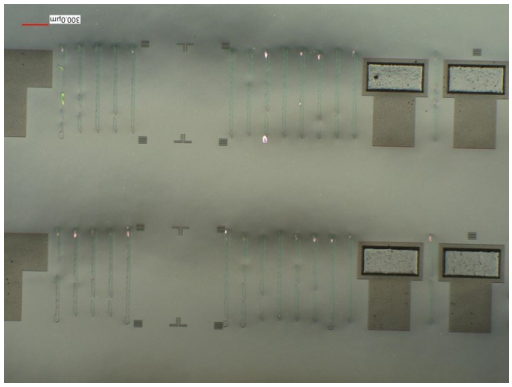

(b) Part of the membrane sticks to the dicing foil and is pulled off.

Figure 6.14: Damage occurring in case the UV-sensitive dicing foil is pulled off wrongly.

In the case of the UV-sensitive dicingfoil, after applying the UV light, the foil should be pulled off in the length direction of the SiO_2 membrane rectangles. So starting from either the top or bottom side of the wafer. In the case of using the acetone dicingfoil, the dicingfoil together with the diced sample needs to be dipped into acetone liquid. The foil releases itself from the sample and the diced samples need to be fished out of the solution. Besides, dicing through the membrane, even at a slow speed (1-2mm/s), does cause damage to the thin membrane.

To take this into account a two-step dicing process has been developed. First, the UV-sensitive dicing foil is used and attached to the top of the wafer to support the membrane. The wafer is diced in pieces by means of seven cuts. These cuts are indicated in Figure 6.15a. In this way, several pieces of the wafer, each containing multiple devices, are obtained. After applying the right amount of UV-light, the dicing foil is pulled off in the length direction, which avoids damage of the SiO_2 membrane. In Figure 6.15b the non-damaged membranes are visible. These smaller pieces of the wafer are individually diced during the second step.

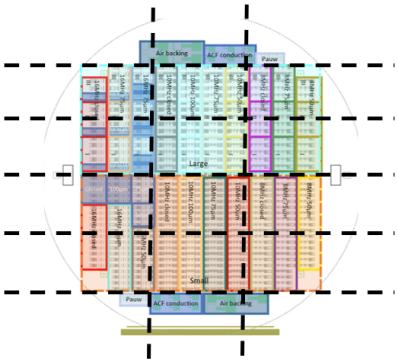

(a) Dicing lines during the first step of the dicing process.

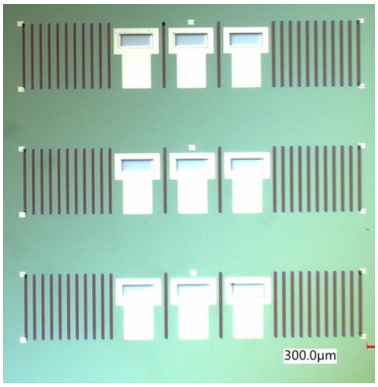

(b) Survived SiO_2 membranes after removal of the dicing foil in the correct direction.

Figure 6.15: Step 1 of the dicing process.

Second, a piece from the previous dicing step is attached to the acetone-sensitive dicingfoil. The dicingfoil is attached to the top of the wafer, to support the membrane. This piece is diced into individual elements. Since dicing the SiO_2 membrane directly causes damage, a thin silicon edge is preserved, so the dicing occurs at the silicon (Figure 6.16a). In that way, the SiO_2 membrane is preserved and individual devices with intact membranes are obtained. After dicing, the diced sample is placed in a bath with acetone liquid and the devices are detached from the dicing foil. After, these devices need to be fished out of the liquid which should be done with care. Figure 6.16b shows a diced device that is detached from the acetone-sensitive dicingfoil and fished out from the acetone bath. As can be observed, some dirt is left on the surface of the device after the acetone evaporates. These are some

residues from the sticking layer of the dicing foil. Rinsing the device in acetone for some minutes does dissolve all the residues resulting in a clean device.

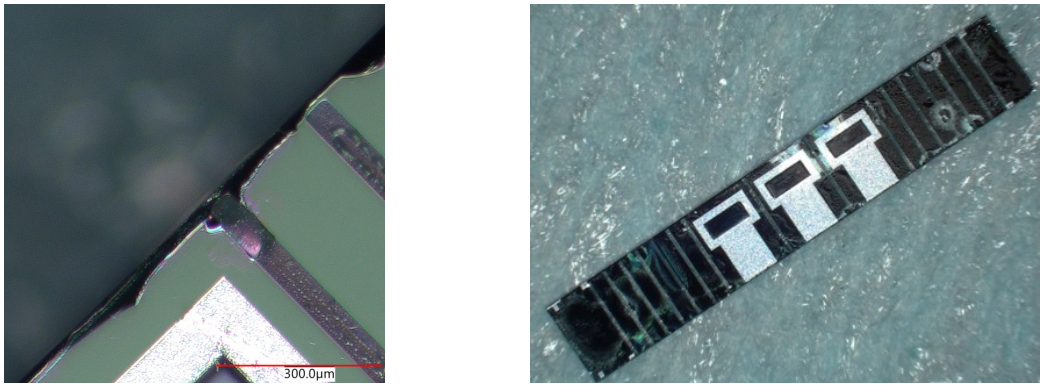

(a) The thin silicon edge left during dicing to avoid membrane damage. **(b)** A diced device removed from the acetone-sensitive dicing foil.

Figure 6.16: Step 2 of the dicing process.

In step J of the process flow, the PZTs are placed on the diced device. Although it is feasible to place the elements by hand, the T-300 bonder pick-and-place tool has been used since it makes the placement faster and more accurate. As the ACF is already attached to the PZT, it is not possible to pick the PZT from the top with the pick-and-place tool. The picking motion is accomplished by pressing the element and then lifting it based on the vacuum pressure. However, during the pressure the ACF does stick to the substrate and the vacuum pressure is not enough to lift the transducer. Therefore, the vacuum is turned on without picking any element and the element is manually attached to the tip. After, the beam splitter is used to correctly position the PZT above the device and the tool places the transducer with a bit of force on the substrate. In Figure 6.17a some 8.4 MHz PZTs placed with the T-300 bonder on the substrate are shown. Although the beamsplitter is used for alignment, some variation does exist. Due to the small size, the 16.2 MHz PZT has been placed with a self-made tip. An overview of the setup of the T-300 bonder pick-and-place can be found in Figure 6.17b.

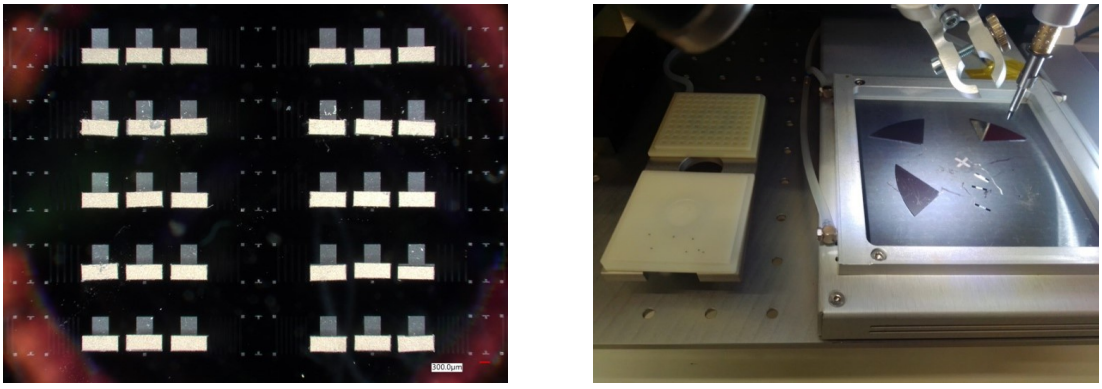

(a) 8.4 MHz PZTs placed on a substrate using the T-300 bonder. **(b)** The pick-and-place setup of the T-300 bonder.

Figure 6.17: The PZT placement on the device using the T-300 bonder pick-and-place.

After the PZT placement, the top connection between the transducers needs to be made. For this purpose, a wirebonder could be used. However, wire attachment on PZTs is difficult as they can resonate with the US used to bind the wire. In that way, the binding is weak or it does not bind. Another issue is the adhesion of the wire to the top of the PZT. As the PZT has a layer of nickel on top, the normal cheapest option of Aluminum bonding is not sticking to that metal layer. This could be solved by evaporation of another metal layer on top of the PZT or using a more expensive metal to bind with, like gold wire. However, both solutions are more expensive in money and time. Finally, using the wirebonder requires tuning the parameters like pressure, heat and time which is time-consuming. Another option is a semi-automatic process using the T-300 bonder. In that case, a 50 μm-thick wire is lifted by the

T-300 bonder. Some conductive epoxy is added to the tip of the wire. Using the T-300 bonder, the wire is placed at the correct spot on the PZT. The heater function is used to cure the epoxy and the wire is attached. An experiment with silver conductive paste (42469, Thermofischer) [2] as conductive epoxy showed that it is possible to cure and bind a wire. The heater function works based on a heat profile. The heat profile needed for the silver conductive paste is shown in Figure 6.18b. Setup during wire attachment is shown in Figure 6.18a. The disadvantage of this approach is that each wire needs to be cured individually.

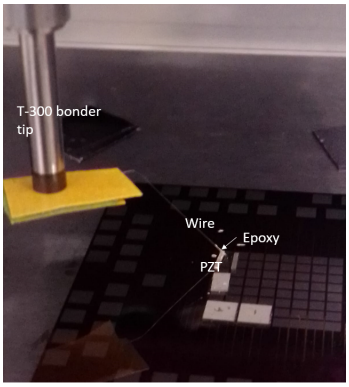

(a) The setup during semi-automatic wire attachment using the T-300 bonder.

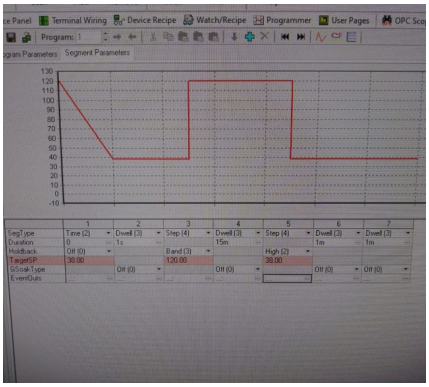

(b) The heat profile used to cure the silver conductive paste.

Figure 6.18: The semi-automatic wire attachment technique using the T-300 bonder.

Although the PZTs are small, it is possible to wirebond them by hand. This is the third possible approach. Since it is a prototype design and this approach is less time-consuming, the choice was made to do manual wire attachment. During manual wire attachment, a 50 μm-thick tungsten wire has been used. This wire is placed on top of the PZTs on a device, using tweezers. After, with a needle tip conductive epoxy is applied to attach the wire to the PZT. From experiments, it became clear that the Alfa Aeser silver epoxy is conducting very well, but it gives hardly any mechanical support. Therefore, the wire breaks off easily. Another conductive epoxy is EPOTEK-H20E [3]. This two-component epoxy gives more mechanical support, but the conduction is not good and varies. The best way of attaching a wire to a PZT-based US transducer is first curing the silver conductive paste and second curing some conductive epoxy on top. In this way, the conduction is guaranteed and the connection is more mechanically robust. Wires have been attached in both a 2-wire and a 5-wire configuration. These configurations are shown in Figure 6.19a and Figure 6.19b respectively.

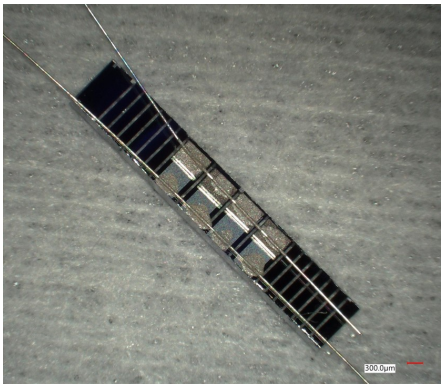

(a) The 2 wire configuration.

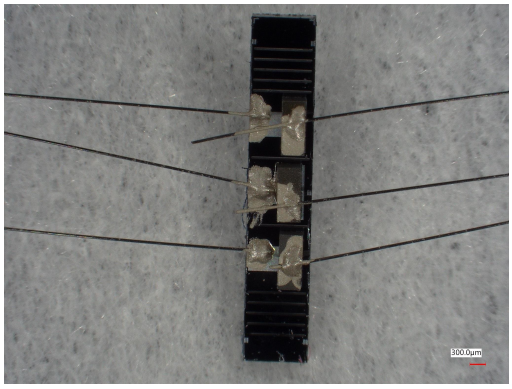

(b) The 5 wire configuration.

Figure 6.19: The manual wire attachment configurations.

[2] https://assets.thermofisher.com/DirectWebViewer/private/document.aspx?prd=ALFAA42469 PDF MTR CLP1 EN 2020-12-31%2010:38:15 Silver%20conductive%20adhesive%20paste

[3] https://www.epotek.com/docs/en/Datasheet/H20E.pdf

The final steps are the encapsulation with parylene-C and the removal of the parylene-C from the tips of the wires, so they can be connected to the measurement setup. Parylene-C has been chosen as an encapsulation material, as it has good conformality, good water resistance (Req. M-4), it is acoustically transparent for thin layers, it is biocompatible (Req. S-2). Moreover, coating is a standard wafer-level microfabrication process (Chapter 3). The disadvantages like brittleness are not outweighing the benefits. In addition, the layer thickness could be increased to make the layer mechanically more robust. Parylene-C is also acting as the flexible material within the island-bridge design. The SiO_2 membranes are covered by parylene-C and after, the parylene-C holds the silicon islands in place with supporting mechanical flexibility. The device is coated with 5 μm-thick parylene, which translates to 10 grams of the dimer. Moreover, a 3D-printed holder has been designed. The 3D file can be found in '3D print files' under the name of *parylene holder - chapter 5* (DWG/STL). In that way, the devices hang during the coating and do not stick to any surface after the coating. It is then easier to remove the device, without damaging it.

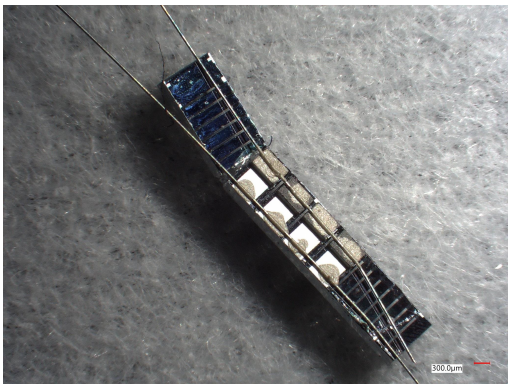

(a) A parylene-C coated device.

(b) A 3D-printed holder to hang the devices for parylene-C coating.

Figure 6.20: The parylene-C coating processing step.

In step L, the parylene-C is stripped from the tips of the wire by means of tweezers. In that way, they become conductive and can be attached to the measurement setup (Req. M-7).

7

Device characterization

In this chapter, the US measurements will be discussed. The measurements have been done in a planar and curved configuration. Both the measurement setup and the results will be discussed. In addition, part of this chapter will discuss the flexibility and curvature of the device and how the SiO_2 membrane behaves from a material science point of view.

7.1. The measurement setup

First, every transducer is measured in a planar configuration. This has been done to verify whether each transducer is functioning and to have a reference measurement for the measurement in the curved configuration. In addition, the resonance frequency of the transducers and the beam profile can be measured.
The measurement setup for the planar measurement consists of a 3D-printed holder, a prototyping PCB and a self-made cable. The design consists of a planar bar, which can be connected to the screw connection of the existing setup for the water tank. In addition, it has a square with two pins on which the prototyping PCB can be placed. The prototyping PCB is attached using sticky tack glue pads. In this way the prototyping PCB can be easily swapped in between the planar and curved 3D-printed holder. Finally, the front consists of a bar with a slit in which the device can be placed. The prototyping PCB has a 5-pin screw connector soldered on top. This connector is connected via wires at the bottom to the KK 2.45/.100 MOLEX wire connector which is soldered behind the screw connector.

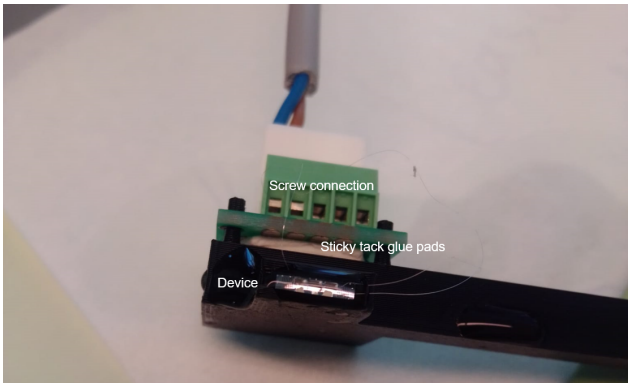

(a) The front-side of the 3D-printed holder with a device inside, together with prototyping PCB and connected to the self-made cable.

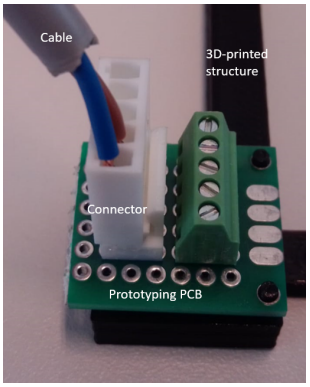

(b) The side-view of the 3D-printed holder with the prototyping PCB and connected to the self-made cable.

Figure 7.1: The planar measurement setup.

The wire itself is a U242 LAPP cable STUTTGART 2x0.5 mm wire. At one side two rings are soldered (Figure 7.2b) so the wire can be easily attached to the multi-contact Staubli clips of the function generator (Req. M-7). On the other side, the female KK 2.54/.100 crimps are soldered which are placed

in the KK254/.100 crimp housing (MOLEX) [1]. In this way, the planar measurement setup can be easily decoupled from the wire (Figure 7.2a). The measured resistance from the top of the wire to the screw connections is 2.3 Ω.

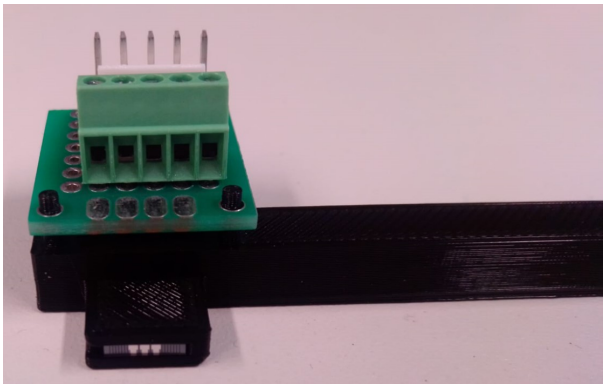

(a) The front-side of the 3D-printed holder with a device inside, together with prototyping PCB and disconnected from the self-made cable.

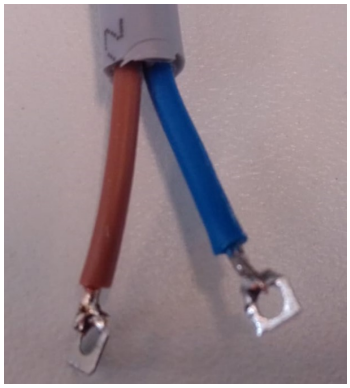

(b) The rings at the tip of the wire for the connection with the function generator.

Figure 7.2: The planar measurement setup.

The device is driven by a function generator (RIGOL DG4202) which supplies a burst of 10 V_{pp} consisting of 30 pulses and having a 1 ms period. The burst contains 30 pulses and the frequency can be adapted based on the device. The period is 1 ms. The device is hung inside a watertank by means of a resin-printed holder (Figure 7.3). In this resin-printed holder, the 3D-printed holder can be placed and fixed with a screw connection. The US is measured using a fibre-optic hydrophone from Precision Acoustics[2]. This fibre-optic hydrophone can be precisely moved with a motorized 3D-axis stage (GAMPT soundfield scanning drive SFS630). The fibre-optic needle is driven and read out by a Fibre-optic Hydrophone System. This system biases the needle and amplifies the signal. The 50Ω output of this system is connected to a 50Ω impedance inlet of an oscilloscope (Agilent Technologies DSO-X 3032A). By means of a Matlab script and GUI the function generator, the motorized stage and the oscilloscope can be controlled and measurements can be executed.

The fibre-optic needles have their own calibration data. Based on that calibration data the sensitivity for a certain frequency can be obtained. For a frequency sweep, the data should be adjusted according to the calibration data for each frequency. For this purpose, a Matlab-script has been written.

There are multiple advantages of using a fibre-optic hydrophone over the more standard needle hydrophones. First, the small tip size (10μm diameter) gives more precise measurements in the case of small transducers. Second, due to the small tip diameter, measurements can be done in smaller space which is beneficial in the curved setup. Finally, the fibre-optic hydrophone has a flat directional response for angles till +/-80°.
The mean sensitivity in the range of 2 to 18 MHz is 250 mV/MPa. Moreover, the measurement uncertainty for the range of 1 to 8 MHz is 9% and for the range of 9 to 20 MHz 11%.
For the curved measurements, a different holder has been designed. This holder is similar to the planar holder except for the circular slit in which the device can be put. This circular slit has a diameter of 3 mm as the device has a thickness of around 1 mm and the inner radius should be 2 mm. Due to the tensile force of the wires, the device can be pulled out of the curved slit. Adding a small layer of sticky tack glue pad in the curved slit and pressing the device inside, fixes the device. The prototyping PCB can be switched between the planar and curved holder. In Figure 7.4 the 3D-printed holder together with the prototyping PCB can be seen.

[1] https:
tools.molex.com/pdm_docs/sd/022012057_sd.pdf
[2] https:
www.acoustics.co.uk/wp-content/uploads/2022/07/Fibre-Optic-Hydrophone-System-V2-FOHSV2-TDS-V2-0722.pdf

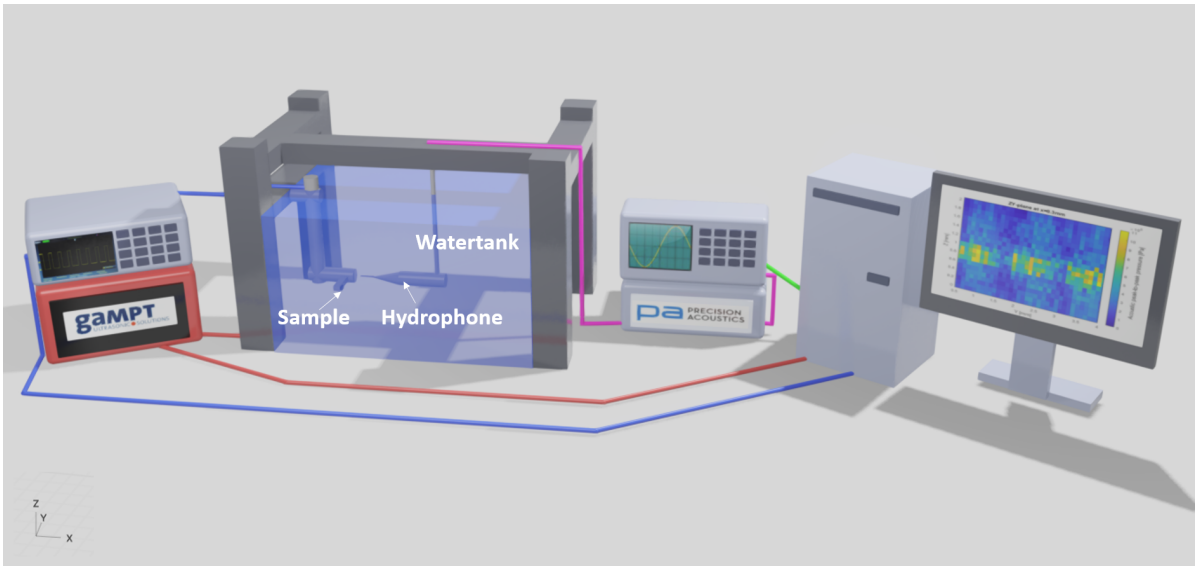

Figure 7.3: The measurement setup from left to right: the function generator, the 3D-axis motorized stage, the watertank with a hydrophone, the oscilloscope, the hydrophone amplifier, the computer with software.

7.2. Device curving

During dicing a thin edge of silicon is left as a frame for the device and to keep the SiO_2 membrane intact. After finishing the measurements in the planar configuration, the device needs to be curved. During this curving the thin silicon frame is broken and the devices become flexible due to the parylene-C coating (Figure 7.5b). The curvature is done by pressing the planar device inside the curved holder with a cotton swap, to avoid damaging the parylene-C layer. In Figure 7.5a a curved device in the curved holder can be seen. During this bending the SiO_2 membrane breaks and the parylene-C keeps everything together, creating a flex-to-rigid design (Figure 7.5c). The device has a cuff shape with an inner radius of 0.95 mm corresponding to requirements M-2 and M-9.

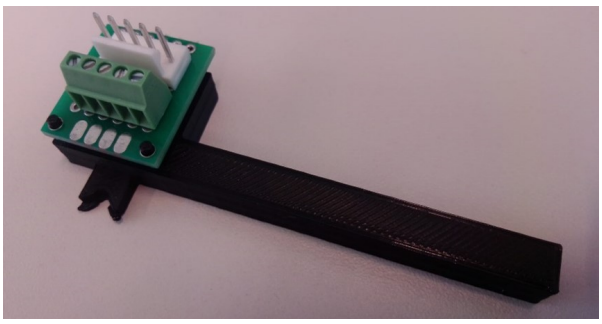

Figure 7.4: The curved holder.

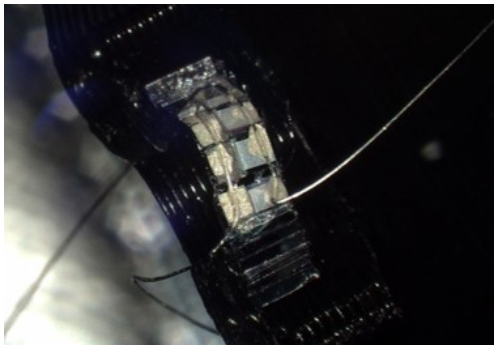

(a) A device being curved in the 3D-printed curved holder.

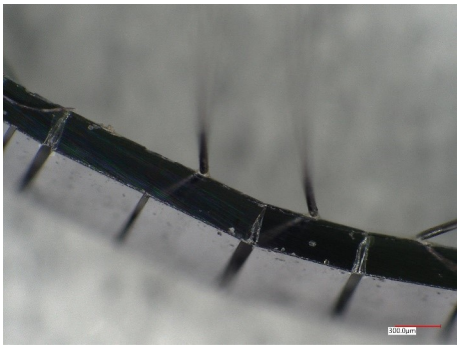

(b) The thin silicon edge breakage after bending.

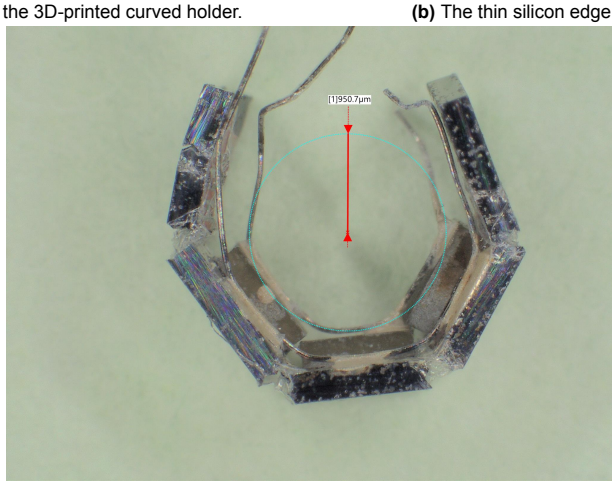

(c) The parylene-C holding the silicon islands in place.

Figure 7.5: The bending of the device.

From a material science perspective, it is interesting how the 1μm thick SiO_2 membrane behaves during the process steps and what happens when it breaks. As mentioned in Chapter 6 the SiO_2 membrane breaks when it is diced through. In Figure 7.6a the different ways of breakages are shown. In some cases, only the top part is torn apart and the largest part of the membrane is still intact. In other cases, the membrane breaks through the middle in an organic way or part of the membrane is torn apart and disappears. In Figure 7.6b the result can be seen of bending the device without the parylene-C coating. The result is that the silicon part is torn off and the membrane is entirely broken, except for some parts which are still visible.

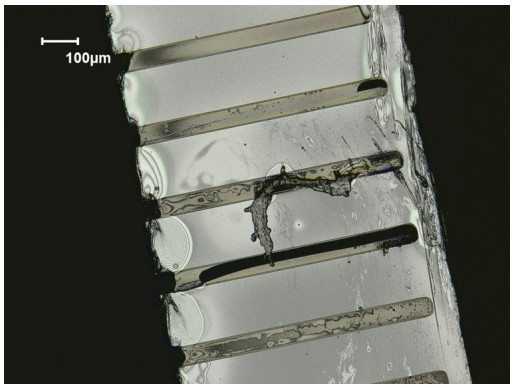

(a) Broken SiO_2 membranes after dicing.

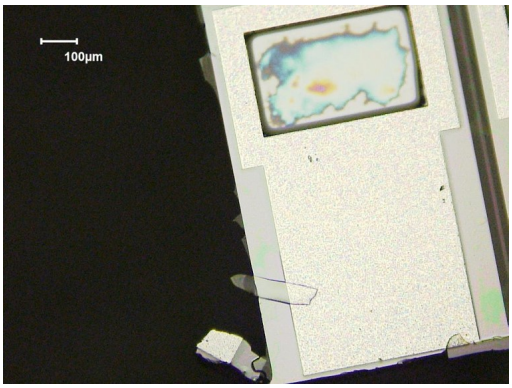

(b) Broken SiO_2 membrane when bending without parylene-C.

Figure 7.6: The membrane breakage during dicing and bending.

After the parylene-C coating, the SiO_2 membrane is encapsulated in a parylene-C layer. For small angles of bending the SiO_2 membrane stays intact as can be seen in Figure 7.7a. For larger angles of

bending the SiO_2 membrane breaks in the middle having an organic breaking line (Figure 7.7b). In the final scenario, the device is bent and stretched. The resulting membrane can be seen in Figure 7.7c. Due to the parylene-C, some parts of the SiO_2 membrane are preserved, but they are detached from the silicon islands. In all the previous scenarios it can be seen that the parylene-C takes care of the flexible connection between the silicon islands and hold them in place even after stretching.

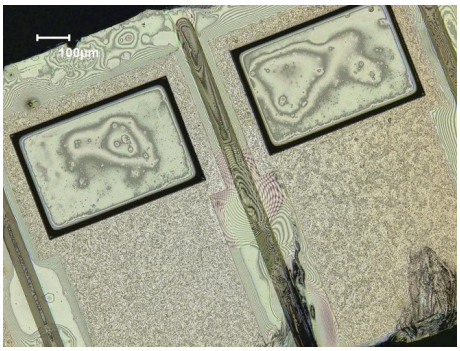

(a) The intact SiO_2 membrane after a small bending angle.

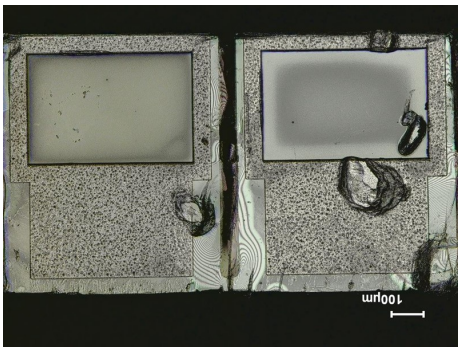

(b) The broken SiO_2 membrane after a larger bending angle.

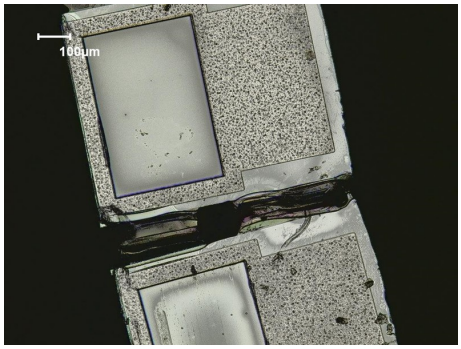

(c) The broken SiO_2 membrane after a larger bending angle and stretching movement.

Figure 7.7: The encapsulated SiO_2 membrane in parylene-C after some bending scenarios.

7.3. US measurements

The measurements which are done, are listed in Table 7.1. The results of the first and sixth measurements will be shown and discussed in the next part of this chapter. The other measurement results can be found in Appendix F.

For the planar configuration, five measurements are done. First, a frequency sweep has been performed (Figure 7.9a). For the 8.4 MHz transducers, this frequency sweep is from 1-16 MHz. For the 16 MHz transducers, the frequency sweep is from 1-25 MHz. The step size is 0.1 MHz. From Figure 7.9a it can be seen that the resonance peak for the 8.4 MHz devices is around 8.4 MHz (deviating from 8.2-8.4 MHz). This corresponds with the simulations (Appendix E). For one of the 16.2 MHz devices, it can be seen that the resonance frequency is shifted a bit more (the 9th measurements in Appendix F). As the PZT-based US transducers are smaller for the higher frequency of 16.2 MHz, the variations in the process flow might have more impact on the resonance frequency and might explain the larger offset (from the expected 16.2 MHz to 18.3 MHz) of one of the 16.2 MHz transducers. In the same frequency response of this 9th measurement, an artifact can be found at 20 MHz. This artifact is caused by a drastic drop in the sensitivity of the calibrated fibre-optic needle. This artifact might also be the cause of the shifted resonance peak in the measurements.

A large, second peak is observed at lower frequencies below 4 MHz. During wire attachment, the silver conductive paste and the conductive epoxy together with the wire are attached at the top of the PZT. This can cause lower frequency harmonics. Another reason might be partial detachment as this can induce harmonics as well [94].

The second part of the measurements is the ZY-plane scans. This is the place parallel to the surface of the transducers. These scans have been executed at a x-distance of 0.3 mm (Figure 7.8a),

Table 7.1: US characterization measurements.

Measurement	# of wires	Wire attachment	Frequency [MHz]	Design	Fibre-optic needle	Peak pressure [MPa] Planar @ 1 mm	Peak pressure [MPa] Curved @ 1 mm
1	2	silver conductive paste	8.3	Airbacking	11	1 MPa	-
2	2	silver conductive paste	8.4	Non-Airbacking	11	1 MPa	-
3	2	silver conductive paste	8.3	Non-Airbacking	11	1 MPa	-
4	2	silver conductive paste & conductive epoxy	8.3	Non-Airbacking	10	700 kPa	700 kPa
5	6	silver conductive paste & conductive epoxy	8.3	Non-Airbacking	10	900 kPa	1.1-2 MPa
6	6	silver conductive paste & conductive epoxy	8.3	Non-Airbacking	10	1 MPa	1.6-2.6 MPa
7	6	silver conductive paste & conductive epoxy	8.2	Airbacking	1	1 MPa	-
8	6	silver conductive paste & conductive epoxy	8.4	Airbacking	1	600 kPa	-
9	2	silver conductive paste	16.1	Non-Airbacking	10/1	1.1 MPa	800 kPa
10	2	silver conductive paste	16.1	Non-Airbacking	1	1.4 MPa	1.4 MPa

1 mm (Figure 7.8b) and 2 mm (Figure 7.8c) from the surface of the transducers. This distance is measured based on the travel time of a burst (from transmitter to receiver) and knowing the velocity of sound in the water medium. The step size is 0.1 mm. From the figures, it can be seen that the peak acoustic pressure of each element varies between the 700 kPa and the 1 MPa at distances of 0.3 and 1 mm fulfilling requirement S-3. However, there is variation in the acoustic pressure among the PZT-based US transducers which might have several reasons. First, as the PZT attachment is semi-automatic with ACF, the conduction per transducer is different. Moreover, the elements can have different heights as the compression of the ACF can vary. Another reason might be a bit of tilting during the measurements. As the scanning field 3D axis stage can not correct for tilt, the distance between the transducers and the fibre-optic hydrophone might be slightly different. As the measurements are done within a short distance from the top of the transducers, these small variations result in observable variations of acoustic output pressure among the PZT-based US transducers during the measurements.

Based on the assumption that the transducers are perfectly symmetrical the acoustic profile of each transducer should be symmetric as well. However, from the figures (Figure 7.8 and Figure F.1) it can be seen that some distortion exists. This distortion comes due to the attachment of the wire and the add-on of epoxy on top of the transducers.

The final measurement is an x-sweep starting at a distance of 0.3 mm and moving to 10.3 mm from the surface with a step size of 0.01 mm (Figure 7.9b). From this measurement, it can be observed that the transducer has a short near-field with a focal spot around 0.8-1 mm. After, the acoustic pressure decreases in the far field. These observations do agree with the intended focal length of 1 mm. Moreover, the scans at a distance of 0.3 mm are in the near field, the scans at a distance of 1 mm are in the focal spot (or close by) and the scans at 2 mm are in the far field. This matches the pressure magnitudes of the transducers in each scan. Moreover, the focal spot of an individual PZT-based US transducer has a size of 100 μm by 200 μm. The S_{tx} reaches 110 kPa/V.

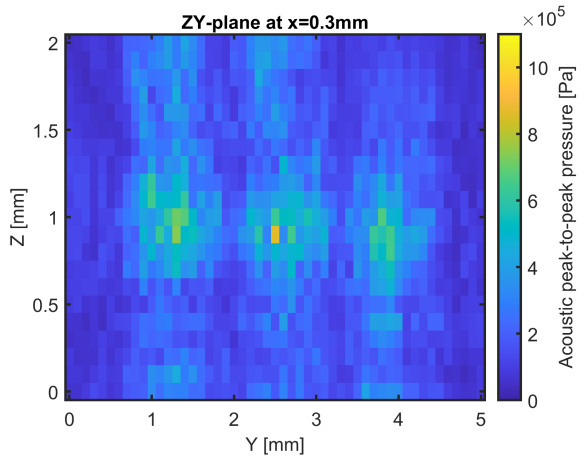

(a) The acoustic profile at a distance of 0.3 mm.

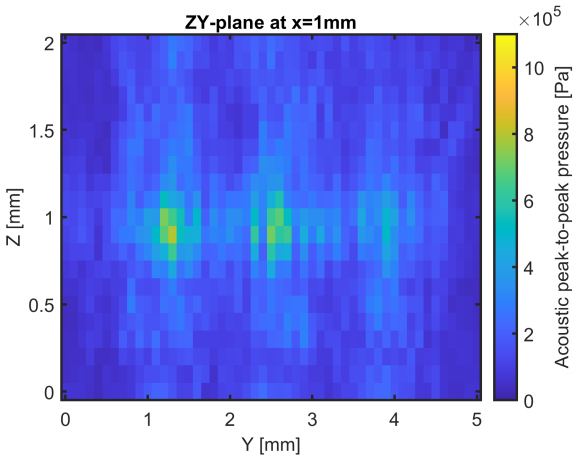

(b) The acoustic profile at a distance of 1 mm.

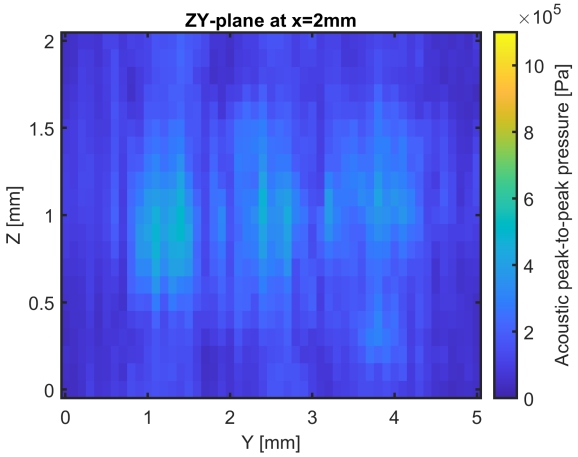

(c) The acoustic profile at a distance of 2 mm.

Figure 7.8: The acoustic profiles for different distances.

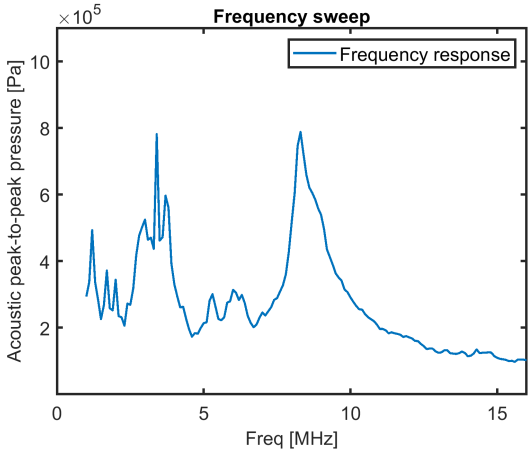

(a) The frequency response of a 8 MHz transducer.

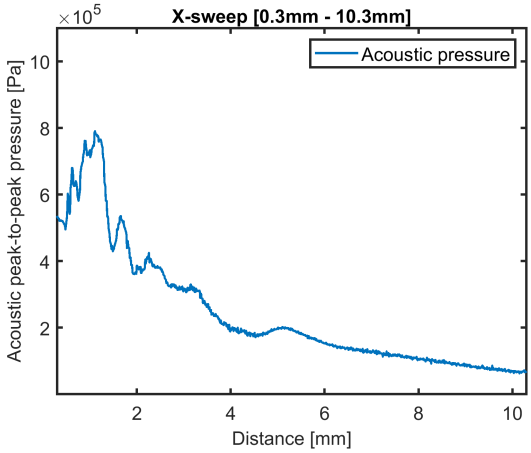

(b) The x-sweep plot from 0.3 mm to 10.3 mm from the surface.

Figure 7.9: The frequency and x-sweep plots.

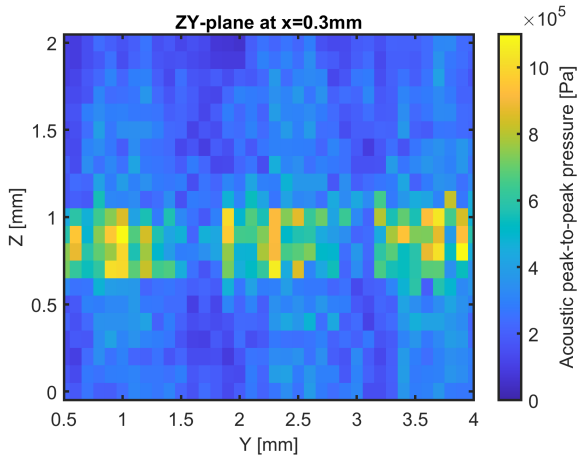

(a) The acoustic profile at a distance of 0.3 mm.

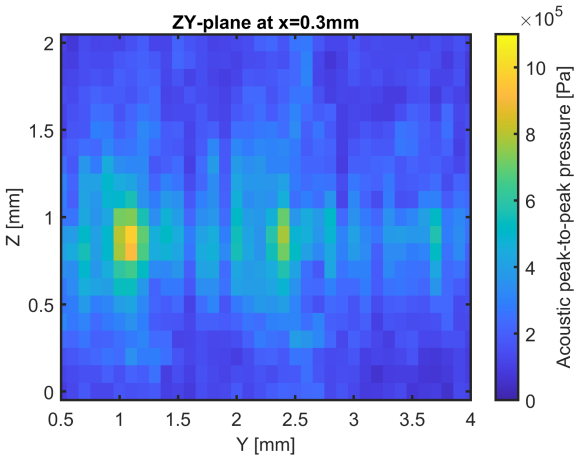

(b) The acoustic profile at a distance of 1 mm.

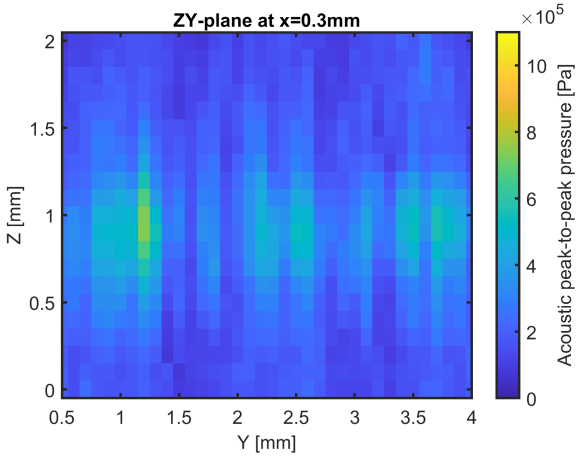

(c) The acoustic profile at a distance of 2 mm.

Figure 7.10: The acoustic profiles for different distances.

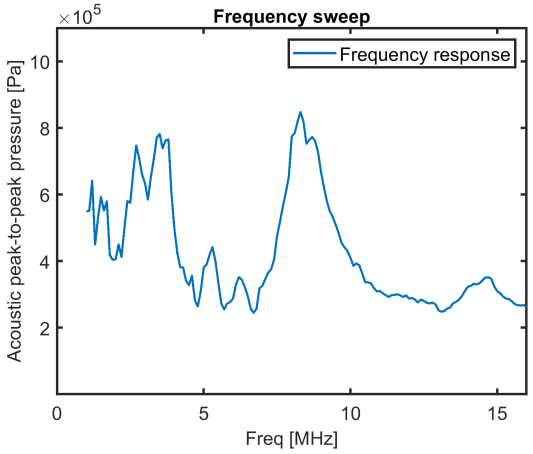

(a) The frequency response of a 8 MHz transducer.

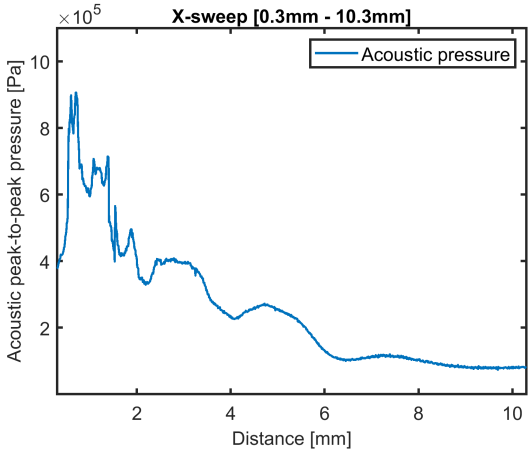

(b) The x-sweep plot from 0.3 mm to 10.3 mm from the surface.

Figure 7.11: The frequency and x-sweep plots.

Several times during measurements, (part of) the PZT-based US transducers failed. A vulnerability was the wire attachment as the wires break easily during the placement of the implants in the holder for measurements. Therefore, during some measurements, only two transducers are visible, as the third transducer is broken (the 2nd and 3rd measurement in Appendix F) This has been improved by using

both silver conductive paste and conductive epoxy and individual wiring of each transducer.

Another issue that existed was the water inlet. Although the whole device is coated with parylene-C, still the devices degraded over time (therefore, not all the measurements shown in Appendix F have a clear focal spot or US profile). This might be caused due to mechanical detachment of the ACF or the PZT overtime during the vibrations. Another reason might be the brittleness of parylene-C. The microcracks can cause water inlet leading to corrosion of the Aluminum metal layer. It is also possible that the parylene-C is damaged when the device is put in the holder.

During the 6th and 7th measurements, only a few measurements were possible as the device failed afterward (Appendix F). A possible reason might be that since the PZTs are placed semi-automatic some variation exists, the PZT with ACF does not totally seal the airbacking well. The micro-cavities are not sealed by parylene-C afterward and might lead to a water inlet. This water inlet decreases the performance of the transducers causing a low pressure output.

The sample of the 1st measurement has been hung in the water tank for 5 days after the measurements were taken as shown in Figure 7.8 and Figure 7.9. After these 5 days, another frequency measurement was taken. The result is shown in Figure 7.12. The pressure output is decreased from 800 kPa to 200 kPa. This indicates that water leakage affects performance and the parylene-C is not encapsulating the whole device in case of airbacking.

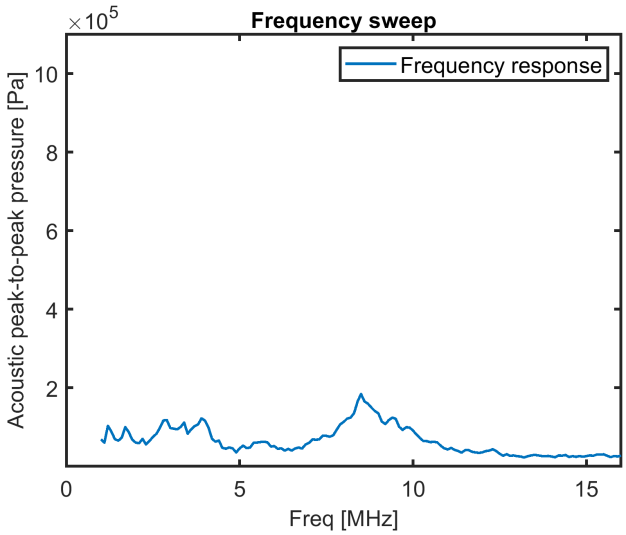

Figure 7.12: The frequency sweep after 5 days in the water tank.

Due to issues with wire breakage, no curved measurements could be done with the devices of the first three planar measurements. After using the silver conductive paste and the conductive epoxy, the device was partly preserved as can be seen from the results of the fourth measurement (Appendix F). Improving the wire attachment with individual wiring, gave successfully bent devices.

In Figure 7.10 and Figure 7.11 the planar measurements for the device of the sixth measurement are shown. These have similar features as discussed before, except for the distortion of the acoustic profile, since now the wires are attached in the width direction and not in the length direction.

After the planar measurement, the device is curved as shown in Figure 7.14a. In this configuration, the measurements shown in Figure F.13 are obtained. It can be seen that the pressures are higher than for a single device in the planar configuration. For the near field, the pressure is doubled while for the focal spot, the pressure is increased by 45% (Figure 7.14).

The focal spot is not exactly in the middle of the curved device. This is due to the non-perfect curvature of the device itself and the small angle it has in the holder. The focal spot is around 200 x 200 μm

which is slightly larger than in the simulations. The S_{tx} is 160 kPa/V.

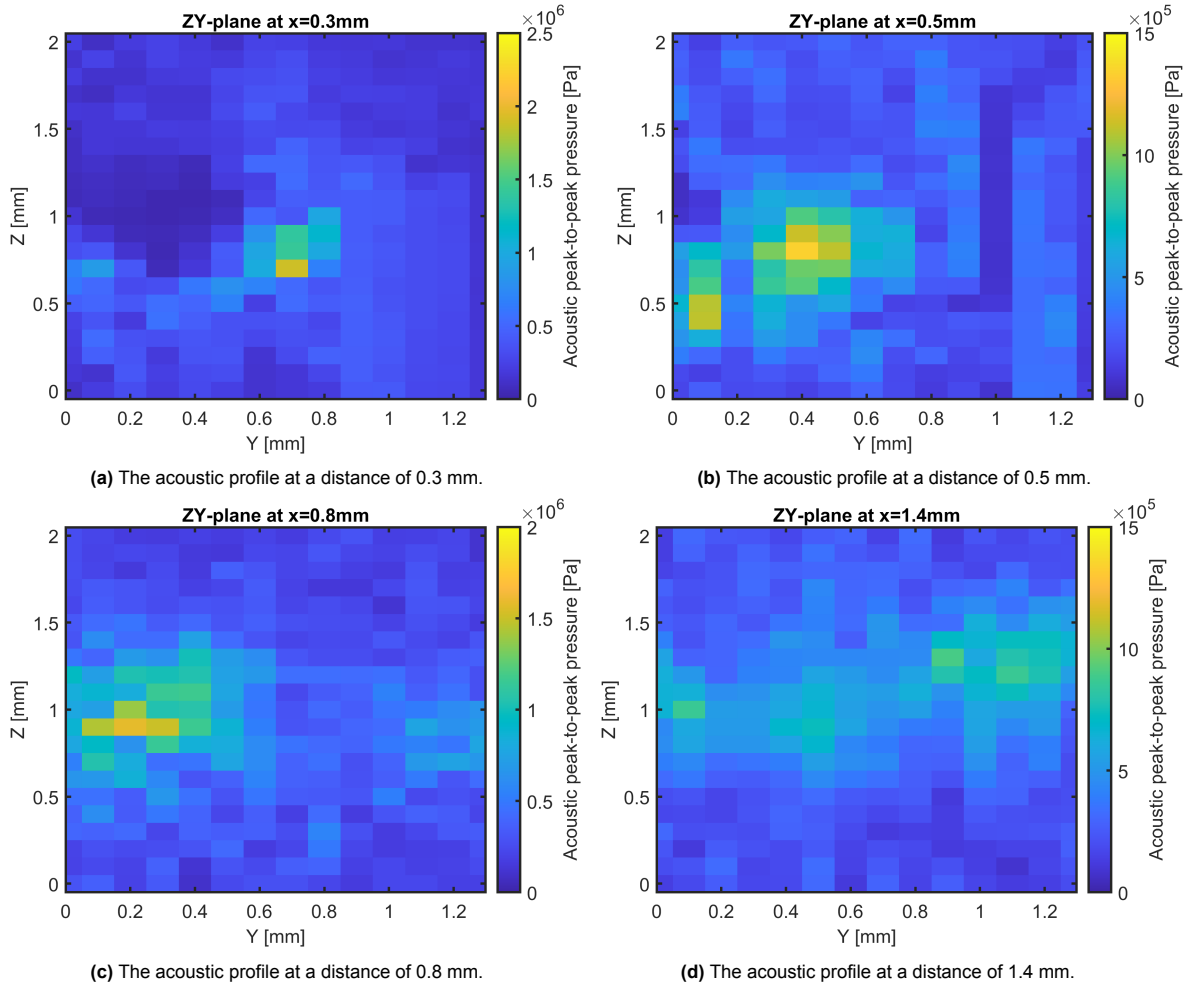

(a) The acoustic profile at a distance of 0.3 mm.

(b) The acoustic profile at a distance of 0.5 mm.

(c) The acoustic profile at a distance of 0.8 mm.

(d) The acoustic profile at a distance of 1.4 mm.

Figure 7.13: The acoustic profiles for different distances.

This measurement shows the proof-of-concept that it is possible to integrate PZT-based US transducers in a cuff-shaped implant. This curvature has a positive effect on the output pressure due to constructive interference as the overall pressure is increased compared to the acoustic pressure of an individual device in the planar configuration. The pressure magnitude between the planar and curved measurement is compared in Figure 7.14. The crosses indicate the peak pressures of the actual measurements. The striped line is an interpolation. In the planar configuration, only three measurements are done: one in the near field, one in the focal spot, and one in the far field. Therefore, the drop in between the near-field and the focal spot, which is normally part of the focal profile is not visible.

Comparing the airbacking and non-airbacking devices, no difference can be observed from the measurements. This might be explained by the scenario in which the ACF, which is 25 μm thick fills the 20 μm deep airbacking wells. In that case, the airbacking effect is removed or even neglected.

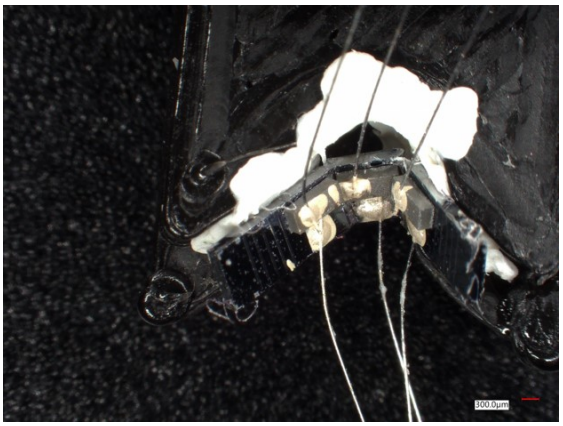

(a) The curved 8 MHz device.

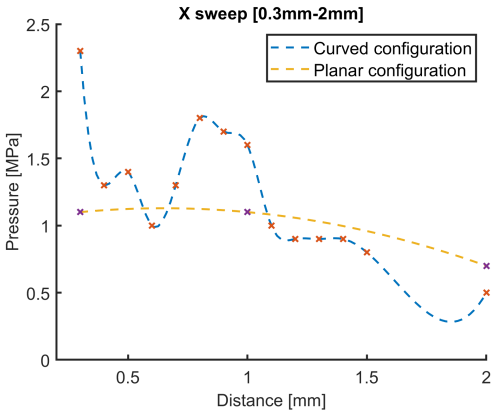

(b) The acoustic peak pressures of the curved and planar measurements compared.

Figure 7.14: The curved device and output pressures are compared.

8

Recommandations

The main challenge during the thesis project was the wafer-level microfabrication process flow. Although the process flow consisted mainly of standard wafer-level microfabrication techniques, the machinery needed for it, was prone to damage and errors.
Moreover, after dicing the PZT, wire attachment and coating needed to be done. Since the devices are only 7x1 mm large and the PZTs are even sub-mm sizes, it was difficult to perform the final microfabrication steps. Since it was partly a manual process it is recommended to add a handling frame to the design next time. A handling frame makes the device itself larger during the manual processes and it can be detached after the final processing step.

Improving the manual steps is also recommended since it is difficult to prepare a device and it is prone to variations. However, this is part of the future work and is thus described in Chapter 9. For the design, a curved diameter of 2 mm has been used throughout this project. The 2 mm has been chosen since this is the size of the VN at the site of stimulation and other research used this size as well, which makes it more reliable to compare the research (Chapter 5). The next time it is recommended to make the cuff diameter 50% larger. Literature shows that tissue trauma is reduced by increasing the cuff diameter by 50% [30], [31]. As the microfabrication process flow is scalable this will not be an issue for the process itself.

The differences between the pressure profile in the simulations and the measured profiles could be assigned to the simplifications and idealities in the simulation model. In the simulation, only the PZT, an airbacking well, and a perfectly cylindrical parylene-C ring are taken into account. In reality, fabrication non-idealities, island-bridge instead of pure parylene-C, manual variations during PZT placement, and the attachment of the tungsten wire degrade the PZT-based US transducer performance leading to a different pressure profile. Moreover, the distortion of the focal spot might result from the non-perfect curvature and PZT placement variations. Due to small misalignments and tilting of the sample in the watertank during measurements in the planar configuration, there is a difference between the measured acoustic pressures among the PZT-based US transducers. This could be improved by increasing the level of detail in the simulation model and researching what the impact will be on the accuracy of the simulation outcomes. Moreover, the measurement setup could be extended by a correction device for tilting. In addition, a technique for equal compression of the PZT-based US transducers could be designed.

The island-bridge structure with silicon islands and parylene-C interconnects gives flexibility and the ability of the device to have a curvature of 2 mm in diameter. However, as parylene-C is brittle by nature, it is still a vulnerability and the device should be handled with care. The robustness could be improved by increasing the layer thickness or creating a multilayer on top which protects the underlying parylene-C layer. However, this might affect the acoustic performance as the attenuation could increase, depending on the layer thickness, material properties, and the driving frequency. A biocompatible, transparent and cuff-implant-suitable alternative is Polydimethylsiloxane (PDMS) [84]. Research shows that this material can be used in combination with parylene-C as an encapsulation layer [95], [96].

For the metal layer, AlSi (99%/1%) is used. However, during measurements, device failure occurs. This is likely due to the non-optimized adhesion between the parylene-C and the metal tracks and the high water vapor transmission rate (WVTR) of parylene-C [97]. In that case, a multilayer encapsulation might increase the robustness. A multilayer encapsulation could be used for acoustic matching as well. Post-treatment of the metal layer could improve the robustness as well [98].

9 Future work

In this thesis project, a microfabricated prototype, cuff implant design, in which PZT-based US transducers are embedded, has been developed. In this chapter future work will be pointed out in order to optimize the design and extend functions. For some of the topics, some pre-research has been done during the thesis. These results are included in the subsequent sections.

9.1. Wirebonding

As explained in Chapter 6 during this thesis the manual wire attachment technique has been chosen, due to its speed and low costs. As described in that section (Chapter 6), this part can be optimized by investigating the use of a wire bonder machine. Although the US used for wirebonding can interfere with the PZT-based US transducers and can thus lead to failure of the wirebond, wirebonding can be used for PZT according to the literature. A way to avoid the interference of US is by fixing the PZT (e.g. can be done manually by tweezers) to change its resonance frequency, so it will not vibrate and the wirebonding can succeed. Within this topic, it is important to research the optimal wirebonding parameters, like heat, time and pressure, the choice between ball and wedge bonding and the optimal wire material (gold, aluminum, tungsten, etc.)

9.2. Top connection

As an alternative for the wire as the top connection, an evaporated metal layer can be used. However, implementing this option will change the process flow accordingly. Instead of steps 11 and 12 mentioned in Chapter 6, the steps provided in Figure 9.1 should be taken. It is important that during these steps, the contact pads are covered with a layer that can be removed at the end (e.g. tape).
After dicing, the individual devices should be coated with a parylene-C layer, as the metal top layer is only allowed to make connections between the top sides of the PZTs. Otherwise, the metal will short the PZTs. In step 12, the parylene-C from the top sides of the PZTs should be removed. This can be done by chemical etching or laser hatching [75], [79], [80], [82].

In the case of chemical etching, the backside should not contain parylene-C due to contamination. Therefore, during parylene-C coating, the device should be covered at the backside. It could be placed on a glass plate. For chemical etching, a mask should be added. This can be done using a soft photoresist mask (AZ9260 or AZ4620) or a hard mask (titanium). The photoresist mask is faster to include in the process flow, but it is limited by the maximal coating thickness. Moreover, the photoresist will be etched at the same pace as the parylene-C. The hard mask is more difficult to implement in the process, since for this step also a patterning step is needed. However, the metal mask does not need to be thick, as the etching process is more selective towards parylene-C. A hard mask of titanium is etched 40 times slower than parylene-C.
Laser hatching can be used to remove the parylene-C on a metal layer. Some experiments have been done using the OPTEC laser cutter. The spot size of the laser beam is 20 μm and the parameters that need to be tuned are the speed [mm/s], diode current [A], repetitions, and pitch [mm]. The laser cutter does not have rotational compensation. A way to compensate for rotational errors is to rotate

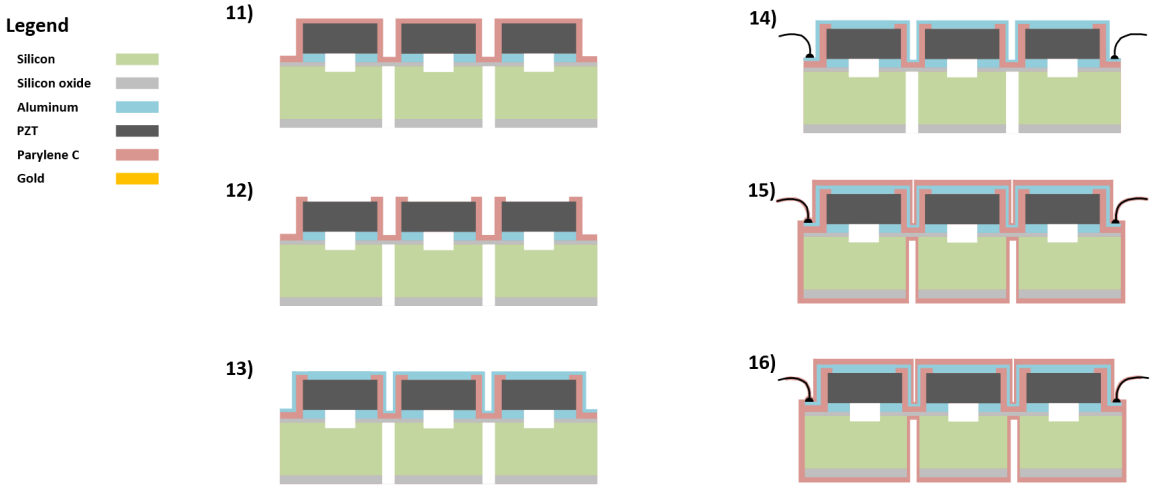

Figure 9.1: The microfabrication process steps for an evaporated metal layer.

the design in AutoCAD according to the offset angle. This offset angle can be obtained by measuring 2 points along a line, using the OPTEC laser cutter, which should be straight. The angle can then be obtained using the formula:

$$sin^{-1}(\frac{\delta y}{\delta x}) \tag{9.1}$$

were δy and δx are the difference between the x1 and x2 and y1 and y2 respectively. The angle should be negatively inserted in the AutoCAD software to compensate. In addition, the movement of the laser gains a bit of offset during the laser cutting. This means that laser cutting small structures at regular intervals cannot be done precisely. Besides, the parameters that are found during an experiment and applied another day can have a different result, as the laser beam has a bit of drift regarding intensity for the same parameters. The best results were obtained with a 2-step hatch approach. In the first hatch step, the velocity is 10 mm/s, the diode current is 2.3 A and the hatch pitch is 0.01 mm. For the second hatch step, the velocity is 20 mm/s, the diode current is 2.3 A and the hatch pitch is 0.005 mm. In Figure 9.2a the left part of the figure shows the result after both hatch steps, while the right side shows the result after the first hatch step. After scratching the surface it became visible that not all the parylene-C is removed by this approach (Figure 9.2b). Therefore, future work could be done on improving these parameters.

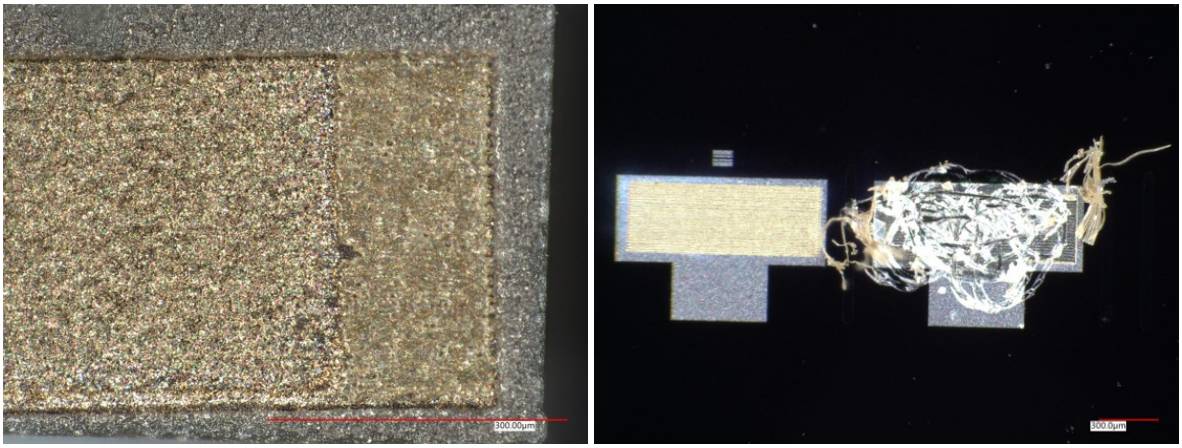

(a) The result after the 2-step hatch.

(b) The remaining parylene-C residue.

Figure 9.2: The laser hatching results.

After the parylene-C is removed, the elements can be put inside the CHA solution metal evaporator. For this, a holder should be designed. The evaporation consists of a seed layer and the actual metal

layer. Multiple combinations are possible. The adhesion between parylene-C and metal is poor, but a combination of titanium as the seed layer and gold as the metal layer gives the best results [83].

After the metal evaporation, a wire should be attached to the top layer for measurement purposes (this can be done by either wirebonding or manual attachment) and again coated with parylene-C to protect it against water inlet and corrosion. After the second parylene-C coating, the tips of the wire-bonded wires should be cleaned from the parylene-C and the cover on the contact pads should be removed. The contact pads can then be wirebonded or another connection method can be thought of. After this connection, the device should be parylene-C coated for the third and final time.

9.3. Matching layer

According to theory, acoustic pressure transfer can be enhanced when the transducer is matched to the medium (Req. C-1). The output magnitudes will be higher, the bandwidth will be increased and fewer reflections of the signal at the interfaces do exist (Chapter 3). For this purpose, matching layers can be used. Based on the research of [99]–[101] these matching layers can be implemented using the mass-spring concept. This means that interchanging layers of metal (mass) and polymers (spring) can match the PZT to a water medium. For this concept, the one-dimensional wave model has been used to calculate the thickness of the needed layers. In the case of the prototype explained in this thesis, the Nickel layer on the PZT could be neglected as it is only 100 nm (according to Piezo.com). In addition, the evaporated metal top connection (explained in section 9.2) can be neglected as it will be only a few tens of nanometers thick as well. In addition, the matching layer stack should have parylene-C as the final material, as this is the encapsulation layer of the whole device. This leads to the model shown in Figure 9.3.

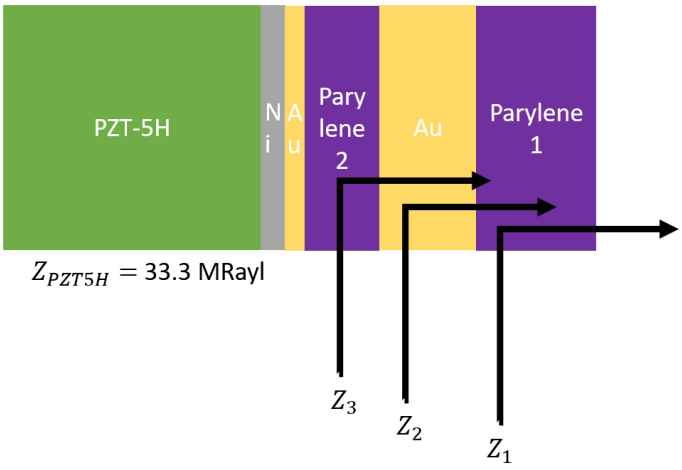

Figure 9.3: The matching layer model.

Using the one-dimensional wave model, the microwave transmission line equations can be used for obtaining the equivalent input characteristic acoustic impedance per layer:

$$Z_1 = Z_{parylene1}\frac{Z_{water} + j * Z_{parylene1} * tan(\frac{\omega}{v_{s\_parylene} * t_{parylene1}})}{Z_{parylene1} + j * Z_{water} * tan(\frac{\omega}{v_{s\_au} * t_{parylene1}})} \tag{9.2}$$

$$Z_2 = Z_{Au}\frac{Z_1 + j * Z_{Au} * tan(\frac{\omega}{v_{s\_Au} * t_{Au}})}{Z_{Au} + j * Z_1 * tan(\frac{\omega}{v_{s\_Au} * t_{Au}})} \tag{9.3}$$

$$Z_3 = Z_{parylene2}\frac{Z_2 + j * Z_{parylene2} * tan(\frac{\omega}{v_{s\_Ni} * t_{parylene1}})}{Z_{parylene2} + j * Z_2 * tan(\frac{\omega}{v_{s\_Ni} * t_{parylene2}})} \tag{9.4}$$

To match the layers, a Loci of the transducers on a Smith chart can be plotted. This is done in Figure 9.4. A script has been written to optimize the matching in such a way that it is acoustically matched, but that

the layer thicknesses are realistic. In this script also the impact of variation of layer thicknesses during processing is included, as this is something to be aware of. Based on this optimization the following

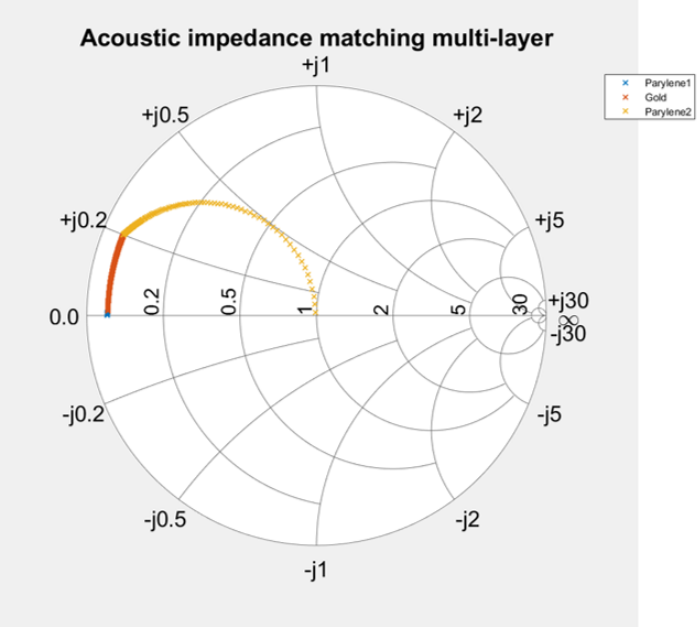

Figure 9.4: Impedance matching shown in the imaginary field.

layer thicknesses were obtained:

- $parylene1 = 5\ \mu m$
- $Au = 3.1\ \mu m$
- $parylene2 = 0.129\ \mu m$

The gold layer should become relatively thick, but it is possible to process such a layer with microfabrication techniques either evaporation or sputtering.

9.4. Beamstearing and a focussed cuff implant

In this project, beamsteering has not been taken into account due to the complexity of the process. However, each individual transducer in the current design could be diced with the right kerf to get the capability of beamsteering. In addition, the routing should be adapted. Implementing beamsteering activates the property of steering the beam wherever you want in the nerve (Chapter 3).

To increase the focal pressure and to stimulate at multiple spots simultaneously, the light reflection technique (used in fiber optic cables) could be researched (1 in Figure 9.5). The implant could have two reflector sides with angled PZTs generating US beams crossing each other at stimulation spots. Both the feasibility and the losses of US reflection should be researched.

To increase the focal pressure even more a special 3D shape could be microfabricated (2 and 3 in Figure 9.5). In that way, more than four PZT-based US transducers could be used to stimulate a certain spot whereas opposing PZT-based US transducers are avoided. The PZT-based US transducers could be placed at the top (2 in Figure 9.5), on either side, or at the bottom of the nerve. Moreover, the PZT-based US transducers could be placed around the nerve, but at an angle with respect to the nerve (3 in Figure 9.5).

9.5. Implantation

Another thing that could be researched further is creating a design that is optimal for implantation. In this thesis, it was out of scope how the design should be implanted in the end. Therefore, during design,

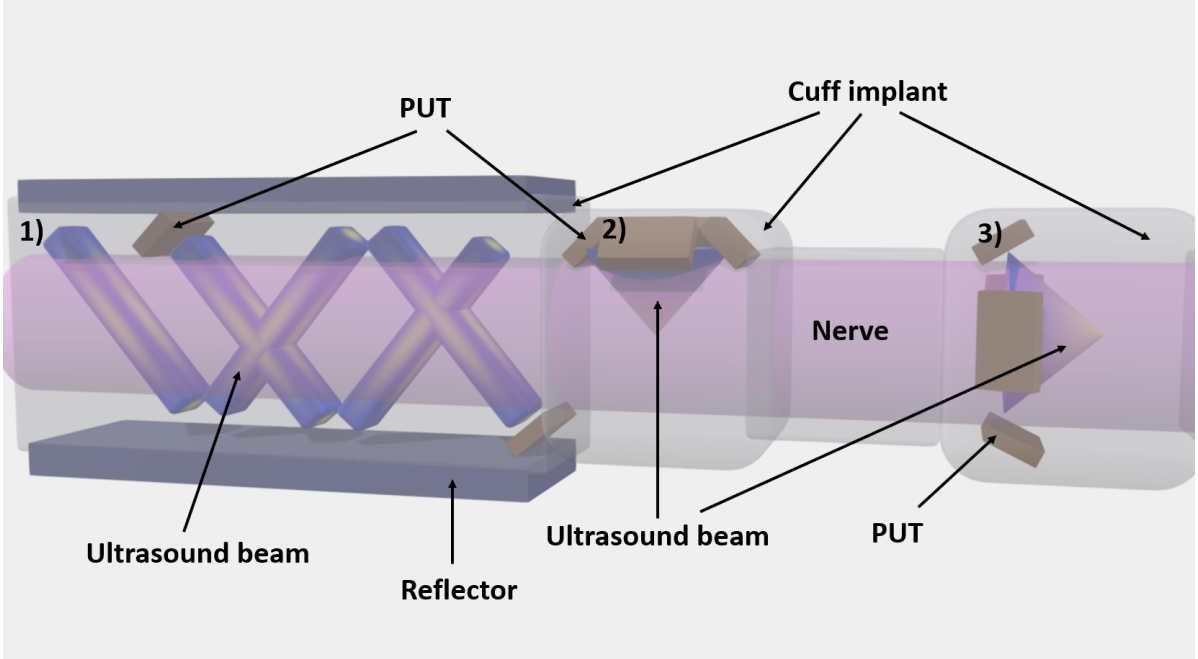

Figure 9.5: The concept of a focussed cuff implant where 1) shows the beam reflection technique. 2) and 3) show a 3D focussed cuff implant with a top orientation (2) and a ring orientation (3).

it has not been taken into account. However, in the case of the next steps for research, like implantation in animals, it is worth investigating how the design can be adapted in such a way the implantation is done in an easy way.

9.6. Materials

Another thing to investigate is the use of shape-memory alloys (SMA) in the process (Req. C-2). The special SMA that is thought of is Nitinol [88], currently being used in vascular treatment. However, it could be used to shape the implant after implantation in a predefined way. This will reduce the variations which normally occur during the implantation of implants. Fewer variations in curvature and attachment to the nerve mean that the focal spot and pressure can be better predefined and will lead to more reliable neuromodulation.

In Chapter 3 the usage of metamaterials has been briefly discussed. In this thesis, the usage of these materials has not been explored, but according to the literature, they show useful and outstanding characteristics. Therefore, it will be worth investigating the use of these materials in the design to solve issues that arose during this thesis.

9.7. PMN-PT

Finally, in this thesis project, PZT-5H sheets have been used, as these are the most reliable, off-the-shelf, bulk PZT-based US transducers and are not too expensive. To improve the focal pressure, the literature shows that PMN-PT has better characteristics in generating US (Chapter 3). Although PMN-PT is more expensive and brittle than PZT-5H, it is worth investigating this option as a replacement for PZT-5H in order to obtain higher focal pressures.

10

Conclusion

This thesis proposes a 1 mm by 7 mm wafer-level microfabricated, island-bridge cuff implant with an inner diameter of 2 mm. COMSOL Multiphysics simulations have been performed to investigate the effect of the number of PZT-based US transducers, simulate the impact of airbacking, and verify the design. The wafer-level microfabrication and assembly consist of standardized and scalable process steps.

Although multiple designs have been developed, an 8.4 MHz device has been successfully tested in both planar and curved configurations. Three commercial PZT-5H PZTs are integrated and it has a focal length of 1 mm. This device generates 0.9 MPa on average at the focal spot of each individual PZT-based US transducer in a planar configuration (S_{tx} = 110 kPa/V) whereas, 1.6 MPa is generated at the focal spot in curved configuration (S_{tx} = 160 kPa/V). The focal spot of the curved device is 200 μm by 200 μm which is slightly larger than in the simulations.

The measurements show the potential of a cuff-shape design with a PZT-based US transducer array as the output focal pressure is increased by at least 45% (taking the peak pressures at the focal spot for both the planar (1.1 MPa) and curved (1.6 MPa) configuration) compared to the measured focal pressures of the single devices in the planar configuration. Moreover, comparing this focal pressure of the curved configuration with research regarding the integration of cMUT technology into a cuff-implant or other PZT-based designs, this device can generate more output pressure.
In conclusion, the integration of PZT-based US transducers in a cuff-shaped design is a promising technique for cranial nerve stimulation and opens a new path for developing an implant for VNS.

References

[1] R. Vadlapatla, E. Y. Wong, and S. G. Gayakwad, "Electronic drug delivery systems: An overview," *Journal of Drug Delivery Science and Technology*, vol. 41, pp. 359–366, 2017, ISSN: 1773-2247. DOI: 10.1016/j.jddst.2017.08.008.

[2] S. Najarian, M. Fallahnezhad, and E. Afshari, "Advances in medical robotic systems with specific applications in surgery—a review," *Journal of Medical Engineering & Technology*, vol. 35, no. 1, pp. 19–33, 2011, ISSN: 0309-1902. DOI: 10.3109/03091902.2010.535593.

[3] Q. Wu, J. Liu, X. Wang, *et al.*, "Organ-on-a-chip: Recent breakthroughs and future prospects," *BioMedical Engineering OnLine*, vol. 19, no. 1, 2020, ISSN: 1475-925X. DOI: 10.1186/s12938-020-0752-0.

[4] J. Blackmore, S. Shrivastava, J. Sallet, C. R. Butler, and R. O. Cleveland, "Ultrasound neuromodulation: A review of results, mechanisms and safety," *Ultrasound in Medicine & Biology*, vol. 45, no. 7, pp. 1509–1536, 2019, ISSN: 0301-5629. DOI: 10.1016/j.ultrasmedbio.2018.12.015.

[5] C. O. Oluigbo and A. R. Rezai, "Addressing neurological disorders with neuromodulation," *IEEE Transactions on Biomedical Engineering*, vol. 58, no. 7, pp. 1907–1917, 2011. DOI: 10.1109/TBME.2010.2102758.

[6] H. A. S. Kamimura, A. Conti, N. Toschi, and E. E. Konofagou, "Ultrasound neuromodulation: Mechanisms and the potential of multimodal stimulation for neuronal function assessment," *Front Phys*, vol. 8, 2020, ISSN: 2296-424X (Print) 2296-424x. DOI: 10.3389/fphy.2020.00150.

[7] M. E. Downs, S. A. Lee, G. Yang, S. Kim, Q. Wang, and E. E. Konofagou, "Non-invasive peripheral nerve stimulation via focused ultrasound less or greater in vivo less or greater," *Physics in Medicine and Biology*, vol. 63, no. 3, p. 035 011, Jan. 2018. DOI: 10.1088/1361-6560/aa9fc2.

[8] M. G. Kim, H. A. S. Kamimura, S. A. Lee, C. Aurup, N. Kwon, and E. E. Konofagou, "Image-guided focused ultrasound modulates electrically evoked motor neuronal activity in the mouse peripheral nervous system in vivo," *Journal of Neural Engineering*, vol. 17, no. 2, p. 026 026, 2020, ISSN: 1741-2552. DOI: 10.1088/1741-2552/ab6be6.

[9] V. Cotero, H. Miwa, J. Graf, *et al.*, "Peripheral focused ultrasound neuromodulation (pfus)," *Journal of Neuroscience Methods*, vol. 341, p. 108 721, 2020, ISSN: 0165-0270. DOI: 10.1016/j.jneumeth.2020.108721.

[10] S. Kawasaki, V. Giagka, M. De Haas, *et al.*, "Pressure measurement of geometrically curved ultrasound transducer array for spatially specific stimulation of the vagus nerve," in *2019 9th International IEEE EMBS Conference on Neural Engineering (NER)*, IEEE. DOI: 10.1109/ner.2019.8717064.

[11] D. A. Groves and V. J. Brown, "Vagal nerve stimulation: A review of its applications and potential mechanisms that mediate its clinical effects," *Neuroscience & Biobehavioral Reviews*, vol. 29, no. 3, pp. 493–500, 2005, ISSN: 0149-7634. DOI: 10.1016/j.neubiorev.2005.01.004.

[12] H. Yuan and S. D. Silberstein, "Vagus nerve and vagus nerve stimulation, a comprehensive review: Part i," *Headache: The Journal of Head and Face Pain*, vol. 56, no. 1, pp. 71–78, 2016, ISSN: 0017-8748. DOI: 10.1111/head.12647.

[13] N. Jayaprakash, W. Song, V. Toth, *et al.*, "Organ- and function-specific anatomical organization of vagal fibers supports fascicular vagus nerve stimulation," *Brain Stimulation*, vol. 16, no. 2, pp. 484–506, 2023, ISSN: 1935-861X. DOI: 10.1016/j.brs.2023.02.003.

[14] M. Settell, B. Knudsen, A. Dingle, *et al.*, *Functional vagotopy in the cervical vagus nerve of the domestic pig: Implications for vagus nerve stimulation*, Nov. 2019. DOI: 10.1101/856989.

[15] H. Yuan and S. D. Silberstein, "Vagus nerve and vagus nerve stimulation, a comprehensive review: Part ii," *Headache: The Journal of Head and Face Pain*, vol. 56, no. 2, pp. 259–266, 2016, ISSN: 0017-8748. DOI: 10.1111/head.12650.

[16] R. L. Johnson and C. G. Wilson, “A review of vagus nerve stimulation as a therapeutic intervention,” *Journal of Inflammation Research*, vol. Volume 11, pp. 203–213, 2018, ISSN: 1178-7031. DOI: 10.2147/jir.s163248.

[17] M. Panebianco, A. Rigby, and A. Marson, “Vagus nerve stimulation for focal seizures,” *Cochrane Database of Systematic Reviews*, vol. 2022, Jul. 2022. DOI: 10.1002/14651858.cd002896.pub3.

[18] J.-H. Lee, I.-J. Cho, K. Ko, E.-S. Yoon, H.-H. Park, and T. S. Kim, “Flexible piezoelectric micromachined ultrasonic transducer (pmut) for application in brain stimulation,” *Microsystem Technologies*, vol. 23, no. 7, pp. 2321–2328, 2017, ISSN: 0946-7076. DOI: 10.1007/s00542-016-2912-5.

[19] R. H. Howland, “Vagus nerve stimulation,” *Current Behavioral Neuroscience Reports*, vol. 1, no. 2, pp. 64–73, 2014, ISSN: 2196-2979. DOI: 10.1007/s40473-014-0010-5.

[20] E. W. Dirr, Y. A. Patel, L. Lester, F. Delgado, and K. J. Otto, “Targeted vagus nerve stimulation does not disrupt cardiac function in the diabetic rat,” 2019. DOI: 10.1109/embc.2019.8857474.

[21] E. J. Juan, R. González, G. Albors, M. P. Ward, and P. Irazoqui, “Vagus nerve modulation using focused pulsed ultrasound: Potential applications and preliminary observations in a rat,” *International Journal of Imaging Systems and Technology*, vol. 24, no. 1, pp. 67–71, 2014, ISSN: 0899-9457. DOI: 10.1002/ima.22080.

[22] V. Colucci, G. Strichartz, F. Jolesz, N. Vykhodtseva, and K. Hynynen, “Focused ultrasound effects on nerve action potential in vitro,” *Ultrasound in medicine & biology*, vol. 35, no. 10, pp. 1737–47, 2009, ISSN: 1879-291X (Electronic) 0301-5629 (Print) 0301-5629 (Linking). DOI: 10.1016/j.ultrasmedbio.2009.05.002.

[23] J. L. Foley, J. W. Little, and S. Vaezy, “Effects of high-intensity focused ultrasound on nerve conduction,” *Muscle & nerve*, vol. 37, no. 2, pp. 241–50, 2008, ISSN: 0148-639X (Print) 0148-639X (Linking). DOI: 10.1002/mus.20932.

[24] W. D. O’Brien, “Ultrasound–biophysics mechanisms,” *Progress in Biophysics and Molecular Biology*, vol. 93, no. 1, pp. 212–255, 2007, ISSN: 0079-6107. DOI: 10.1016/j.pbiomolbio.2006.07.010.

[25] T. Costa, C. Shi, K. Tien, J. Elloian, F. A. Cardoso, and K. L. Shepard, “An integrated 2d ultrasound phased array transmitter in cmos with pixel pitch-matched beamforming,” *IEEE Transactions on Biomedical Circuits and Systems*, vol. 15, no. 4, pp. 731–742, 2021. DOI: 10.1109/TBCAS.2021.3096722.

[26] K. H. Elaine N. Marieb, *Human Anatomy & Physiology*. Harlow: Pearson, 2019.

[27] Vasiliki Giagka, *Subthreshold membrane phenomena*, Lecture2_SubthresholdMembrane Phenomena_2022.pdf, Feb. 2022.

[28] T. Q. B. Institute, *Axons: The cable transmission of neurons*, Last accessed 14 December 2022. [Online]. Available: https://qbi.uq.edu.au/brain/brain-anatomy/axons-cable-transmission-neurons.

[29] B. Scheid and S. Chakrabartty, “Feasibility of hybrid ultrasound-electrical nerve stimulation for electroceuticals,” in *2017 IEEE International Symposium on Circuits and Systems (ISCAS)*, pp. 1–4, ISBN: 2379-447X. DOI: 10.1109/ISCAS.2017.8050555.

[30] W. Xiong, H. Yu, and Z. H. Li, “Design and simulation of a parylene-based three-dimensional cuff electrode for peripheral nerve stimulation,” *Key Engineering Materials*, vol. 609-610, pp. 1459–1463, 2014.

[31] L. C. Robinson and K. R. Winston, “Relationship of vocal cord paralysis to the coil diameter of vagus nerve stimulator leads,” *Journal of Neurosurgery JNS*, vol. 122, no. 3, pp. 532–535, 2015. DOI: 10.3171/2014.10.JNS14640.

[32] K. B. Kim, D. K. Hsu, B. Ahn, Y. G. Kim, and D. J. Barnard, “Fabrication and comparison of pmn-pt single crystal, pzt and pzt-based 1-3 composite ultrasonic transducers for nde applications,” *Ultrasonics*, vol. 50, no. 8, pp. 790–797, 2010, ISSN: 0041-624X. DOI: 10.1016/j.ultras.2010.04.001.

[33] F. J. Rodriguez, D. Ceballos, M. Schuttler, *et al.*, "Polyimide cuff electrodes for peripheral nerve stimulation," *Journal of Neuroscience Methods*, vol. 98, no. 2, pp. 105–118, 2000, ISSN: 0165-0270. DOI: 10.1016/s0165-0270(00)00192-8.

[34] B. H. Bonham and L. M. Litvak, "Current focusing and steering: Modeling, physiology, and psychophysics," *Hearing Research*, vol. 242, no. 1, pp. 141–153, 2008, ISSN: 0378-5955. DOI: 10.1016/j.heares.2008.03.006.

[35] M. Gierthmuehlen and D. T. T. Plachta, "Effect of selective vagal nerve stimulation on blood pressure, heart rate and respiratory rate in rats under metoprolol medication," *Hypertension Research*, vol. 39, no. 2, pp. 79–87, 2016, ISSN: 0916-9636. DOI: 10.1038/hr.2015.122.

[36] R. B. Budde, M. T. Williams, and P. P. Irazoqui, "Temporal interference current stimulation in peripheral nerves," 2022. DOI: 10.1101/2022.07.20.500811.

[37] K. A. Yildiz, A. Y. Shin, and K. R. Kaufman, "Interfaces with the peripheral nervous system for the control of a neuroprosthetic limb: A review," *Journal of NeuroEngineering and Rehabilitation*, vol. 17, no. 1, 2020, ISSN: 1743-0003. DOI: 10.1186/s12984-020-00667-5.

[38] W. Jensen, S. Micera, X. Navarro, *et al.*, "Transverse intrafascicular multichannel electrode (time) system for treatment of phantom limb pain in amputees," 2010.

[39] Z. Xiang, S. C. Yen, S. Sheshadri, *et al.*, "Progress of flexible electronics in neural interfacing - a self-adaptive non-invasive neural ribbon electrode for small nerves recording," *Adv Mater*, vol. 28, no. 22, pp. 4472–9, 2016, ISSN: 0935-9648. DOI: 10.1002/adma.201503423.

[40] S. Lee, S.-C. Yen, S. Sheshadri, *et al.*, "Flexible epineural strip electrode for recording in fine nerves," *IEEE Transactions on Biomedical Engineering*, vol. 63, no. 3, pp. 581–587, 2016, ISSN: 0018-9294. DOI: 10.1109/tbme.2015.2466442.

[41] Y. J. Ma, Y. C. Zhang, S. S. Cai, *et al.*, "Flexible hybrid electronics for digital healthcare," *Advanced Materials*, vol. 32, no. 15, 2020, ISSN: 0935-9648. DOI: 10.1002/adma.201902062.

[42] S. H. Lee, J. H. Jung, Y. M. Chae, J. Y. Kang, and Ieee, "Fabrication and characteristics of the implantable and flexible nerve cuff electrode for neural interfaces," in *4th International IEEE/EMBS Conference on Neural Engineering*, ser. International IEEE EMBS Conference on Neural Engineering, 2009, pp. 80–+, ISBN: 978-1-4244-2072-8. DOI: 10.1109/ner.2009.5109239.

[43] K.-I. Song, S. E. Park, S. Lee, H. Kim, S. H. Lee, and I. Youn, "Compact optical nerve cuff electrode for simultaneous neural activity monitoring and optogenetic stimulation of peripheral nerves," *Scientific Reports*, vol. 8, no. 1, 2018, ISSN: 2045-2322. DOI: 10.1038/s41598-018-33695-2.

[44] M. Haugland, "A flexible method for fabrication of nerve cuff electrodes," in *18th Annual International Conference of IEEE Engineering-in-Medicine-amd-Biology-Society*, ser. Proceedings of the Annual International Conference of the Ieee Engineering in Medicine and Biology Society, vol. 18, 1997, pp. 359–360, ISBN: 0-7803-3812-X.

[45] H. Yu, W. Xiong, H. Zhang, W. Wang, and Z. Li, "A parylene self-locking cuff electrode for peripheral nerve stimulation and recording," *Journal of Microelectromechanical Systems*, vol. 23, pp. 1025–1035, 2014.

[46] M. J. Freeberg, M. A. Stone, R. J. Triolo, and D. J. Tyler, "The design of and chronic tissue response to a composite nerve electrode with patterned stiffness," *Journal of Neural Engineering*, vol. 14, no. 3, p. 036 022, 2017, ISSN: 1741-2560. DOI: 10.1088/1741-2552/aa6632.

[47] E. H. Rijnbeek, N. Eleveld, and W. Olthuis, "Update on peripheral nerve electrodes for closed-loop neuroprosthetics," *Frontiers in Neuroscience*, vol. 12, 2018, ISSN: 1662-453X. DOI: 10.3389/fnins.2018.00350.

[48] M. Dali, O. Rossel, D. Andreu, *et al.*, "Model based optimal multipolar stimulation without a priori knowledge of nerve structure: Application to vagus nerve stimulation," *Journal of Neural Engineering*, vol. 15, no. 4, p. 046 018, 2018, ISSN: 1741-2560. DOI: 10.1088/1741-2552/aabeb9.

[49] A. S. Dukhin and P. J. Goetz, “Chapter 3 - fundamentals of acoustics in homogeneous liquids: Longitudinal rheology,” in *Characterization of Liquids, Nano- and Microparticulates, and Porous Bodies Using Ultrasound*, ser. Studies in Interface Science, A. S. Dukhin and P. J. Goetz, Eds., vol. 24, Elsevier, 2010, pp. 91–125. DOI: 10.1016/S1383-7303(10)23003-X.

[50] ITIS foundation, *Tissue db density*, Last accessed 16 December 2022. [Online]. Available: https://itis.swiss/virtual-population/tissue-properties/database/density/.

[51] H. S. Gougheri, A. Dangi, S.-R. Kothapalli, and M. Kiani, “A comprehensive study of ultrasound transducer characteristics in microscopic ultrasound neuromodulation,” *IEEE Transactions on Biomedical Circuits and Systems*, vol. 13, no. 5, pp. 835–847, 2019, ISSN: 1932-4545. DOI: 10.1109/tbcas.2019.2922027.

[52] S. W. Ellingson, “Electromagnetics i,” in LibreTexts, 2022, p. 283. [Online]. Available: https://phys.libretexts.org/Bookshelves/Electricity_and_Magnetism/Book%5C%3A_Electromagnetics_I_(Ellingson).

[53] V. T. Rathod, “A review of acoustic impedance matching techniques for piezoelectric sensors and transducers,” *Sensors*, vol. 20, no. 14, p. 4051, 2020, ISSN: 1424-8220. DOI: 10.3390/s20144051.

[54] F. Akasheh, T. Myers, J. Fraser, S. Bose, and A. Bandyopadhyay, “Development of piezoelectric micromachined ultrasonic transducers,” *Sensors and Actuators A: Physical*, vol. 111, pp. 275–287, Mar. 2004. DOI: 10.1016/j.sna.2003.11.022.

[55] S. school of physics, *Acoustic impedance, intensity and power*, https://www.animations.physics.unsw.edu.au/jw/sound-impedance-intensity.html.

[56] H. Liu, J. Geng, Q. Zhu, *et al.*, “Flexible ultrasonic transducer array with bulk pzt for adjuvant treatment of bone injury,” *Sensors*, vol. 20, no. 1, p. 86, 2019, ISSN: 1424-8220. DOI: 10.3390/s20010086.

[57] M. Plaksin, S. Shoham, and E. Kimmel, “Intramembrane cavitation as a predictive bio-piezoelectric mechanism for ultrasonic brain stimulation,” *Physical Review X*, vol. 4, no. 1, 2014, ISSN: 2160-3308. DOI: 10.1103/physrevx.4.011004.

[58] T. Heimburg and A. D. Jackson, “On soliton propagation in biomembranes and nerves,” *Proceedings of the National Academy of Sciences*, vol. 102, no. 28, pp. 9790–9795, 2005, ISSN: 0027-8424. DOI: 10.1073/pnas.0503823102.

[59] S.-J. Oh, J. M. Lee, H.-B. Kim, *et al.*, “Ultrasonic neuromodulation via astrocytic trpa1,” *Current Biology*, vol. 29, no. 20, 3386–3401.e8, 2019, ISSN: 0960-9822. DOI: 10.1016/j.cub.2019.08.021.

[60] A. S. Vivien Gibbs David Cole, *Ultrasound physics and technology, How, Why and When?* Edinburgh; New York: Churchill Livingstone, 2009.

[61] L. Bian, K. Zhu, Q. Wang, *et al.*, “Performance enhancement of ultrasonic transducer made of textured pnn-pzt ceramic,” *Journal of Advanced Dielectrics*, ISSN: 2010-135X. DOI: 10.1142/s2010135x22440039.

[62] K. Shen and M. M. Maharbiz, “Design of ceramic packages for ultrasonically coupled implantable medical devices,” *IEEE Transactions on Biomedical Engineering*, vol. 67, no. 8, pp. 2230–2240, 2020, ISSN: 0018-9294. DOI: 10.1109/tbme.2019.2957732.

[63] W. Kang, J. Jung, W. Lee, J. Ryu, and H. Choi, “A thickness-mode piezoelectric micromachined ultrasound transducer annular array using a pmn–pzt single crystal,” *Journal of Micromechanics and Microengineering*, vol. 28, no. 7, p. 075 015, 2018, ISSN: 0960-1317. DOI: 10.1088/1361-6439/aab9d4.

[64] Z. Wang, Q.-T. Xue, Y.-Q. Chen, *et al.*, “A flexible ultrasound transducer array with micro-machined bulk pzt,” *Sensors*, vol. 15, no. 2, pp. 2538–2547, 2015, ISSN: 1424-8220.

[65] R. K. Rob Carter, *Introduction to piezoelectric transducers*. Wildwood; Woburn: Piezo.com. [Online]. Available: https://piezo.com/pages/piezoelectric-transducers-abstract.

[66] R. K. Rob Carter, *Material properties*, https://support.piezo.com/article/62-material-properties, 2020.

[67] N. Yamamoto, Y. Yamashita, Y. Hosono, and K. Itsumi, “Electrical and physical properties of repoled pmn–pt single-crystal sliver transducer,” *Sensors and Actuators A: Physical*, vol. 200, pp. 16–20, 2013, ISSN: 0924-4247. DOI: 10.1016/j.sna.2012.10.002.

[68] D.-W. Wu, Q. Zhou, X. Geng, C.-G. Liu, F. Djuth, and K. Shung, “Very high frequency (beyond 100 mhz) pzt kerfless linear arrays,” *IEEE Transactions on Ultrasonics, Ferroelectrics, and Frequency Control*, vol. 56, no. 10, pp. 2304–2310, 2009, ISSN: 0885-3010. DOI: 10.1109/tuffc.2009.1311.

[69] J. Elloian, J. Jadwiszczak, V. Arslan, J. D. Sherman, D. O. Kessler, and K. L. Shepard, “Flexible ultrasound transceiver array for non-invasive surface-conformable imaging enabled by geometric phase correction,” *Scientific Reports*, vol. 12, no. 1, 2022, ISSN: 2045-2322. DOI: 10.1038/s41598-022-20721-7.

[70] Y. Li, X. Jiang, B. Liang, J.-C. Cheng, and L. Zhang, “Metascreen-based acoustic passive phased array,” *Physical Review Applied*, vol. 4, no. 2, 2015, ISSN: 2331-7019. DOI: 10.1103/physrevapplied.4.024003.

[71] W. Liu, C. Zhu, and D. Wu, “Flexible and stretchable ultrasonic transducer array conformed to complex surfaces,” *IEEE Electron Device Letters*, vol. 42, no. 2, pp. 240–243, 2021, ISSN: 0741-3106. DOI: 10.1109/led.2020.3045037.

[72] H. Fang, J. Zhao, K. J. Yu, *et al.*, “Ultrathin, transferred layers of thermally grown silicon dioxide as biofluid barriers for biointegrated flexible electronic systems,” *Proceedings of the National Academy of Sciences*, vol. 113, no. 42, pp. 11 682–11 687, 2016, ISSN: 0027-8424. DOI: 10.1073/pnas.1605269113.

[73] A. Wadood, “Brief overview on nitinol as biomaterial,” *Advances in Materials Science and Engineering*, vol. 2016, pp. 1–9, 2016, ISSN: 1687-8434. DOI: 10.1155/2016/4173138.

[74] S. Jiang, X. J. Liu, J. P. Liu, *et al.*, “Flexible metamaterial electronics,” *Advanced Materials*, ISSN: 0935-9648. DOI: 10.1002/adma.202200070.

[75] J. Ortigoza-Diaz, K. Scholten, C. Larson, *et al.*, “Techniques and considerations in the microfabrication of parylene c microelectromechanical systems,” *Micromachines*, vol. 9, no. 9, p. 422, 2018, ISSN: 2072-666X. DOI: 10.3390/mi9090422.

[76] Z. Jing, Y. Guo, M. Ren, *et al.*, “Improving mechanical and water vapor barrier properties of the parylene c film by uv-curable polyurethane acrylate coating,” *e-Polymers*, vol. 21, no. 1, pp. 830–844, 2021, ISSN: 1618-7229. DOI: 10.1515/epoly-2021-0047.

[77] M. Khaw, F. Mohd-Yasin, and N. Nguyen, “Microcalorimeter: Design considerations, materials and examples,” *Microelectronic Engineering*, vol. 158, pp. 107–117, 2016, ISSN: 0167-9317. DOI: 10.1016/j.mee.2016.03.050.

[78] J. C. Barrese, N. Rao, K. Paroo, *et al.*, “Failure mode analysis of silicon-based intracortical microelectrode arrays in non-human primates,” *Journal of Neural Engineering*, vol. 10, no. 6, p. 066 014, 2013, ISSN: 1741-2560. DOI: 10.1088/1741-2560/10/6/066014.

[79] E. Mengi and Y.-C. Tai, “Parylene etching techniques for microfluidics and biomems,” in DOI: 10.1109/memsys.2005.1453993.

[80] L. Zhang, Y. Liu, Z. Li, and W. Wang, “Sf6 optimized o2 plasma etching of parylene c,” *Micromachines*, vol. 9, no. 4, p. 162, 2018, ISSN: 2072-666X. DOI: 10.3390/mi9040162.

[81] S. Horn, *Common problems with parylene*, https://blog.paryleneconformalcoating.com/wp-content/uploads/2021/03/Common_Parylene_Problems.pdf.

[82] O. R. Musaev, P. Scott, J. M. Wrobel, J. A. Wolf, and M. B. Kruger, “Uv laser ablation of parylene films from gold substrates,” *Journal of Materials Science*, vol. 46, no. 1, pp. 183–187, 2011, ISSN: 0022-2461. DOI: 10.1007/s10853-010-4906-5.

[83] S. Seok, H. Park, and J. Kim, “Characterization and analysis of metal adhesion to parylene polymer substrate using scotch tape test for peripheral neural probe,” *Micromachines*, vol. 11, no. 6, p. 605, 2020, ISSN: 2072-666X. DOI: 10.3390/mi11060605.

[84] I. Miranda, A. Souza, P. Sousa, *et al.*, "Properties and applications of pdms for biomedical engineering: A review," *Journal of Functional Biomaterials*, vol. 13, no. 1, p. 2, 2021, ISSN: 2079-4983. DOI: 10.3390/jfb13010002.

[85] J. Chungprempree, S. Charoenpongpool, J. Preechawong, N. Atthi, and M. Nithitanakul, "Simple preparation of polydimethylsiloxane and polyurethane blend film for marine antibiofouling application," *Polymers*, vol. 13, no. 14, p. 2242, 2021, ISSN: 2073-4360. DOI: 10.3390/polym13142242.

[86] T. Stieglitz, H. Beutel, M. Schuettler, and J. U. Meyer, "Micromachined, polyimide-based devices for flexible neural interfaces," *Biomedical Microdevices*, vol. 2, no. 4, pp. 283–294, 2000, ISSN: 1387-2176. DOI: 10.1023/a:1009955222114.

[87] K. Domansky, D. C. Leslie, J. Mckinney, *et al.*, "Clear castable polyurethane elastomer for fabrication of microfluidic devices," *Lab on a Chip*, vol. 13, no. 19, p. 3956, 2013, ISSN: 1473-0197. DOI: 10.1039/c3lc50558h.

[88] Y.-M. Han, S.-B. Hwang, S.-T. Lee, J.-M. Lee, and G.-H. Chung, "Polyurethane-covered self-expandable nitinol stent for malignant biliary obstruction: Preliminary results," *CardioVascular and Interventional Radiology*, vol. 25, no. 5, pp. 381–387, 2002, ISSN: 0174-1551. DOI: 10.1007/s00270-002-0439-x.

[89] M. Johnson, *Nitinol specification guidelines*, https://matthey.com/products-and-markets/other-markets/medical-components/resource-library/nitinol-specification-guidelines, 2022.

[90] S. Lavoie, *Laser cutting system and stent fabrication*, https://www.alliedscientificpro.com/blog/welcome-to-our-blogs-1/laser-cutting-system-and-stent-fabrication-140, 2016.

[91] T. Liu, A. Dangi, J. N. Kim, *et al.*, "Flexible thin-film pzt ultrasonic transducers on polyimide substrates," *Sensors (Basel)*, vol. 21, no. 3, 2021, ISSN: 1424-8220. DOI: 10.3390/s21031014.

[92] Comsol, *Acoustics module user's guide*, https://doc.comsol.com/5.4/doc/com.comsol.help.acoAcousticsModuleUsersGuide.pdf.

[93] G. K. Wardhana, M. Mastrangeli, and T. L. Costa, "Maximization of transmitted acoustic intensity from silicon integrated piezoelectric ultrasound transducers," in *2022 IEEE International Ultrasonics Symposium (IUS)*, 2022, pp. 1–4. DOI: 10.1109/IUS54386.2022.9957646.

[94] N. P. Yelve, M. Mitra, and P. Mujumdar, "Higher harmonics induced in lamb wave due to partial debonding of piezoelectric wafer transducers," *NDT & E International*, vol. 63, pp. 21–27, 2014, ISSN: 0963-8695. DOI: 10.1016/j.ndteint.2014.01.004.

[95] N. B. Babaroud, R. Dekker, W. Serdijn, and V. Giagka, "Pdms-parylene adhesion improvement via ceramic interlayers to strengthen the encapsulation of active neural implants," 2020. DOI: 10.1109/embc44109.2020.9175646.

[96] N. B. Babaroud, R. Dekker, O. Holk, *et al.*, "Investigation of the long-term adhesion and barrier properties of a pdms-parylene stack with pecvd ceramic interlayers for the conformal encapsulation of neural implants," 2021. DOI: 10.23919/empc53418.2021.9584961.

[97] K. Nanbakhsh, M. Kluba, B. Pahl, *et al.*, "Effect of signals on the encapsulation performance of parylene coated platinum tracks for active medical implants," 2019. DOI: 10.1109/embc.2019.8857702.

[98] M. A. Mahmood, D. Chioibasu, A. Ur Rehman, S. Mihai, and A. C. Popescu, "Post-processing techniques to enhance the quality of metallic parts produced by additive manufacturing," *Metals*, vol. 12, no. 1, p. 77, 2022, ISSN: 2075-4701. DOI: 10.3390/met12010077.

[99] X. Yang, C. Fei, Xinhaosun, S. Hou, and J. Chen, "Multi-layer polymer-metal structures for acoustic impedance matching in high-frequency broadband ultrasonic transducers design," in 2019. DOI: 10.1109/ultsym.2019.8926175.

[100] C. Fei, J. Ma, C. T. Chiu, *et al.*, "Design of matching layers for high-frequency ultrasonic transducers," *Applied Physics Letters*, vol. 107, no. 12, p. 123 505, 2015, ISSN: 0003-6951. DOI: 10.1063/1.4931703.

[101] M. Toda and M. Thompson, “Detailed investigations of polymer/metal multilayer matching layer and backing absorber structures for wideband ultrasonic transducers,” *IEEE Transactions on Ultrasonics, Ferroelectrics, and Frequency Control*, vol. 59, no. 2, pp. 231–242, 2012, ISSN: 0885-3010. DOI: 10.1109/tuffc.2012.2183.

A

Piezoelectric motors

Figure A.1 gives an overview of the different common types of piezoelectric motors. For each type the displacement, force and resonant frequency are expressed in piezoelectric parameters.

PIEZOELECTRIC CONFIGURATION	FREE DEFLECTION	BLOCKED FORCE	RESONANT FREQUENCY	GENERAL FEATURES
	CANTILEVER BENDING MOTOR			
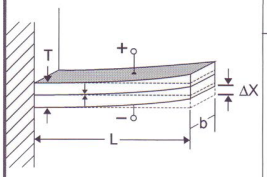	$\frac{3\, d_{31}\, L^2\, E}{2\, T}$	$\frac{3\, d_{31}\, Y\, b\, T^2\, E}{8\, L}$	$\frac{.16\, T}{L^2}\sqrt{\frac{Y_{11}}{\rho}}$	5 mm 10 - 500 grams 10 - 500 Hz $1 - $100
	SIMPLE BENDING MOTOR			
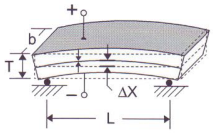	$\frac{3\, d_{31}\, L^2\, E}{8\, T}$	$\frac{3\, d_{31}\, Y\, b\, T^2\, E}{2\, L}$	$\frac{.48\, T}{L^2}\sqrt{\frac{Y_{11}}{\rho}}$	INCREASING DISPLACEMENT INCREASING FORCE INCREASING RESONANT FREQUENCY INCREASING COST
	TRANSVERSE (D31) CONTRACTION MOTOR			
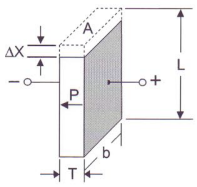	$d_{31}\, L\, E$	$d_{31}\, Y\, A\, E$ where $A = b\, T$	$\frac{1}{2\, L}\sqrt{\frac{Y_{11}}{\rho}}$	
	LONGITUDINAL (D33) EXTENSION MOTOR			
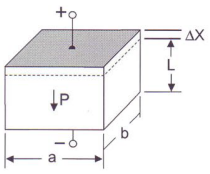	$d_{33}\, L\, E$	$d_{33}\, Y\, A\, E$ where $A = a\, b$	$\frac{1}{2\, L}\sqrt{\frac{Y_{33}}{\rho}}$	
	SHEAR MODE MOTOR			
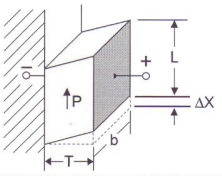	$d_{15}\, T\, E$	$d_{15}\, G\, A\, E$ where $A = b\, L$	$\frac{1}{2\, T}\sqrt{\frac{Y_{55}}{\rho}}$	µM 10^3 Kg 1 MHz $100

Figure A.1: Spectrum of motor transducers in piezoelectric applications [65].

B

Piezoelectric notation and parameters

Piezoceramics exhibit different behavior depending on strain and temperature. The three-axis notation is used to describe the directions. The first subscript is the direction of the electric field or dielectric displacement, while the second subscript denotes the mechanical stress or strain [65]. Essential parameters of piezoelectric materials are [65]:

- E - electric field [V/m] - $E = -g * T$
- g - piezoelectric voltage coefficient [V*m/N]
- D - dielectric displacement [C/m^2] - $D = d * T$
- d_D - piezoelectric charge coefficient [C/N]
- T - mechanical stress [N/m^2] (Tensile stress is positive, compressive stress is negative)
- S - mechanical strain [-] - $S = d * E$
- d_S - piezoelectric strain coefficient [m/V]
- k - coupling coefficient [-] (A measure for conversion of electrical energy into mechanical energy [the square equals the ratio of mechanical energy output to the electrical energy input])
- K - relative dielectric constant [-] (The ratio of the piezoceramics permittivity to that of empty space [$\epsilon_0 = 8.854e - 12F/m$])
- Y - Young's Modulus [N/m^2] (the ratio of stress to produce a unit of strain, describes the stiffness)

These parameters can contain a superscript that indicates the experimental setup. Four superscripts are mainly used:

- T - Constant Stress (mechanically free)
- S - Constant Strain (mechanically clamped)
- E - Constant Electric Field (electrodes short-circuited)
- D - Constant Electric Displacement (electrodes open-circuited)

C

Piezoelectric material characteristics

Table C.1 shows the characteristics of some often used bulk PZT types.

Table C.1: The different PZT ceramics and their parameters.

Parameters	Units	**PMN-PT [32] [66]**	**PMN-PZT [63]**	**PNN-PZT [61]**	**Textured PNN-PZT (3 vol. %BT) [61]**	**PZT-based 1-3 composite [32]**	**PZT-5A [32] [66]**	**PZT-5H [54] [61] [66]**	**PZT-5J [66]**
Z (acoustic impedance)	[Mrayls]	28.8	-	30.50	29.4	13.4	33.7	33.3	-
v (Longitudinal acoustic velocity)	[m/s]	3600	-	4010	3920	3200	4350	4500	-
Y_{33} **(Young's modulus)**	[Gpa]	-	-	-	-	-	49/54	49	53
ϕ **(Density)**	[g/cm^3]	8.12	-	7.6	7.5	4.19	7.75/7.95	7.4/7.87	7.9
g_{33} **(Voltage constant)**	[10^{-3} Vm/N]	35	-	-	-	19.7	24.8/23.2	19	21.3
d_{33} **(Charge constant)**	[pC/N]	1780	>2000	680	920	593	374/390	680/650	485
k_{33} **(Coupling coefficient)**	[-]	0.92	0.93	0.51	0.55	0.75	0.71	0.75	0.74
ϵ_{33} **(Permittivity)**	[F/m]	-	8000	2832	2230	-	-	3287	-
T_c **(Curie temperature)**	[° C]	140-170	150	203	203	-	350	191/225	270

D

KLM model

Obtaining the matching layer properties while maximizing the bandwidth and the maximum efficiency, can be done using the Krimholtz, Leedom and Matthaei (KLM) transmission line model [53] [51] [32]. The model is shown in Figure 3.8.

The electrical to mechanical coupling is described by the turn ratio ϕ:1. The ϕ can be found by the formula:

$$\phi = k_t(\frac{\pi}{\omega_0 C_0 Z_c})^{1/2} sinc(\frac{\omega}{2\omega_0}) \tag{D.1}$$

where k_t is the electromechanical coupling factor, while Z_c is the acoustic impedance. C_0 is the transducer clamped capacitance and defined as:

$$C_0 = \epsilon^s A/t \tag{D.2}$$

where ϵ^s is the clamped dielectric constant and A the transducer cross-section area. ω_0, the half-wavelength resonant frequency, is defined as:

$$\omega_0 = \frac{\pi v_a}{t} \tag{D.3}$$

where v_a is the stiffened acoustic velocity.
In the KLM model the transducer dimensions and k_t are represented by C', a capacitor in series with C_0. However, C' can often be neglected since it is way smaller than C_0. Another modeled impedance is L_s. It represents the series inductance [32]. It is obtained via [32]:

$$L_s = \frac{1}{(2\pi f_0)^2 C_0} \tag{D.4}$$

The transformer's secondary side represents the mechanical part. Two generated acoustic waves propagate through two transmission lines with a length of t/2. One is the interface with the backing layer having an impedance Z_B and the other is the interface with the front matching layer having an impedance Z_F. When Z_F and Z_B are smaller than Z_c the transmission line has a resonance close to ω_0. In that case, the input electrical impedance is [51]:

$$R_0 = \frac{4K_T^2}{\pi\omega_0 C_0}(\frac{Z_c}{Z_B + Z_F}) \tag{D.5}$$

Using broadband considerations while using the KLM model for a single quarter-wavelength matching layer, the acoustic impedance of the matching layer (Z_M) is defined as [53]:

$$Z_M = Z_0^{1/3} Z_B^{2/3} \tag{D.6}$$

Extending this to a double layer gives the first matching layer Z_{M1}:

$$Z_{M1} = Z_0^{4/7} Z_B^{3/7} \tag{D.7}$$

And for the second matching layer Z_{M2}:

$$Z_{M2} = Z_0^{1/7} Z_B^{6/7} \tag{D.8}$$

E

Cuff-shaped simulations

In this appendix, the acoustic pressure and intensity profiles for four different polymers as ring materials are shown.

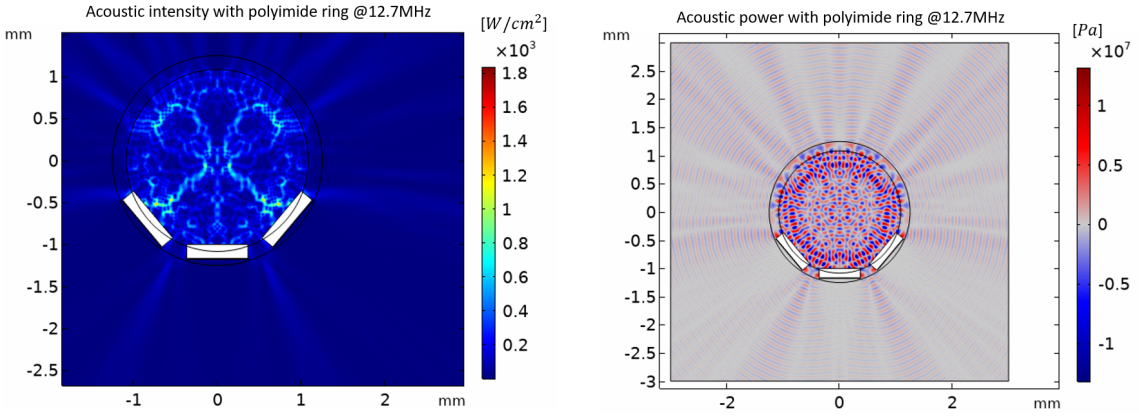

(a) The acoustic intensity $[mm/cm^2]$.

(b) The acoustic pressure $[Pa]$.

Figure E.1: The acoustic intensity and pressure for a cuff-shaped design with polyimide as ring material.

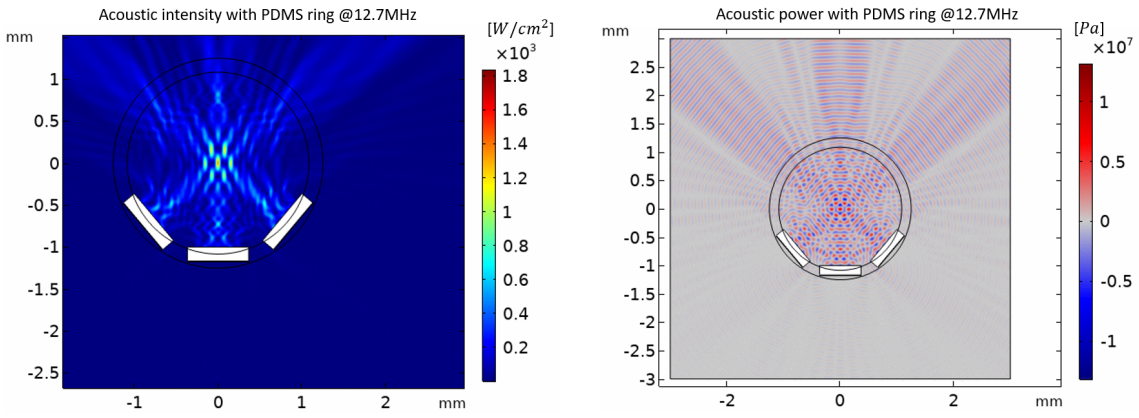

(a) The acoustic intensity $[mm/cm^2]$.

(b) The acoustic pressure $[Pa]$.

Figure E.2: The acoustic intensity and pressure for a cuff-shaped design with PDMS as ring material.

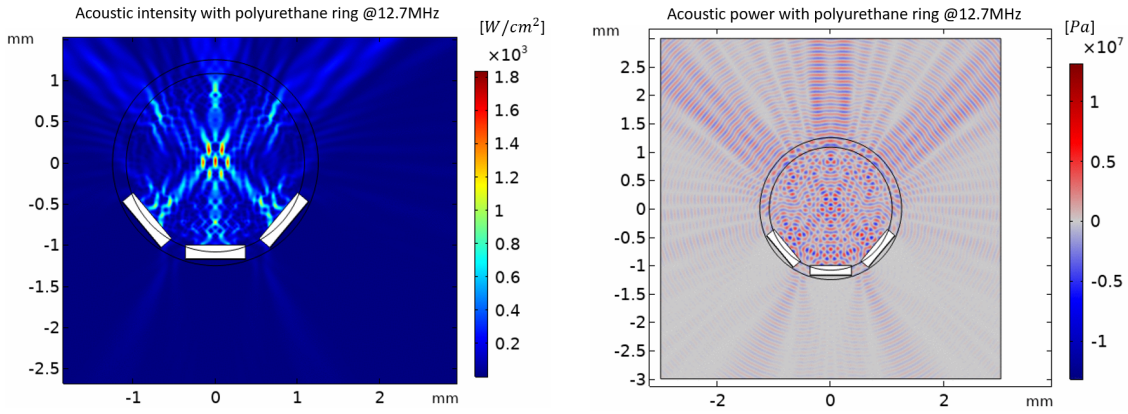

(a) The acoustic intensity $[mm/cm^2]$.

(b) The acoustic pressure $[Pa]$.

Figure E.3: The acoustic intensity and pressure for a cuff-shaped design with polyurethane as ring material.

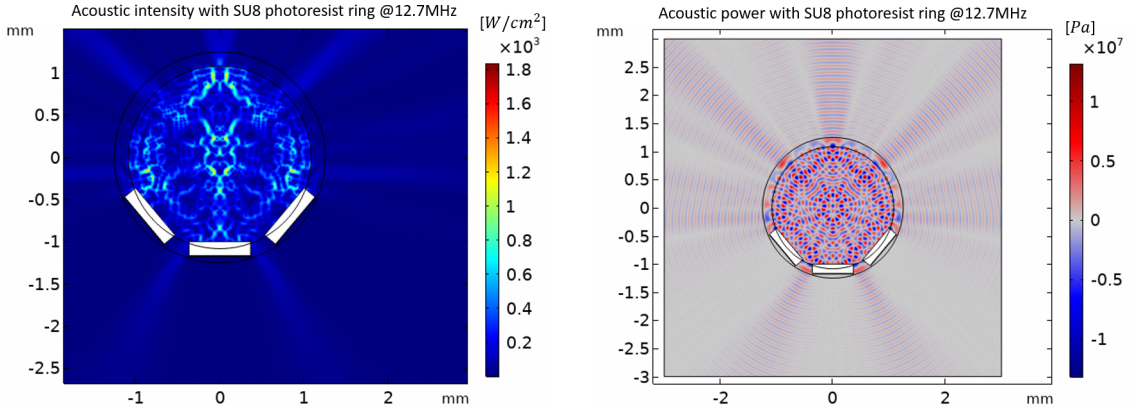

(a) The acoustic intensity $[mm/cm^2]$.

(b) The acoustic pressure $[Pa]$.

Figure E.4: The acoustic intensity and pressure for a cuff-shaped design with SU8 photoresist as ring material.

F

Measurement results

This appendix shows the measurement results of the measurements which are not presented in the main text of Chapter 7. In the caption, the measurement configuration is described.

F.1. Measurement 2

During the second measurement only two out of three transducers were transmitting acoustic waves. Therefore, only two focal spots are visible in Figure F.1c and Figure F.1d. Moreover, the frequency sweep has been performed from 1-10 MHz. Since the other sweeps have been done from 1-16 MHz, an axis till 16 MHz has been used. Due to device failure after curving, no curved measurements are obtained.

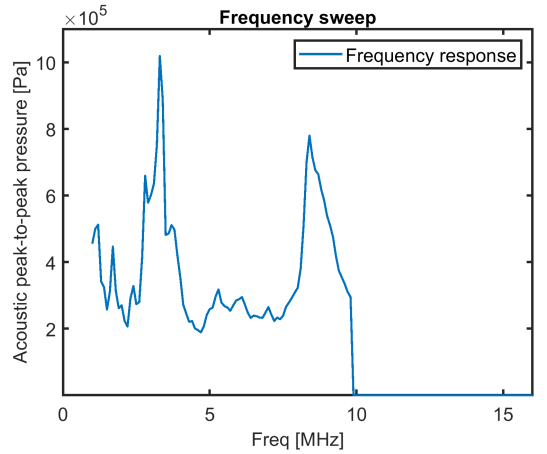

(a) The frequency sweep for a 8 MHz transducer.

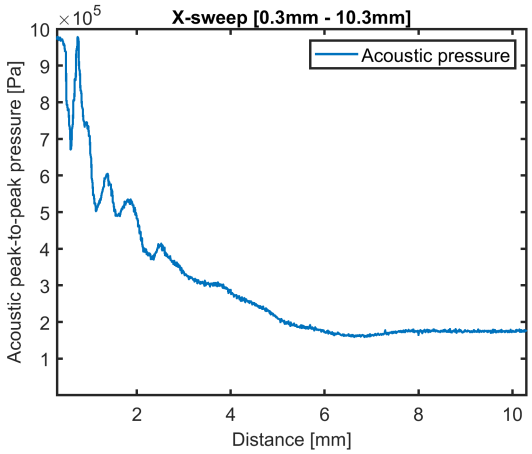

(b) The x-sweep from 0.3 mm to 10.3 mm from the surface.

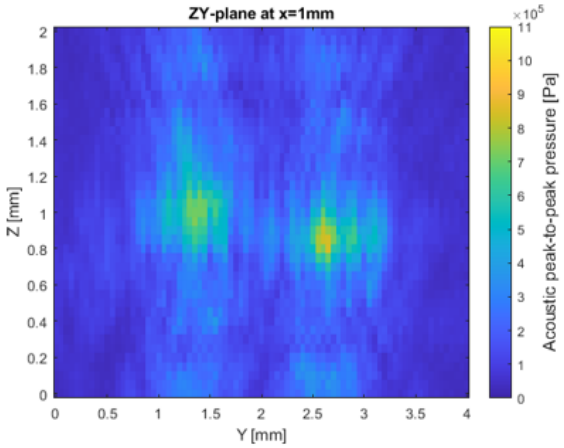

(c) The acoustic profile at a distance of 1 mm.

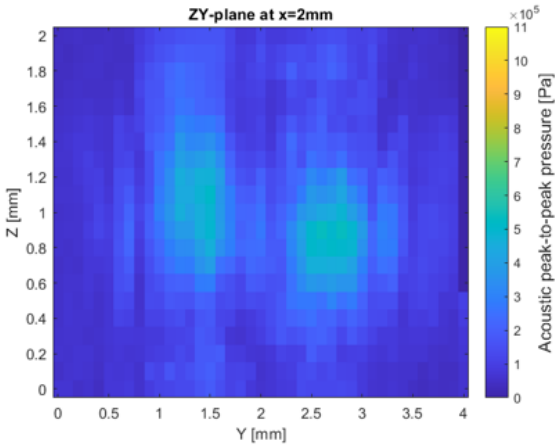

(d) The acoustic profile at a distance of 2 mm.

Figure F.1: The acoustic measurements for measurement 2.

F.2. Measurement 3

During the third measurement only two out of three transducers were transmitting acoustic waves. Therefore, only two focal spots are visible in Figure F.2.

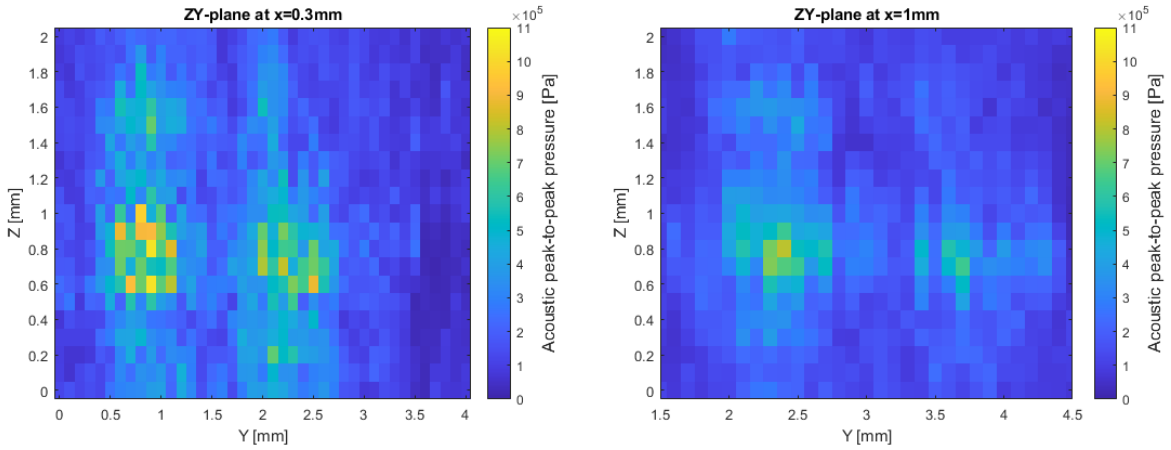

(a) The acoustic profile at a distance of 0.3 mm.

(b) The acoustic profile at a distance of 1 mm.

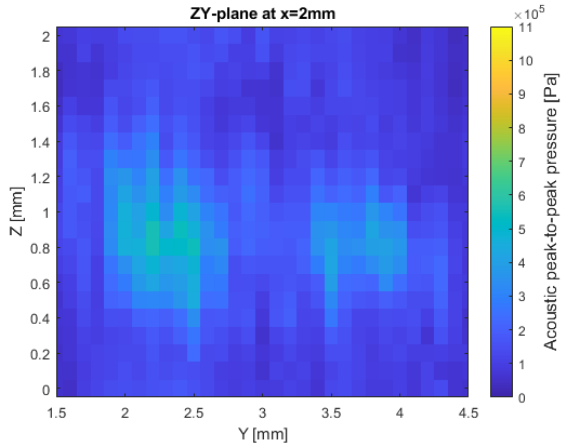

(c) The acoustic profile at a distance of 2 mm.

Figure F.2: The acoustic profiles for different distances.

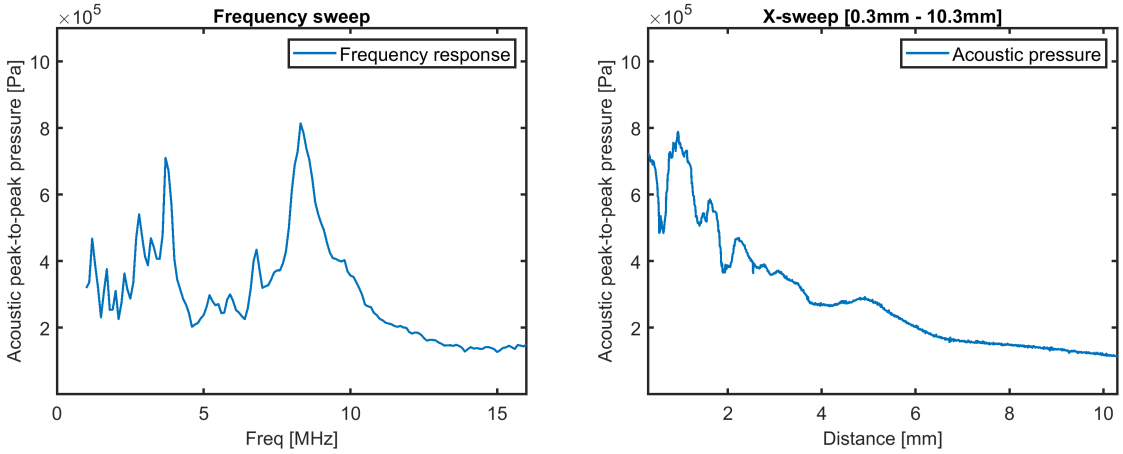

(a) The frequency response of a 8 MHz transducer.

(b) The x-sweep plot from 0.3 mm to 10.3 mm from the surface.

Figure F.3: The frequency and x-sweep plots.

F.3. Measurement 4

In the fourth measurement, the three transducers are emitting acoustic waves. However, an artifact around 3.8 MHz exists (Figure F.5a). This might be caused due to partial detachment or loading of the transducer by wire and epoxy (Chapter 7). This device has been curved and measured. The first curvature gave low acoustic pressures (Figure F.6b). Therefore, the curvature was adapted and new measurements were performed. The acoustic pressure is in the range of the pressure during planar measurements. In the focal spot (a distance of 1 mm) some small increase of pressure can be observed (compare Figure F.4b and Figure F.7c).

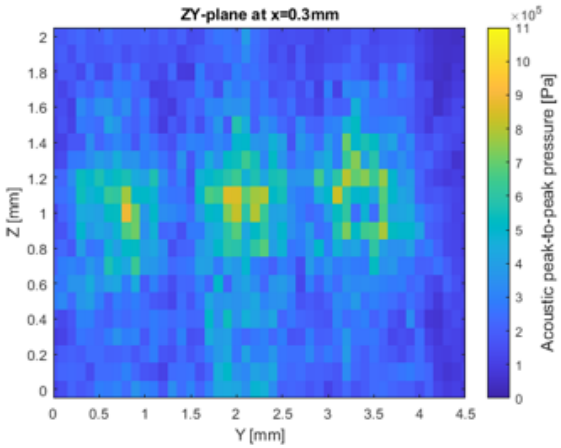

(a) The acoustic profile at a distance of 0.3 mm.

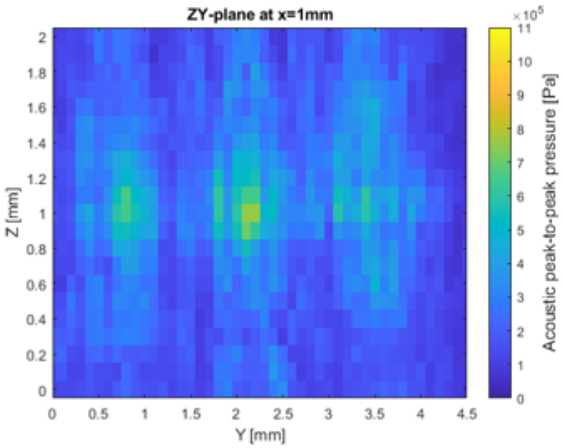

(b) The acoustic profile at a distance of 1 mm.

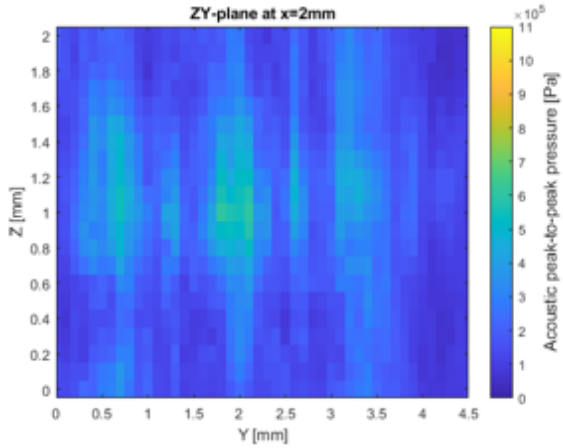

(c) The acoustic profile at a distance of 2 mm.

Figure F.4: The acoustic profiles for different distances.

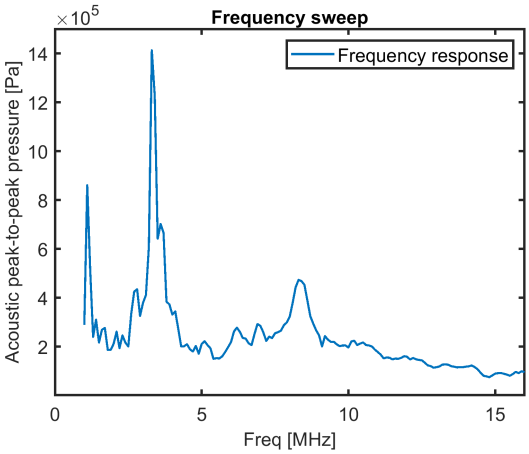

(a) The frequency response of a 8 MHz transducer.

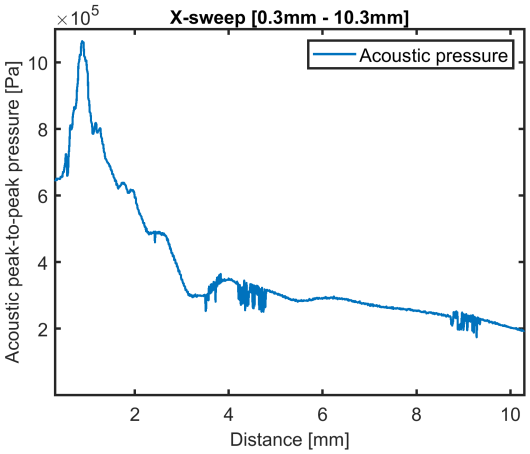

(b) The x-sweep plot from 0.3 mm to 10.3 mm from the surface.

Figure F.5: The frequency and x-sweep plots.

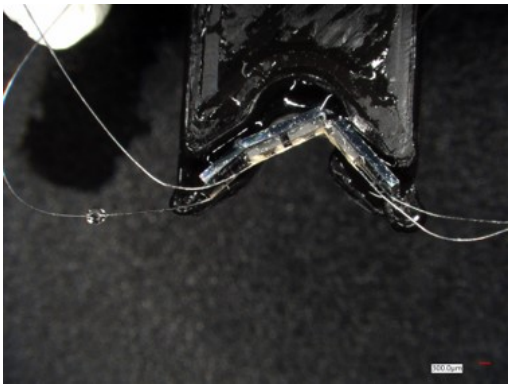

(a) The curved device.

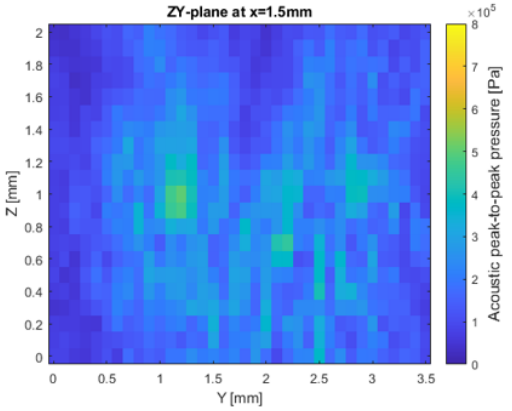

(b) The acoustic profile at a distance of 1.5 mm in the curved configuration.

Figure F.6: The first curved measurement.

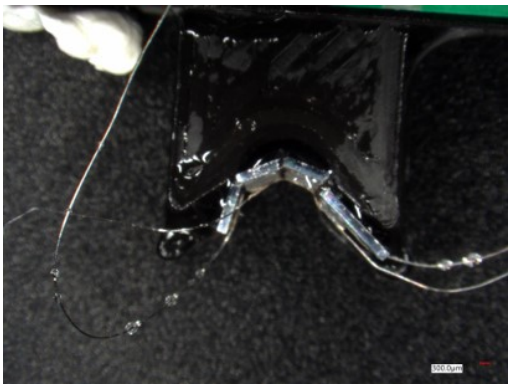

(a) The curved device.

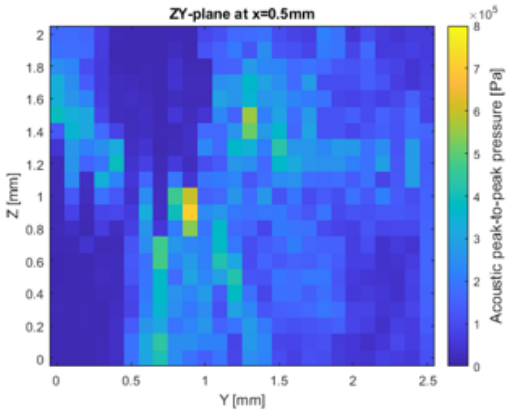

(b) The acoustic profile at a distance of 0.5 mm in the curved configuration.

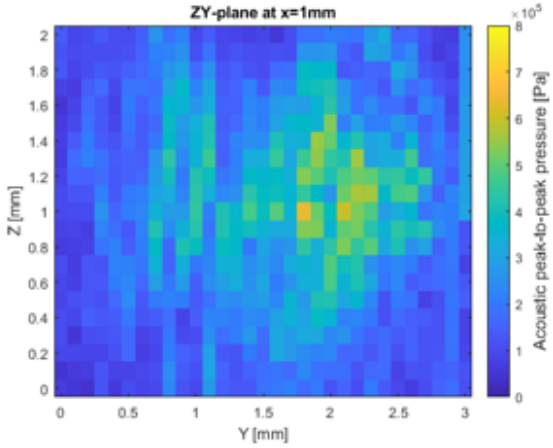

(c) The acoustic profile at a distance of 1 mm in the curved configuration.

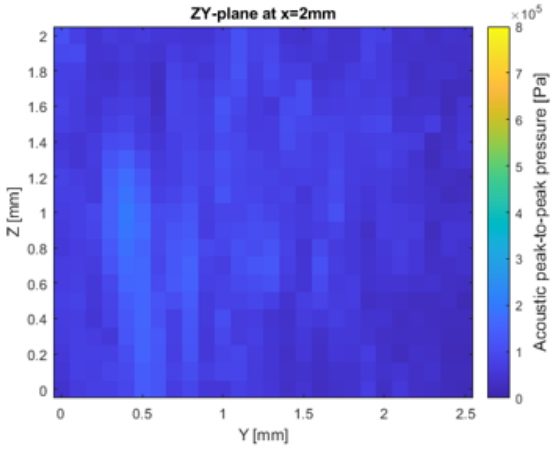

(d) The acoustic profile at a distance of 2 mm in the curved configuration.

Figure F.7: The second curved measurement

F.4. Measurement 5

During the fifth measurement, all three transducers were transmitting acoustic waves (Figure F.8). This device has been curved. During the first curvature, an airbubble was present inside the curved device, covering some transducer elements. However, even then an increase of pressure is observed. After, the airbubble was removed and new measurements were performed (Figure F.12). In Figure F.12b the focal spot is almost reached. However, after that measurement the device broke and a measurement of the focal spot at 1 mm could not be taken. The acoustic pressure is in the same range as during planar measurements. An increase was expected at the focal spot, but this could not be verified.

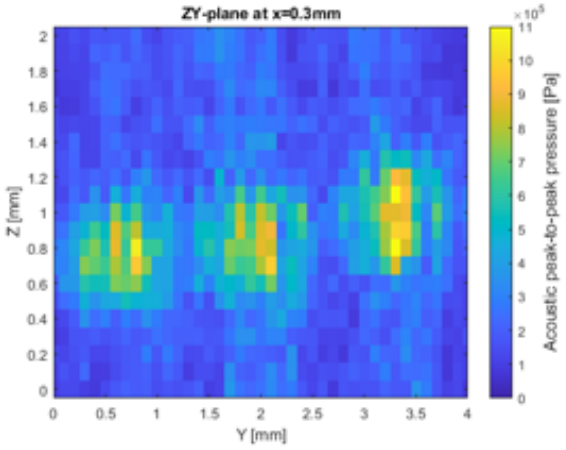

(a) The acoustic profile at a distance of 0.3 mm.

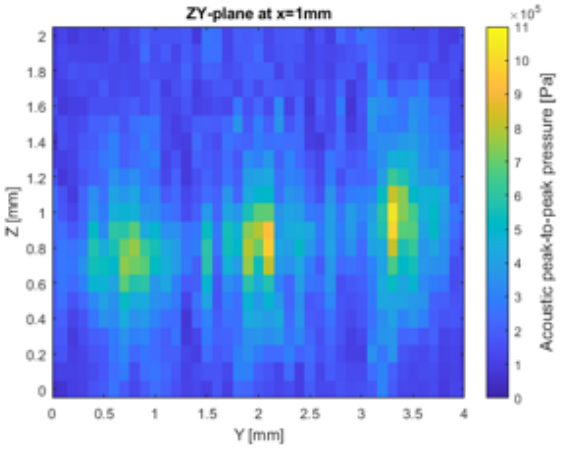

(b) The acoustic profile at a distance of 1 mm.

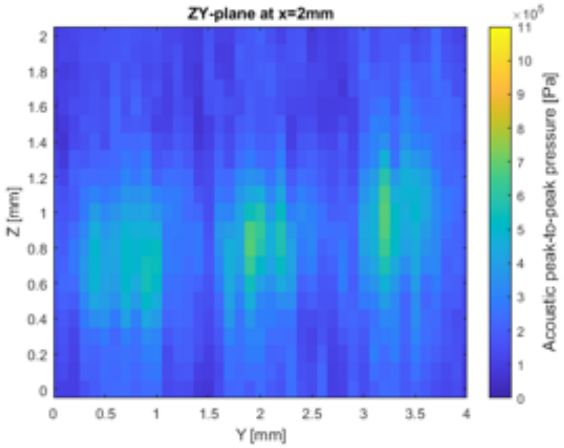

(c) The acoustic profile at a distance of 2 mm.

Figure F.8: The acoustic profiles for different distances.

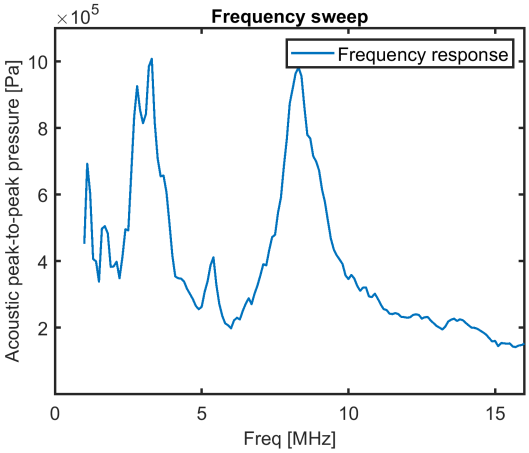

(a) The frequency response of a 8 MHz transducer.

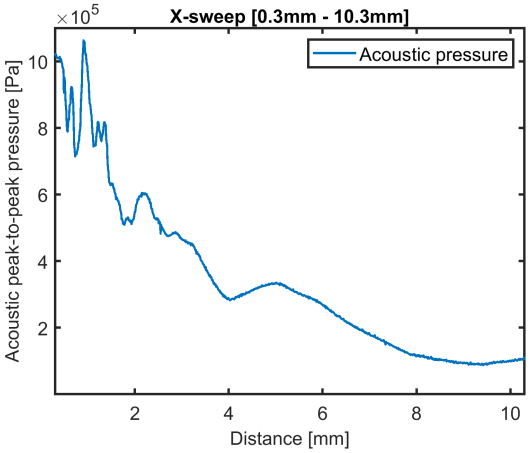

(b) The x-sweep plot from 0.3 mm to 10.3 mm from the surface.

Figure F.9: The frequency and x-sweep plots.

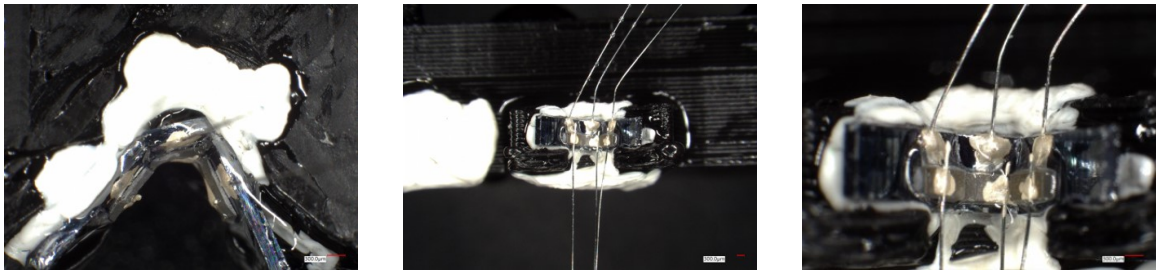

(a) Topview of the curved device. **(b)** Frontview of the curved device zoomed out. **(c)** Frontview of the curved device zoomed in.

Figure F.10: The curved device.

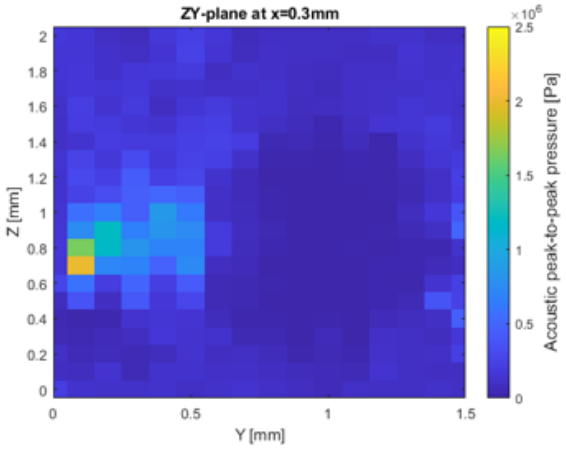

(a) The acoustic profile at a distance of 0.3 mm in curved configuration with airbubble.

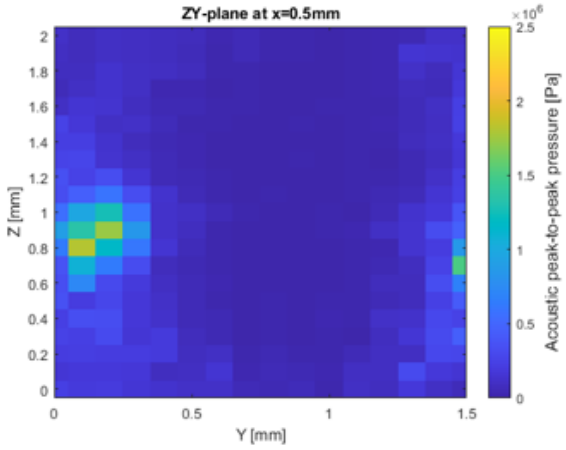

(b) The acoustic profile at a distance of 0.5 mm in curved configuration with airbubble.

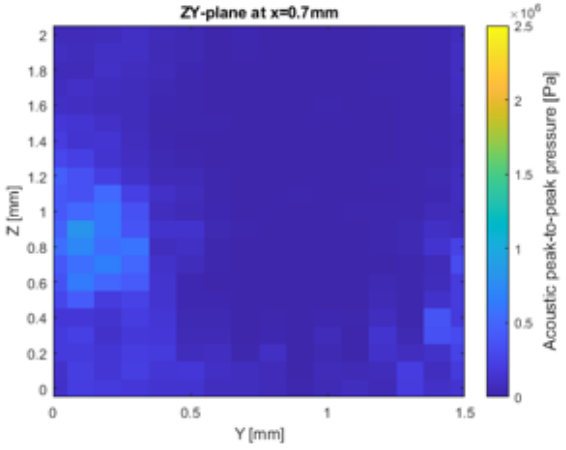

(c) The acoustic profile at a distance of 0.7 mm in the curved configuration with airbubble.

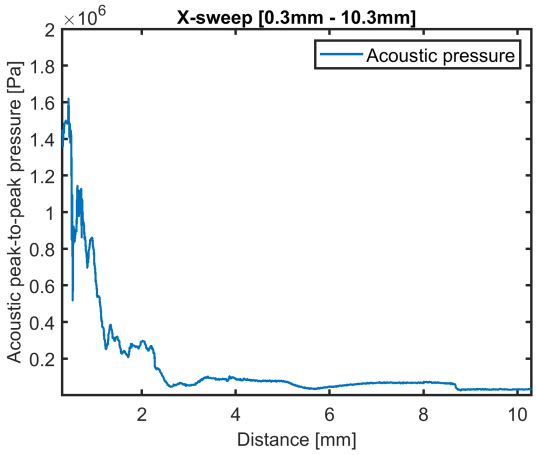

(d) The x-sweep in the curved configuration with airbubble.

Figure F.11: The curved measurement with airbubble.

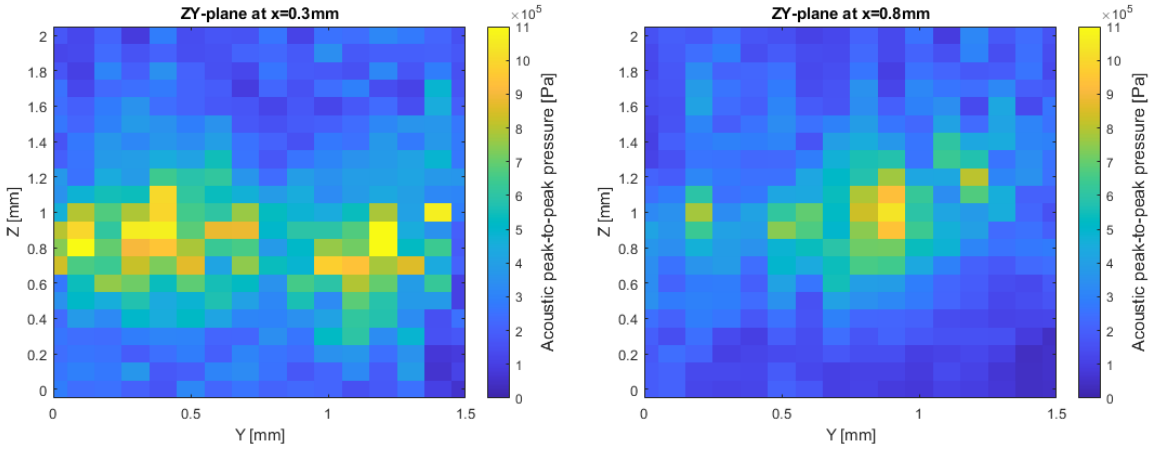

(a) The acoustic profile at a distance of 0.3 mm.

(b) The acoustic profile at a distance of 0.8 mm.

Figure F.12: The acoustic profile at different distances for a curved configuration.

F.5. Measurement 6

In this section, the additional measurements in the curved configuration are shown which are not included in Chapter 7. The sixth measurement is described in Chapter 7.

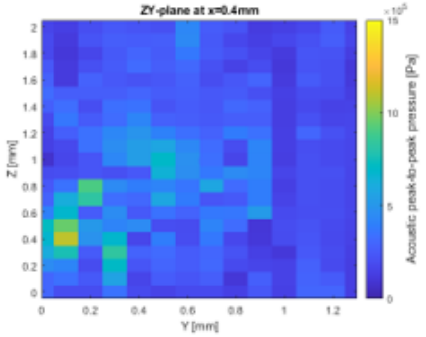

(a) The acoustic profile at a distance of 0.4 mm.

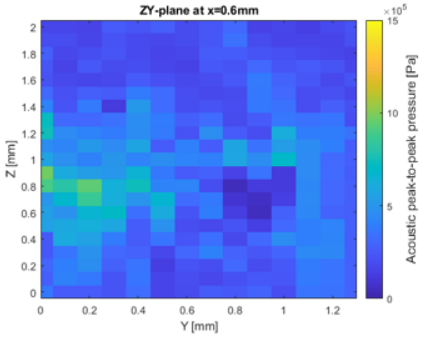

(b) The acoustic profile at a distance of 0.6 mm.

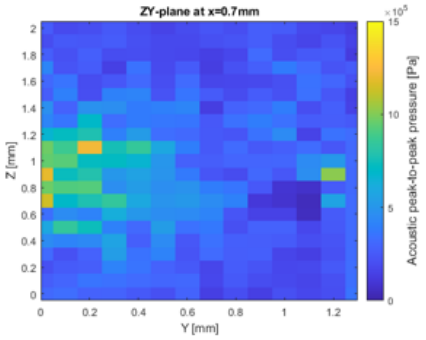

(c) The acoustic profile at a distance of 0.7 mm.

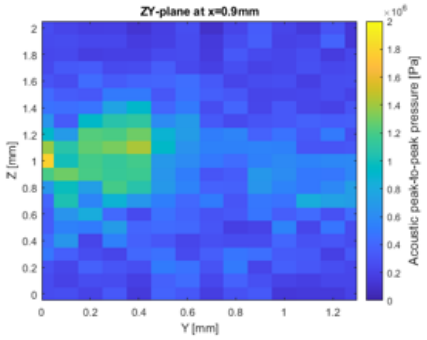

(d) The acoustic profile at a distance of 0.9 mm.

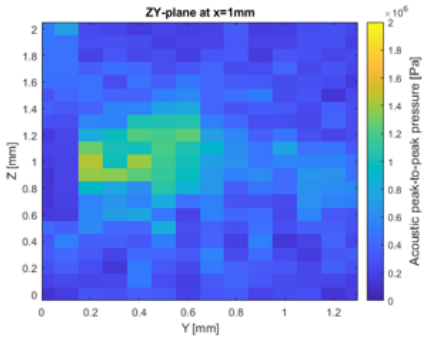

(e) The acoustic profile at a distance of 1 mm.

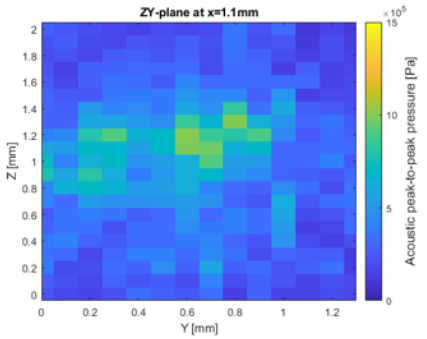

(f) The acoustic profile at a distance of 1.1 mm.

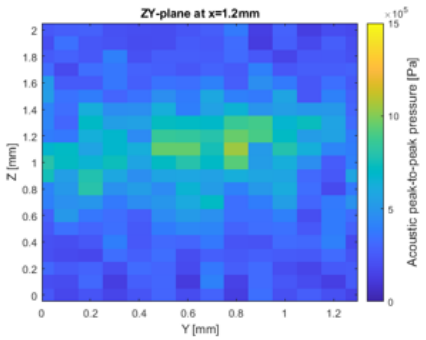

(g) The acoustic profile at a distance of 1.2 mm.

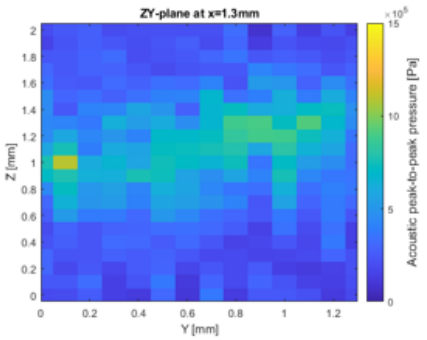

(h) The acoustic profile at a distance of 1.3 mm.

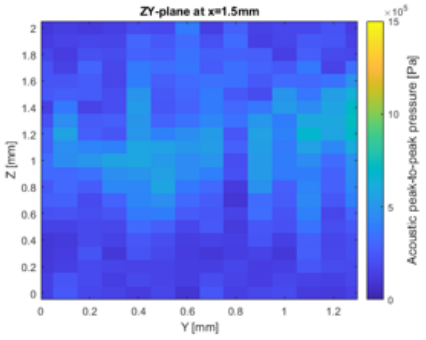

(i) The acoustic profile at a distance of 1.5 mm.

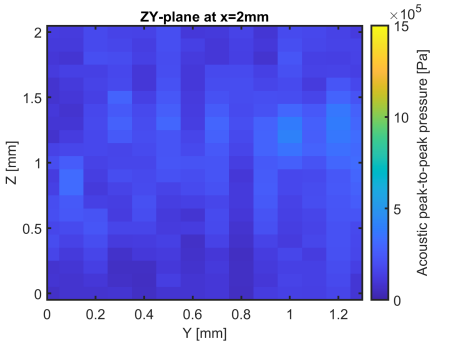

(j) The acoustic profile at a distance of 2 mm.

Figure F.13: The acoustic profile at different distances for a curved configuration.

F.6. Measurement 7

During the seventh measurement only one transducer was transmitting acoustic waves. However, this device broke after the second planar scan and the frequency sweep (Figure F.14c) shows the decreased output pressure afterward. Therefore, this measurement has been aborted. The first planar scan has been done using a 0.2 mm step size, the second planar scan used a 0.1 mm step size.

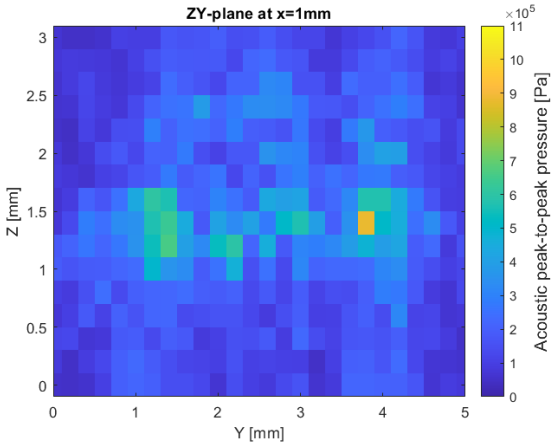

(a) The acoustic profile at a distance of 1 mm with a stepsize of 0.2 mm.

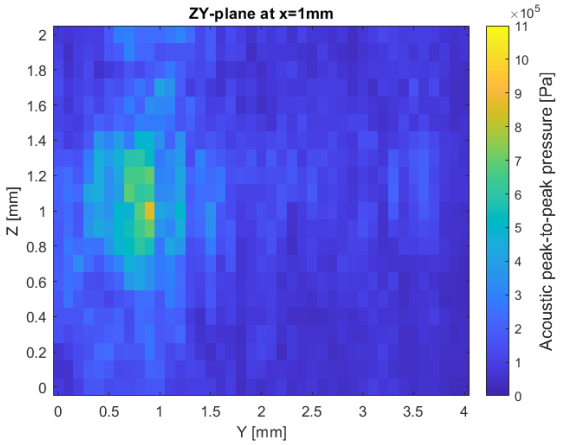

(b) The acoustic profile at a distance of 1 mm with a stepsize of 0.1 mm.

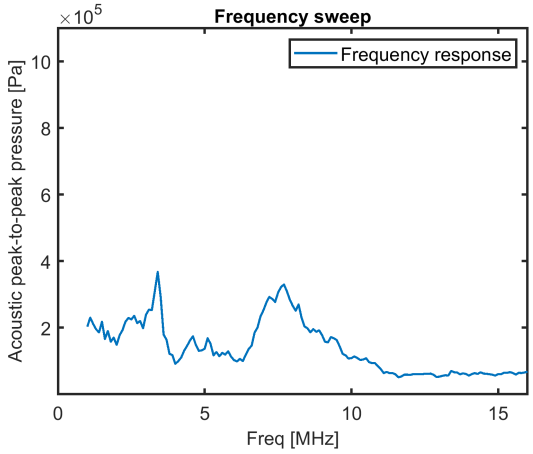

(c) The frequency response.

Figure F.14: Measurements with an airbacked device.

F.7. Measurement 8

During the eighth measurement, low acoustic pressure was observed, which did not match the previous measurements. The hypothesis is that something went wrong with the attachment of the ACF, resulting in a bad electrical connection. Therefore, this measurement has been aborted.

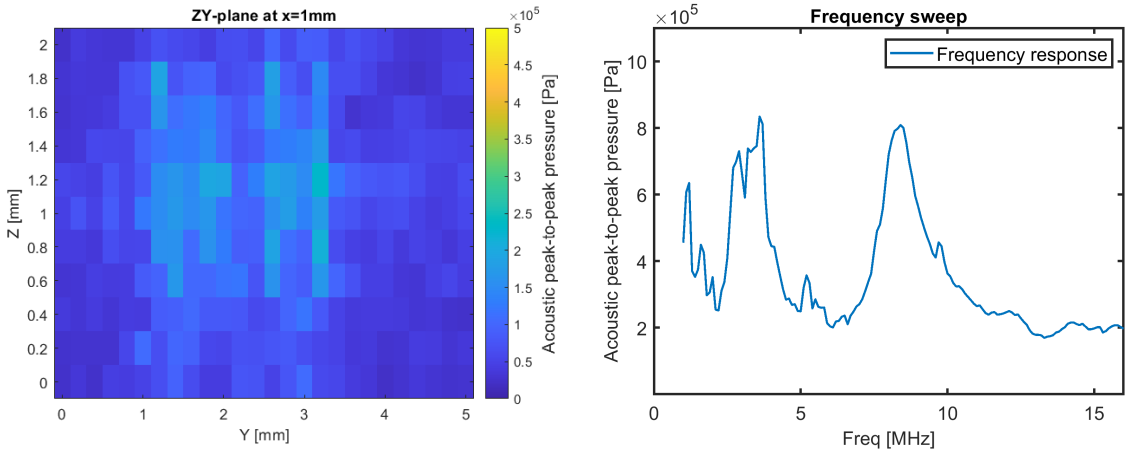

(a) The acoustic profile at a distance of 1 mm.

(b) The frequency response.

Figure F.15: Measurements with an airbacked device.

F.8. Measurement 9

This measurement is the first measurement done with a 16 MHz device. The planar scans show four transducers transmitting acoustic waves (Figure F.16). The artifact in the frequency sweep (Figure F.17a) is discussed in Chapter 7. After the device was curved, other measurements were performed (Figure F.18). The device broke after two scans and the focal spot was not determined. Therefore, an increase in acoustic pressure at the focal spot was not verified.

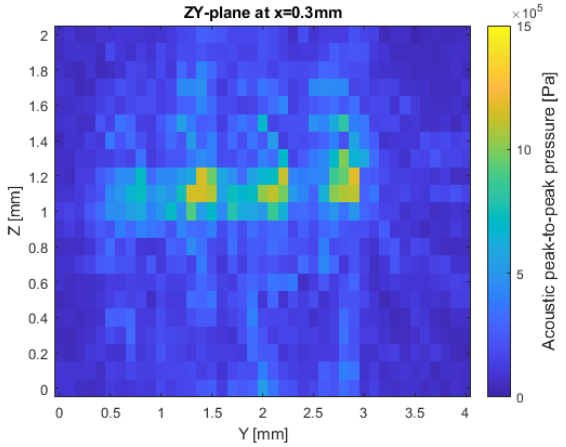

(a) The acoustic profile at a distance of 0.3 mm.

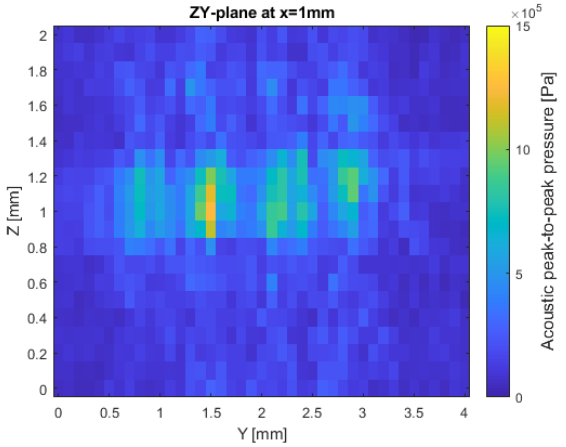

(b) The acoustic profile at a distance of 1 mm.

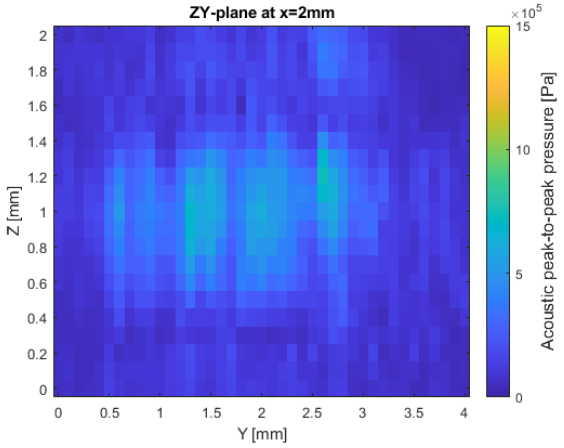

(c) The acoustic profile at a distance of 2 mm.

Figure F.16: The acoustic profiles for different distances.

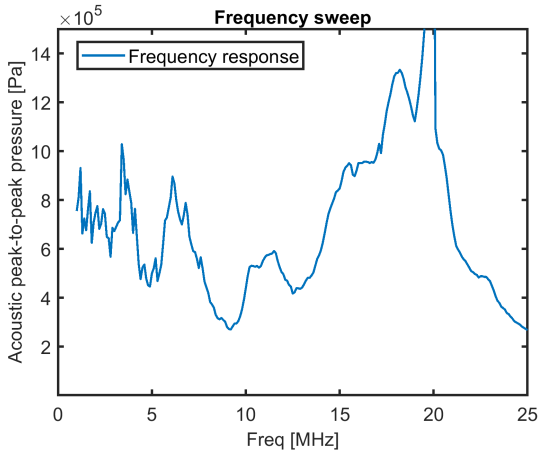

(a) The frequency response of a 16 MHz transducer.

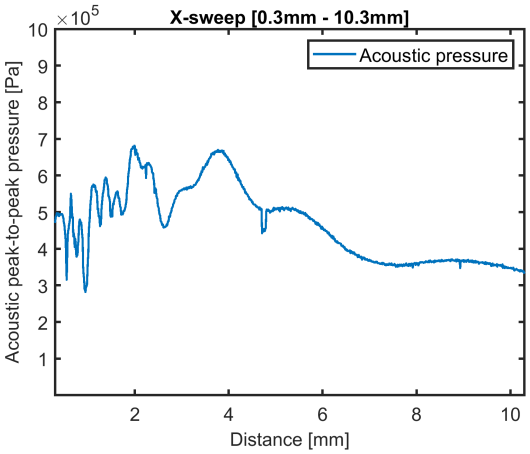

(b) The x-sweep plot from 0.3 mm to 10.3 mm from the surface.

Figure F.17: The frequency and x-sweep plots.

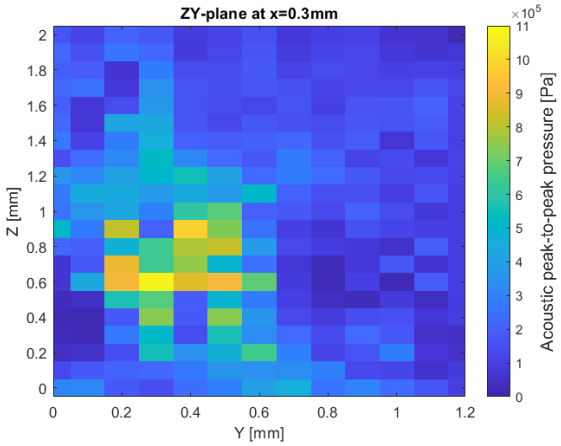

(a) The acoustic profile at a distance of 0.3 mm.

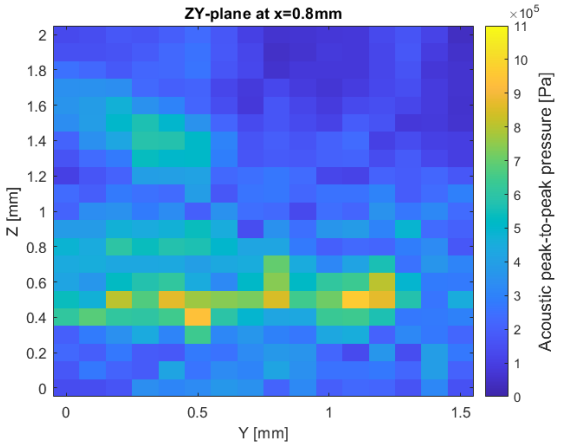

(b) The acoustic profile at a distance of 0.8 mm.

Figure F.18: The acoustic profiles for different distances for a curved configuration.

F.9. Measurement 10

During the tenth measurement, another 16 MHz device was tested. The planar output pressures reached a relatively high level of around 1.4 MPa compared to previous measurements. However, the pressure dropped severely after curving and the pressure profile was not as expected. Therefore, the hypothesis is that the wire of one or two transducers was detached during curvature. As the 16 MHz transducers are smaller and more fragile than the 8 MHz transducers, the detachment of wires occurred frequently.

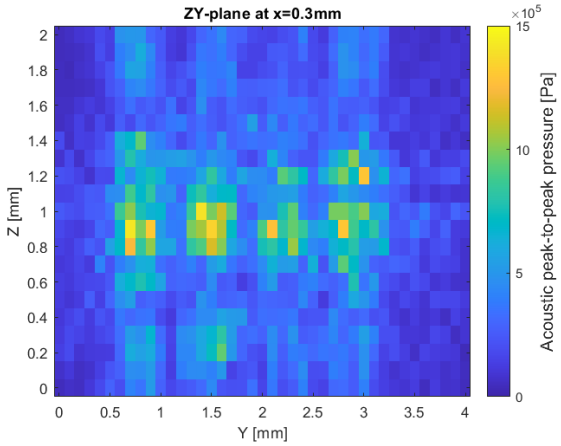

(a) The acoustic profile at a distance of 0.3 mm.

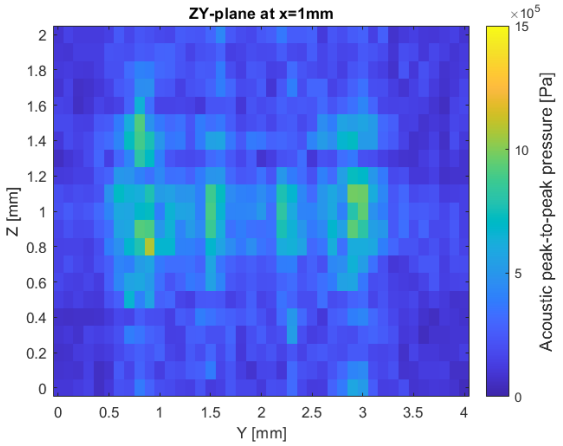

(b) The acoustic profile at a distance of 1 mm.

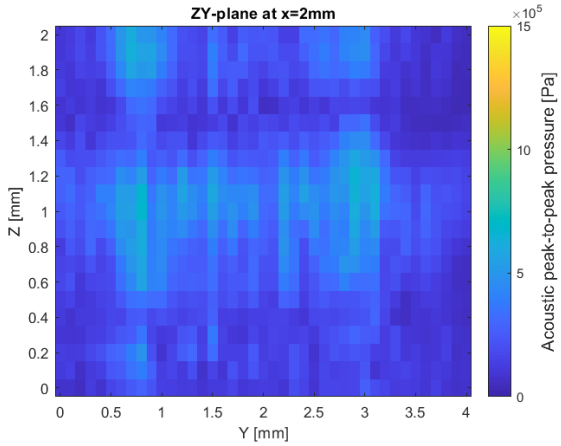

(c) The acoustic profile at a distance of 2 mm.

Figure F.19: The acoustic profiles for different distances.

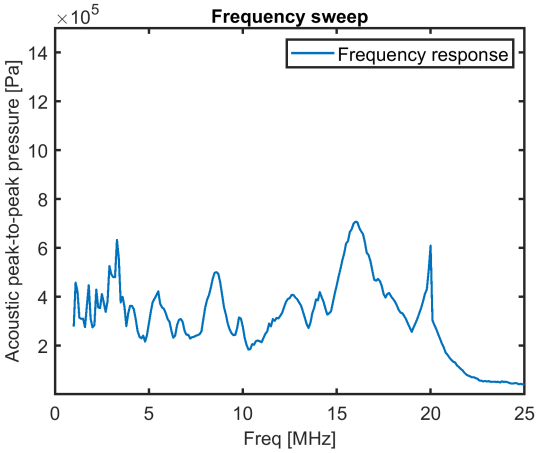

(a) The frequency response of a 16 MHz transducer.

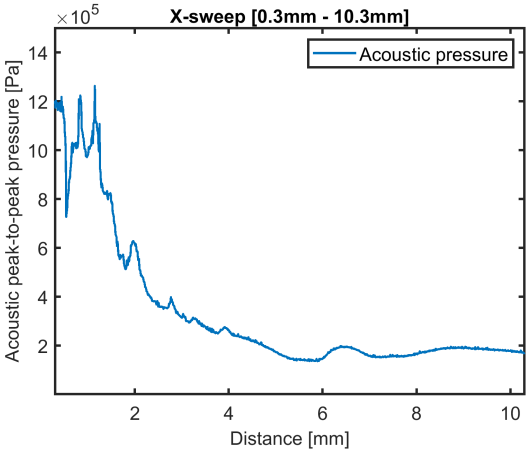

(b) The x-sweep plot from 0.3 mm to 10.3 mm from the surface.

Figure F.20: The frequency and x-sweep plots.

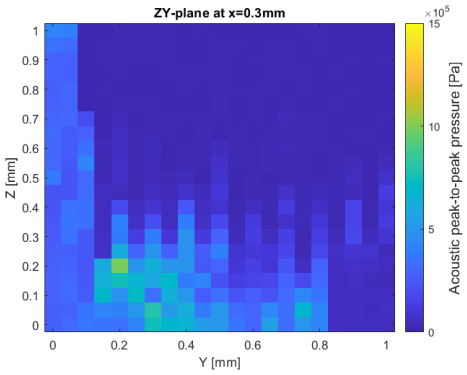

(a) The acoustic profile at a distance of 0.3 mm.

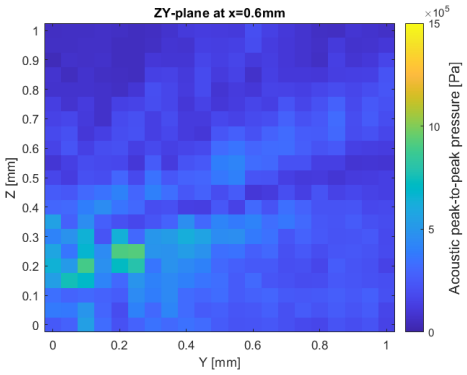

(b) The acoustic profile at a distance of 0.6 mm.

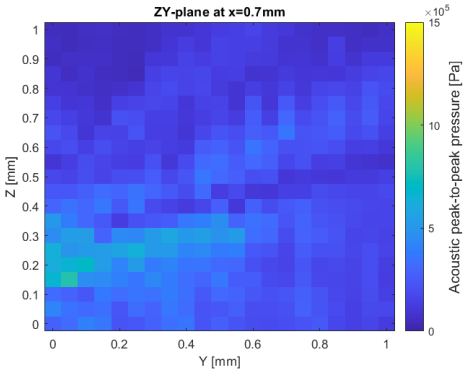

(c) The acoustic profile at a distance of 0.7 mm.

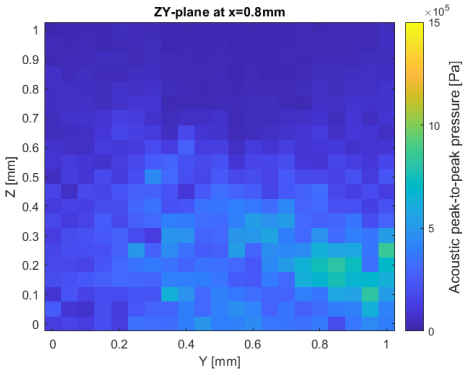

(d) The acoustic profile at a distance of 0.8 mm.

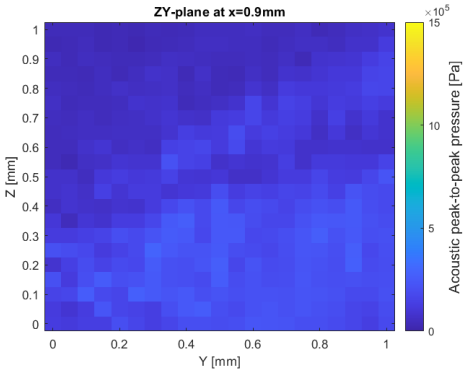

(e) The acoustic profile at a distance of 0.9 mm.

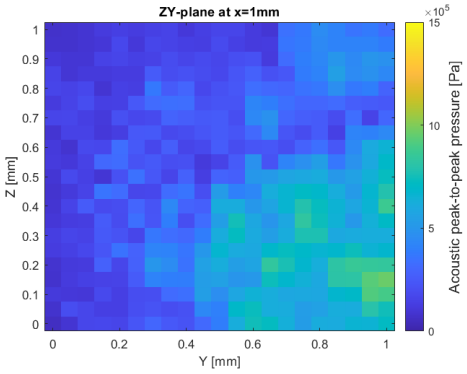

(f) The acoustic profile at a distance of 1 mm.

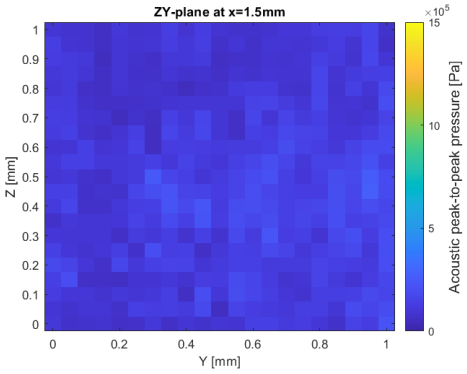

(g) The acoustic profile at a distance of 1.5 mm.

Figure F.21: The acoustic profile at different distances for a curved configuration.